DOCTORAL THESIS

Search for supersymmetry with the ATLAS detector at the Large Hadron Collider in final states with two hadronically decaying τ-leptons

Fantastic taus and Where to Find Them

UNIVERSITY OF SUSSEX

A thesis submitted in fulfilment of the requirements for the degree of Doctor of Philosophy

in the

Experimental Particle Physics Research Group
School of Mathematical and Physical Sciences

Author:
Mario GRANDI

Supervisor:
Prof. Fabrizio SALVATORE

19th August 2021

To my parents Lorenzo and Giovanna, who have guided and supported me through the years.

To my closest friends, who I shared this crazy journey with.

To Olivia, who inspires me to be better every day and I would be lost without.

ACKNOWLEDGEMENTS

As much as I have enjoyed my time spent as an undergraduate at the University of Sussex, these last 3.5 years have been the most amazing time I've spent at Sussex, largely due to my supervisor Fabrizio Salvatore. Your incredible guidance, support, and kindness both on work-related and personal aspects of the PhD, kept me inspired and motivated to carry out my research and grow as a person and a physicist. I could not have wished for a better mentor to help me with this journey. Thank you from the bottom of my heart. I also would like to thank my second supervisor, Antonella De Santo, who was always ready to support me with her immeasurable knowledge and kindness whenever I needed it.

A massive thanks must go Mark Sutton whom, in his röle of my technical supervisor, singlehandedly taught me the large majority of my current knowledge and skills. I hope you enjoyed as much as I did our long evenings spent chatting in front of a computer or a cold beer. I would also like to extend a special thank you to Fabrizio Miano for his incredible help and support during the very beginning of my PhD (and for letting me use your latex template!). As for Alex, Iacopo, Kate, Tom, Batool, and Benedict, I thank you all for all the help and assistance you provided, both at work and outside. Sometimes what is needed to become a better researcher is something as trivial as rolling a natural 20 on the right day.

I am grateful to all the members of ATLAS involved in the ID trigger, direct-stau and Fake-Tau Task-Force. In particular: Stefan, Xuai, Antonio, Vojtech, and Kassem, who have continuously provided me with an incredible amount of help and support.

I would also like to thank all my colleagues around the world, who have now become some of my closest friends and have made this time spent at Sussex truly special: Dani, Marco, Odrej, Meirin, Fabio, Fabrizio (EWK), Giuseppe, and Sebby. A huge thanks to the Mario Spina and Ioannis Xiotidis, my comrades on this epic odyssey, for the cheerful presence, constant support, and friendship you have provided.

I would also like to thank Mario and Alex for listening to my physics rants, and to their wives Lucia and Bri, for stopping us and providing the wine and the fun times that we desperately needed. I am grateful to Luca for the moral support and for sharing with me all his PhD experiences both the good and the bad, and for never being disappointed by my performance. I should also thank Lilly for keeping me company throughout these last couple of months, even when I didn't want it.

Thank you Mary-Lynn and Patrick for the helpful cheering and support you provided throughout the years.

To my friends around the globe that have known me for many years and have, despite the distances and time, kept our friendships alive and have encouraged me through these years, I thank you.

To all my family, who has always encouraged and supported me, was my safety net and my source of drive, I wish to give you the biggest *thank you*. Mamma and Papis, you are the reason

of how and why I've been able to reach this point. You inspired me to push myself beyond what I believed I was capable of. All I have become is all thanks to you. Ciccio e Tere, thank you for pushing me intellectually (and sometimes physically) and for always being by my side.

Finally, to you my love, Olivia. Your love, kindness, patience and encouragements made me do what I thought was impossible. None of this would have happened without you, and everything I strive to be is because you.

I, Mario GRANDI, hereby declare that this thesis has not been and will not be, submitted in whole or in part to another university for the award of any other degree.

Brighton,
19th August 2021

Mario GRANDI

University of Sussex
School of Mathematical and Physical Sciences
Experimental Particle Physics Research Group

DOCTORAL THESIS

Search for supersymmetry with the ATLAS detector at the Large Hadron Collider in final states with two hadronically decaying τ-leptons

Fantastic taus and Where to Find Them

by Mario GRANDI

ABSTRACT

In this thesis I present all the work that I have done during my PhD. First, I will present the search for the supersymmetric partner of the τ-lepton in 13 TeV proton-proton collisions at the LHC using data collected between 2015 and 2018 by the ATLAS detector. This search uses events with two hadronically decaying τ-leptons and missing transverse momentum in the final states. In this analysis I have been responsible for the signal region optimisation, the optimisation of the triggers and the theory systematic calculation. Results were interpreted considering natural supersymmetric extensions to the standard model in the R-parity conserving decays. No significant excess was observed and stringent exclusion limits were set. During my PhD I have also had leading involvement in the characterisation of the performances of the Inner Detector Trigger, which I will discuss in this thesis. Finally, stemming from my analysis work, I had major involvement in the study of a novel technique for estimating the contribution of mis-identified τ-leptons in signal enriched regions. A tool using this technique is currently under development in the ATLAS collaboration, that will become ATLAS approved in the very near future.

CONTENTS

INTRODUCTION

I may make you feel, but I can't make you think.

Jethro Tull

Leucippus and Democritus, two Greek philosophers in the 5th century BC, were the first recorded people to propose the idea that matter is composed of small indivisible particles called atoms. Particle physics has come a long way since then, culminating in the 20th century with the overwhelming success of the Standard Model (SM) [1] and the discovery of sub-atomic particles. We have now a better understanding of the matter that constitutes the universe than we've ever had, albeit that can be said to be true for any point in the history of mankind. Perhaps what differs now is that we have a better understanding of what we know we don't know. Thanks to the technological advances achieved in the last century, particle physicists have been able to study the most elusive of elementary particles at energies that were only present moments after the Big Bang. This resulted in many discoveries being made and many questions answered. But there are still fundamental problems that need to be solved before we can really understand this universe we inhabit.

The SM provides a framework that describes the known elementary particles and their interactions. Its robustness and prediction powers have been tested experimentally many times by a large plethora of different experiments, some of which have been based at the European Organization for Nuclear Research (CERN) such as the Large Electron-Positron Collider (LEP), which tested the so-called electroweak sector, and the A Toroidal LHC ApparatuS (ATLAS) and Compact Muon Solenoid (CMS) experiments at LHC, which were the first to identify the Higgs boson. However, the SM is still incomplete as it fails to address problems such as in the Higgs sector or explain *dark matter*. One of the most established extensions to the SM proposed to address these issues is Supersymmetry (SUSY). In this hypothesis fermion-boson symmetry is introduced, giving SM particles corresponding SUSY partners, with a mass around the 1 TeV scale. The SUSY extension gives rise to a particle that fits the characteristics of dark matter and is able to provide a natural solution to the hierarchy problem introduced by the Higgs boson mass.

This thesis presents the work carried out over a 3.5-year Doctor of Philosophy (PhD) degree in the search of SUSY focusing on the direct stau-slepton ($\tilde{\tau}$) production from proton-proton collisions with fully hadronic final state and missing transverse momentum. The author was part of the group, within the ATLAS collaboration, that performed this analysis using data recorded between 2015 and 2018 at centre-of-mass energies of $\sqrt{s}$= 13 TeV at the LHC. The resulting work has been described in a paper published in the *Physical Review D* journal [2] in February 2020. The thesis will begin with Chapter 1, which described the theoretical concepts and motivations for SUSY searches along with their current status. This will be followed by a description of the experimental apparatus given in Chapter 2. A general description of the ATLAS trigger system alongside with the work performed by the author on the ATLAS Inner Detector (ID) trigger, as part of his qualification task, is presented in Chapter 3. The work done in the study of the performance of the ID trigger has been summarised in a paper currently undergoing the last steps of the ATLAS review process before being submitted for publication. Chapter 4 presents the analysis carried out by the author as part of the direct-stau analysis team within the ATLAS SUSY working group. The author had major contributions in the optimisation of the signal region definitions with the performance study done on combined τ-lepton triggers, and in the estimation of theory uncertainties for the main SM background processes. The author has also had significant contribution in the development of a novel technique used for the estimation of mis-identified jets faking tau-leptons (fake-τ) in the ATLAS detector, called *Universal Fake Factor* method. Once fully developed this method will be available to any analysis involving τ-leptons, alongside with a tool that will use this method as basis to estimate the contribution of fake-τ's in any given region. A full description of the method, tool development, and most recent results is given in Chapter 5. The work carried out by the author in several studies centred around future searches of the $\tilde{\tau}$ for Run-3 of the LHC are described in Chapter 6. A strong emphasis is given towards the study of stau-producing SUSY signals in association with jets originating from Vector Boson Fusion topologies for the exploration of the compressed stau mass region. Studies on ongoing work towards the developments of trigger, to target these SUSY scenarios for Run-3 and the High-Luminosity LHC are also presented.

THE STANDARD MODEL AND BEYOND

1

Many times I've lied, many times I've listened, many times I've wondered how much there is to know.

Led Zeppelin

The Standard Model (SM) is the theoretical framework used to describe the physics of elementary particles and their interaction. Although it has had significant success in describing and predicting particle and their properties, it also possesses several limitations such as the non-natural radiative corrections to the Higgs boson mass at Plank mass scale energies, and does not predict the existence of dark matter. Beyond Standard Model (BSM) hypotheses aim to address these limitations by providing valid extensions to the SM at high energies. One of such extensions is Supersymmetry (SUSY), which postulates the existence of a new symmetry that links fermions to bosons and introduces additional particles called sparticles. The production and detection of these sparticles would allow for a new range of phenomena to be tested experimentally.

In Section 1.1 an overview of the SM of particle physics is presented, together with its limitations. Section 1.2 provides a discussion of the proposed SUSY extension to the SM to address some of these limitations. Finally, Section 1.3 presents an overview of current experimental results on the search of Electroweak SUSY at the Large Hadron Collider (LHC), which are relevant for the studies shown in this thesis.

1.1 The Standard Model

All the phenomena of particle physics, in terms of the properties and interaction of the known fundamental particles, is attempted to be explained by the SM [1]. The SM describes all matter as composed by 4 distinct types of particles. The first two are *leptons* and *quarks* and are spin-$\frac{1}{2}$ fermion, the third are a set of *gauge bosons* that act as "force carriers", and the last is the Higgs boson. There is good experimental evidence that supports the SM of particle physics as it was

able to be used to successfully predict the existence of many particles including the W and Z bosons, and Higgs boson, all of which have been observed first at European Organization for Nuclear Research (CERN) [3–7].

The SM is a Quantum Field Theory (QFT) [8] that describes particles as excitations of their corresponding quantum field, which give rise to the particle's intrinsic physical properties (mass, charge, spin, colour etc...) and is able to describe the weak, electromagnetic and strong forces.

The elementary particles described by the SM can be generally classified by their spin properties. *Fermions*, which correspond to leptons and quarks and are generally referred to as "matter" particles, possess half-integer spin in units of $\hbar$, while *bosons*, known as the "information" carrier, have integer-spin values. The spin-1 bosons are known as the gauge bosons and are generally considered as the "force" mediators. Figure 1.1 shows the elementary particles of the SM known today, separated into the different groups described above.

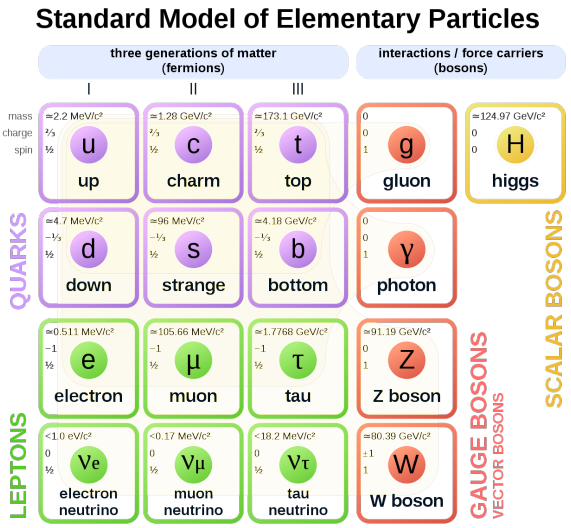

Figure 1.1: Elementary particles of the SM. Fermions are separated into quarks (purple) and leptons (green) and arranged into columns according to generation. The fourth and fifth columns show the Gauge (red) and Higgs (yellow) bosons, respectively. Approximate values of the masses are given.

Symmetries and Gauge Groups

As mentioned in the previous section, the SM uses QFT to describe particle dynamics by Lagrangian field densities:

$$\mathcal{L} = \mathcal{L}(\varphi, \partial_\mu \varphi), \tag{1.1}$$

where φ is a fermion field and $\partial_\mu \varphi$ is the partial derivative four-vector of all generalised spatial coordinates. The equations of motion of a system, as described using Lagrangian formalism, are derived by minimising the action $\mathcal{S}$, where:

$$\mathcal{S} = \int \mathcal{L}\, dt. \tag{1.2}$$

Noether's theorem states that every differentiable symmetry of the action of a physical system, $\mathcal{S}$, has a corresponding conservation law [9]. Here, a symmetry is a property of a physical system that under certain transformations remains preserved.

The SM is described as a QFT *gauge theory*, meaning that its Lagrangian is invariant under a set of gauge transformations [10]. A gauge transformation is a continuous set of local transformations between all possible gauges, forming a *Lie group*, which can be represented through

a basis of linear transformations. For each group generator associated to any Lie group, a corresponding *gauge field* emerges. These fields relate to the symmetry transformations at different points in space-time, and their corresponding quanta are called *gauge bosons*.

The full SM gauge symmetry group can be described as:

$$U(1)_Y \otimes SU(2)_L \otimes SU(3)_C, \tag{1.3}$$

where each term represents a symmetry group to which the strong, electromagnetic (EM) and weak interactions can be associated. In equation 1.3, Y represents the hypercharge which relates the electric charge (Q) to the third component of the weak isospin (I_3) via the Gell-Mann-Nishijima formula $Q = I_3 + \frac{1}{2}Y$ [11, 12]. The "handedness" is represented by L, while the colour charge by C. Handedness refers to the relative direction of helicity with respect to the direction of momentum, so that a system whose spin direction is the same as the momentum is called "right-handed", and one with opposite directions is called "left-handed". I_3 can either be $+\frac{1}{2}$ or 0 for right-handed or for left-handed particles, respectively.

Fermions

The SM attempts to describe all physical matter[1] using twelve particles, called fermions, separated into two groups, quarks and leptons. Within each group the particles can be further separated into three sets of $SU(2)_L$ weak isospin doubles, called *generations*, that change with increasing mass. Quarks can be denoted as:

$$\begin{pmatrix} u \\ d \end{pmatrix}_L \quad \begin{pmatrix} c \\ s \end{pmatrix}_L \quad \begin{pmatrix} t \\ b \end{pmatrix}_L, \tag{1.4}$$

where each flavour pair consists of an "up" (*up*, *charm*, *top*) and "down" (*down*, *strange*, *bottom*) type, with a charge of $+\frac{2}{3}$ and $-\frac{1}{3}$ in units of electron charge (e), respectively. The corresponding anti-quark particles have opposite charges of $-\frac{2}{3}$ for the *anti-up* ($\bar{u}$), *anti-charm* ($\bar{c}$) and *anti-top* ($\bar{t}$), and $+\frac{1}{3}$ for *anti-down* ($\bar{d}$), *anti-strange* ($\bar{s}$), and *anti-bottom* ($\bar{b}$), in units of e. Analogously to electric charge, quarks also have colour charge, which exists in three different states: *red*, *green*, and *blue*. Quarks cannot propagate as free particles but must instead be grouped into colourless hadronic matter, known as *hadrons*. Hadrons composed of quark-antiquark pairs (e. g. the *pions* π^0, $\pi^\pm$) are know as *mesons* while three-quark hadrons (e. g. protons and neutrons) are known as *baryons*. In addition to the electric charge, Q, quarks have another characteristic quantum number called Baryon number, (B), with a value of $\frac{1}{3}$ ($-\frac{1}{3}$) for each quark (anti-quark) that must be conserved in all known interactions.

Similarly to quarks, leptons can also be grouped by generation into:

$$\begin{pmatrix} \nu_e \\ e^- \end{pmatrix}_L \quad \begin{pmatrix} \nu_\mu \\ \mu^- \end{pmatrix}_L \quad \begin{pmatrix} \nu_\tau \\ \tau^- \end{pmatrix}_L, \tag{1.5}$$

[1] with some note-worthy exceptions such as dark matter which will be discussed later in the chapter

where a chargeless neutrino (ν) is assigned for each charged lepton: *electron* (e), *muon* (μ), and *tau* (τ). Each lepton has a characteristic quantum number, similar to the Baryon number, that must be conserved in all interactions, called Lepton number. There are three types of lepton numbers, according to each lepton type (L_e, L_μ, L_τ) with values of 1 or -1 for leptons or anti-leptons, respectively.

For the quarks and leptons shown in 1.4 and 1.5, L denotes the "left-handedness" of the fermions, for which there are also corresponding "right-handed" singlets, with the exception of neutrinos (anti-neutrinos) which are uniquely left-handed (right-handed).

A summary of the quarks and leptons described above along with their relative characteristic quantum numbers is given in table 1.1.

Table 1.1: Summary of quarks and leptons described in the SM with corresponding symbols, charge, and Baryon/Lepton quantum numbers given. Anti-particles posses same quantum properties but with opposite sign.

Quarks	Symbol	Charge (Q)	Baryon Number (B)	Lepton Number (L_e,	L_μ,	L_τ)
up	u	$+\frac{2}{3}$	$\frac{1}{3}$	0	0	0
charm	c	$+\frac{2}{3}$	$\frac{1}{3}$	0	0	0
top	t	$+\frac{2}{3}$	$\frac{1}{3}$	0	0	0
down	d	$-\frac{1}{3}$	$\frac{1}{3}$	0	0	0
strange	s	$-\frac{1}{3}$	$\frac{1}{3}$	0	0	0
bottom	b	$-\frac{1}{3}$	$\frac{1}{3}$	0	0	0

Lepton	Symbol	Charge (Q)	Baryon Number (B)	Lepton Number (L_e,	L_μ,	L_τ)
electron	e	-1	0	1	0	0
muon	μ	-1	0	0	1	0
tau	τ	-1	0	0	0	1
electron neutrino	ν_e	0	0	1	0	0
muon neutrino	ν_μ	0	0	0	1	0
tau neutrino	ν_τ	0	0	0	0	1

Electromagnetic Interactions

The electromagnetic interactions are described in the SM by Quantum Electrodynamics (QED), and are mediated by the photon (γ). QED is an *abelian* gauge theory described by the symmetry group $U(1)$, meaning that the 1×1 generator is able to only self-commute, resulting in the fact that the electrically neutral photon is unable to self-interact [13]. The electromagnetic force affects fermions (with the exception of neutrinos, which are only affected by the weak force) via the exchange of photons, with a coupling constant value of

$$\alpha_{EM} = \frac{e^2}{4\pi} \sim \frac{1}{137}, \tag{1.6}$$

where e is the electric elementary charge.

Weak Interactions

The weak force interactions, denoted by Equation 1.3 by the $SU(2)_L$ term, are associated to the "handedness" of the particles and behave in a non-abelian nature. This means that the three 2×2 generators of which the $SU(2)_L$ group is comprised, do not commute. The weak interaction, thus, only couples with left-handed chiral fields via the W boson, which correspond to the charged current, while both left- and right-handed chiral fields can couple to the Z boson, that

corresponds to the neutral current. Even though both leptons and quarks have both left- and right-hand components, neutrinos (anti-neutrinos) only have the left-handed (right-handed) component observable in nature. The consequence of this is that the W boson coupling is the only interaction that can change quark flavour, and can also violate both *parity* and *charge-parity* symmetry [14].

The weak force mediators have also significant masses, as show in table 1.2, which results in short life-spans of $\mathcal{O}(10^{-25}\text{s})$. Consequently, the weak force acts on relatively short distances of $\mathcal{O}(10^{-18}\text{m})$. The coupling constant of the weak interaction at zero momentum transfer is:

$$\alpha_{weak} \sim \frac{1}{30} \tag{1.7}$$

Strong Interactions

The theory that describes the strong interactions in the SM, i. e. the $SU(3)_C$ symmetry group in Equation 1.3, is Quantum Chromodynamics (QCD). In QCD, the strong force is mediated by the massless and electrically neutral *gluon* (g), which couples to the quark's quantum property known as colour charge. Colour charge allows quarks to be described as color triplets (*red*, *green*, *blue*), each with identical strong interactions that allow colours of the same quark flavour to exist in the same bound state without violating the Pauli exclusion principle. This leads to three important features of QCD:

Confinement: all quarks are bound to colourless hadrons and cannot be observed as free particles. This can be achieved with the combination of three quarks (anti-quarks) with all three colours (anti-colours) in *baryons*, or as *mesons* where the colour and baryon number cancel.

Hadronisation: gluons are non-abelian, meaning that they can self-interact and generate virtual gluons in quantities proportional to the distance between the two interacting quarks. This gives the strong force a range of $\mathcal{O}(10^{-15}\text{m})$, but with an increasing force strength as the distance also increases. As the energy required to separate the two quarks increases, there comes a point at which it is energetically preferable to produce a pair of hadrons from the vacuum, than to increases the distance any further. The continuous production of hadrons, which form a "jet" cone, proceeds until the energy is low enough to form bound hadron states.

Asymptotic freedom: the strong force coupling constant (α_S) is the strongest of all the forces described, where $\alpha_S = 1$ at zero momentum transfer. α_S is also correlated to the four-momentum squared (Q^2), where the four-momentum vector ($\vec{Q}$) describes the energy and momentum of a particle in 3-dimensional space, and the length of the four-momentum vector is associated to the rest energy of the particle. The correlation between α_S and Q^2 can be given to a good approximation by:

$$\alpha_S \propto \frac{1}{n_f \log\left(\frac{Q^2}{\Lambda^2_{QCD}}\right)}, \tag{1.8}$$

where n_f is the number of quarks with mass below Q^2 and Λ_{QCD} is the QCD characteristic scale, for $Q^2 >> \Lambda^2_{QCD}$. As Q^2 approaches Λ_{QCD}, the value of α_S will quickly diverge. As such, QCD cannot be described at low energies using perturbation theory. On the other hand, at high energy scales α_S becomes sufficiently small, such that perturbation theory can be applied and the interactions between quarks and gluons becomes weaker, enabling quarks to behave as free particles.

The properties and mediators described in the above sections are summarised in Table 1.2.

Table 1.2: Summary of the forces and mediations described in the SM with corresponding masses and charge values.

Force	Name	Symbol	Mass [GeV]	Charge [e]
Electromagnetic	Photon	γ	0	0
Weak	W	$W^{\pm}$	80.379	± 1
	Z	Z^0	91.1876	0
Strong	Gluon	g	0	0

Electroweak Unification

Below the electroweak scale ($\mathcal{O}(246)$ GeV) the EM and weak interactions behave as described above. However, in the early universe the two interactions were merged together as described by the electroweak unification mechanism as proposed by Sheldon Glashow, Abdus Salam, and Steven Weinberg [15–17], with the electroweak symmetry group $SU(2)_L \otimes U(1)_Y$. For the Lagrangian to remain invariant, the unified electroweak force introduces four massless un-physical bosons $W_\mu^{\alpha=1,2,3}$ and B_μ, associated to the four physical bosons described by the SM, $W^{\pm}$, Z and γ. To obtain the physical bosons the gauge bosons have to mix as:

$$W_\mu^{\pm} = \frac{1}{\sqrt{2}}\left(W_\mu^1 \mp i W_\mu^2\right) \tag{1.9}$$

$$A_\mu = W_\mu^3 \sin\theta_W + B_\mu \cos\theta_W \tag{1.10}$$

$$Z_\mu = W_\mu^3 \sin\theta_W - B_\mu \cos\theta_W \tag{1.11}$$

where θ_W is the experimentally determined *Weinberg angle*, or *weak mixing angle*. The $W^{\pm}$ vector field, $W_\mu^{\pm}$, are formed by the linear combination of the W_μ^1 and W_μ^2 bosons, whereas the Z and photon vector fields (Z_μ and A_μ) are formed by the mixing of the B_μ and W_μ^3. The mass terms for both bosons and fermionic fields are forbidden by the electroweak gauge as they are not invariant under gauge transformations. The W and Z bosons have, nonetheless, been experimentally proven to have mass [13], meaning that the electroweak symmetry must be broken. This introduces an additional complex scalar field, the Higgs field, which couples to bosons and fermions giving them mass.

1.1.1 The Higgs Mechanism

The SM Lagrangian can be described as the sum of the Lagrangians of the electroweak ($\mathcal{L}_{EWK}$) and strong ($\mathcal{L}_{QCD}$) interactions, and the masses of the elementary particles ($\mathcal{L}_{Mass}$):

$$\mathcal{L}_{SM} = \mathcal{L}_{EWK} + \mathcal{L}_{QCD} + \mathcal{L}_{Mass} \tag{1.12}$$

The spontaneous symmetry breaking of $SU(2)_L \otimes U(1)_Y$ is described by the Higgs mechanism [18, 19], which preserves the gauge symmetry in the SM, without requiring the insertion of the mass term, $\mathcal{L}_{Mass}$, by hand, thus maintaining the SM Lagrangian as a re-normalisable theory. The Higgs mechanism introduces the most general scalar potential permitted under the restrictions of $SU(2)_L$ invariance and advisability, in the form of:

$$V(\varphi) = \mu^2 \varphi^\dagger \varphi + \lambda(\varphi^\dagger \varphi)^2, \tag{1.13}$$

where μ and $\lambda > 0$ are additional parameters to the complex scalar doublet under $SU(2)_L$, identified as the Higgs field, φ, and given by:

$$\varphi = \begin{pmatrix} \varphi^+ \\ \varphi^0 \end{pmatrix} = \frac{1}{\sqrt{2}} \begin{pmatrix} \varphi_1 + i\varphi_2 \\ \varphi_3 + i\varphi_4 \end{pmatrix}, \tag{1.14}$$

and depicted in Figure 1.2. For the case where $\mu^2 < 0$, $V(\varphi)$ describes the potential with local

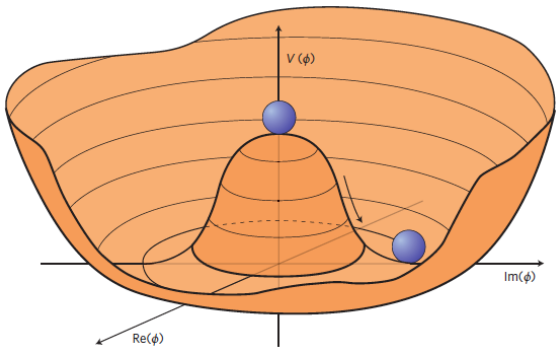

Figure 1.2: Visualisation of the "Mexican hat" Higgs potential in the complex imaginary plane. The movement from the centre of the potential to the trough corresponds to the massive Higgs boson [20].

maximum at $\varphi = 0$, surrounded by minima in the region defined by $\varphi = \sqrt{\frac{-\mu^2}{\lambda}} \equiv v$, also known as the Vacuum Expectation Value (VEV). The resulting shape that the Higgs potential forms in the three dimensions of complex plane of φ and $V(\varphi)$ is commonly referred to as the "Mexican hat." The underlying $SU(2)$ symmetry of the Lagrangian is therefore preserved, but the field picks up the non-zero ground state VEV, *spontaneously* breaking the symmetry.

The interaction of the VEV of the Higgs field and the $SU(2) \otimes U(1)$ gauge fields, $W_\mu^{\alpha=1,2,3}$, allows for massive $W^\pm$ and Z bosons, while the photon remains massless. Fermions are expected to gain mass from the Higgs field VEV interacting with the Yukawa couplings of the particles.

The Higgs mechanisms is verifiable as it predicts the existence of a new scalar, the Higgs boson, with mass:

$$M_h = 2\lambda v^2. \tag{1.15}$$

The Higgs boson mass must to be determined experimentally due to the free parameter of the theory, λ, which cannot be known a priori. In 2012, the A Toroidal LHC ApparatuS (ATLAS) and Compact Muon Solenoid (CMS) experiments at CERN observed a Higgs-like particle with mass of 125 GeV [6, 7]. The couplings of the Higgs boson as predicted by the SM have, since then, been observed by many different analyses and channels, as shown by Figure 1.3.

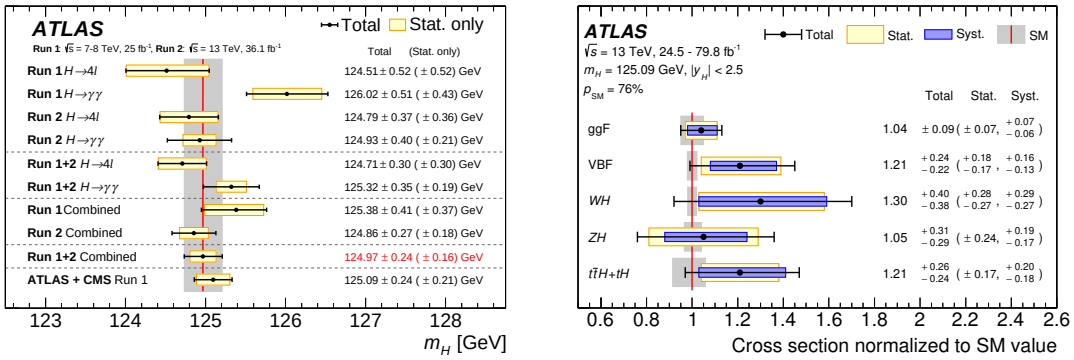

(a) (b)

Figure 1.3: (a) Summary of Higgs boson measurements from individual and combined analyses from ATLAS and CMS using Run 1 and Run 2 data. Statistical-only and total uncertainties are shown by horizontal yellow band and black error bars, respectively. Central value with corresponding total uncertainty for combined ATLAS Run 1 +2 measurements are shown by the red vertical line and gray shaded column, respectively. Taken from Ref. [21]. (b) Summary of Higgs boson cross-sections, normalised to their SM predictions and with SM branching fractions assumed. Total, systematic, and statistical uncertainties in measurements are shown by black error bars, blue boxes, and yellow boxes, respectively. The gray band indicate the theory uncertainty in the cross-section predictions. Taken from Ref. [22].

1.1.2 Weaknesses of the Standard Model

The SM is an extremely powerful tool able to explain and predict many of the phenomena observed in particle physics. It has also been extensively validated at several experiments at varius colliders, e. g.: the Large Electron-Positron Collider (LEP) at CERN, Tevatron at Fermilab, and SPEAR/PEP at SLAC. The agreement between the measured and expected cross-sections for several SM processes have been determined and found to be in extremely good agreement. Nonetheless, the SM has some fundamental limitations and deficiencies that cannot be explained using the current model, suggesting that it is still incomplete. This section will describe some of the limitations of the SM that could be solved with theoretical extensions such as SUSY.

Hierarchy Problem: The coupling of the Higgs field to the fermions causes the Higgs' mass to receive several contributions from one-loop corrections, as shown by Figure 1.4. The expression of the quantum loop contributions from the fermionic fields in the difference between the observed Higgs mass (m_H^2) and the *bare* mass (m_0^2) (Lagrangian parameter), is expressed as:

$$\Delta m_H^2 = -\frac{|\lambda_f|^2}{8\pi^2}\Lambda_{UV}^2 + \cdots, \tag{1.16}$$

where λ_f is the coupling constant to the fermion field (Yukawa coupling), and Λ^2_{UV} is the ultraviolet momentum cut-off, which is the highest mass scale at which the theory is still valid [23]. If the Λ^2_{UV} is of the order of the Plank scale ($\mathcal{O}(10^{19})$ GeV), the quadratic nature would cause the measured Higgs mass, m^2_H, to quickly diverge from the bare Higgs mass, m^2_0 becoming approximately 30 orders of magnitude larger. This large difference violates *naturalness*, a property that states that ratios between free parameters must not be larger than one or two orders of magnitude, and that the fine-tuning cancellation between the quadratic radiative corrections and the bare mass would indicate an incomplete theory [24, 25].

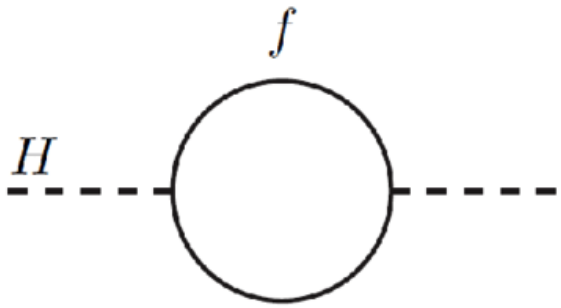

Figure 1.4: One-loop fermionic quantum correction with coupling λ_f to the Higgs mass.

Gauge Coupling Unification: The running of gauge coupling is predicted by the SM. Although the electroweak unification occurs at $\mathcal{O}(10^2)$ GeV, it does not occur for the strong force. Figure 1.5 shows a representation of the electromagnetic (blue), weak (red), and strong (green) interactions as a function of energy. The three lines are shown to not meet at any point, indicating that they fail the Grand Unification Theory (GUT) [26] criteria, which requires all the interactions to converge at one point. A possible solution to this problem could be the introduction of new physics that would allow for all interactions to converge at one singular point. This will be discussed in more detail in Section 1.2.

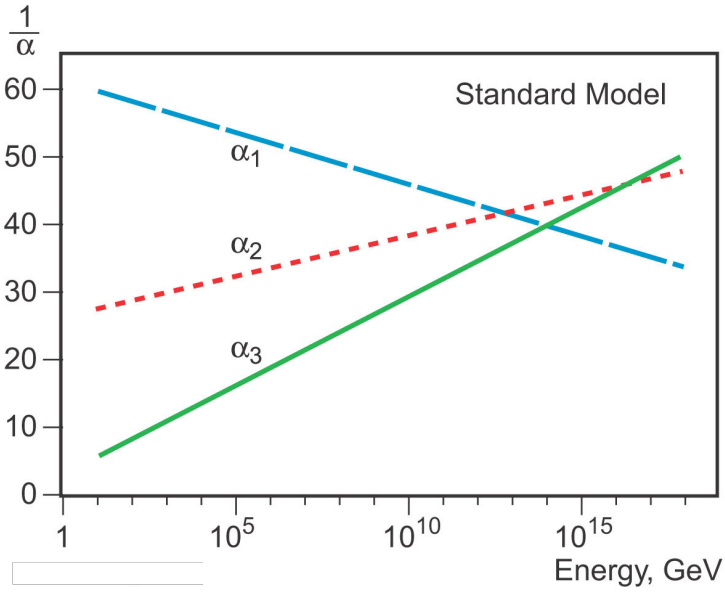

Figure 1.5: Running coupling constants of the electromagnetic (blue), weak (red) and strong(green) interactions in the SM. The three lines do not converge, which goes against the idea of a GUT. [26]

Electroweak Baryogenesis: The overwhelming excess of matter compared to anti-matter in the universe (i. e. baryonic asymmetry) is of great concern when discussing the SM. For the level of excess observed in our universe there must be:

1. At least one baryon number violating process
2. CP violation
3. Interactions outside of equilibrium

This set of requirements are called the Sakharov conditions [27], and are required for baryogenesis to occur, and to reproduce the observed excess of baryons to photon ratio [28, 29]:

$$\frac{n_B - \bar{n}_B}{n_\gamma} = 6 \times 10^{-10} \frac{\text{excess baryons}}{\text{photons}}, \tag{1.17}$$

where n_B, $\bar{n}_B$, and n_γ are the number of baryon, anti-baryons, and photons in the universe. The above conditions can, in theory, be fulfilled within the SM since the first condition is satisfied by quantum effects associated to the weak interaction. The Cabibbo-Kobayashi-Maskawa (CKM) mixing, which describes the mixing of quark generations, fulfils the second condition, while the third is met via electroweak phase transitions. However, experimental values of CKM mixing and the measured Higgs mass seem to suggest that the latter two conditions are not satisfied to a sufficient degree to account for the observed disparity. This in turn suggests the existence of physics beyond the SM that can provide new sources of CP violation, and additional Higgs fields to modify the electroweak phase transitions [30].

Dark Matter: Observations of the rotation of galaxies was one of the first pieces of experimental evidence to suggest the existence of Dark Matter (DM) [31]. The rotational velocity of matter in galaxies as a function of their radial distance from the centre, shown in Figure 1.6, is found to be considerably higher than expected in the outer arms of the galaxy, if only visible matter (disk) is taken into account. Only by the addition of invisible (dark) matter found in halos around galaxies does the rotational velocity fit the predictions. Gravitational lensing and measurements of the Cosmic Microwave Background Radiation (CMBR) have been used to validate the existence of dark matter, and have been found to be consistent with this hypothesis[2]. DM, which has been calculated to account for ~ 27% of the universe (~ 85% of all matter), seem to only interact via gravity and the weak force, and is therefore hypothesised to be a Weakly Interacting Massive Particle (WIMP) [29, 32–34]. Although SM neutrinos can fulfil some of the WIMP criteria, they are not massive enough to account for the galaxy rotational curve observation, leaving no SM particle as a suitable dark matter candidate.

[2] An alternative hypothesis is a modified theory of general relativity on galactic scales, the details of which are beyond the scope of this thesis.

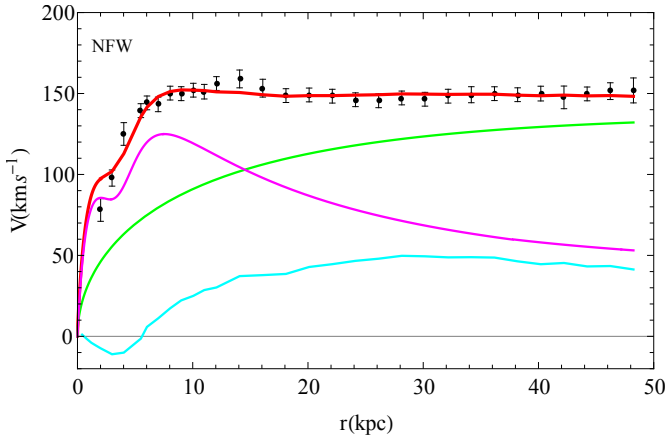

Figure 1.6: Navarro, Frenken and White (NFW) DM mass modelling for galaxy NGC 3198. Circular velocity data (black points with error bars) are shown with models for the stellar disk (magenta line), the DM halo profile (green line), and the neutral Hydrogen contribution (azure line). The combination of contritions from all models is depicted by the thick red line, which shows that contribution from DM is required to account for the velocities observed at large radial distances. [35]

1.2 Supersymmetry

A proposed extension that could account for many of the issues not explained in the SM is SUSY, which introduces new particles, called SUSY particles or *sparticles* (where "s" stands for "superpartner"), by adding a new space-time symmetry that transforms a particle's spin by $\Delta s = \pm\frac{1}{2}$ via a quantum operator, Q. This results in all SM fermions having a bosonic superpartner and vice versa:

$$\begin{aligned} Q|Boson\rangle &= \left|Fermion\right\rangle \\ Q\left|Fermion\right\rangle &= |Boson\rangle\,, \end{aligned} \tag{1.18}$$

thus creating a *supermultiplet* between the SM and SUSY particles, where the two components have the same masses and quantum numbers, but different spins. SUSY particles are denoted by a "~" placed atop of the symbol corresponding to their SM counterpart. The convention used to name superpartners is to use the SM particle name with the "ino" suffix, when describing the superpartner of a boson (e. g. *Higgsino* is the superpartner of the Higgs boson), while for fermions an "s" prefix is used instead (e. g. *stau* is the superpartner of the tau lepton). Therefore, *Squarks* and *sleptons* are the superpartners of the SM quarks and leptons, respectively, differing only by $\Delta s = \frac{1}{2}$. The left- and right-handed fermions (f_L, f_R) and their equivalent SUSY superpartners ($\tilde{f}_L, \tilde{f}_R$) are known as *supermultiplets*. SM vector bosons also have a corresponding spin-$\frac{1}{2}$ fermion superpartner, grouped into *gauge multiplets*. In order for this model to satisfy Noether's theorem and be renormalisable, the SUSY particles are expected to have identical masses and quantum numbers, besides spin, to their SM partner. The superpartners of the SM gauge bosons, generally called *gauginos*, can be further identified by the names *gluino*, *Wino*, and *Bino* for the gluon, W_μ, and B_μ boson fields, respectively. The SM Higgs boson and its SUSY partner, the *higgsino*, have on the other hand two supermultiplets, each coupling to either the up- ($H_u, \tilde{H}_u$) or down-type ($H_d, \tilde{H}_d$) fermions, giving them mass.

The introduction of new particles by SUSY can provide a solution to the hierarchy problem, described in Section 1.1.2, as the Higgs mass square potential would receive corrections from a new scalar in the form:

$$\Delta m_H^2 = -\frac{|\lambda_S|^2}{16\pi^2}\Lambda_{UV}^2 - 2m_S^2 + \cdots\,, \tag{1.19}$$

where λ_S is the coupling of SUSY particles to the Higgs field [36, 37]. Since the couplings are the same but with opposite sign to their fermionic counterparts, the quadratic divergence is cancelled, thus resolving the hierarchy problem. The experimental mass of the Higgs boson can be obtained without performing any unnatural *tuning* of the parameters, making SUSY a *natural* theory.

The scale dependence of the running coupling constants will also be affected by the addition of new particles, as they will contribute with a new set of coefficients derived from additional gauge interactions. The three lines in Figure 1.7 show the electromagnetic (blue), weak (red) and strong (green) interactions in the Minimal Supersymmetric Standard Model (MSSM) [38, 39]. The MSSM is a supersymmetric extension to the SM that requires a minimal amount of supersymmetric partners in order to solve the hierarchy problem. In this SUSY model, which will be described in more detail below, the thee lines converge, indicating that it can provide the basis for a GUT.

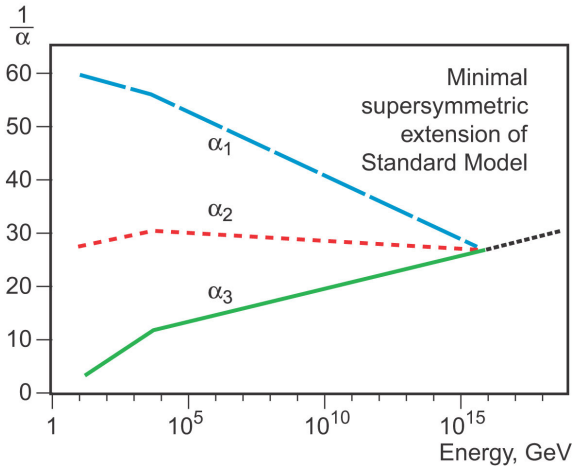

Figure 1.7: Running coupling constants of the electromagnetic (blue), weak (red) and strong(green) interactions in the MSSM. The three lines converge in this model, this supporting a GUT.

Searches for SUSY have resulted with no superpartners being observed at the same masses of their SM counterparts. This indicates that SUSY must be a broken symmetry, which would allow superpartner particles to have masses higher than their SM counterparts. The only restriction is that if the masses of the SUSY particles are too high (close to the Planck scale), the hierarchy problem would not be solved. The mechanism of *soft* SUSY breaking overcomes this problem by imposing constraints on the masses of the sparticles.

1.2.1 Soft SUSY breaking

SUSY predicts the masses of the superpartners to have the same mass as their SM counterparts. Experimental evidence shows that this isn't the case, as no SUSY particles have yet been discovered, suggesting that SUSY cannot be an exact symmetry. As discussed in Section 1.1.1, the mass of SM particles is given via the electroweak symmetry breaking. To maintain a spontaneous mechanism that breaks the symmetry, in the MSSM, sparticles are allowed to have mass before the electroweak symmetry breaking occurs. The total MSSM Lagrangian can therefore be defined as:

$$\mathcal{L}_{\text{MSSM}} = \mathcal{L}_{\text{SUSY}} + \mathcal{L}_{\text{soft}}, \tag{1.20}$$

where $\mathcal{L}_{\text{SUSY}}$ contains the original SUSY interaction terms and $\mathcal{L}_{\text{soft}}$ contains the new mass terms that are present due to the symmetry breaking. The *soft* breaking refers to SUSY being

maintained as a natural theory, where the sparticles masses are required to be not much greater than ~ 1 TeV, in order to preserve it as a solution to the hierarchy problem. The introduction of the new mass terms with opposite sign to their fermionic SM counterparts gives additional quantum loop corrections to the Higgs mass shown by equation 1.19 that cancel out the quadratic divergence, thus solving the hierarchy problem. A new set of parameters that determine the mixing between the flavour of eigenstate and the SUSY phenomenology are introduced by this extension to the SM. The full extent of the parameters and phenomenology introduced by SUSY will be discussed in more detail in the following sections.

Mass spectrum

In the MSSM the electroweak symmetry breaking is applied to all sparticles, taking into account the enhanced Higgs sector, which mixes the masses of the particles to form mass eigenstates.

Higgs Boson The two Higgs supermultiplets $(\tilde{H}_u, \tilde{H}_d)$ mix together to form five mass eigenstates of the Higgs boson. These include two charged Higgs states $H^{\pm}$ and three neutral Higgs bosons, A^0, H^0, and h. By convention, h is the lightest Higgs boson corresponding to the 125 GeV boson first observed by CMS and ATLAS in 2012.

Charginos and Neutralinos The neutral Winos $(\tilde{W}^0)$, Binos $(\tilde{B}^0)$, and Higgsinos $(\tilde{H}^0)$ mix to form the four *neutralinos* $(\chi^0_{i=1,2,3,4})$ via the following matrix:

$$\begin{pmatrix} \tilde{\chi}^0_1 \\ \tilde{\chi}^0_2 \\ \tilde{\chi}^0_3 \\ \tilde{\chi}^0_4 \end{pmatrix} = \begin{pmatrix} M_1 & 0 & -c_\beta m_Z s_W & s_\beta m_Z c_W \\ 0 & M2 & c_\beta m_Z c_W & -s_\beta m_Z c_W \\ -c_\beta m_Z s_W & c_\beta m_Z s_W & 0 & -\mu \\ s_\beta m_Z c_W & -s_\beta m_Z c_W & -\mu & 0 \end{pmatrix} \begin{pmatrix} \tilde{B}^0 \\ \tilde{W}^0 \\ \tilde{H}^0_u \\ \tilde{H}^0_d \end{pmatrix}, \tag{1.21}$$

where c_β, s_β, c_W, and s_W are shorthands for $\cos(\beta)$, $\sin(\beta)$, $\cos(\theta_W)$, and $\sin(\theta_W)$, respectively. m_W and m_Z are the W and Z boson masses, while θ_W and $\tan(\beta)$ are the ratios of the: electroweak coupling constant, and VEVs of the two Higgs doublet fields, respectively. Similarly, the charged Winos $(\tilde{W}^{\pm})$ and Higgsinos $(\tilde{H}^{\pm})$ mix to form the *charginos* $(\chi^{\pm}_{i=1,2})$ via the matrix:

$$\begin{pmatrix} \tilde{\chi}^{\pm}_1 \\ \tilde{\chi}^{\pm}_2 \end{pmatrix} = \begin{pmatrix} M_2 & \sqrt{2} m_w s_\beta \\ \sqrt{2} m_w c_\beta & \mu \end{pmatrix} \begin{pmatrix} \tilde{W}^{\pm} \\ \tilde{H}^{\pm} \end{pmatrix}. \tag{1.22}$$

By convention, the indices used for the charginos and neutralinos are used in increasing order of mass, making $\tilde{\chi}^0_1$ and $\tilde{\chi}^{\pm}_1$ the lightest neutralino and charginos, respectively.

Squarks and Sleptons Similarly to charginos and neutralinos, slepton's and squark's mass-mixing are also regulated by mass matrices whose terms provide corrections to the nominal mass of the sparticles. For sleptons and squarks, these corrections depend on the squared value of the mass of their SM partners and specific mixing angles. This becomes particularly important for the more massive third generation quarks (bottom and top) and

leptons (tau), but is otherwise negligible. The mass matrix for the sfermions ($\tilde{f}$) for the up ($\tilde{u}$), down ($\tilde{d}$) and slepton ($\tilde{\ell} = \tilde{e}, \tilde{\mu}, \tilde{\tau}$) scalars is given as :

$$\mathcal{M}^2_{\tilde{f}} = \begin{pmatrix} m^2_{\tilde{f}_L} & a_f m_f \\ a_f m_f & m^2_{\tilde{f}_R} \end{pmatrix}, \tag{1.23}$$

where

$$\begin{aligned}
m^2_{\tilde{f}_L} &= \begin{cases} M^2_{\tilde{Q}} + m^2_u + m^2_Z \cos 2\beta \left(\frac{1}{2} - \frac{2}{3}\sin^2\theta_W\right), & \tilde{f} = \tilde{u} \\ M^2_{\tilde{Q}} + m^2_d - m^2_Z \cos 2\beta \left(-\frac{1}{2} - \frac{1}{3}\sin^2\theta_W\right), & \tilde{f} = \tilde{d}\,, \\ M^2_{\tilde{L}} + m^2_\ell - m^2_Z \cos 2\beta \left(\frac{1}{2} - \sin^2\theta_W\right), & \tilde{f} = \tilde{\ell} \end{cases} \\
m^2_{\tilde{f}_R} &= \begin{cases} M^2_{\tilde{u}} + m^2_u + m^2_Z \cos 2\beta \frac{2}{3}\sin^2\theta_W, & \tilde{f} = \tilde{u} \\ M^2_{\tilde{d}} + m^2_d - m^2_Z \cos 2\beta \frac{1}{3}\sin^2\theta_W, & \tilde{f} = \tilde{d}\,, \\ M^2_{\tilde{\ell}} + m^2_\ell - m^2_Z \cos 2\beta \sin^2\theta_W, & \tilde{f} = \tilde{\ell} \end{cases} \\
a_f m_f &= \begin{cases} m_u (A_u - \mu \cot\beta), & \tilde{f} = \tilde{u} \\ m_d (A_d - \mu \tan\beta), & \tilde{f} = \tilde{d}\,. \\ m_\ell (A_\ell - \mu \tan\beta), & \tilde{f} = \tilde{\ell} \end{cases}
\end{aligned} \tag{1.24}$$

The mass parameters with a tilde, shown in the above set of equations, refer to the soft SUSY breaking squark and slepton mass parameters, while the mass parameters without a tilde are the usual quark and lepton masses. The parameters μ and $\tan\beta$ are the previously mentioned higgsino mass parameters and ratio of Higgs field VEVs, respectively. The mixing effect of the off-diagonal elements of the matrix, shown in Equation 1.23, make it so that the stop ($\tilde{t}_1$) is the lightest squark and $\tilde{\tau}$ is the lightest slepton in the MSSM.

The full list of gauge and mass eigenstates of sparticles predicted by the MSSM are listed in Table 1.3 for reference.

1.2.2 *R*-Parity

Several interactions not found in the SM are introduced by the MSSM, some of which directly violate total baryon and lepton number. A discrete symmetry, R-parity, is introduced to remove these violations. With it, a conserved quantum number is given for each particle, defined as [36]:

$$P_R = (-1)^{3(B-L)+2s}, \tag{1.25}$$

where B, L and s are the baryon, lepton and spin quantum numbers, respectively. SM particles have $P_R = +1$, while SUSY particles have $P_R = -1$. If R-parity is exactly conserved then there can't be any particle-sparticles interaction mixing, and every interaction vertex must contain an even number of $P_R = -1$ sparticles. Consequently, this results in some important phenomenological consequences:

Table 1.3: Gauge and mass eigenstate of SUSY particles introduced in the MSSM. First and second generation sparticles have very small Yukawa and soft couplings, which result in degenerate mass and gauge eigenstates. For third generation sparticles the Yukawa coupling is non negligible resulting in divergent gauge and mass eigenstates.

Name	Spin	Gauge Eigenstates	Mass Eigenstates
squarks ($\tilde{q}$)	0	$\tilde{u}_L$, $\tilde{u}_R$, $\tilde{d}_L$, $\tilde{d}_R$	(same)
		$\tilde{c}_L$, $\tilde{c}_R$, $\tilde{s}_L$, $\tilde{s}_R$	(same)
		$\tilde{t}_L$, $\tilde{t}_R$, $\tilde{b}_L$, $\tilde{b}_R$	$\tilde{t}_1$, $\tilde{t}_2$, $\tilde{b}_1$, $\tilde{b}_2$
Sleptons ($\tilde{\ell}$)	0	$\tilde{e}_L$, $\tilde{e}_R$, $\tilde{\nu}_e$	(same)
		$\tilde{\mu}_L$, $\tilde{\mu}_R$, $\tilde{\nu}_\mu$	(same)
		$\tilde{\tau}_L$, $\tilde{\tau}_R$, $\tilde{\nu}_\tau$	$\tilde{\tau}_1$, $\tilde{\tau}_2$, $\tilde{\nu}_\tau$
Higgs Bosons	0	H_u^0, H_d^0, H_u^+, H_d^-	h^0, H^0, A^0, $H^\pm$
Neutralinos	1/2	$\tilde{B}^0$, $\tilde{W}^0$, $\tilde{H}_u^0$, $\tilde{H}_d^0$	χ_1^0, χ_2^0, χ_3^0, χ_4^0
Charginos	1/2	$\tilde{W}^\pm$, $\tilde{H}_u^+$, $\tilde{H}_d^-$	$\chi_1^\pm$, $\chi_2^\pm$
Gluinos	1/2	$\tilde{g}$	(same)
Gravitino	3/2	$\tilde{G}$	(same)

- In a collider experiment, sparticles can only be produced in even numbers (usually two at a time)
- The Lightest Supersymmetric Particle (LSP) must be absolutely stable and thus a good candidate for dark matter [40].
- Each sparticle (other than the LSP) must eventually decay into an odd number of LSPs.

In this work only R-parity conserving scenarios are considered[3], with the electrically neutral and weakly interacting $\tilde{\chi}_1^0$ assumed to be the LSP.

1.2.3 Phenomenology of MSSM

The unconstrained MSSM has $\mathcal{O}(100)$ parameters, once *soft* SUSY breaking occurs, in addition to the SM ones. To reduce the number of free parameters, a set of phenomenologically motivated assumptions are made to derive simpler models:

- There are no additional sources of CP-violation introduced.
- There are no Flavour Changing Neutral Currents (FCNC)
- The first and second-generations sfermions have identical (*degenerate*) masses [41]

[3] *R*-Parity Violating (RPV) scenarios are also being investigated by the particle-physics community but are beyond the scope of this thesis.

The above constraints to the MSSM result in a smaller set of observable parameters, summarised in Table 1.4. These parameters are used to define the so-called Phenomenological MSSM (pMSSM).

Table 1.4: MSSM parameters introduced by *soft* SUSY breaking.

Description	Parameters
Mass of Bino, Wino, and Gluino	M_1, M_2, M_3
Mass of speudo-scalar Higgs boson	M_A
Masses of first- and second- generation squarks	$m_{\tilde{q}}$, $m_{\tilde{u}_R}$, $m_{\tilde{d}_R}$
Masses of third-generation squarks	$m_{\tilde{Q}_L}$, $m_{\tilde{t}}$, $m_{\tilde{b}}$
Masses of first- and second- generation sleptons	$m_{\tilde{l}}$, $m_{\tilde{e}_R}$
Masses of third-generation sleptons	$m_{\tilde{L}}$, $m_{\tilde{\tau}_R}$
Mass parameter of Higgs and higgsino	μ
Two-higgs doublet fields VEV ratio	$\tan\beta$

To further reduce the parameter space, in order to make pMSSM searches easier to exclude, *simplified models* are used. In simplified MSSM models, only particles that contribute to the production of a certain signal process are considered, while the other SUSY masses are ignored. Therefore, number of parameters are drastically reduced to only the masses of the studied sparticles, allowing for much stronger constraints to be made.

The simplified model considered in this thesis is the production of $\tilde{\tau}$ from proton-proton (pp) interactions. Production of SUSY particles mediated by electroweak interactions are possible from hadronic final states, albeit at lower cross-section compared to squark and sgluino production. Figure 1.8 shows some electroweak SUSY production modes, that allow for parton-parton interaction to produce di-slepton events.

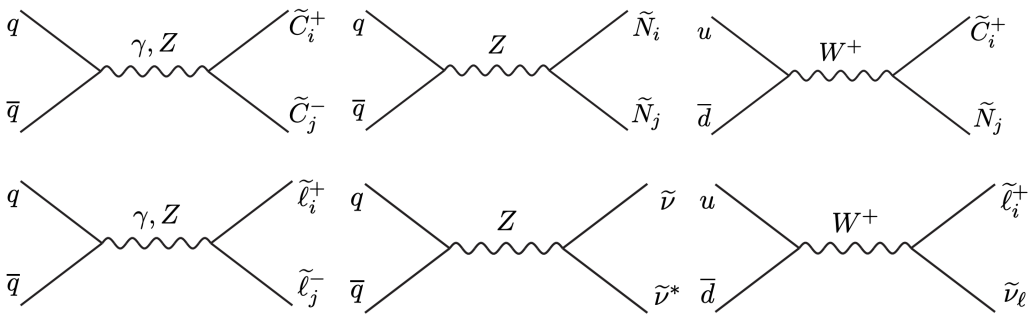

Figure 1.8: Production channels of gauginos and sleptons with hadronic final states via electroweak mediators. For these diagrams $C_i^{\pm} = \chi_{i=1,2}^{\pm}$ and $N_j = \chi_{j=1,2,3,4}^{0}$ [36].

SUSY cross-section production generally scales with increasing centre-of-mass energy, and decreases with the masses of the sparticles. Figure 1.9 shows the production cross-section as a function of particle masses for each initial sparticle pair, in pp collisions at centre-of-mass energy of $\sqrt{s} = 13$ TeV. Recent experimental results show that masses of the squarks and gluinos are excluded up to around 1 TeV for massless $\tilde{\chi}_1^0$ [42, 43]. At these mass regimes, the slepton pair production becomes the dominant process, assuming a light slepton ($\mathcal{O}(100)$ GeV) compared

to the channels for the squark and gluino production.

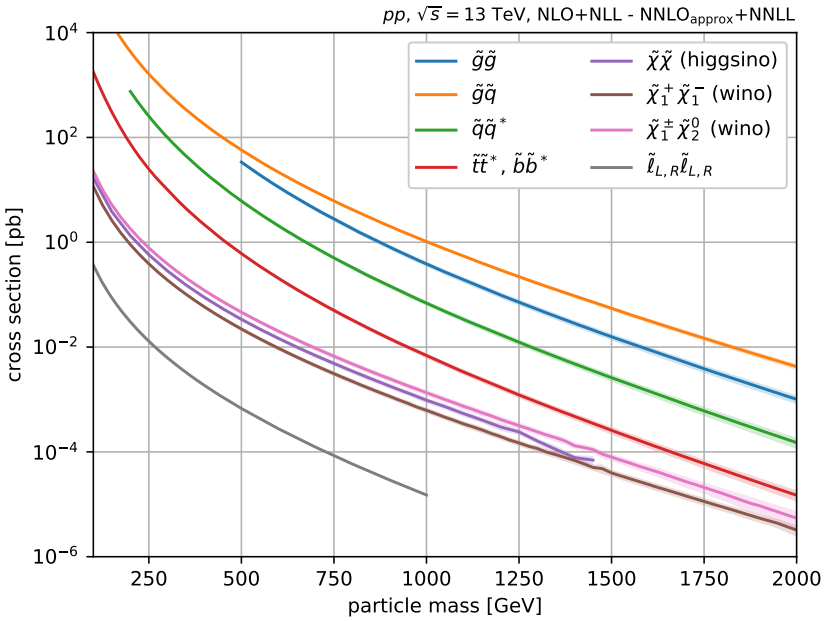

Figure 1.9: Theoretical cross-section values computed at NLO and NNLO$_{approx}$+NNLL for sparticle production, as function of their mass, in pp collisions at $\sqrt{s}$= 13 TeV. All other SUSY sparticles not considered in the cross-section calculation are assumed to be heavy and decoupled. [44]

1.3 Electroweak SUSY searches

Many different production modes of SUSY particles can be experimentally explored at the LHC. Electroweak SUSY production refers to the direct production of sleptons, charginos and neutralinos via the methods described above. This thesis will focus on the direct production of the stau ($\tilde{\tau}$) with τ-lepton and $\tilde{\chi}_1^0$ final states. This process, along with its experimental challenges and limitations, will be discussed in more detail in Chapter 4.

In this section, an overview of the decay patterns of the relevant SUSY particles for this analysis will be given. This will be followed by the current status of electroweak SUSY searches at the LHC, and will be concluded with the motivations for current and further searches.

Sparticles decays

The lighter masses of the sleptons, compared to the gauginos and higgsinos, makes them the favourable decay mode of the $\tilde{\chi}^{\pm}$ and $\tilde{\chi}^0$, where the possible two-body decays are:

$$\tilde{\chi}_i^0 \to Z\tilde{\chi}_j^0, W^{\mp}\tilde{\chi}_j^{\pm}, h^0\tilde{\chi}_j^0, \ell\tilde{\ell}, \nu\tilde{\nu}, \left[A^0\tilde{\chi}_j^0, H^0\tilde{\chi}_j^0, H^{\pm}\tilde{\chi}_j^{\mp}, q\tilde{q}\right], \tag{1.26}$$

and

$$\tilde{\chi}_i^{\pm} \to W^{\pm}\tilde{\chi}_j^0, Z\tilde{\chi}_j^{\pm}, h^0\tilde{\chi}_j^{\pm}, \ell\tilde{\nu}, \nu\tilde{\ell}, \left[A^0\tilde{\chi}_j^{\pm}, H^0\tilde{\chi}_j^{\pm}, H^{\pm}\tilde{\chi}_j^0, q\tilde{q}'\right]. \tag{1.27}$$

The final states shown in bracket are energetically less favourable. Gaugino decays will favour the $\tilde{\tau}$, as it is the lightest slepton.

Right-handed sleptons favour decays to the bino-like lightest neutralino compared to left-handed sleptons, which decay more favourably to wino-like charginos and neutralinos. This is due to the higher weak interaction coupling, mediated by the winos, compared to the smaller electromagnetic coupling, which is mediated by the binos. Sleptons are able to decay via the following modes:

$$\tilde{\ell} \rightarrow \ell \tilde{\chi}_j^0, \nu \tilde{\chi}_j^{\pm}, \tag{1.28}$$

and

$$\tilde{\nu} \rightarrow \nu \tilde{\chi}_j^0, \ell \tilde{\chi}_j^{\pm}, \tag{1.29}$$

as long as lepton flavour is conserved. Slepton decay modes containing $\tilde{\chi}_1^0$ particles are favoured over the other heavier gauginos, due its lighter mass.

Status and motivation

Up to now there has been no success in uncovering SUSY particles by any experiment. This allows experiments to set limits on the masses and cross-sections of the expected SUSY particles.

Both ATLAS [45–47] and CMS [48, 49] collaborations have performed experiments to search for top-squarks ($\tilde{t}$). A summary of the results collected by the ATLAS experiment, as of May 2020, are shown in Figure 1.10, using pp collision data collected between 2009 and 2012 at $\sqrt{s}$ = 8 TeV and between 2015 and 2018 at $\sqrt{s}$ = 13 TeV at the LHC. The searches shown in this figure consider the $\tilde{t}_1 \rightarrow t\tilde{\chi}_1^0$ decay process and are able to exclude top-squark masses of up to 1.2 TeV (for massless LSP) at 95% Confidence Level (CL).

Searches for gluino production in pp collisions have also been performed by the ATLAS and CMS collaborations. A summary of the results achieved by the ATLAS collaboration, as of May 2020, are shown in Figure 1.11. Data collected from pp collisions between 2009 and 2018 at $\sqrt{s}$ = 8 TeV and $\sqrt{s}$ = 13 TeV for the simplified model in which $\tilde{g} \rightarrow t\tilde{t}\tilde{\chi}_1^0$ has been used to produce these plots. Limits are obtained for the gluino mass up to 2.2 TeV for massless LSP.

The $\tilde{t}$ and $\tilde{g}$ production searches, thus far, have placed limits on their masses to at least 1 TeV or more. This provides strong motivation for the search for electroweak SUSY production at the LHC, since it would become the dominant form of SUSY production, as discussed in Section 1.2.3.

Direct $\tilde{\tau}$-lepton SUSY production searches are very challenging due to the low cross-section of the signal SUSY events compared to the SM background processes, and the difficulties of reconstructing τ-lepton objects in the ATLAS detector. Nonetheless, direct $\tilde{\tau}$ production analyses are extremely important for probing the mass of the $\tilde{\tau}$, which is expected to be the lightest slepton. Searches at LEP [51] set a lower limit on the mass of the $\tilde{\tau}$ of 86.6 GeV at 95% CL for a massless $\tilde{\chi}_1^0$. Similar searches performed by the ATLAS and CMS collaborations using data collected at $\sqrt{s}$= 8 GeV set the lower limits at 109 GeV and 125 GeV, respectively [52–54].

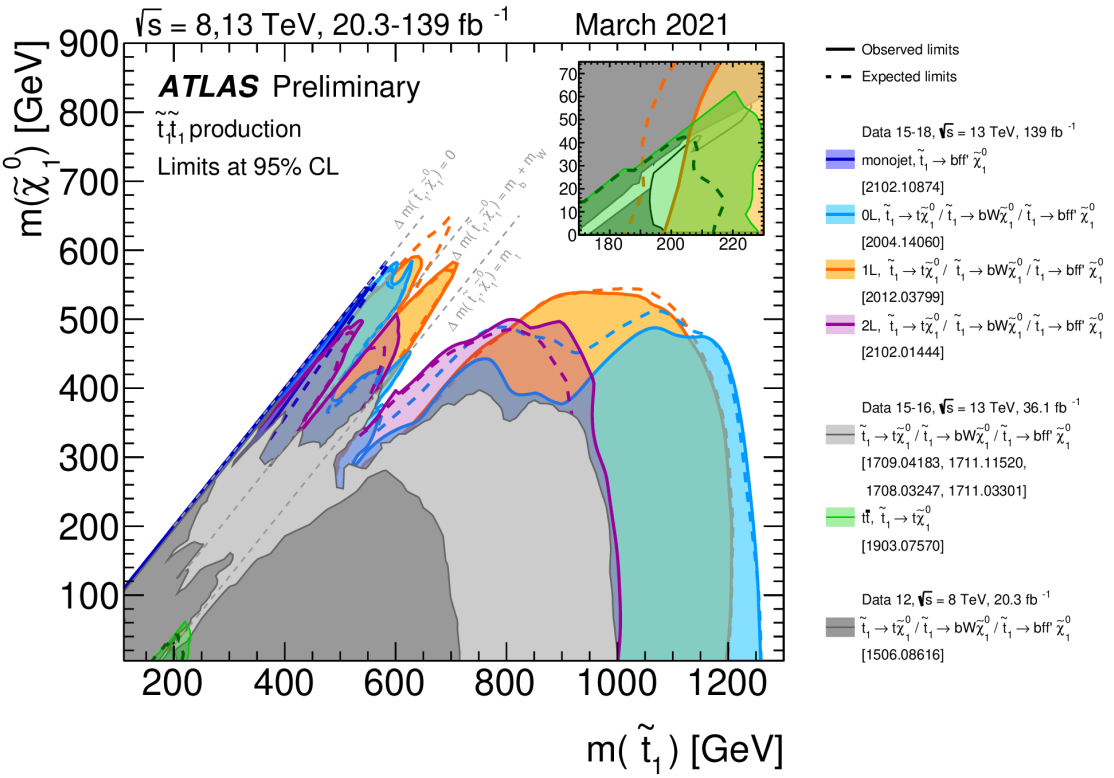

Figure 1.10: Observed and expected exclusion limits on the mass of the $\tilde{t}$ squark. Plots are produced using 20.3 fb^{-1} and 139 fb^{-1} of proton-proton collision data collected at $\sqrt{s}$= 8 TeV and $\sqrt{s}$= 13 TeV at the LHC, by the ATLAS experiment. Limits are set at the 95% CL. [50]

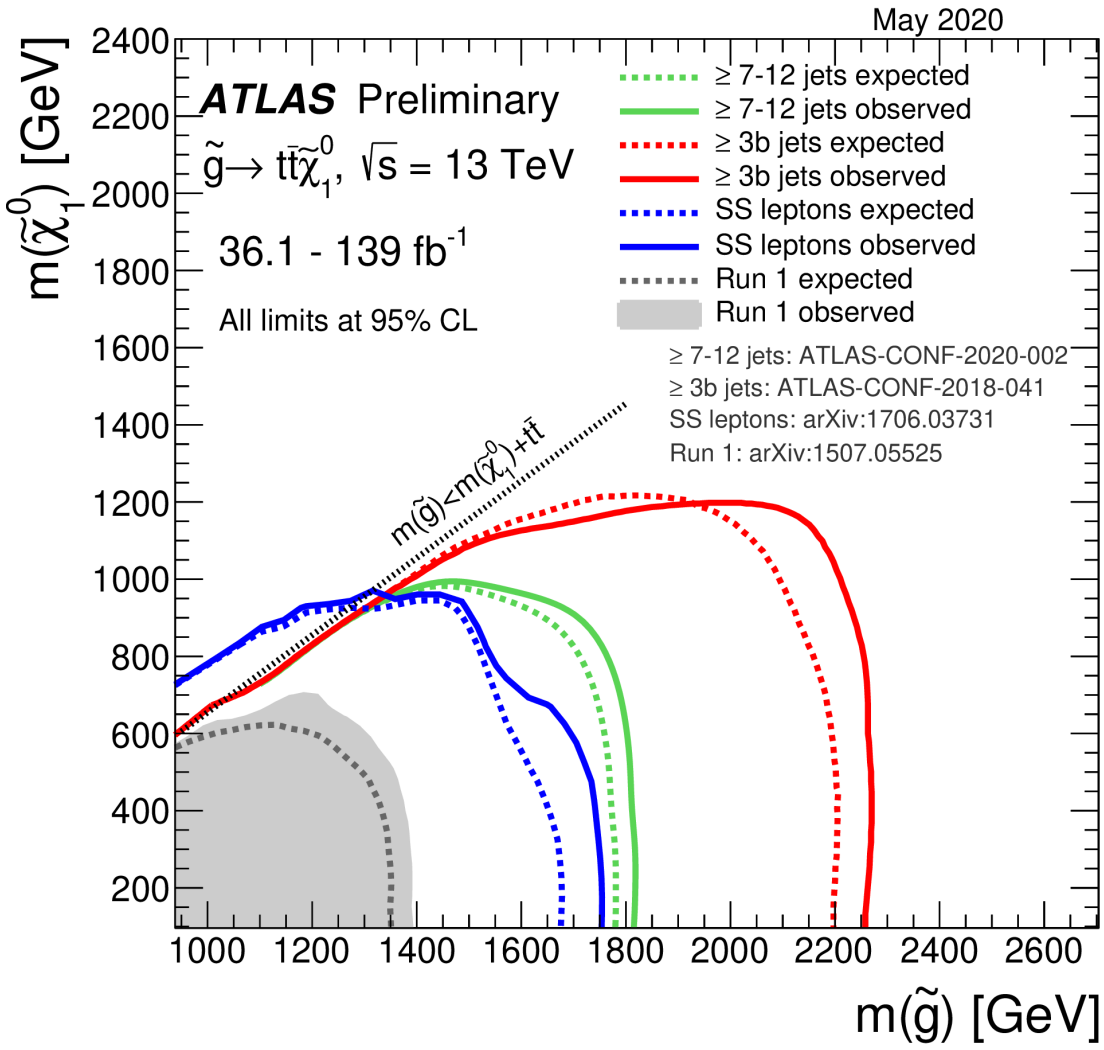

Figure 1.11: Observed and expected exclusion limits on the mass of the gluino ($\tilde{g}$). Plots are produced using 20.3 fb^{-1} and 139 fb^{-1} of proton-proton collision data collected at $\sqrt{s}$= 8 TeV and $\sqrt{s}$ = 13 TeV at the LHC, by the ATLAS experiment. Limits are set at the 95% CL. Black dashed line shows the limit for which the total mass of the final state particles is equal to the gluino mass. Exclusion limits are allowed to be above this line as it does not violate the strict $m(\tilde{g} < m(\chi_1^0))$ limit. [50]

THE ATLAS EXPERIMENT

2

I am just a dreamer, but you are just a dream.

Neil Young

The LHC is the largest collider in the world and has been providing proton-proton (pp) collisions at a centre-of-mass energy of $\sqrt{s}$= 13 TeV between 2015 and 2018 to several experiments situated around its ring. ATLAS is one of the four main experiments [1] that collects and analyses the pp collision data provided by the LHC. The analyses presented in this thesis have been performed using the data collected by the multi-purpose ATLAS detector during the so-called Run-2 data taking period, that lasted between 2015 and 2018. In this chapter an overview of the LHC and ATLAS will be presented, with a detailed focus on the most relevant components that constitute the ATLAS detector. Section 2.1 will present a general overview of the LHC functionality and performance. The overall ATLAS detector and its constituent sub-detectors will be described in Section 2.2. In Section 2.3 the ATLAS trigger system and strategy for cleverly selecting data is presented. A more in-depth description of the Trigger algorithms the author has been involved in will be presented in Chapter 3.

2.1 The Large Hadron Collider

Currently, the LHC [55] is the largest and most powerful particle accelerator in the world, which has delivered approximately 160 fb^{-1} of pp collision data with a centre-of-mass energy of $\sqrt{s}$= 13 TeV during the Run-2 data collection period which spanned between 2015 and 2018. The LHC was designed to help provide answers to some of the fundamental open questions in particle physics by accessing information from collisions happening at unprecedented energies and luminosities. It is located at the CERN in Geneva, at the border between Switzerland and France, and consists of a 27-kilometre ring 50-175 meters below ground, made of super-

[1] Where the other three are CMS (Compact Muon Solenoid), ALICE (A Large Ion Experiment), and LHCb (Large Hadron Collider beauty).

conducting magnets, with two separate beam pipes containing proton (or heavy-ion) beams travelling in opposite directions.

Strong electromagnetic fields, generated by coils made of special electric cables operating in a superconductive regime, are used to guide the particle beams around the LHC ring. A total of 1,232 superconducting dipole magnets are used to bend the beams around the ring, while 392 quadrupole magnets are used to focus the beam as it is accelerated. These magnets are kept at a temperature below 1.7 K, in order to maintain their superconductive properties and create an average magnetic field of 8.3 T. Radiofrequency (RF) cavities, with an electromagnetic field oscillating at 400 MHz, are used to accelerate the beam particles around the ring. Charged particles that pass through the cavity are affected by the EM field, which transfers energy pushing them forward along the beam line. The particle beam is not continuous, but is instead sorted into "bunches," where high (low) energy protons will arrive earlier (later) and be decelerated (accelerated) so that they stay close in energy [56].

Runs and performance

So far there have been two data collection periods ("Runs") since the LHC first went live in 2008. The first operational run, referred to as Run-1, occurred between 2009 and 2013, in which the LHC provided 5 fb^{-1} and 20 fb^{-1} of integrated luminosity at $\sqrt{s}$= 7 TeV, and 8 TeV, respectively. This was followed by a two-year upgrade program during which the LHC was not running (Long Shut-down 1 (LS1)). During the LS1 many aspects of both the LHC and ATLAS detector where changed or upgraded (for example the magnets for the LHC and the trigger system for ATLAS) in order to handle the requirement to circulate 13 TeV beams and collect the resulting higher energy collision data. On June 2015 the LHC restarted to deliver physics data, marking it the beginning of Run-2, which lasted until 2018. In this period the LHC collided up to 10^{11} bunches of protons every 25 ns, resulting in over forty million collisons per second at the design luminosity[2] of $2 \times 10^{34}\,\mathrm{cm}^{-2}\mathrm{s}^{-1}$. Luminosity is defined as [57]:

$$\mathscr{L} = f\frac{n_b N_1 N_2}{4\pi\sigma_x\sigma_y}, \tag{2.1}$$

where n_b is the number of bunches in an accelerator, N_1 and N_2 are the number of protons per bunch (which in the case of the LHC is assumed to be equal) in each colliding beam, f is the revolution frequency of the bunches, and $4\pi\sigma_x\sigma_y$ is the transverse area of the bunches at the interaction point, described by the Gaussian widths in the horizontal (σ_x) and vertical dimensions (σ_y) of the beam. The instantaneous luminosity ($\mathscr{L}$) relates to the event rate ($\frac{dN}{dt}$) and the cross section (σ) of a specific process via the equation:

$$\frac{dN}{dt} = \mathscr{L}\sigma_{\text{events}}. \tag{2.2}$$

The number of interaction per bunch crossing is generally referred to as *pile-up* (μ) [58], and can be expressed as

$$\mu = \frac{\mathscr{L}\sigma_{\text{inel.}}}{n_{\text{bunch}} f_r}, \tag{2.3}$$

[2] The highest luminosity the detector was design to cope with.

where $\sigma_{\text{inel.}}$ is the total inelastic cross-section, n_{bunch} is the number of circulating bunches, and f_r is the bunch frequency. Figure 2.1 shows the mean number of interactions per bunch crossings averaged over a specific luminosity block ($\langle\mu\rangle$) found to be ranging from 13.4 up to 37.8 during the Run-2 data taking period, which was a significant increase from the 9.7-20.1 reached in Run-1.

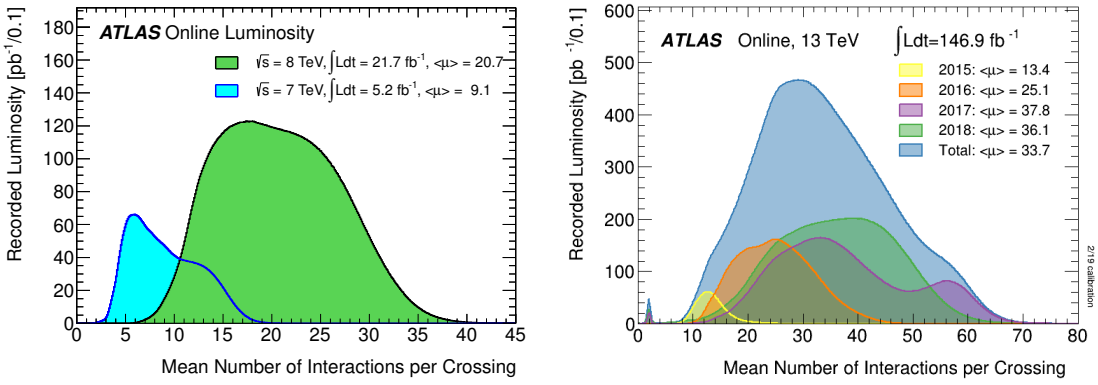

(a) Run-1 (2011-2012)

(b) Run-2 (2015-2018)

Figure 2.1: Luminosity-weighted mean number of interaction per crossing in the ATLAS detector during stable beams for pp collisions at centre-of-mass energy of 13 TeVfor (a) Run-1 (2011-2012) and (b) Run-2 (2015-2018) data collection periods.

Accelerator stages

To reach their maximum energy in the LHC, protons need to be accelerated in various stages by different smaller accelerators. The first stage of proton acceleration is performed by the Linear Accelerator 2 (LINAC2), which accelerates the protons in the beam to 50 MeV; the Proton Synchrotron Booster (PSB) accelerates the protons to 1.4 GeV. The resulting beam is then injected into the Parton Shower (PS), which brings the beams to 25 GeV, and then into the Super Proton Synchrotron (SPS), which allows the protons to reach 450 GeV. At this point the beams are separated into bunches with a 25 ns spacing and introduced into the LHC where they travel in opposite directions while accelerating to the required centre-of-mass energy of 13 TeV. A sketch of the machinery used for the injection and acceleration of the proton beam can be seen in Figure 2.2. The LHC also operates heavy ion runs, which begin the acceleration process in the Linear Accelerator 3 (LINAC3) and the Low Energy Ion Ring (LEIR), before following the same acceleration chain as the protons.

The yellow points visible along the gray oval used to represent the LHC in the schematics shown in Figure 2.2 represent the four large detectors situated at the collision points: the Large Hadron Collider beauty (LHCb) [60] that focuses on flavour physics; A Large Ion Collider Experiment (ALICE) [61], which is specialised in heavy ion physics; and the multi-purpose CMS [62], and ATLAS detectors. There are many other smaller experiments situated at CERN both in the cavers about the collision points and around the site, but these are beyond the scope of the thesis and will not be discussed further.

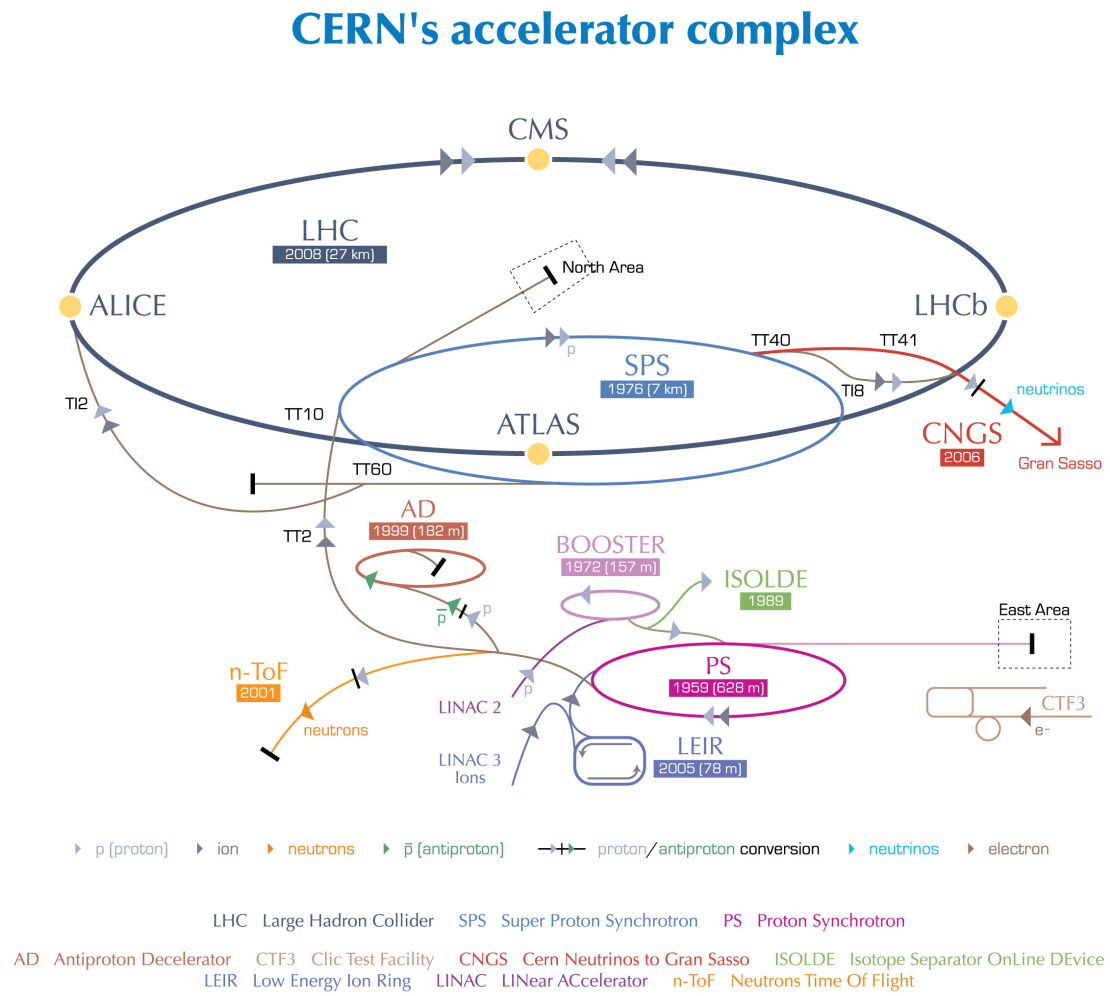

Figure 2.2: Schematics of CERN accelerator complex. The LHC is represented by the larger gray oval line, with the smaller machines used for early-stage accleration and to provide beams for other experiments shown in different colors [59].

2.2 The ATLAS detector

The ATLAS detector was designed to be a multi-purpose detector able to collect the data with the highest luminosity available by the LHC. The ATLAS detector has a forward-backward cylindrical geometry with respect to the interaction point, totalling in about 45 m in length and 25 m in diameter. It was designed to reconstruct and measure physics objects, such as electrons, muons, photons, and hadronic jets, that are essential for the core physics programmes at the ATLAS experiment. Various sub-systems (sub-detectors) are used to observe all possible decay products in a nearly 4π steradians of solid angle.

A schematic of the ATLAS detector and its components is shown in Figure 2.3. The sub-detector system closest to the interaction point is the Inner Detector (ID), which is a core component of the tracking system, and consists of the Silicon Pixel Tracker (Pixel), SemiConductor Tracker (SCT), and Transition Radiation Tracker (TRT). A 2 T magnetic field, generated by a thin superconducting solenoid which envelops the ID, bends the trajectories of the charged particles originating from the interaction process, and allows for the measurement of their

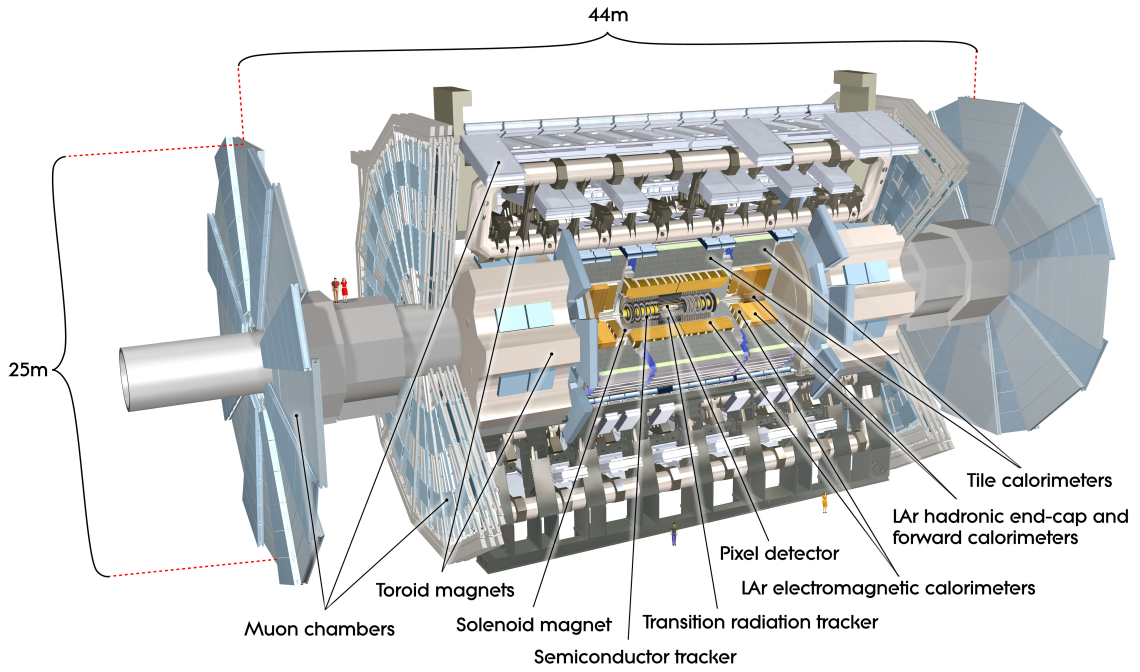

Figure 2.3: Schematics of cut-away ATLAS detector with labelled sub-systems. The dimensions of the detector are 25 m in height and 45 m with an overall weight of approximately 7000 tonnes [59].

transverse momentum. The next layers of the detector are composed of the Electromagnetic and Hadronic Calorimeters, which are used to perform precise energy measurements of photons and electrons in the former, and hadronic jets in the latter. The outermost layer of the detector is composed by the Muon Spectrometer (MS), which is located in a 4 T magnetic field generated by the barrel and end-cap toroids, and is tasked with the detection of tracks originating from penetrating muons. The magnets and sub-detectors that compose the ATLAS detectors will be discussed in more detail in the following sections.

The ATLAS coordinate system

A coordinate system with its origin at the interaction point of the detector is used for the spatial definition of the sub-detectors and kinematic measurements of physics processes. The z-axis runs along the beam line, with the $x-y$ plane perpendicular to the beam, and the x and y axes pointing from the origin towards: the centre of the LHC ring, and the surface of the earth, respectively.

Spherical coordinates are used, with ϕ being the azimuthal angle around the beam axis, and θ being the polar angle measured from the positive z-axis. Other coordinates known as rapidity y and pseudorapidity η are used instead of θ, which is susceptible to a boost in the beam direction. The angle ϕ, on the other hand, is invariant under a boost in the beam direction. Rapidity is generally used for massive objects, such as jets, and is defined as:

$$y = \frac{1}{2} \cdot \ln \left[\frac{E + p_z}{E - p_z} \right], \tag{2.4}$$

where E is the energy of the particle and p_z is the z-component of the momentum. For light relativistic particles, for which masses can be neglected, the rapidity can be reduced to the quantity:

$$\eta = -\ln\left[\tan\left(\frac{\theta}{2}\right)\right], \tag{2.5}$$

called "pseudorapidity". In the (η,ϕ) space the angular distance between two objects can be defined as:

$$\Delta R = \sqrt{\Delta\eta^2 + \Delta\phi^2}, \tag{2.6}$$

where $\Delta\eta$ and $\Delta\phi$ are the difference in pseudorapidity and azimuthal angle between the objects. Other widely used kinematic variables include the transverse momentum (p_T) and transverse missing energy $E_{\mathrm{T}}^{\mathrm{miss}}$. The transverse momentum describes the momentum of a particle in the transverse plane to beam line. It is thus measured in the $x-y$ plane and is defined as:

$$p_T = \sqrt{p_x^2 + p_y^2}, \tag{2.7}$$

where p_x and p_y are the x and y components of the momentum. The transverse missing energy is instead used to describe the transverse momentum of all the "invisible" particles (i. e. particles not detected by the ATLAS detector), since we know that the initial transverse momentum of the system was 0 and due to conservation of momentum, the final transverse momentum must also be 0. Therefore, a measured non-zero total "visible" momentum $\vec{p}_T^{\,\mathrm{vis}}$ indicates that there must be an equivalent amount of missing transverse momenta $\vec{p}_T^{\,\mathrm{miss}}$ with magnitude $E_{\mathrm{T}}^{\mathrm{miss}}$, defined as:

$$E_T^{\mathrm{miss}} = |\vec{p}_T^{\,\mathrm{vis}}| = |\vec{p}_T^{\,\mathrm{miss}}| = |\sum_i \vec{p}_T^{\,\mathrm{vis,i}}|. \tag{2.8}$$

2.2.1 Magnet System

The ATLAS magnet system is composed of three separate sets of magnets, used to generate the magnetic field needed to bend the trajectory of charged particles in order to measure their momenta, the details of which will be described in more detail below. Figure 2.4 shows the geometry of the system, which measures 26 m in length and 22 m in height, and is composed by: the central solenoid located around the ID, the barrel toroid which spans the length of the detector, and the end-cap toroids which are located at each end of the detector. More details on each set of magnets is given below. The magnets are made of Niobium-Titanium (NbTi), a material that allows the magnets to operate in the superconductive conditions required to generate strong magnetic fields.

The Central Solenoid: it is located between the ID and the Electromagnetic Calorimeter (ECAL). It has an inner and outer radius of 2.46 m and 2.56 m, with an axial length of 5.8 m. It is designed to generate a 2 T axial magnetic field, used to bend charged particle trajectories as they travel through the ID, providing the ATLAS experiment with accurate measurements of the momentum up to 100 GeV [64].

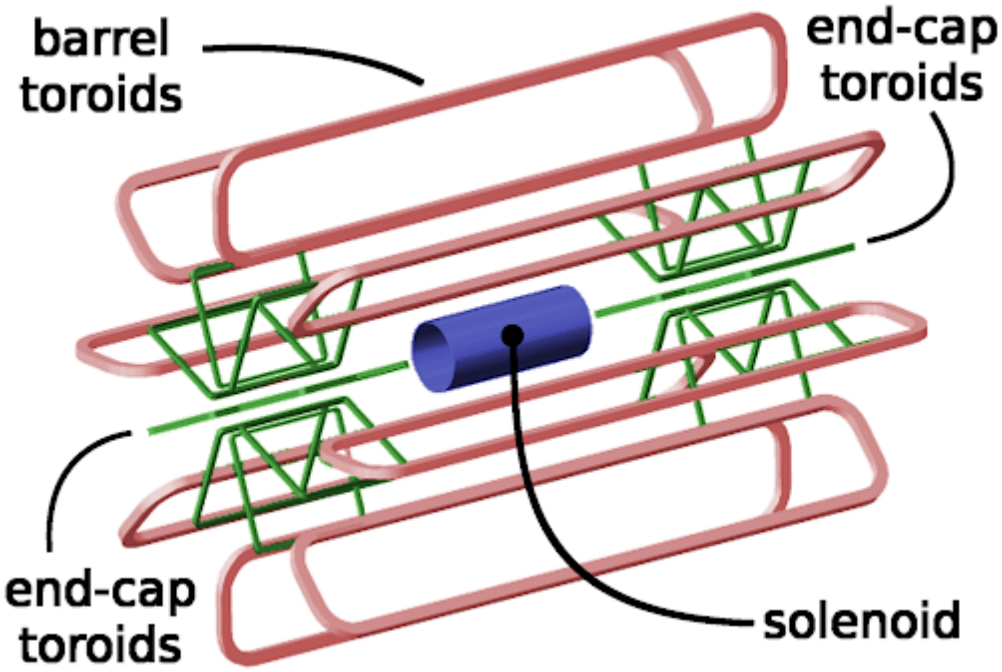

Figure 2.4: Schematics of the ATLAS magnet system used in the ATLAS detector (taken from [63])

Barrel and End-cap toroids: these are the other two sets of toroid magnets used in the ATLAS detector for the measurement of muon particles. On the outer edge of the detector, measuring 25.3 m in length and with an outer and inner diameter of 9.4 m and 20.1 m, respectively, is the barrel toroid. It is comprised of eight coils that provide 0.5 T toroidal magnetic field each acting perpendicular to the beam pipe, for a total field of 4 T, to the muon spectrometer. The end-cap toroid also provides a 4 T magnetic field, but are located at the ends of the detector, as shown in Figure 2.4 in order to be able to measure the highly energetic muons travelling close to the beam pipe. The end-cap toroids are 5 m long and 10.7 m in diameter [65].

2.2.2 Inner Detector

The ID is the sub-detector component of the ATLAS detector closest to the interaction region. It is designed to accurately reconstruct charged particle tracks used in the selection of physics objects. Different elements are used in the ID, as shown by Figure 2.5, to ensure that all particles within a range of $|\eta| < 2.5$ and $p_{\mathrm{T}} > 0.5$ GeV can be measured. Primary and Secondary vertices are accurately measured by the Pixel layer, composed of the Pixel and Insertable B-Layer (IBL), whose outgoing tracks are then detected by the SCT and finally identified by the TRT. A more detail description of each section of the ID is given below.

Pixel: The Pixel [67] detector is composed of three layers of silicon pixels formed into 1,456 and 288 identical sensorchip-hybrid modules for the barrel and end-caps, respectively. Each module contains 46,080 readout channels, or pixels, each with a surface area of

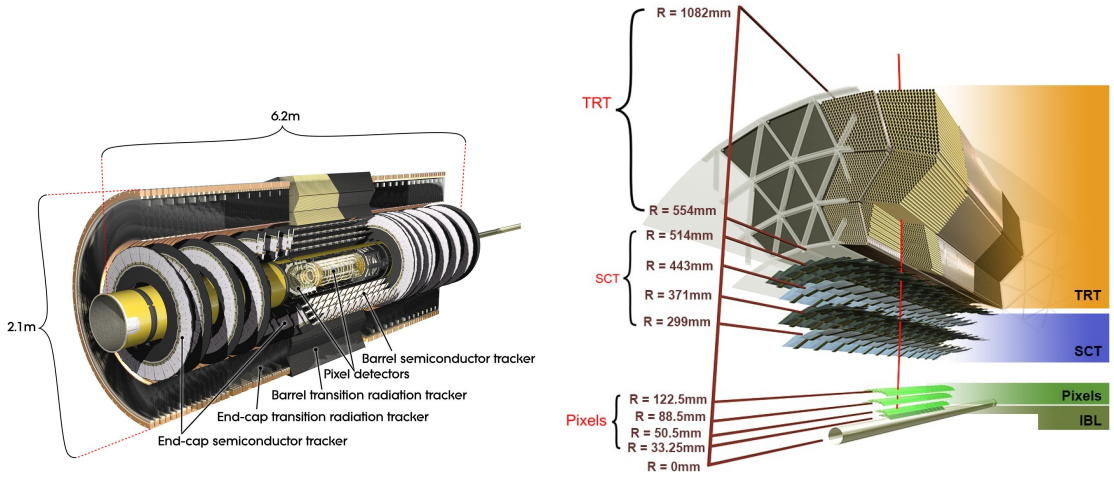

(a) Overview of the ATLAS ID with labels and dimensions.

(b) Schematics of ATLAS ID and its sub-detectors

Figure 2.5: The ATLAS inner detector (taken from [66])

$50 \times 400\,\mu\text{m}^2$, for a total of approximately 80 million pixels in the whole system (barrel and end-cap) [68]. The whole of the silicon pixel detector measures 48.4 cm in diameter and 6.2 m in length, covering $|\eta| < 2.5$ in pseudorapidity with three concentric layers placed at 50.5 mm, 88.5 mm, and 122.5 mm along the barrel. Three additional layers are located at the end-caps of both ends of the ID, for a total of 6 layers. This is done so that when a charged particle traverses the layers, the three space-points can be determined and consequently the track and vertices can be reconstructed.

IBL: The IBL [69] was added during the LS1 period to improve the vertex finding by a factor of 1.4 and impact parameter reconstruction by a factor of 2 with respect to Run-1 (see Chapter 3 for a more details description of the performance of vertex tracking in Run 2). It is part of the Pixel section of the ID and is comprised of 6 million channels, with each pixel measuring $50 \times 250\,\mu$m.

SCT: The SCT [70] consists of four concentric barrel layers of silicon micro-strip detectors with 2,112 modules, while the end-caps have nine layers with a total of 1,976 modules, each. It was designed for precision measurements of positions using four points (corresponding to eight silicon layers) obtained as track hits as a particle crosses the layers, and is used for precise momentum reconstruction for pseudorapidities $|\eta| < 2.5$. The SCT layers are located at 299 mm, 371 mm, 443 mm, and 514 mm from the interaction point, as shown by Figure 2.5(b), with each module having an intrinsic resolution of 17 μm and 580 μm in the $R-\phi$ and z directions, respectively. A reduced granularity can be used whist maintaining the same level of performance, compared to the pixel detector, because it is located further away from the interaction region and thus has to cope with reduced particle density.

TRT: The TRT [71] consists of three barrel rings, with 32 modules each, and 18 end-caps units

with 224 layers. A total of 370,000 cylindrical drift tubes (straws) of 4 mm diameter and 1.44 m in length are filled with a mixture of 70%Xe + 27%CO_2 + 3%O_2. These are positioned parallel to the beam pipe in the barrel and radial in the end caps. The combination of gases have been chosen and tested to have good X-ray absorption, and increase the electron drift velocity and photon quenching. An aluminium coat around the straws is used as the cathode, with a 30 μm gold-plated tungsten wire through the centre of the straw tube as the anode. As a charged particle travels trough the TRT, the gas in the straw tubes is ionised causing the electrons to drift to the anode, which records this as a hit. The TRT can also perform particle identification through the detection of transition radiation photons, which are emitted when highly relativistic charged particles cross boundary between mediums with different dielectric constants. In the TRT this is done by polypropylene fibres (foils), which are interwoven between the barrel (end-cap) straws, that enable the production of transition radiation in the form of X-rays. The amount of radiation produced can be used to distinguish between, e. g. electrons and charged pions, as the amount of radiation would depend on how relativistic the charged particle is.

2.2.3 Calorimeters

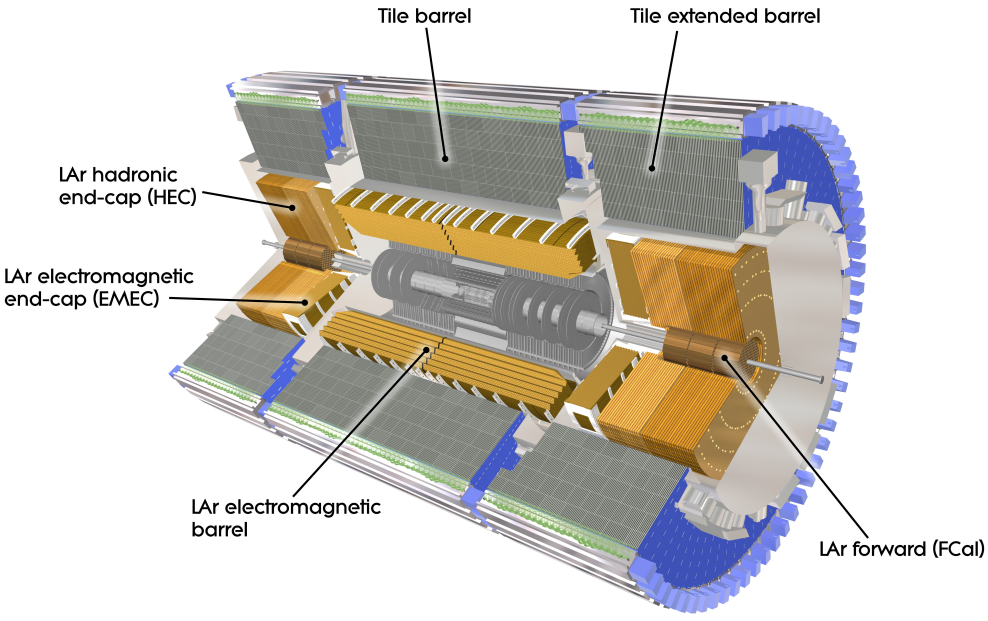

Figure 2.6: Labelled schematics of the ATLAS ECAL and HCAL system. [65]

The ATLAS calorimeters are designed to measure the energy of electromagnetic (ECAL) and hadronic (HCAL) interacting particles. The energy of electromagnetically interacting particles, such as electrons, positrons, or photons, is measured in the ECAL [72], which is comprised of one barrel and two end-cap sensors located around the central solenoid. The HCAL [73] is also comprised of one barrel and two end-cap sectors and it is located around the ECAL, so that particles travelling through the detector will have to first go through the ECAL. The HCAL

is tasked with the detection and measurement of the energy deposited by hadronic showers. This is done by using tile sensors in the barrel made of scintillating plastic, while Liquid Argon (LAr) is used in the end-caps. Figure 2.6 shows a detailed schematics of the calorimeter system used by the ATLAS detector. More detail of the ECAL and HCAL geometry, functionality, and materials is given in the following paragraphs.

ECAL The ECAL utilises LAr to measure electromagnetic showers that occur when a high-energy electron or photon travel through the fluid. Photons that are above a few MeV will interact primarily via pair production, in which a highly energetic photon will interact with a nucleus to create a electron-positron pair. High-energy electrons and positrons, on the other hand, will produce photons via Bremsstrahlung. These two processes will continue in the ECAL until the energy of the emitted photons falls below the pair production threshold. At that point, the energy loss of the electron will start to dominate. The ECAL uses an "accordion"-geometry, shown in Figure 2.7, comprised of multiple layers of LAr sampler and lead (Pb) absorber, to achieve a full ϕ coverage with no non-interactive regions (referred to as "cracks"), and fast extraction of signals from both front or read end of the electrodes. The barrel and end-cap sectors provide a pseudorapidity coverage of up to $|\eta| < 1.475$ and $1.375 < |\eta| < 3.20$, with the junction between the barrel and end-cap components being defined as a crack region from which any signal should be discarded. An additional thin LAr layer with no absorber is placed in front of the calorimeter in the $|\eta| < 1.8$ region. This layer is designed to correct for the energy lost, as particles enter the calorimeter, by taking a measurement just before the majority of the electromagnetic shower is developed.

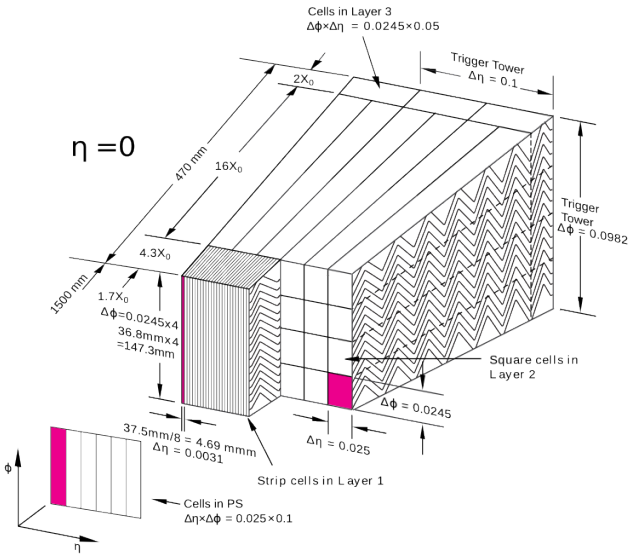

Figure 2.7: Schematics of the ECAL accordion-geometry. [65]

HCAL: Steel and scintillating tiles, coupled with optical fibres, are read out by photo-multipliers in the HCAL. A central barrel, 5.64 m long covering $|\eta| < 1.0$, and two extended barrels, 2.91 m long covering a region $0.8 < |\eta| < 1.7$ make up the HCAL. Each cylinder is com-

posed of 64 modules, each of which is made of three layers. The forward region, closest to the beam, is covered by a LAr Forward Calorimeter (FCal). The smallest section of the calorimeter module is a cell with a $\Delta\phi \times \Delta\eta = 0.1 \times 0.1$ granularity for the two innermost layers and $\Delta\phi \times \Delta\eta = 0.2 \times 0.1$ for the outermost one.

2.2.4 Muon spectrometer

Muon particles are minimal interacting and are thus able to travel through the entire ATLAS detector. Therefore, MS [74] is designed to accurately measure the momenta of these particles. It is located within the 4 T magnetic filed generated by the long barrel toroid, described in Section 2.2.1, and is comprised of three concentric chambers in the barrel region with an outer radius of 10 m, and three layers of chamber planes perpendicular to the beam pipe in the end-caps at a maximum distance of 21.5 m (as shown in Figure 2.8). High precision momentum

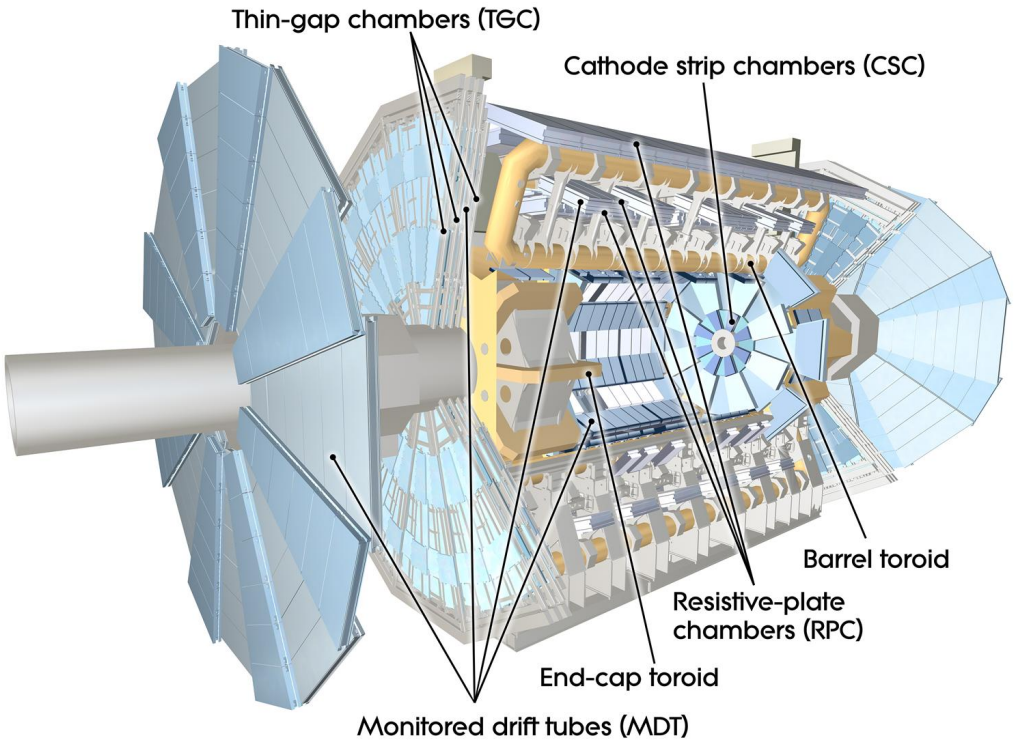

Figure 2.8: Computer generated schematics of the ATLAS MS system (taken from [65]) .

measurements are possible by performing high precision tracking on the deflected trajectories of the charged muons as they travel through the different layers of the MS. The large barrel toroid covers a region of $|\eta| < 1.4$, while two end-cap toroids deflect tracks between $1.6 < |\eta| < 2.7$. A combination of both magnets is used for the "transition" region $1.4 < |\eta| < 1.6$. Two types of chambers are used in the barrel: the Monitored Drift Tubes (MDTs) and Resistive-Plate Chambers (RPCs). The MDTs are also present in the end-cap layers, along with Cathode Strip Chambers (CSCs) and Thin-Gap Chambers (TGCs). A more detailed description of each of the chamber systems used in the MS is given in the following paragraphs.

MDTs are 29.97 mm diameter drift tubes, filled with pressurised 93%Ar + 7%CO_2 gas, employed in most of the pseudo-rapidity range to provide measurements of track coordinates in the bending direction. Electrons resulting from the ionization of the gas from a penetrating muon are collected by a tungsten-rhenium wire, measuring 50 μm in diameter, located at the centre of the tube. Three to eight layers of drift tubes are used in both barrel and end-caps to allow a total of twenty measurements for each track. MDTs can achieve an average resolution of 80 μm per tube, or about 35 μm per chamber.

CSCs are used in the innermost tracking layer for the higher particle flux and muon-track density forward direction ($2 < |\eta| < 2.7$), due to their higher rate capability and time resolution compared to MDTs. CSC consist of two disks with eight chambers each, where each chamber contains four multi-wire proportional chambers with four cathode plates. The chambers are filled with 80%Ar + 20%CO_2 gas, with the cathode strips aligned both parallel and perpendicular to the anode wires, to provide precision and transverse coordinates. The achieved resolutions of the CSC is 40 μm in the bending plane and 5 mm in the transverse plane.

TGCs are very similar to CSC and compliment the precision tracking system provided by the MDT and CSC by delivering track information within a few tens of nanoseconds after the passage of the particle. Like CSC, they are multiwire proportional chambers filled with 55%CO_2+45%n-pentane gas, with the cathode plates 2.8 mm and the anode wires 1.8 mm apart. This configuration, along with high electric field, results in very good time resolutions. TGCs are essential for providing muon triggering and secondary complementary coordinates, orthogonal to the precision measurements, in the end-caps for the $1.05 < |\eta| < 2.7$ region. Nine space-points are recorded for every track using a TGC.

RPCs are also used, like TGCs, to provide muon triggering and secondary coordinates in the barrel for $|\eta| < 1.05$. They are parallel electrode-plate detectors, made of plastic laminate 2 mm distance apart, filled with 94.7%$C_2H_2F_4$ + 5%Iso − C_4H_{10} + 0.3%SF_6 gas. A maximum of six space-points are recoded for every track.

2.3 The ATLAS Trigger and Data Acquisition

The LHC provides the ATLAS experiment with ~40 MHz of pp collisions. A sophisticated Trigger and Data Acquisition (TDAQ) [75, 76] system is used to reduce this rate of data down to manageable levels (~1 kHz) by storing only events that contain potentially "interesting" physics. A two level trigger system has been used during Run 2, consisting of a hardware-based trigger, named Level-1 (L1), and a software-based trigger, called High Level Trigger (HLT). Low granularity information from the calorimeter and muon spectrometer systems is processed by the L1 to identify so-called Region of Interests (RoIs) before making a decision. Event data from other sub-detectors and systems is stored in memory until the L1 decision is taken. Upon passing the rapid L1 selection, the event data is passed to the HLT system. The HLT is made of software

running on computer cluster (HLT farm), which use information not available to the L1 such as finer-granularity calorimeter inputs and precious measurements from the MS, to further analyse the event-data and decide whether to keep or discard the event. The flow of data through the L1 and HLT system is managed by the data acquisition system, which eventually passes all accepted events into data streams for offline physics, monitoring, and detector analyses. Objects that do not meet the L1 or HLT requirements are discarded. The ATLAS trigger system is discussed in detail in Chapter 3.

2.4 The detection and measurement of τ-leptons

The τ-lepton has a mass of ~1.777 GeV and a proper decay length of 87 μm [77], and can decay either leptonically ($\tau \rightarrow \ell \nu_\ell \nu_\tau$, $\ell = e, \mu$) or hadronically ($\tau \rightarrow$hadrons ν_τ,hadrons= $\pi^\pm, \pi^0$), typically before reaching active regions of the ATLAS detector. The hadronic tau lepton decay represents 65% of all possible decay modes, where the decay products can be with one or three charged pions (generally referred to as 1- or 3-prong) in 72% and 22% of all cases, respectively. Figures 2.9 shows a set of feynman diagrams describing the allowed first order decay processes for the τ-lepton, separated between the leptonic, one charge pion (1-prong), and three charged pions (3-prong) final states. The neutral and charged hadrons stemming from the τ-lepton decay make up the visible part of the τ_{had} lepton, and are, therefore, extremely important when identifying and reconstructing this object.

In the ATLAS experiment only hadronically decaying τ-leptons (τ_{had}) are considered as τ-objects. τ-leptons that decay to a lepton are considered as the final state lepton (i. e. τ-lepton decaying to an electron is considered as an offline electron by the ATLAS algorithms). τ-leptons can be identified within the ATLAS detector as they will have a displaced vertex, resulting from the τ-lepton mean lifetime. They will then produce a distinct number of charged particles, that can be measured and tracked by the ID, corresponding to the decay process of the τ-lepton (1-prong or 3-prong). The hadronic jets originating from the τ-lepton generally will be collimated and well isolated. This will result with the ECAL registering a clusters of energy deriving from the charged and neutral hadrons produced by the τ-lepton, with the full energy deposit of the hadrons collected by the HCAL.

Due to the complex nature of the τ-lepton and the quick decision time required by the ATLAS trigger, the online and offline identification and reconstructions are performed differently. A summary of the different reconstruction, identification, and calibration procedures performed online and offline is provided below.

2.4.1 Online hadronic τ-lepton Reconstruction and Identification

For the online τ-lepton identification required for the trigger decision, the Level-1 will construct a trigger tower defined in the ECAL and HCAL with coarse granularity. A core region is made up of a set of 2×2 trigger towers and a requirement on the sum of the total transverse

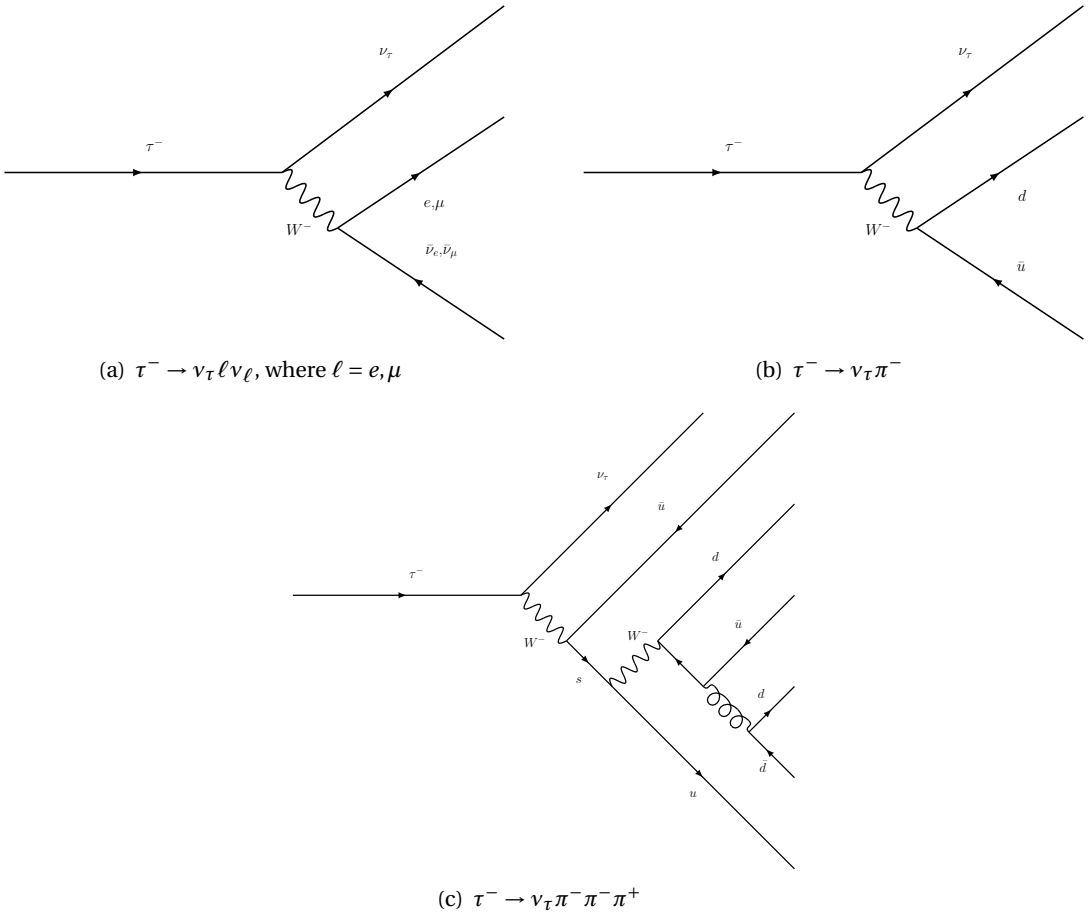

(a) $\tau^- \to \nu_\tau \ell \nu_\ell$, where $\ell = e, \mu$

(b) $\tau^- \to \nu_\tau \pi^-$

(c) $\tau^- \to \nu_\tau \pi^- \pi^- \pi^+$

Figure 2.9: Feynman diagrams illustrating the allowed first-order decay processes for the τ-lepton. The final state particles can either be (a) a lepton and neutrinos, (b) one changed pion and a neutrino, or (c) three charged pions and a neutrino. Additional neutral pions may also be produced in the hadronic τ-lepton decay. Only τ-leptons that decay to hadrons are reconstructed as τ_{had} objects by the ATLAS detector.

energy of the two highest adjacent trigger towers is placed. At HLT, the energy is re-calculated using Local hadronic Calibration (LC)-calibrated TopoClusters of finer granularity calorimeter cells in a $\Delta R = 0.2$ cone around the L1 tau direction. A multistage tracking process, described in detail in Chapter 3, is used to identify tracks from the τ-lepton candidate. The track and calorimeter information derived from the HLT are used to calculate a number of pileup corrected variables used as inputs to an online Boosted Decision Tree (BDT) algorithm similar to the one used offline for τ-lepton identification described below.

2.4.2 Offline hadronic τ-lepton Reconstruction and Identification

The τ_{had} offline reconstruction algorithm uses jets formed by the anti-k_t algorithm with distance parameter $R = 0.4$ and clusters of calorimeter cells, calibrated using a LC as input seeds for the reconstruction algorithm. These seed jets must also satisfy a $p_{\mathrm{T}} > 10$ GeV and $|\eta| < 2.5$ requirement. Tracks associated to the τ_{had} candidate must also follow some criteria. They are required to be within a cone of $\Delta R < 0.2$ around the τ_{had} candidate direction and also satisfy the following criteria: $p_{\mathrm{T}} > 1$ GeV, at least two associated hits in the pixel detector (including

IBL), and at least seven hits total in the pixel and SCT detector. More details on the requirements and methodology of τ_{had} reconstruction can be found in Reference [78].

The reconstruction efficiency of the visible τ_{had} is defined as the fraction of 1-prong (3-prong) τ_{had} decays which are reconstructed as a 1-track (3-track) visible τ_{had} candidate by the ATLAS detector and reconstruction algorithm divided by the number of true visible τ_{had} objects in the event (truth $\tau_{\text{had-vis}}$) and identified at truth level using the truth matching method, described in more details in Section 5.2. Figure 2.10 shows the reconstruction efficiency for 1-prong and 3-prong τ_{had} with respect to true visible τ_{had} p_{T} ($p_T^{\tau_{\text{had-vis}}}$). The efficiency is relatively constant for 1-prong decays with respect to the transverse momentum of the visible τ_{had}, peaking at around 75% at 100 GeV with a slow drop towards the higher values of momentum due to two separate effects. Very high-p_{T} τ-leptons may decay after the first pixel detector and fail the requirement on the number of hits. Secondly, the probability of wrongly classifying an electron from photon conversion as a charged hadron from a τ-lepton decay also increases with p_{T}, thus increasing the probability of assigning the incorrect number of charged particles to the tau decay. For the 3-prong decay, the efficiency is found to be ranging between 50-75%. The reduction in efficiency observed for the 3-prong decays in the low-p_{T} bins is due to the minimum transverse momentum requirement on the charged decay products. At high-p_{T} the increase collimation of the decay products results in an increased probability of missing a track due to overlapping trajectories [78].

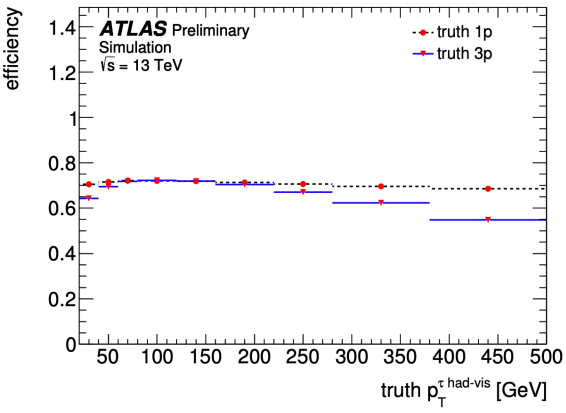

Figure 2.10: Efficiency for reconstructing the same number of tracks as the number of charged decay products of the tau lepton as a function of visible τ_{had} p_{T}. (taken from [78])

The identification of visible τ_{had} candidates to discriminate τ-lepton decays from hadronic jet offline follows the approach described in Reference [78] for Run-1, and the first half of Run-2 (up to 2018), where a BDT [78] multivariate technique is used to distinguish between the true visible τ_{had} objects for QCD processes. For the second half of Run-2 (2018-onwards) the BDT-based tau identification algorithm was superseded by the Recursive Neural Network (RNN) identification algorithm described in Reference [79]. This was found to have a rejection power about two times better than the previously used BDT-based classifier for any given signal selection efficiency. The RNN algorithms uses a set of low-level (individual) and high-level (calculated) input variables for tracks and clusters associated to the τ-lepton candidate. Low-level variables include the track transverse momentum, transverse and longitudinal impact parameters, angular distance to the visible τ_{had} axis, and number of hits on the track in the different Silicon (Si) detector layers, the TopoCluster transverse energy, angular distance to the visible τ_{had} axis, and the cluster moments. High-level observables include transverse momentum of the seed jet, transverse momentum at the LC scale, the fraction of transverse energy at EM

scale deposited in the central region of the calorimeters around the τ_{had} axis, the maximum track ΔR, the transverse impact parameter significance of the leading track, and many more. The full description of the Multivariate Algorithm (MVA) sctructure and parameters used can be found in Reference [79].

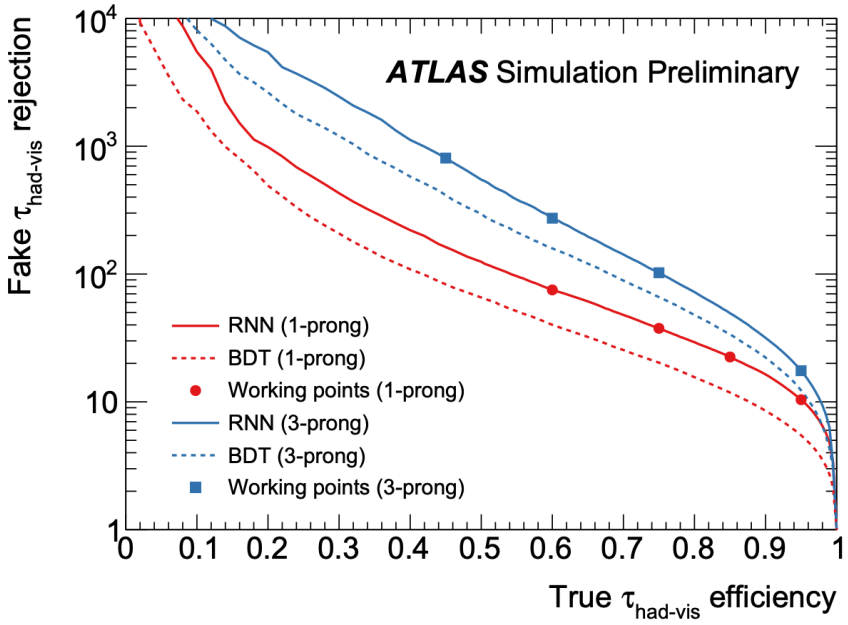

Figure 2.11: Rejection power for jets misidentified as visible τ_{had} (fake visible τ_{had}) depending on the true visibltτ_{had} efficiency. Shown are the curves for 1-prong (red) and 3-prong (blue) visible τ_{had} candidates using the RNN-based (full line) and the BDT-based (dashed line) identification algorithms. The markers indicate the four defined working points *Tight, Medium, Loose and Very loose* with increasing signal selection efficiencies (taken from [79]).

The rejection power against misidentified τ_{had} as a function of the true visible τ_{had} selection efficiency, for both BDT and RNN classifiers (independently for 1-prong and 3-prong candidates), is shown in Figure 2.11. Four working points, with increasing background rejection (*Very loose*, *Loose*, *Medium* and *Tight*), are generally used in ATLAS physics analyses. The corresponding signal selection efficiencies and rejection powers are given in Table 2.1

Table 2.1: List of defined working points with fixed true visible τ_{had} selection efficiencies and the corresponding background rejection factors for misidentified visible τ_{had} in multi-jet events for the BDT and RNN classifiers (taken from [79]).

	Signal Efficiency		Background Rejection BDT		Background Rejection RNN	
Working Point	1-prong	3-prong	1-prong	3-prong	1-prong	3-prong
Tight	60%	45%	40	400	70	700
Medium	75%	60%	20	150	35	240
Loose	85%	75%	12	61	21	90
Very Loose	95%	95%	5.3	11.2	9.9	16

It is important to note that the rejection power for jets misidentified as visible τ_{had} objects is strongly dependent on the reconstructed τ_{had} p_{T} (as well more weakly dependent on η and $\langle\mu\rangle$) [79]. Figure 2.12 shows the background rejection in multi-jet events for the *Medium* working point for both BDT and RNN classifiers as a function of reconstructed τ_{had} p_{T}. The

rejection power is found to increase with increasing p_{T}.

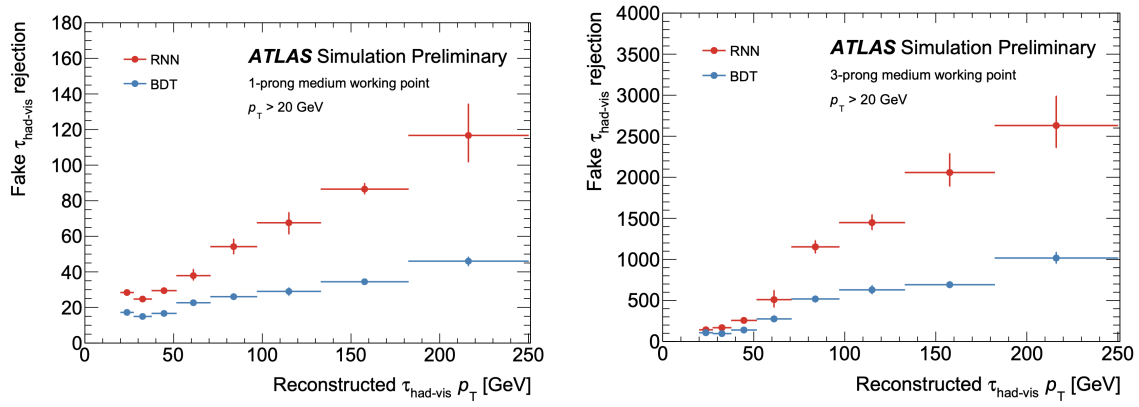

(a) (b)

Figure 2.12: Rejection power for jets misidentified as visible τ_{had} (fake visible τ_{had}) for (a) 1-prong and (b) 3-prong as a function of their transverse momentum p_{T}. The rejection power is shown for the *Medium* working point for both RNN-based (red) and BDT-based (blue) classifiers. (taken from [79]).

2.4.3 Offline hadronic τ-lepton Energy Calibration

The energy scale calibration of τ-leptons uses calorimeter information only. After the reconstruction, τ_{had}candidates are calibrated at the LC scale which corrects for the calorimeter non-compensation and for the energy deposited in dead material or outside TopoClusters. The τ_{had} energy scale is additionally adjusted by subtracting the energy contribution originating from pileup interactions and applying a response correction to account for the following possible τ_{had} effects: decay products not reaching the calorimeter, not depositing enough energy to create TopoClusters, or notdetected within $\Delta R = 0.2$ of the reconstructed visible τ_{had} candidate. No other effects are taken into account towards the energy scaale calibration of the τ-lepton. A more detailed description of the energy scale calibration process performed by the ATLAS experiment during Run-2 can be found in Reference [78].

THE ATLAS TRIGGER SYSTEM

3

There are patterns I must follow,
just as I must breath each breath.
Like a rat in a maze, the path before
me lies.

Simon & Garfunkel

The ATLAS Inner Detector trigger system, together with its performance for Run-2, will be presented in this chapter. A brief introduction of the motivation behind the need of a trigger system, together with its implementation in ATLAS, will be discussed. The L1 and HLT stages of the trigger will be discussed in Sections 3.2 and 3.3, respectively. Section 3.5 will be dedicated to the description and performance of the tracking and triggering performed by the inner detector trigger system for electrons, muons, taus and $b-$jet triggers. The study of the performance of these triggers has been part of the author's *qualification task* and the results have been collected in a paper that is currently under collaboration review. The study of the tau-triggers in particular are extremely important for the analysis discussed in Chapter 4, the identification of τ-leptons discussed in Chapter 5, and the development of future low-p_{T} triggers discussed in Chapter 6.

3.1 Overview

In 2016, 2017 and 2018 the ATLAS detector recorded 35.6 fb^{-1}, 46.9 fb^{-1}, and 60.6 fb^{-1} respectively of pp collision data at centre-of-mass energy of 13 TeV. Due to storage and processing limitations, it is not feasible to store all the information about the collisions after every bunch crossing. Therefore, the ATLAS trigger system [80, 81] is indispensable for reducing the read-out rate without discarding potentially interesting events for the ATLAS physics programme. The trigger operates with a multi-level architecture, consisting of both hardware- and software-based real-time algorithms for the identification of interesting events.

The TDAQ system is comprised of the first-level hardware-based L1 trigger, followed by the software-based HLT. Figure 3.1 shows schematic of the architecture structure of the TDAQ

system, including the Fast Tracker (FTK) system which was being commissioned during the Run-2 data collection period and was, therefore, not used for the results shown here. The L1 Calorimeter (L1Calo) and L1 Muon (L1Muon) triggers are used as inputs to the Central Trigger Processor (CTP), which performs the trigger decision in real-time (online). The events that pass the L1 selection are buffered in the Read-Out System (ROS) [82] so that they can be ready for distribution to a farm of the HLT processing nodes. Because of the extremely high data volume in the SCT and Pixel detectors, these can only be read out following a L1 accept and as such the HLT is the first stage at which tracks can be reconstructed in the silicon layers. The HLT receives information on the Region of Interest (RoI) defined by the L1 to perform the reconstruction in the trigger algorithms. RoIs are extended wedge-shaped spatial regions in the detector used to reduce the amount of data (between 2%-6% of total volume of data [83]) to be transferred and processed. The geometry of an RoI in the HLT changes between the different object candidates to be reconstructed, but it is generally constructed as a region originating from and extending along the beam-line (see Section 3.4 for further details).

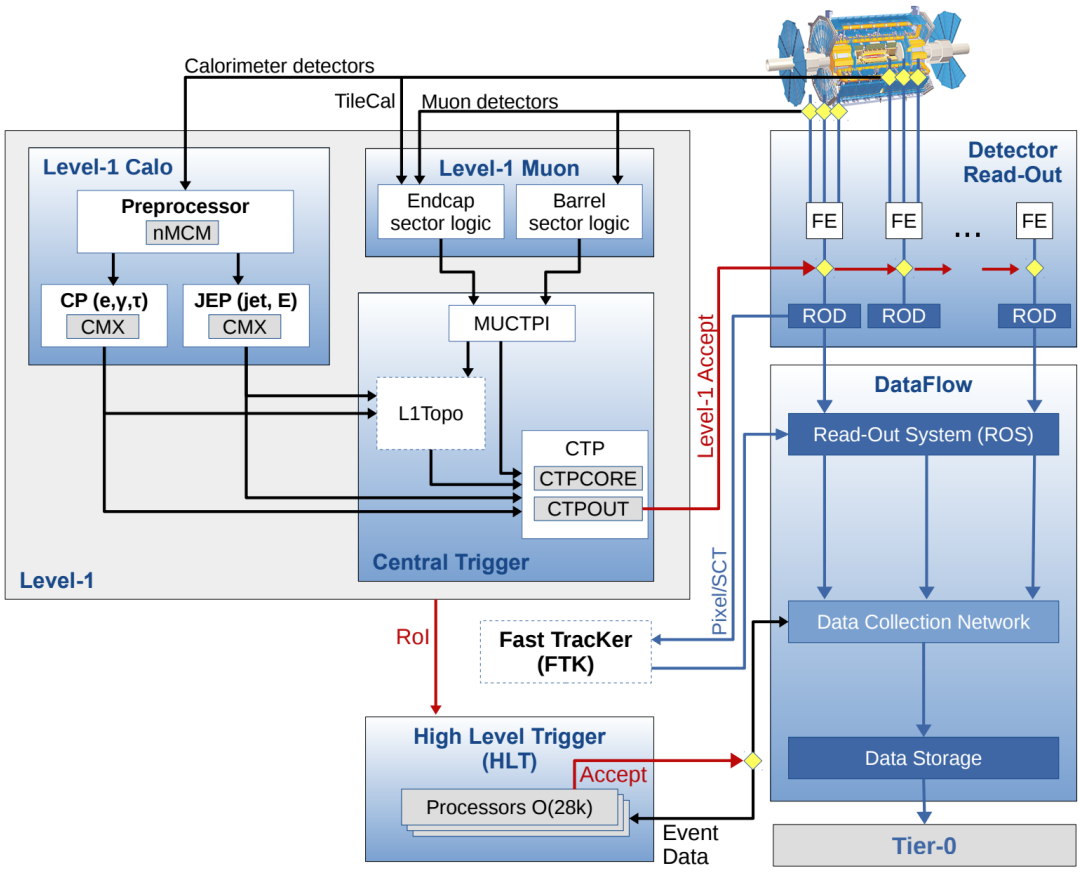

Figure 3.1: The ATLAS TDAQ system in Run 2 with emphasis on the components relevant for triggering [80]. The FTK system was being commissioned during Run 2 was thus not used for the results shown here.

The ATLAS triggers are configured into different categories. Triggers are generally defined as *trigger chains* which start from a L1 trigger and specify a sequence of reconstruction and selection steps required for the signature of interest. The naming convention is as follows:

TriggerLevel_TypeAndThreshold_Identification_Isolation_L1Thresholds,

where "TriggerLevel" refers to either L1 or HLT and "TypeAndThreshold" refers to the type of object that is being triggered (e, μ, τ, jet, etc.) and its energy threshold. If any identification and/or isolation criteria are used, they are appended to the end of the *trigger chain* name i. e.: `HLT_tau25_medium1_tracktwo` is a tau trigger at HLT level with a 25 GeV energy threshold, using "medium" identification criteria, and with between 1 and 3 tracks in the inner detector ("*tracktwo*"). The energy threshold and identification criteria used to identify the trigger object are have been discussed in detail in Section 2.4. For HLT triggers, any additional L1 requirements are described in the "L1Thresholds" and appended to the end of the trigger chain.

It is important to note that not all triggers need or are able to run at their full rate, due to the high luminosity achieved at the LHC and abundance of trigger objects (e. g. single jet triggers). In these cases, a sub-sample of events passing the trigger requirements are enough. Therefore, some triggers have a purposefully decreased output rate, known as *prescale*, which can be applied at L1 and/or at the HLT. A trigger with a prescale of N would indicate that the trigger accepts 1 out of N events.

3.2 Level-1 Trigger

The L1 trigger decision is performed by the CTP, which uses the information gathered by the L1Calo and L1Muon trigger systems. The L1Calo trigger [65, 84] is based on coarse granularity data inputs from the electromagnetic and hadronic calorimeters. It aims to identify high-E_T objects such as electrons and photons, jets and τ-leptons decaying into hadrons as well as events with large $E_{\mathrm{T}}^{\mathrm{miss}}$ and large total transverse energy. For electron/photon and τ triggers, isolation can be required, meaning that the energetic particle must have a minimum angular separation from any other significant energy deposit in the same trigger.

The L1Muon trigger is based on input signals from the muon trigger chambers: RPC in the barrel and TGC in the end-caps. The trigger searches for patterns of hits consistent with high-p_{T} muons originating from the interaction region. Muons are not double counted across the different thresholds.

While the L1 trigger is based only on the multiplicity of trigger objects (or flags indicating which thresholds were passed, for global quantities), information about the geometric location of triggers objects is retained in the muon and calorimeter processors. Once the event is accepted by the L1 trigger, this information is sent as an RoI to the HLT. Due to the high rate of interactions, the latency, which is the the time taken from the pp collision until the L1 trigger decision, must be kept as short as possible. The design of the trigger requires the L1 latency to be less than 2.5 μs. To achieve this aim the L1 trigger is implemented as a system of purpose-built hardware processes. The L1 trigger is thus able to reduce the peak data rate from 40 MHz (rate of collision at LHC) down to a more manageable 100 kHz.

3.3 High-Level Trigger

Events that pass the L1 are buffered by the ROS and then processed by the HLT. The HLT trigger is able to access information not available to the L1, such as finer-granularity calorimeter inputs, precision measurements from the MS, and tracking information from the ID pixel and SCT. The information provided to the HLT is in the form of RoIs, which allows for faster reconstruction algorithms as the entire range of the detector does not need to be processed. The HLT triggers reconstruct tracks first using a fast but less accurate reconstruction algorithm, which is able to reject the majority of uninteresting events. Following this first stage, a second more precise (but slower) reconstruction algorithm is run using the results of the first stage on the remaining events. Using this software based reconstruction and event acceptance algorithms, the HLT trigger system is able to reduce the peak input rate from 100 kHz, from the L1 trigger, down to 1.2 kHz. Events that are accepted by the HLT are transfered to a local storage at the experiment site and exported to the CERN's computing centre for offline reconstruction [85].

3.4 Inner detector Trigger Tracking

As mentioned previously, to reduce processing time a two-step tracking approach is implemented by the HLT triggers: *fast tracking* and *precision tracking*. The *fast tracking* consists of a trigger specific pattern recognition, while the *precision tracking* relies heavily on offline algorithms, and is seeded with the information from the *fast tracking* step [80, 86].

The tracking of electrons and muons is performed using the standard two-step approach consisting of the *fast tracking* followed by the *precision tracking*. The combination of these two steps is considered to be a single *tracking stage*. The tracking of hadronically decaying taus and b-jets is, however, more complex and thus employs a multi-stage approach in order to reduce the volume of the RoI, and the processing time that would be required if it were done in a single stage.

Fast Tracking

For the inital stage of track finding in the trigger, the Fast Track Finder (FTF) [86] algorithm was developed to provide track candidates that could be used to seed the precision tracking stage. Therefore, the FTF design prioritises track finding efficiency over purity. The FTF pattern recognition is performed by searching for triplets of space-points (*track seeds*) in bins of r and sectors of ϕ, as shown in Figure 3.2. The selection of the triplet begins with the middle space-point, followed by the identification of the *outer* and *inner* space-points at larger and smaller radii, respectively. The inner and outer pair of space-points must be compatible with the nominal interaction region along the beam line. This region can be replaced by a restricted z-region of the RoI along the beam line as also shown by Figure 3.2, in the case of RoI based tracking. The triplet track parameters ϕ_0, transverse momentum p_T, and transverse impact parameter

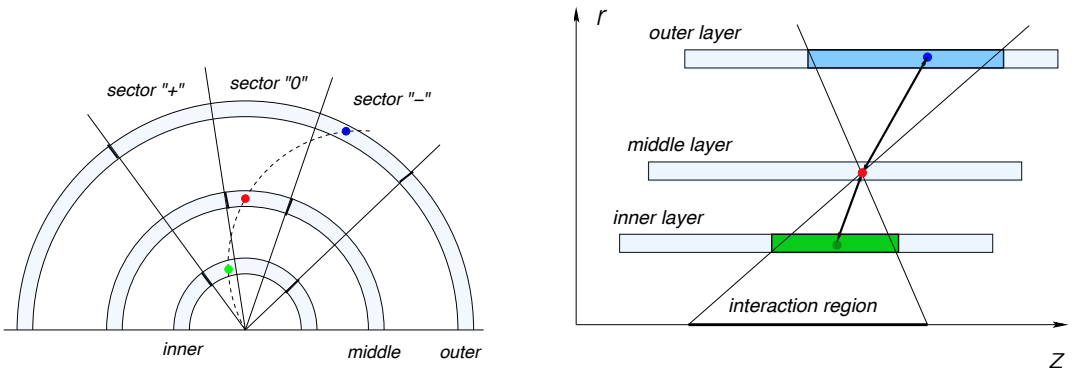

(a) (b)

Figure 3.2: Schematics (a) the track seed information in radial bins and azimuthal sections and (b) tracks seed information in the *r*-*z* plane.

at the point of closest approach to the beam line d_0, are estimated using a conformal transformation [87], with the transformation centre placed in the middle space-point and applying cuts on d_0 and p_T.

Using the track seeds, a simple track finding algorithm optimised for speed is utilised to form the initial track candidates. To remove duplicate tracks that share track seeds, a dedicated algorithm is applied, which retains the tracks of higher quality selected by a fast χ^2 fitter [88]. These preliminary tracks are then passed to the Kalman filter track fitter [89]. For speed the TRT hits are not used in the FTF. Track candidates with too large d_0 values (i. e.above 10 mm for muons and 4 mm for other signatures) are rejected in order to keep the contributions from fake tracks to a manageable level.

Precision Tracking

To limit the Central Processing Unit (CPU) usage, the precision tracking stage applies a version of the offline tracking algorithms [90, 91], configured to run online in the trigger [92, 93], using the FTF tracks as inputs. Track candidates are extended into the TRT in an attempt to select TRT hits at large radii to improve the track momentum resolution. Finally, the final ID track refit is performed using a more precise χ^2 fitter algorithm [94].

The rate of processing for the precision tracking is generally significantly lower than for the fast tracking. This allows for a more detailed handling of the detector conditions and better compensation for detector effects (i. e. inactive sensors or calibration corrections). This results in the precision tracks being much closer in performance to the offline tracks than to the fast tracks. Since the precision tracking uses the tracks and clusters identified by the fast tracking, by definition, the precision tracking efficiency cannot exceed that of the fast tracking.

The overall purpose of the precision tracking is to perform a higher quality fit to improve the purity and quality of the trigger tracks identified by the first stage FTF.

Vertex Reconstruction

Two vertex reconstruction algorithms are used online: a histogramming based algorithm, and the offline vertex algorithm [95,96]. Typically, trigger signatures use the offline vertex algorithm, with the exception of the b-jet trigger which uses both algorithms to maximise the vertex finding efficiency. The simple histogramming algorithm works by histogramming the z_0 position for the point of closest approach to the beam line of each track and then calculates the vertex z position. This is done by using the mean of the bin centres weighted by the number of tracks in each bin for the group of adjacent bins within the 1 mm sliding window which contains the largest number of tracks. All tracks passing some basic quality selection are used and are weighted equally. The second algorithm is based on the offline vertex finder algorithm [96] with modifications applied for online running. Both algorithms only run on tracks that have been reconstructed in the relevant RoI of the track finding.

Multistage Tracking

As mentioned previously, the fast and precision tracking algorithms run in distinct stages, but are considered to be part of a single *tracking stage*, because there is only a single pass of the tracking over any specific RoI. Performing multiple passes of aspects of the tracking is referred as *multistage* tracking. Multistage tracking can run multiple aspects of the tracking in different steps, updating the constructed RoI at each step.

The generic structure of the multistage tracking is illustrated in Figure 3.3 where in a region of the detector the first stage fast tracking is performed over an RoI to identify the event vertex. Given the results of the first stage, the dimensions of the RoI are changed into a different RoI. The second stage executes the fast tracking again, followed by the precision tracking for the tracks found in this second fast tracking stage, run in this new RoI. This process is trigger specific and will be discussed in more detail for the relevant objects below.

Hadronic tau triggers require a larger RoI than for instance electrons, to allow for the opening angle of the tracks from the three prong decay. To limit the tracking CPU usage in this wider RoI, a multistage approach is used, as illustrated by Figure 3.4. In the first stage, the fast tracking is run to identify the position of tau event vertex and leading track along the beam line in a narrow RoI with a full width of 0.2 in both η and ϕ, but fully extended along the beam line in the range of $|z| < 225$ mm, represented by the purple area in the diagram. The RoI is then changed to a wider version with full width 0.8 in both η and ϕ, centred on the z position of the leading track identified by the first stage (as shown by the blue area on the diagram) and limited to $|\Delta z| < 10$ mm with respect to the leading track. The fast tracking is performed in this wider RoI, followed by the precision tracking for the tracks found in this second fast tracking stage. Even though the multistage tracking runs the tracking algorithms repeatedly for the two stages, the combined tracking volume of the first and second stage is still significantly smaller than for the RoI in the single-stage tracking scheme.

The multistage approach reduces the mean processing time for the hadronic tau trigger fast

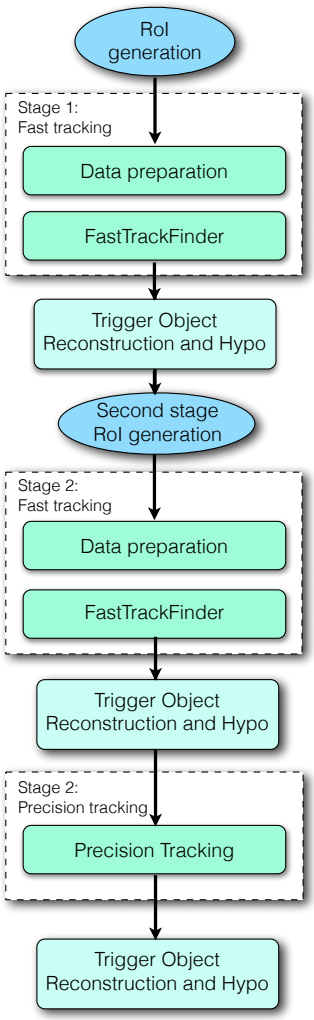

Figure 3.3: Schematics illustrating multistage tracking. And initial first stage is fast tracking performed on an RoI, followed second fast and precision tracking stages run over a second stage RoI.

tracking from 66.2 ± 0.34 ms for the single-stage, down to 23.1 ± 0.11 ms and 21.4 ± 0.09 ms for the first and second stages of the multistage approach, respectively. For the precision tracking the mean processing time was reduced from 12.0 ± 0.07 ms for the single-stage down to 4.8 ± 0.04 ms using the multistage [81].

A similar multistage tracking strategy is adopted for the b-jet trigger. In the first stage, the vertex tracking is used to identify the likely event vertex z position for use in the second stage for jets identified by the jet trigger with transverse energy $E_T > 30$ GeV. For the second stage, separate RoIs about each jet, specialised more tightly at the beam line about the z vertex position identified in the first stage, are used. The tracks are then reconstructed with the fast tracking algorithm in a narrow region with full width of 0.1 in η and ϕ around the jet axis of each jet, but with $|z| < 225$ mm along the beam line. To prevent multiple processing of overlapping regions of the detector, before running the fast tracking, the RoIs about each jet axis are aggregated into a *super RoI*, as shown by Figure 3.5. This super RoI is used to determine which detector elements should be read out by the data preparation stage.

Following this stage, the tracks identified in the super RoI are used for the primary vertex

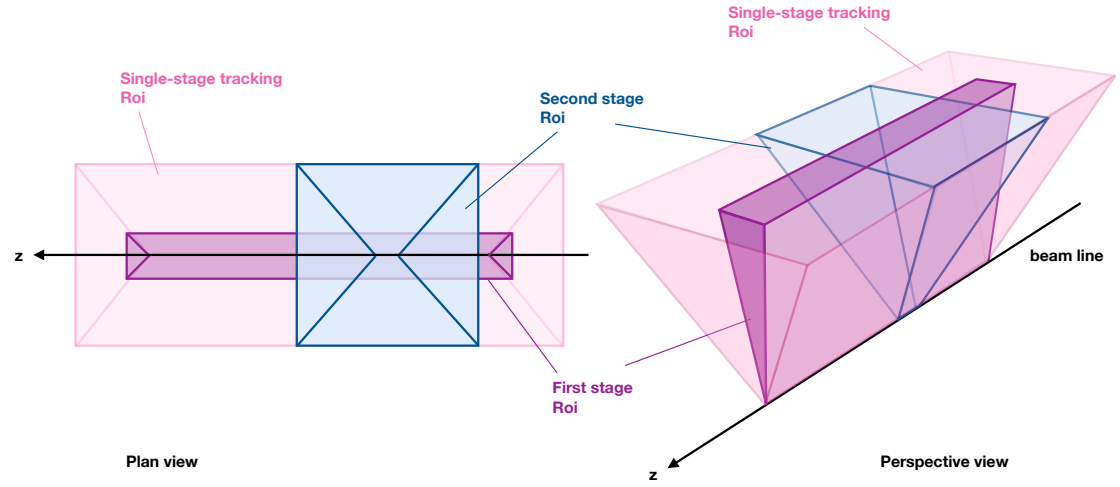

Figure 3.4: Schematics illustrating the RoIs from the single-stage and two-stage tau lepton trigger tracking shown in plane view, ($x-z$ plane) along the transverse direction, and in perspective view, with the z-axis along the beam line. The combined volume of the first and second stages of the two-stage tracking approach (blue and purple areas respectively) is noticeably smaller than the RoI in the single-stage (pink area) tracking scheme.

reconstruction [97]. This vertex is used to define wider RoIs with $|\Delta\eta|$ and $|\Delta\phi|$ less then 0.4 each, with respect to the jets axis, but with $|\Delta z| < 10$ mm relative to the primary vertex z position. These RoIs are used for the second-stage reconstruction which runs the fast tracking in a wider η and ϕ regions about the jets. The precision tracking, primary vertexing, and b-tagging algorithms are all subsequently run. As in the case of the tau multistage tracking, the use of this multistage process reduces the mean processing time from an average ~78.2 ms to ~49.3 ms [81].

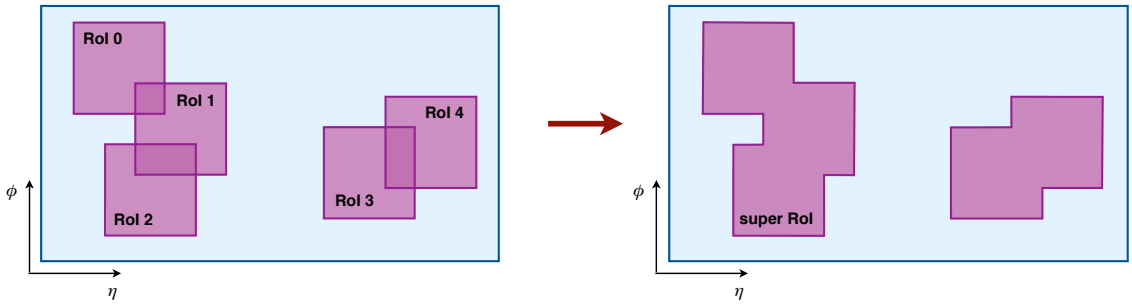

Figure 3.5: A schematic illustrating the creation of the super RoI from all the trigger jets reconstructed with an $E_T >$ 30 GeV.

3.5 ID tracking Performance

The performance of muon and electron triggers is presented for the full available luminosity for the 2016-2018 data collection period, collected at the ATLAS experiment using $\sqrt{s}$= 13 TeV pp collision events. This was possible since the processing for these triggers did not change significantly throughout data taking. For the tau and b-jet signatures, which ran multistage tracking,

significant changes were made to the reconstruction of either the first or second stages of the multistage process over the data collection period. These changes include the modification to the second stage seed finding. Therefore, only results for 2018 are presented in full detail for these signatures.

To remain as unbiased as possible, specific monitoring triggers that do not require a track to be present for the event to be accepted are used for the estimation of efficiency of the tracking. The efficiency, residuals, and resolutions presented below are calculated with respect to the tracks found by the offline reconstruction software [90]. The efficiency is therefore defined as the fraction of offline reference tracks that are matched to a trigger track

$$\mathcal{F} = \frac{\mathrm{N_{trigger}}}{\mathrm{N_{offline}}}, \tag{3.1}$$

where $\mathrm{N_{trigger}}$ is the number of tracks matched to a trigger and $\mathrm{N_{offline}}$ is the number of tracks reconstructed by the offline reconstruction software. For any given offline track, the reconstructed track that matches the closest to a loose preselection cone of size $\Delta R = \sqrt{(\Delta\eta)^2 + (\Delta\phi)^2} = 0.05$ to the offline track, is chosen as a match.

Muon trigger

Figure 3.6 shows the tracking efficiency for medium quality [98] offline muon candidates, using a range of HLT triggers [99] to cover the whole transverse momentum reconstruction spectrum down to 4 GeV, for the fast and precision tracking. Two representative thresholds are used for the offline muon selection: $p_T > 4$ GeV corresponding to the lowest trigger threshold, and $p_T > 20$ GeV for the higher trigger thresholds. The efficiency shown for both the fast and precision tracking is significantly better than 99% and flat as a function of pile-up interaction multiplicity. The small apparent loss in precision tracking for higher p_{T} tracks is primarily caused by the offline reconstruction. Poorly reconstructed candidates of lower p_{T} are occasionally misreconstructed at higher momentum by the offline reconstruction, thus creating a larger expected contribution in the reference sample in the high p_{T} region. Therefore, poorly offline reconstructed low-p_{T} tracks cause the apparent loss in efficiency at higher p_{T}. Hence, it is not an inefficiency derived from the online ID triggers.

The resolutions for the trigger tracks in η and d_0 with respect to the offline muon candidate pseudorapidity and p_{T} are shown in Figure 3.7. The fast and precision tracking d_0 resolutions are found to be better than 25 μm and 20 μm respectively, for muons candidates with offline $p_{\mathrm{T}} > 4$ GeV. The difference in resolution between the two algorithms is due to the fact that the precision tracking performs a higher quality fit using the space points identified by the fast tracking, which improves the purity and quality of the trigger tracks. The degradation of resolution observed at larger pseudorapidities is predominantly due to the increased amount of material through which tracks must travel. The position of the endcap silicon detectors (perpendicular to the beam line) partially ameliorate this, the effect of which can be seen for $|\eta|$ values larger than 1.2, which is the approximate boundary between the barrel and endcap silicon detectors.

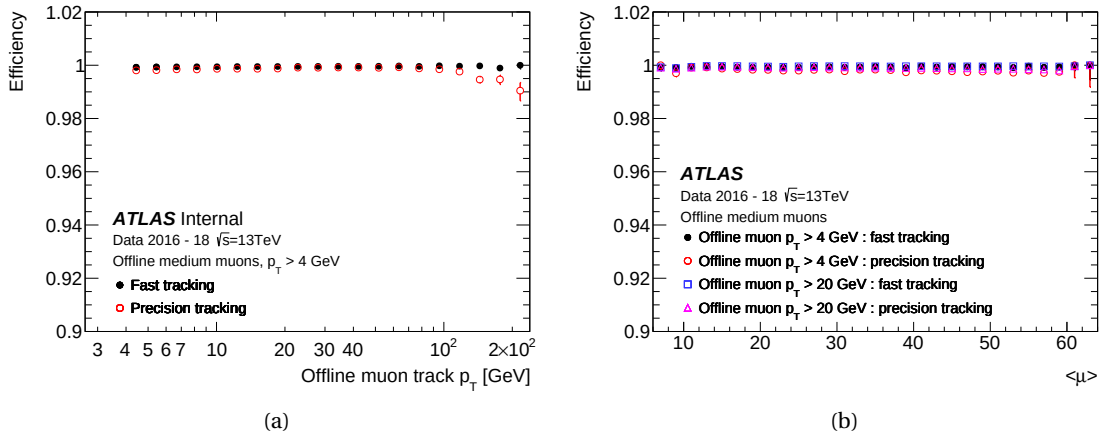

(a) (b)

Figure 3.6: ID trigger efficiency as a function of (a) the offline reconstructed muon p_{T}, (b) the mean pile-up interaction $<\mu>$ for muons selected by 4 GeV and 20 GeV muon support triggers with respect to medium offline muon candidates with $p_{\mathrm{T}} > 4$ GeV or $p_{\mathrm{T}} > 20$ GeV.

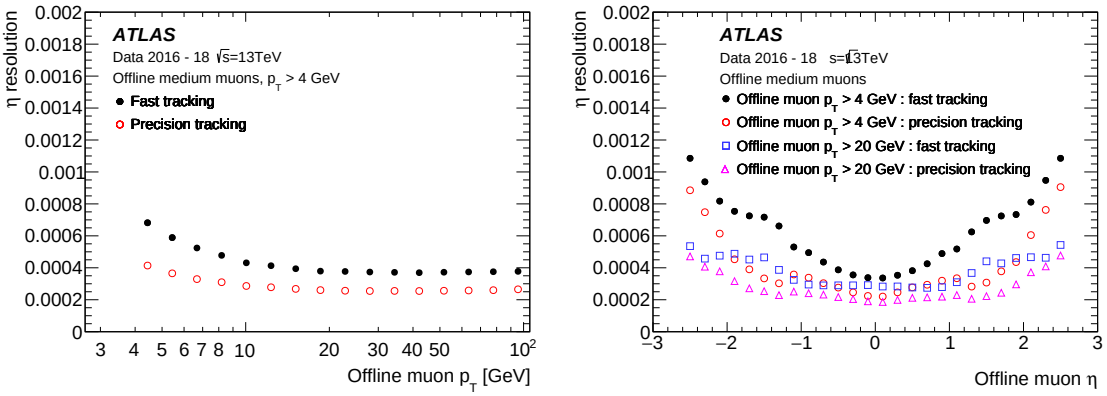

(a) (b)

Figure 3.7: ID trigger track resolution for (a) transverse impact parameter with respect to the beam line (d_0) and (b) pseudorapidity (η) as a function of offline muon η and p_{T} for muons selected by 4 GeV and 20 GeV muon support triggers with respect to medium offline muon candidates with $p_{\mathrm{T}} > 4$ GeV or $p_{\mathrm{T}} > 20$ GeV.

Electron trigger

Offline electron candidates are required to pass the tight identification criteria [100], have at least two pixel hits, an IBL hit if passing through at least one active IBL module, and at least four clusters in the SCT. These requirements have been selected to eliminate poorly reconstructed Brehmsstrahlung candidates and ensure better reconstruction in the pixel detector. A range of HLT triggers are used to cover the whole transverse momentum reconstruction spectrum down to 5 GeV (and $|\eta| < 2.5$), for the offline electron candidate tracks. For the candidates from the 5 GeV, 10 GeV and 26 GeV triggers a selection of $E_T > 5$ GeV, $E_T > 10$ GeV and $E_T > 26$ GeV was applied, respectively. However for all three triggers the same 5 GeV track p_{T} selection was requested. Offline candidates with $E_T/p_T < 0.8$ have been removed (except for the E_T/p_T plot in Figure 3.8(c)), where the E_T is measured in the calorimeter and p_T from the track. This is

done to remove offline candidates where the track p_{T} has been badly overestimated.

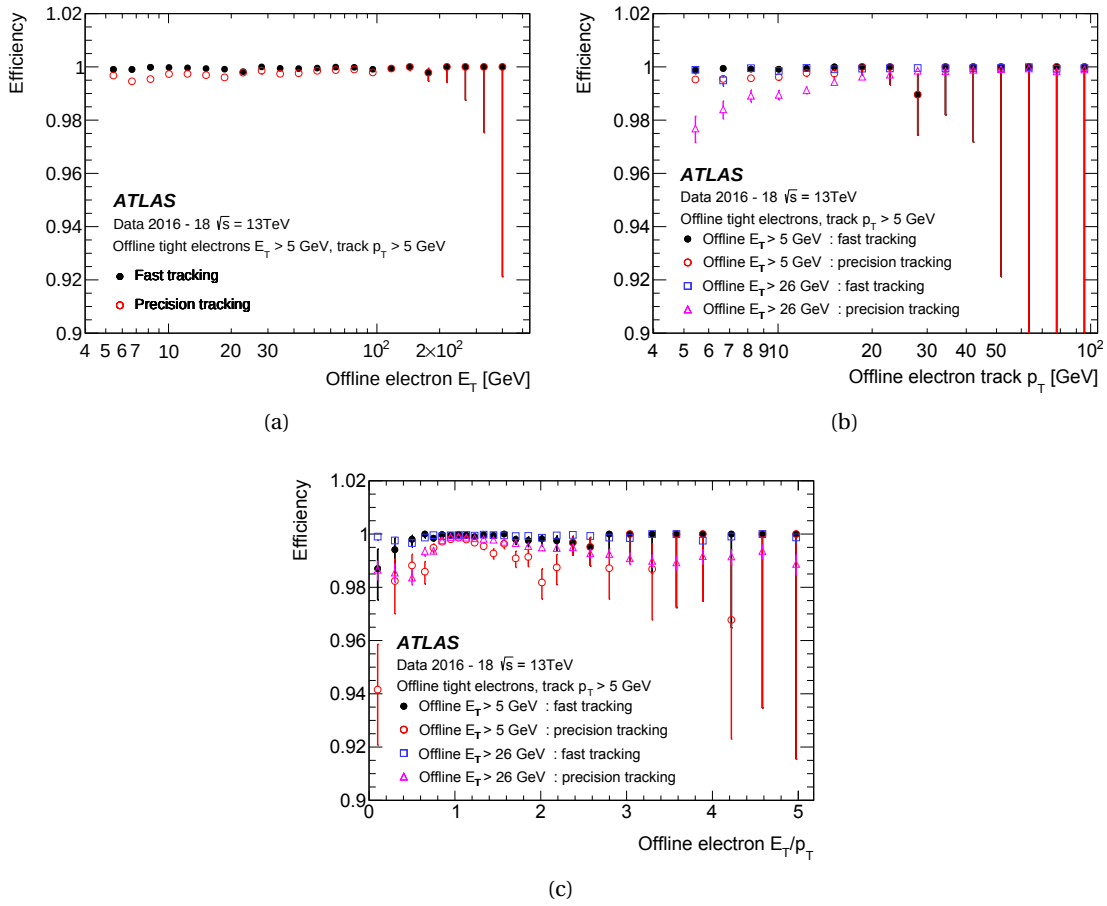

Figure 3.8: ID trigger efficiency as a function of (a) the offline reconstructed electron E_T, (b) the offline reconstructed electron track p_{T}, and (c) offline electron E_T/p_T for electrons selected by 5 GeV and 26 GeV muon support triggers with respect to medium offline muon candidates with $p_{\mathrm{T}} > 5$ GeV or $p_{\mathrm{T}} > 26$ GeV.

Figure 3.8 shows the ID track efficiency for the 5 GeV and 26 GeV electron triggers as a function of offline electron p_{T} and E_T. The efficiencies for the fast and precision track finder are consistently high and exceed 99% for all values of E_T. For tracks candidates from the 26 GeV trigger with p_{T} below 26 GeV, there is significant radiation, which may cause "kinks" in the electron trajectory and thus decrease the track reconstruction efficiency. Even for this case, the efficiency exceeds 97% in the low p_{T} range and reaches above 99% at ~20 GeV. For Figure 3.8(c) the E_T/p_T selection has been relaxed. Here the long tail of values greater than unity represent the Bremsstrahlung candidates which have radiated energy away into the calorimeter, and thus have an E_T value that is greater than the track p_{T}. The contribution of Bremsstrahlung differs when selecting different offline E_T values. For the 5 GeV trigger the Bremsstrahlung will be less than for the 26 GeV trigger. Values with E_T/p_T below unity represent electron candidates that have a track p_{T} that is larger than the calorimeter cluster E_T. This is a consequence of offline low p_{T} tracks being misreconstructed with larger values. These tracks can not have significantly more energy than the cluster, and therefore represent less reliable track p_{T} measurements. There is a clear reduction in the E_T/p_T efficiency for values below unity, but with

only 1% reduction for tracks where the track p_T is 60% higher than might be physically possible. Tracks that have not radiated have an efficiency well over 99%, while the efficiency for tracks that have radiated over half of their original energy is still greater than 98%.

Figure 3.9 shows the resolutions for the track pseudorapidity and $1/p_T$ with respect to the η and p_T of the offline track from the offline electron candidate. Unlike for the events with the 26 GeV selection, events with the 5 GeV selection have no phase space for the electron candidate near the threshold to radiate any Bremsstrahlung photons. As such, tracks with p_T below 26 GeV from the 26 GeV trigger will correspond to electrons that have undergone a significant amount of radiation. Because of this, the resolution of these tracks will be significantly worse than for the tracks with the same p_T but from the 5 GeV trigger. As expected, the resolutions also degrades at larger η for both the higher and lower threshold triggers in both the fast and precision tracking. Despite the worse resolution at low p_T for the tracks from the 26 GeV trigger, when integrated over p_T, the resolution is significantly better than for the lower p_T threshold since only a relatively small fraction of events from the 26 GeV trigger will have low p_T tracks.

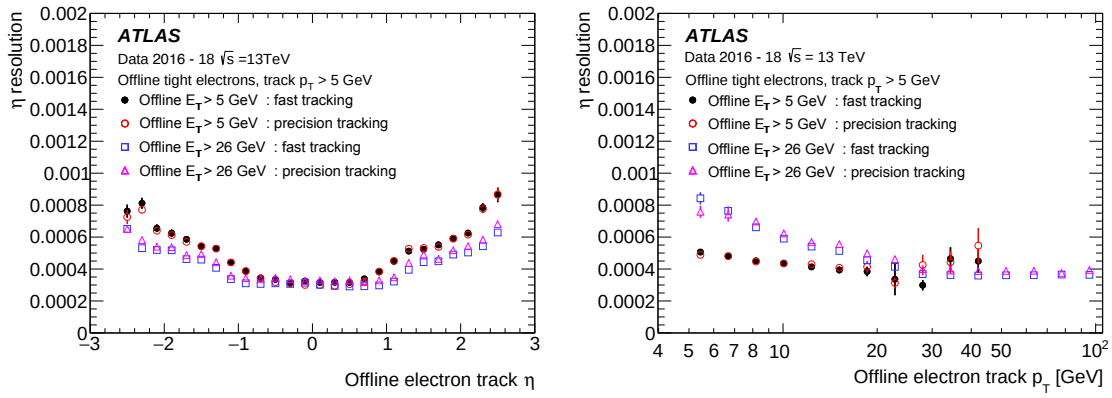

(a) (b)

Figure 3.9: ID trigger track resolution for (a) track pseudorapidity (η) and (b) track $1/p_T$ as a function of offline electron η and p_T for electrons selected by 5 GeV and 26 GeV electron support triggers with respect to tight offline electron candidates with $p_T > 5$ GeV or $p_T > 26$ GeV for both the fast and precision tracking algorithms.

Tau trigger

Figure 3.10 shows the efficiency for the tau tracking with respect to the offline tracking for offline tracks with $p_T > 1$ GeV, originating from decays of offline τ-lepton candidates with $p_T >$ 25 GeV. For the ID trigger tracking a multistage process was used, as described in Section 3.4, where the first stage runs the FTF in a narrow RoI in $\eta - \phi$. In this narrow ϕ region low-p_T tracks (around or below 5 GeV) may bend significantly in the solenoid magnetic field. If these tracks are on or near the edge of the RoI, they may bend outside the region and thus are not reconstructed.

Figure 3.10(b) shows the efficiency for the first stage fast tracking, and for the second stage fast and precision tracking from the data collected in 2018. Due to the RoI containment issue

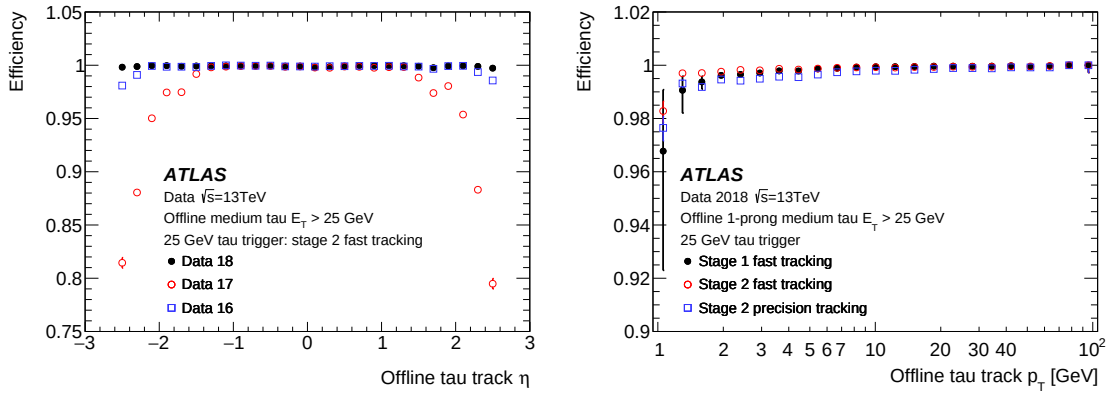

(a) (b)

Figure 3.10: ID trigger efficiency as a function of (a) the offline reconstructed tau η comparing performance between 2016, 2017, and 2018, and (b) the offline reconstructed tau track p_{T} for the first stage fast tracking and second stage fast and precision tracking. The efficiency is evaluated for the 25 GeV tau performance trigger, which does not use any ID tracking information for the selection. Only tracks from tau decays with p_{T}> 1 GeV are used. Bayesian uncertainties are shown.

for low p_{T} tracks just described above, there are fewer samples of tracks near the threshold. This results in lower efficiencies and larger uncertainties for both the fast and precision tracking, but more significantly for the first stage fast tracking due to the narrower RoI used in the initial stage. Efficiencies are nonetheless very high, well above 96.5% everywhere for all fast and precision tracking in first and second stage of multistage tracking and above 99% for second stage precision tracking for tracks with $p_{\mathrm{T}} > 1.2$ GeV. The effect of the changes to the trigger between 2016, 2017 and 2018 can be seen for the second stage fast tracking in Figure 3.10(a). In 2016, a small inefficiency was observed at large pseudorapidities because of the tightening of the second stage RoI about the $z-$position of the leading track. Approximations used in the layer positions for the seed finding were particularly affected by the worse resolution for seeds at large η, causing a significant fraction of the seeds to be rejected. The increased rate due from the higher pile-up occupancy in 2017 required some additional changes to the seed finding used for the FTF tracking, which resulted in the further inefficiencies observed at larger η, leaving the efficiency at central η unaffected. Modifications to take into account the worse seed resolution at large pseudorapidities were under development, but were not ready for the start of data taking in 2017. For 2018, the seed finding was reimplemented which restored the efficiency at large η.

Figure 3.11 shows the resolutions for d_0 with respect to offline track η and p_{T}. As expected, the precision tracking resolution is found to be generally better than the fast tracking resolution. The fast tracking resolution is found to be very similar between the first and second stage for tracks with offline track $p_{\mathrm{T}} > 5$ GeV but different for $p_{\mathrm{T}} < 5$ GeV. This is again due to the RoI containment requirement discussed above. When integrating over p_{T}, the resolution is between 15-20 μm for all pseudorapidities.

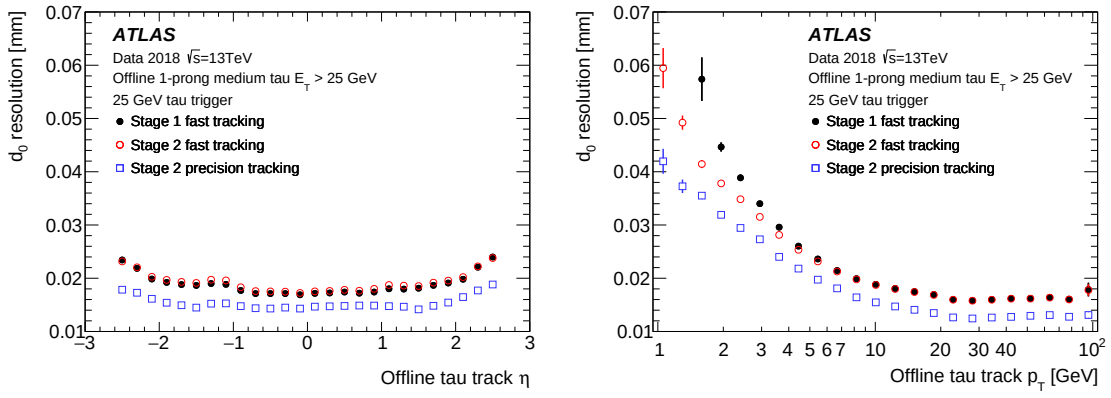

(a) (b)

Figure 3.11: ID trigger track resolution for transverse impact parameter (d_0) as a function of offline tau track (a) pseudorapidity η and (b) transverse momentum (p_T), respectively.

b-jet trigger

The efficiency for the tracking as a function of pile-up interactions $\langle\mu\rangle$ from both stages of the *b*-jet multistage tracking process is shown in Figure 3.12(a), while 3.12(b) compares the precision and fast tracking efficiencies as a function of offline track p_T for the jet tracking from the 55 GeV and 150 GeV threshold triggers. For the vertex finding shown in Figure 3.12(a), only tracks with $p_T > 5$ GeV are reconstructed and thus only offline tracks with p_T above 5 GeV have been selected. For offline tracks above ~1.2 GeV the second stage fast tracking efficiency is better than 99.5% for both 55 GeV and 150 GeV threshold triggers. For tracks near 1 GeV the fast tracking efficiency is better than 98% but the precision tracking efficiency is approximately 85%[1]. This is a consequence of placing a 1 GeV cut on tracks from the precision tracking in the *b*-jet signature for processing latency reasons. The small drop in efficiency with increasing $\langle\mu\rangle$, which is more significant for the precision tracking, is driven largely by the lower efficiencies at low p_T.

Figure 3.13 shows the ID trigger track d_0 resolutions as a function of η and offline track p_T from the fast and precision tracking from the second stage of the *b*-jet trigger for the 55 GeV and 150 GeV signatures. As expected, the precision tracking provides significantly better resolutions for the whole η range and for d_0 values at lower track p_T. However, there is also a slight degradation of the d_0 resolution with increasing p_T for the high E_T jet trigger. This is correlated with a slight loss of pixel hits and thus corresponds to a loss in efficiency for the precision tracking at higher p_T, as found in Figure 3.12. When integrating over p_T, the resolution for the *b*-jet ID trigger second stage precision tracking is between 20-30 (20-35) μm for the 50 (150) GeV trigger.

[1] This is not shown on figure as it would extend the axis range making more relevant features of the distributions more difficult to discern.

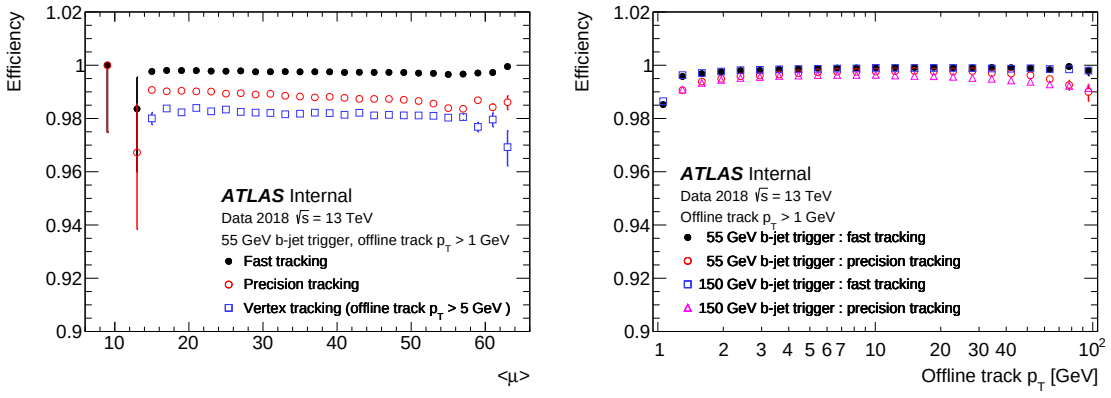

(a) (b)

Figure 3.12: ID trigger efficiency as a function of (a) the mean pileup interaction multiplicity $\langle\mu\rangle$, comparing the RoI based jet tracking with vertex tracking and (b) the offline reconstructed jet track p_{T} for the second stage fast and precision tracking, evaluated for the 55 GeV and 150 GeV b-jet triggers. Bayesian uncertainties are shown.

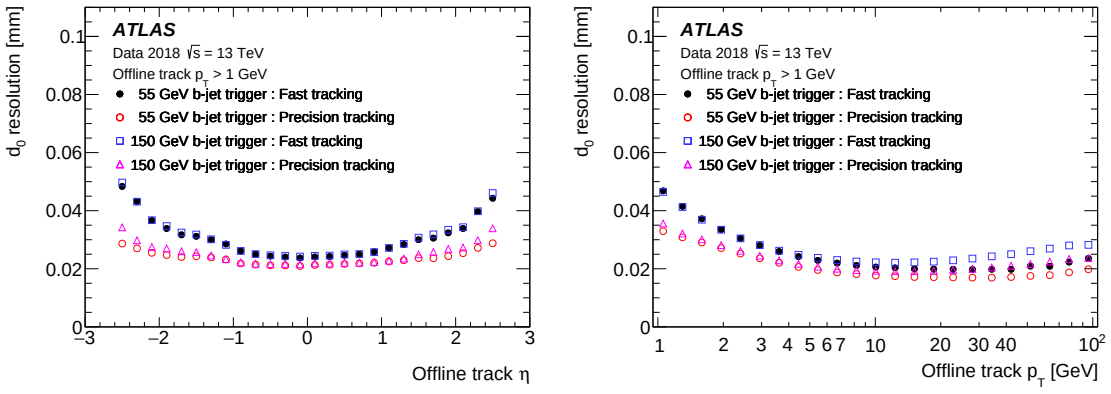

(a) (b)

Figure 3.13: ID b-jet trigger track resolution for transverse impact parameter (d_0) as a function of offline b-jet track (a) pseudorapidity and (b) transverse momentum.

Vertex Finding

For the measurement of performance, the online vertex efficiency is calculated for the single offline vertex candidate from the bunch crossings with the highest sum of the squared transverse momenta. Figure 3.14 shows the efficiency for identifying the vertex candidates in the trigger for the 110 GeV and 420 GeV triggers, as a function of the offline track multiplicity in the super RoI and the mean pile-up interaction multiplicity of the event.

A steep rising edge is found for the vertex finding algorithms with increasing offline track multiplicity. For the histogram based algorithm full efficiency is reached for events with more than four vertex tracks within the RoI, while for the offline based algorithm full efficiency is reached only for events with more than eight vertex tracks. This is due to the tighter track quality required by the offline based algorithm. Due to this higher track quality requirement, some vertices with only a few tracks in the super RoI may not have any tracks remaining with

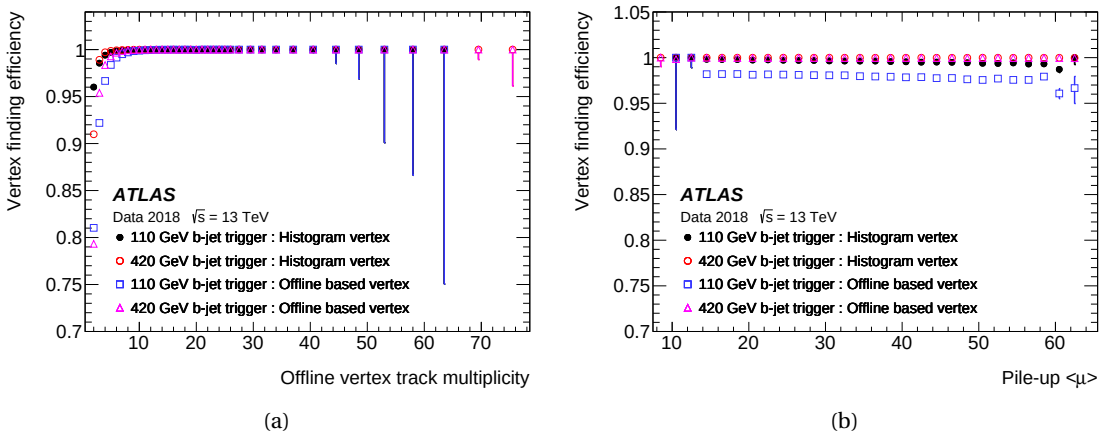

(a) (b)

Figure 3.14: The vertex algorithm ID trigger efficiencies for 110 GeV and 420 GeV E_T threshold b-jet triggers. The efficiencies versus (a) the offline track multiplicity for tracks in the super RoI, and (b) the mean pile-up interaction multiplicity are shown. Bayesian uncertainties are shown.

which to form a vertex once the tracks with lower quality are removed. Higher E_T jet triggers will have significantly higher track multiplicities and larger average track p_{T} making the probability of the track multiplicity for a pile-up vertex matching significantly lower. Both algorithms show a reduction in the efficiency as $\langle\mu\rangle$ increases. This is due to the increased possibility for the offline selection to misidentify the jet vertex candidate within the super RoI. Therefore, as the pile-up interaction multiplicity increases within an event, so do the chances of there being additional tracks from additional vertices within the super RoI. The lower overall efficiency of the offline based algorithm, particularly for the lower E_T threshold trigger, is due to the lower overall track multiplicity in the events passing the trigger. The trigger is therefore still on the rising edge of the efficiency distribution for many events, causing a lower overall efficiency as a function of $\langle\mu\rangle$. For the higher E_T threshold triggers, the multiplicity is higher and thus the algorithm is further along the efficiency curve for most events, resulting in a higher overall efficiency.

The resolution of the vertex z for both online algorithms as a function of the offline track multiplicity and the offline z vertex positions is shown in Figure 3.15. The resolution on the vertex z position for both online algorithms improves with increasing track multiplicity, with the offline based algorithm showing a significantly better resolution. The resolution of both algorithms improves logarithmically with increasing track multiplicity from 100 μm and 70 μm at low track multiplicity, to 30 μm and 20 μm at 50 tracks for the histogram and offline based algorithms, respectively. The higher resolution observed for the high E_T threshold trigger is due to the larger average p_{T} of tracks from the higher E_T jet triggers, such that the track z positions themselves have an intrinsically better z resolution. The resolution as a function of vertex z position is largely constant with a small degradation at around large z values, and a slight trend towards better resolutions for more negative z, particularly for the lower E_T threshold triggers. This is especially evident for the histogram based algorithm and is a consequence of the implementation of the algorithm which selects bins starting from the most negative z bin and keep

it as the original if it finds another bin with the same occupancy.

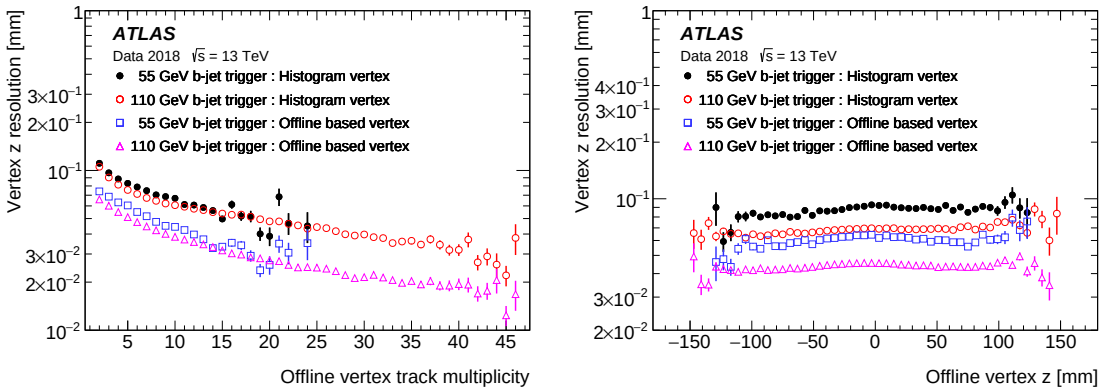

(a) (b)

Figure 3.15: ID vertex reconstruction vertex z position track resolution for 110 GeV and 420 GeV b-jet triggers as a function of (a) the offline track multiplicity and (b) the offline z vertex position.

3.6 Summary

In this chapter the ATLAS trigger, with particular interest in the ID trigger and tracking algorithms and corresponding performance, is presented. The performance in terms of efficiency with respect to the offline algorithms, and resolutions of the ID tracking algorithms for the main physics signatures needed by the ATLAS physics program: muon, electron, tau, and b-jet, are shown. The performance has been excellent even at the very high interaction multiplicities observed at the end of data taking in 2018. The collected results have been reported in a public paper [81] currently undergoing the submission process for publication to the European Physics Journal C. The summarised results reported in the paper have been presented by the author at many conferences, including at: the Large Hadron Collider Physics conference in 2018 [2], The Institute of Electrical and Electronics Engineers Realtime Conference in 2018 [3], and the International Conference on High Energy Physics in 2020 [4]. The study of the performance of these triggers has been part of the *qualification task*[5] of the author. The excellent performance of the ID trigger algorithms demonstrates how the ID trigger continues to lie at the heart of the trigger performance and plays an essential rôle in the ATLAS physics programme.

[2] Link to LHCP 2018 conference material: https://indi.to/tktyf
[3] Link to IEEE RealTime 2018 conference material: https://indi.to/RHgmw
[4] Link to ICHEP 2020 conference material: https://indi.to/fSYKv
[5] To become an ATLAS author active ATLAS researchers must spend 50% of their time on a technical task (for the first year) and 30% the following year.

SEARCH FOR DIRECT STAU PRODUCTION

4

Go closer hold the land feel partly no more than grains of sand. We stand to lose all time a thousand answers by in our hand. Next to your deeper fears we stand. Surrounded by million years.

Yes

This chapter presents the analysis strategy, optimization and results of the search for direct production of the supersymmetric partner of the τ-lepton in all-hadronic final states, using data collected during the Run-2 data-taking period, totalling in 139 fb^{-1} of pp collisions at a centre-of-mass energy $\sqrt{s}$= 13 TeV. In Section 4.1 an introduction to the analysis, including the motivation of the search, the signal process considered and the adopted analysis strategy is presented. Sections 4.2 and 4.3 describe the SUSY and SM Monte Carlo (MC) generated samples used for this analysis. The reconstruction of the particle objects used, in both data and MC, is described in Section 4.4. The study of the combined tau triggers Scale Factors (SFs) and efficiencies used in the selection of relevant events in the analysis Signal Regions (SRs) was performed by the author and is presented in Section 4.5. Section 4.6 describes the SR optimisation performed by the author to isolate the signal events from the SM background, and the background estimation methods performed for the most significant background processes. A major contribution of the author's work has been in the estimation of the systematic uncertainties that affect this analysis, described in Section 4.7. Finally, a description of the statistical analysis used, the corresponding results, and interpretation are given in Sections 4.8, 4.9, and 4.10, respectively.

4.1 Introduction and Strategy

As already discussed in Chapter 1, the SUSY extension to the SM is an appealing hypothesis proposed to solve the fine-tuning problem. If R-parity [101] is conserved, SUSY particles are produced in pairs at the LHC, with the LSP being stable and weakly interacting and thus a

strong candidate for dark-matter. In the MSSM the coloured sparticles (squarks and gluinos) have a high mass, and the weakinos instead have a low mass. In this case, the first signs of SUSY at the LHC would be spotted in events with high lepton multiplicity and low jet activity, such as the decay of the electro-weakinos (charginos $\tilde{\chi}^{\pm}$ and neutralinos $\tilde{\chi}^{0}$) and the sleptons ($\tilde{\ell}$ and $\tilde{\nu}$).

For this analysis only the direct production of $\tilde{\tau}$ from pp interactions at the LHC is considered, as shown by Figure 4.1. The considered final states signature is composed of two hadronically decaying τ-leptons with low jet activity and large missing transverse energy ($E_{\mathrm{T}}^{\mathrm{miss}}$), originating from the neutralinos and neutrinos. The signal considered in this work is generated using a simplified model, where the scalar superpartner of the left-handed τ-lepton ($\tilde{\tau}_{\mathrm{L}}$), right-handed τ-lepton ($\tilde{\tau}_{\mathrm{R}}$), and the lightest neutralino ($\tilde{\chi}_1^0$) are the only SUSY particles considered. In this model, the $\tilde{\chi}_1^0$ is considered to be the LSP while the $\tilde{\tau}_{\mathrm{L}}$ and $\tilde{\tau}_{\mathrm{R}}$ are assumed to be mass-degenerate and have 100% branching fraction into $\tilde{\chi}_1^0$ and τ-lepton.

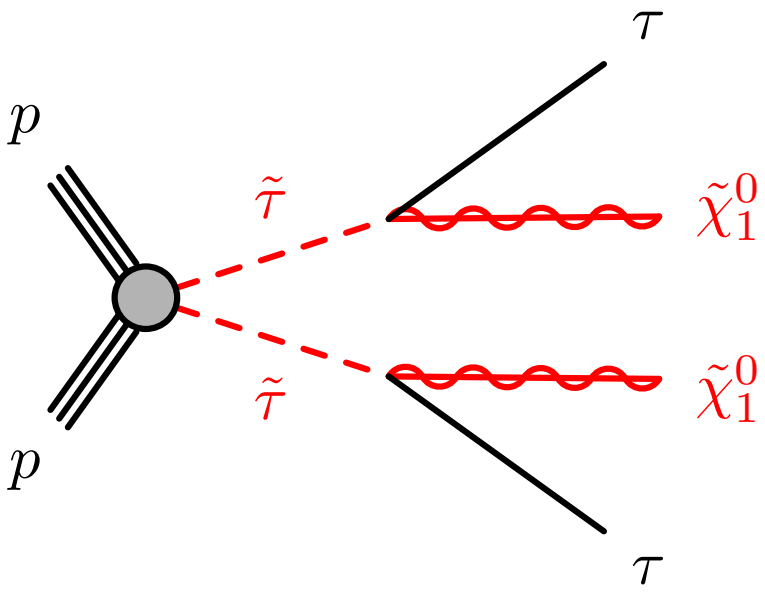

Figure 4.1: Diagram of the decay topology of the signal model considered in this work. A pair production of charged staus and subsequent decay to a di-tau final state.

Final states with hadronic τ-leptons can be experimentally challenging due to the difficulty in the reconstruction and identification of these particles in the ATLAS detector. The methods and challenges of τ-lepton reconstruction and identification will be discussed in more detail later in the chapter. Nonetheless, they are of particular interest in SUSY searches since light sleptons could play an important rôle in the co-annihilation of neutralinos in the early universe, and models with light scalar taus are consistent with dark-matter searches [102].

4.2 SUSY signal

The masses of all charginos and neutralinos, apart from the $\tilde{\chi}_1^0$, are set to 2.5 TeV so that they are decoupled from the phenomenology under study. This leaves only a single kinematically

allowed decay: $\tilde{\tau}^{\pm} \rightarrow \tilde{\chi}_1^0 \tau^{\pm}$. The masses of the other sleptons are also decoupled and not included in the production. The masses of the left-hand and right-hand $\tilde{\tau}$ are degenerate, and vary between 100-400 GeV. The mass of the bino-like $\tilde{\chi}_1^0$ is varied between the range of 0-200 GeV. Most results that will be shown will use reference points with $\tilde{\tau}$ masses of 120 GeV, 280 GeV, and a $\tilde{\chi}_1^0$ mass of 1 GeV to illustrate typical features of the SUSY models that this analysis is sensitive to.

The signal samples for this work have been generated using MADGRAPH5_AMC@NLO 2.6.2 [103] interfaced with PYTHIA 8.186 with the A14 tune [104] for the PS modelling, hadronisation, and underlying event. The NNPDF2.3LO Parton Distribution Function (PDF) [105] has been used for the Matrix Element (ME) calculation, and includes the emission of up to two additional partons. The nominal cross section and its uncertainty has been taken from an envelope of cross section predictions using different PDF sets and factorization and renormalization scales, as described in References [106–110]. The theoretical cross section used at Next-to-Leading-Logarithm Accuracy (NLO + NLL) was 140 (50) fb with $\tilde{\tau}_L\tilde{\tau}_L(\tilde{\tau}_R\tilde{\tau}_R)$ of 120 GeV, and 5.8 (2.2) fb with $\tilde{\tau}_L\tilde{\tau}_L(\tilde{\tau}_R\tilde{\tau}_R)$ of 280 GeV [2].

4.3 SM samples

In order for the analysis to robustly target the desired signal, the accurate modelling of background processes is fundamental. For this type of analysis there is a wide variety of SM processes whose cross sections are significantly larger than of the SUSY signal process of interest. These SM processes constitute the background of the analysis. The definition of a SR must take into account the kinematic properties and multiplicities of the final state particles of the target signal and background processes to achieve the highest possible discrimination between the two. Therefore, the defined signal region will be most sensitive to the target signal events. In order to construct a high sensitivity SR, background processes need to be accurately simulated in MC events. The backgrounds that significantly contribute to the search of direct $\tilde{\tau}$ production in a di-τ+$E_{\mathrm{T}}^{\mathrm{miss}}$ final state scenario, with their relative MC samples, are discussed below [111].

W boson production in association with jets: the production of W bosons with jets is a relevant background for our search, due to the $W \rightarrow \ell\nu$ ($\ell = e, \mu, \tau$) decay, with a Branching Ratio (BR) of ~ 32%. Therefore, production of W + jets events where at least one jet is misidentified as a τ-lepton is an important background to this search.

Z boson production in association with jets: the production of Z bosons in association with jets is one of the main SM backgrounds of our analysis. The Z boson will decay via $Z \rightarrow \ell\ell$ ($\ell = e, \mu, \tau$), with a BR of ~ 10%, contributing significantly to the SM background producing final states with two real taus.

Multi boson production: the production of di- or multi- bosons (VV, VVV where $V = W, Z$), are also a significant source of background events containing real tau leptons. The real

taus in the multi boson production come from the WW and ZZ processes that decay into a $\tau\tau\nu\nu$ final state with BR of ~ 10% and ~ 2%, respectively.

Top single and pair production: single top, $t\bar{t}$ production in association with jets, or top with an additional W or Z boson are collectively referred to as "top" background. The different decays from the single top process are generally separated into the different channel-types (s-channel, t-channel). All these background processes contribute towards the amount of irreducible background present in this analysis. The dominant top-quark decay is $t \to W$ with BR of ~ 99%. This can in turn yield 0-lepton, 1-lepton and 2-lepton final states with 45.7%, 43.8% and 10.5% BR, respectively. The irreducible background contribution will therefore come from the 2-lepton final state, and from the other two channels when there is at least one mis-identified jet in the event.

Higgs boson production: there is a small contribution of from higgs boson events produced by gluon-gluon fusion and vector boson fusion. These events only contribute in small part to the total irreducible background, but have still been included in this analysis.

Multi-jet: multi jet production is the process with the highest cross section among the ones mentioned thus far. Despite the low probability of mis-identifying two jets as real taus, because of the large cross section of this process the background will generate a non-negligible contribution. There is also a significant contribution arising from heavy-flavour multi-jet events containing a real τ-lepton from the heavy-flavour quark decay as part of the total multi-jet estimate.

4.4 Object Definition

Reconstructed objects are required to pass a "loose" selection to be categorised as *baseline* objects. This indicates that these objects have been reconstructed with enough precision and can be used for further analysis. These baseline objects are used as inputs for the Overlap Removal (OR) procedure described in Chapter 5. The resulting objects are referred to as *signal* objects after they pass some additional selection criteria. The baseline and signal objects are defined as:

Taus only the visible part of the τ decay is reconstructed for the candidates that are associated with a Primary Vertex (PV). Taus not associated to a PV are not considered. An energy calibration derived independently of the jet energy scale is applied to the reconstructed τ objects. τ candidates with $p_{\mathrm{T}} < 20$ GeV or $|\eta| > 2.5$, or in the region of $1.37 < |\eta| < 1.52$ are rejected. A total track charge of $\pm$ 1 is required with the presence of 1 or 3 associated tracks. A BDT discriminant is used to reject jets that do not originate from a hadronically decaying tau leptons with a *Medium* working point for the signal taus and a minimum value of 0.01 for the baseline tau (see paragraphs below for more detailed description of reconstruction and identification algorithms with corresponding working points).

Electrons Electrons must pass the Tight (loose) likelihood identification criterion to be signal (baseline) candidates. Signal electrons are required to satisfy an isolation criteria to reduce the number of jets mis-identified as charged leptons.[1] For electrons with p_{T}> 200 GeV this requirement does not apply and instead an isolation requirement using a fixed size cone ($\Delta R < 0.2$) is used. Electrons must have $p_{\mathrm{T}} > 17$ GeV and $|\eta| < 2.47$.

Muons Muon candidates must pass the *Medium* selection criteria, defined in Reference [112], and must satisfy p_{T}> 14 GeV and $|\eta| < 2.7$. A loose fix cut working point is applied to select the isolated signal muons.

Jets and b-tagging Reconstructed jets are calibrated using a Jet Energy Scale (JES) derived from simulation and in situ corrections based on 13 TeV data [113–115]. Jets are required to have $p_{\mathrm{T}} > 20$ GeV and $|\eta| < 2.8$. Events with at least one jet arising from non-collision sources or detector noise are removed [116], resulting in negligible loss of efficiency. An additional *Medium* working point requirement on the Jet Vertex Tagger (JVT) is made for jets with $p_{\mathrm{T}} < 20$ GeV in central ($|\eta| < 2.5$) region of the detector to avoid selecting jets from secondary pp interactions. In ATLAS, reconstructed jets are identified as originating from the hadronisation of a b-quark (b-tagged) via the MV2C10 algorithm [117].

Missing transverse momentum The transverse missing momentum observable ($E_{\mathrm{T}}^{\mathrm{miss}}$) is defined as the size of the vectorial sum p_{T} of all selected and calibrated physics objects in the event, with an extra term added to account for soft energy in the event that is not associated to any of the selected objects. This soft term is calculated from ID tracks associated to the primary vertex to make it more resilient to pileup contamination [118, 119].

The reconstruction algorithms in ATLAS run independently from each other. Thus, it may happen that the detector signatures stemming from one physical object are reconstructed as two or more different objects. To resolve these ambiguities, a procedure is defined which looks for reconstructed objects that lie within a certain cone to decide which particle should be kept or removed. This procedure is commonly referred to as the Overlap Removal Procedure. The fixed set of requirements that the different objects need to pass for the OR procedure used for this analysis are shown in Table 4.1. A more detailed description of the general implementation of the OR procedure is provided in Chapter 5.

4.5 Trigger Strategy

In this section, the trigger strategy used for the selection of relevant events for the search of the direct $\tilde{\tau}$ production is presented.

As discussed in Chapters 2 and 3, physics events are only recorded if they pass a certain trigger with some *online* (i. e. during data taking) object kinematic threshold. In order to ensure

[1] The scalar sum of p_{T} of tracks inside the variable-size cone around the lepton must be less that 15% of the lepton p_{T}. The track isolation cone size is given by $\Delta R = 10\,\mathrm{GeV}/\,p_T$ and must be less than 0.2.

Table 4.1: Consecutive steps of the overlap removal procedure used in the direct stau analysis. All objects used in the OR are baseline objects.

Step	Object removed	Object compared against	Condition
1.	electron	electron	shared track
2.	tau	electron	$\Delta R < 0.2$
3.	tau	muon	$\Delta R < 0.2$
4.	electron	muon	shared ID track
5.	jet	electron	$\Delta R < 0.2$
6.	electron	jet	$\Delta R < 0.4$
7.	jet	muon	N. tracks < 3 and $\Delta R < 0.2$
8.	muon	jet	$\Delta R < 0.4$
9.	jet	tau	$\Delta R < 0.2$

high trigger efficiencies for the full range of the possible SUSY kinematic regimes, the SR is split into two separate and orthogonal regions based on $E_{\mathrm{T}}^{\mathrm{miss}}$. Events with $E_{\mathrm{T}}^{\mathrm{miss}}$> 150 GeV are triggers using the so-called *di-tau*+$E_{\mathrm{T}}^{\mathrm{miss}}$ trigger and target the high $\tilde{\tau}$ mass region signature, as higher values of $E_{\mathrm{T}}^{\mathrm{miss}}$ would be expected for the higher $\tilde{\tau}$ masses. For low $\tilde{\tau}$ mass events, the expectation is that there would be lower $E_{\mathrm{T}}^{\mathrm{miss}}$ values and thus events with $E_{\mathrm{T}}^{\mathrm{miss}}$< 150 GeV are selected using the *asymmetric di-tau* trigger. The use of these two triggers, along with the opposite $E_{\mathrm{T}}^{\mathrm{miss}}$ requirement, ensures orthogonality of the selected events, thus removing the possibility of double counting events by the two triggers. Because of changes to triggers and trigger menus throughout the Run-2 data taking period (2016-2018), the asymmetric di-tau and di-tau+$E_{\mathrm{T}}^{\mathrm{miss}}$ triggers were changed in 2018. The most significant change occurred between 2017 and 2018 where the di-tau triggers were changed to use full tracking information instead of the fast tracking, as denoted by the *tracktwoEF* nomenclature[2]. The lowest unprescaled triggers used for event selection in this analysis throughout the Run-2 data taking period can be found in Table 4.2.

Table 4.2: Lowest unprescaled triggers for Run-2 with two hadronic taus (asymmetric di-tau) or two hadronic taus with missing transverse momentum ($E_{\mathrm{T}}^{\mathrm{miss}}$).

Year	Trigger
	di-tau + E_T^{miss}
2015-2017	HLT_tau25_medium1_tracktwo_tau25_medium1_tracktwo_xe50
2018	HLT_tau60_medium1_tracktwoEF_tau25_medium1_tracktwoEF_xe50
	asymmetric di-tau
2015-2017	HLT_tau80_medium1_tracktwo_L1TAU60_tau50_medium1_tracktwo_L1TAU12
2018	HLT_tau80_medium1_tracktwoEF_L1TAU60_tau60_medium1_tracktwo_L1TAU40

To properly model the efficiency of these combined object triggers on MC simulations the Scale Factors of these combined trigger objects are derived. SF are scaling factors derived from data and applied to the MC, to match the performance observed in the data.

[2] Refer to Section 3.1 regarding the rules and structure used for trigger nomenclature.

Efficiency

The trigger performance is parametrised by the efficiency of the trigger to select events of interest. For combined triggers such as the ones used in this analysis, the efficiency is defined as:

$$\epsilon = \frac{N_S^{\text{trig.}}}{N_S}, \tag{4.1}$$

where N_S is the number of events that pass some set of selection cuts for an arbitrary region, S, and $N_S^{\text{trig.}}$ is the number of events that pass the same region selection and the trigger. To derive the efficiency of combined triggers the individual trigger "legs" that constitute the full trigger are considered to be independent. The efficiency of the single legs of the combined triggers is, thus, derived using MC simulations in a region defined to be abundant with the triggered object. Single τ-lepton triggers, representing the individual trigger legs that constitute the asymmetric di-tau and di-tau+E_T^{miss} triggers, with online thresholds of 25 GeV, 35 GeV, 50 GeV, 60 GeV, and 80 GeV are used. These triggers are evaluated in a region defined to be abundant with W boson production in association with jets with τ_{had} final states, with corresponding selection cuts:

- At least one medium τ-lepton with $p_T > 20$ GeV
- At least one jet with $p_T > 100$ GeV
- Pass E_T^{miss} trigger with $E_T^{\text{miss}} > 200$ GeV

Using the above selection, the transverse momentum distributions for the triggered and non-triggered τ-lepton are derived, as shown in Figure 4.2 (so called *turn on* curves). In these plots, the p_T distributions for the leading tau object in each SM samples are shown when using the different triggers. Using equation 4.1, the efficiency with respect to the non-triggered distribution is also shown in the bottom plot of the figures. Vertical dashed lines are used to show offline thresholds that can be applied to ensure that the triggering is performed on the plateau of the efficiency distribution and thus, where the trigger is at highest performance. Higher online threshold triggers have lower offline thresholds to increase the acceptance in the higher p_T regions to improve statistics. These offline thresholds found for the single leg tau triggers have been validated in additional regions described in Appendix A.

The turn on curves for the single leg E_T^{miss} trigger, with online energy threshold of 50 GeV, have been derived in a similar region as the one defined above but without any requirements on the E_T^{miss}. Figure 4.3 shows the resulting turn on curve for the single leg E_T^{miss} trigger. The associated offline threshold is found to be around 200 GeV. However, these distributions can only be used as reference to evaluate the effect of the E_T^{miss} trigger on the E_T^{miss} kinematics distribution and cannot be used to determine the efficiency of the E_T^{miss} trigger leg used in the di-tau+E_T^{miss} trigger as it should be derived in a region that is abundant with missing transverse energy originating from the τ-lepton decay process. The high turn on threshold value seen in

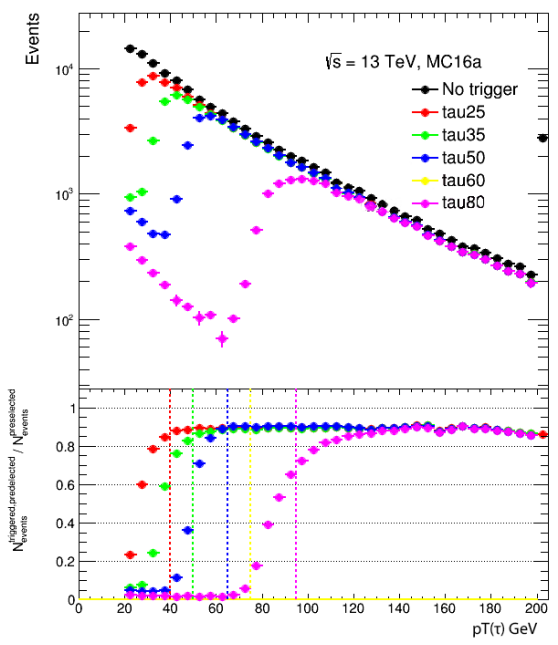

(a)

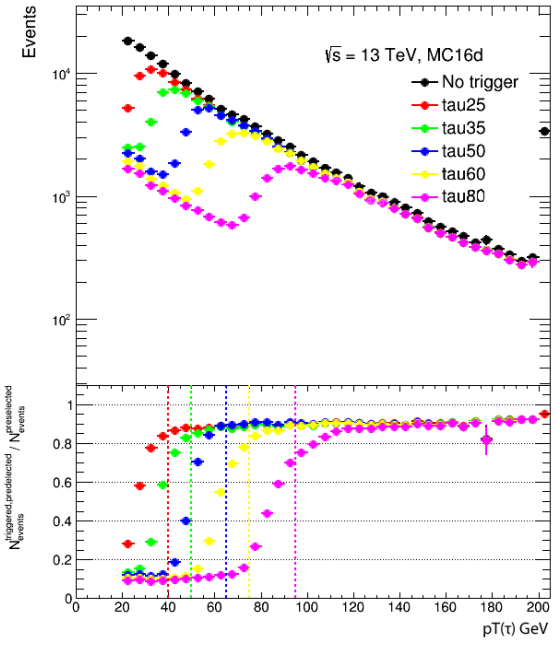

(b)

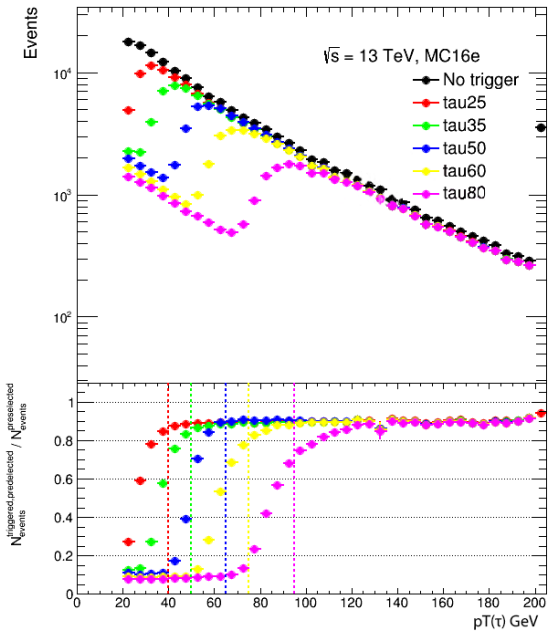

(c)

Figure 4.2: Turn-on curves of single tau triggers on SM background samples, simulated in MC for (a) 2015-2016, (b) 2017, and (c) 2018 data. Dashed line represents estimated turn-on thresholds.

these distributions is a consequence of triggering on $E_{\mathrm{T}}^{\mathrm{miss}}$ originating from decay processes with one fake-τ object and $E_{\mathrm{T}}^{\mathrm{miss}}$ originating from the decay process itself (e. g. $W \to \mu\nu_{\mu}$).

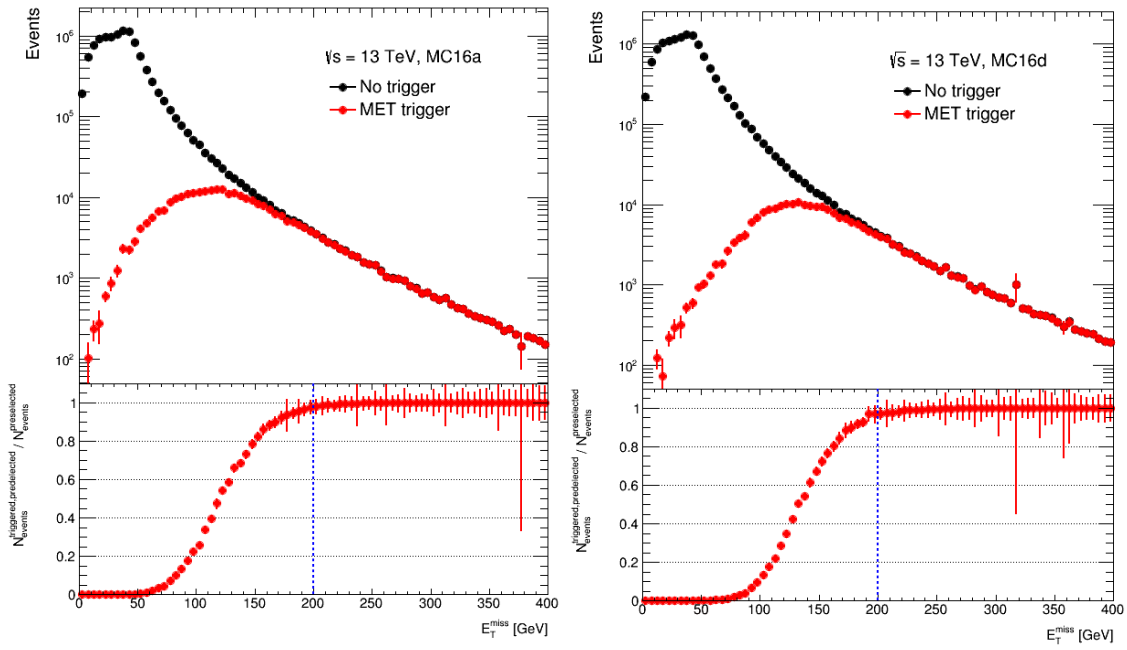

(a)

(b)

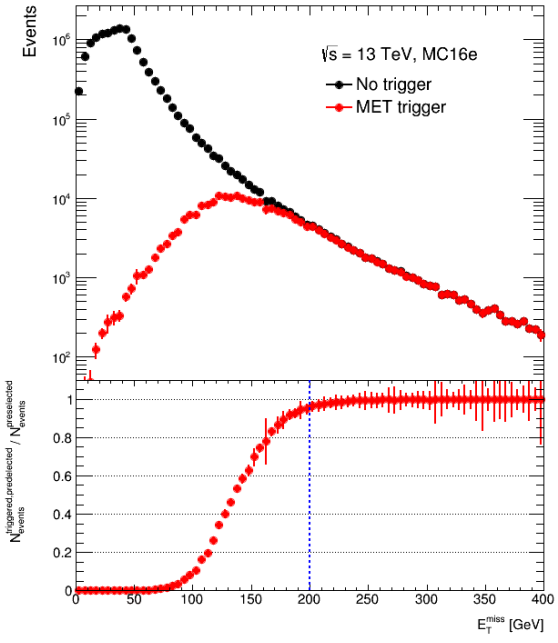

(c)

Figure 4.3: Turn-on curves of 50GeV online threshold $E_{\mathrm{T}}^{\mathrm{miss}}$ trigger on SM background samples, simulated in MC for (a) 2015-2016, (b) 2017, and (c) 2018 data. Dashed line represents estimated turn-on thresholds.

To study the performance of the $E_{\mathrm{T}}^{\mathrm{miss}}$ trigger, a new region is defined in order to isolate the $W \to \tau\nu_{\tau}$ decay, using the following selection:

- One medium τ-lepton with $p_{\mathrm{T}} > 20$ GeV

- No light leptons (e, μ)
- No b-tagged jets
- $m(\tau, E_T^{miss}) > 70$ GeV
- $E_{\mathrm{T}}^{\mathrm{miss}} > 120$ GeV

The invariant mass requirement between the $E_{\mathrm{T}}^{\mathrm{miss}}$ and τ-lepton is used to select events from the W + jets decay process. A $E_{\mathrm{T}}^{\mathrm{miss}}$> 120 GeV requirement is used to also remove events from other SM background processes, which is possible to do in part due to the fact that only a small amount of performance will be lost, because of the large inefficiency of $E_{\mathrm{T}}^{\mathrm{miss}}$ triggers at low missing transverse momentum values. Due to the inherent bias in the number of total events of the prescaled $E_{\mathrm{T}}^{\mathrm{miss}}$ trigger leg, a *tag and probe method* must be used to check the efficiency. In the tag and probe method an orthogonal unprescaled trigger is used to select the relevant events (known as the *tag trigger*). The prescaled trigger in question (known as *probe trigger*), is then checked to see if it has also triggered for the selected event. The efficiency for the tag and probe method is then calculated as the ratio of probed events over the number of events that have been tagged:

$$\epsilon = \frac{N_{T\&P}}{N_P}. \tag{4.2}$$

For this analysis, a known unprescaled single tau trigger (*tag*) is used to select relevant events. The $E_{\mathrm{T}}^{\mathrm{miss}}$ trigger is then checked to see if it has also been fired (*probe*) in these events. A 160 GeV online threshold single tau trigger is used as the probe trigger with an offline $p_{\mathrm{T}} > 180$ GeV requirement to ensure that events on the trigger plateau are selected. Figure 4.4 shows the τ-lepton p_{T} and $E_{\mathrm{T}}^{\mathrm{miss}}$distributions for the events that pass the tag and probe selection in this region. MC simulated SM background processes are used to evaluate the kinematic distribution of data. The simulated background processes and data distributions are found to have good agreement, with the W + jets as the main contributing background process.

Using Equation 4.2 the trigger efficiencies in both the combined SM background samples and collected data can be derived, as shown by the bottom plot of Figure 4.5, while the top plots shows the number of events that pass the tag (black) and tag+probe (red) trigger requirements as a function of transverse missing energy, respectively. The efficiency exceeds 90% in both data and background at around 150 GeV (shown by red dotted line), above which it quickly increases to 100% for higher $E_{\mathrm{T}}^{\mathrm{miss}}$ values. Using these trigger efficiencies, the $E_{\mathrm{T}}^{\mathrm{miss}}$ trigger SF values are derived and are shown in Figure 4.6 for the range of offline $E_{\mathrm{T}}^{\mathrm{miss}}$ values above 120 GeV. Due to the use of offline reconstructed $E_{\mathrm{T}}^{\mathrm{miss}}$ and high threshold selection the resulting turn-on curve are relatively slow, compared to the expected turn-on curve for online $E_{\mathrm{T}}^{\mathrm{miss}}$. The SF are found to be approaching unity for large $E_{\mathrm{T}}^{\mathrm{miss}}$ values, thus indicating the MC simulations to be a good at estimating the performance of the $E_{\mathrm{T}}^{\mathrm{miss}}$ trigger in data. Because of changes in the trigger menu between data collection years, the simple $E_{\mathrm{T}}^{\mathrm{miss}}$ trigger was only turned on for data collected in 2016, and was not available for the data collected in the later years.

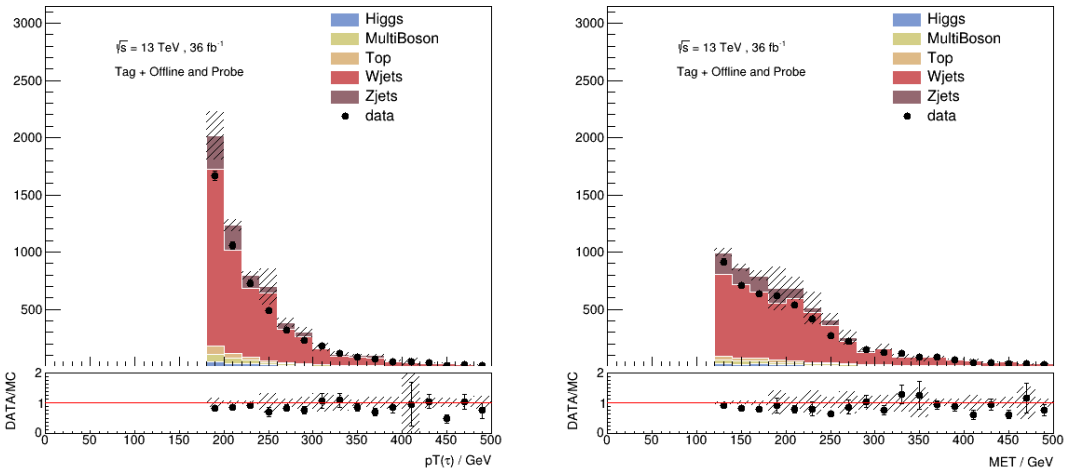

Figure 4.4: Kinematic distributions of τ-lepton p_{T} (left) and $E_{\mathrm{T}}^{\mathrm{miss}}$ (right) for Tag and Probe method selection. SM background are shown by the stacked histograms while data is represented by black markers. Statistical uncertainties are shown by shaded area.

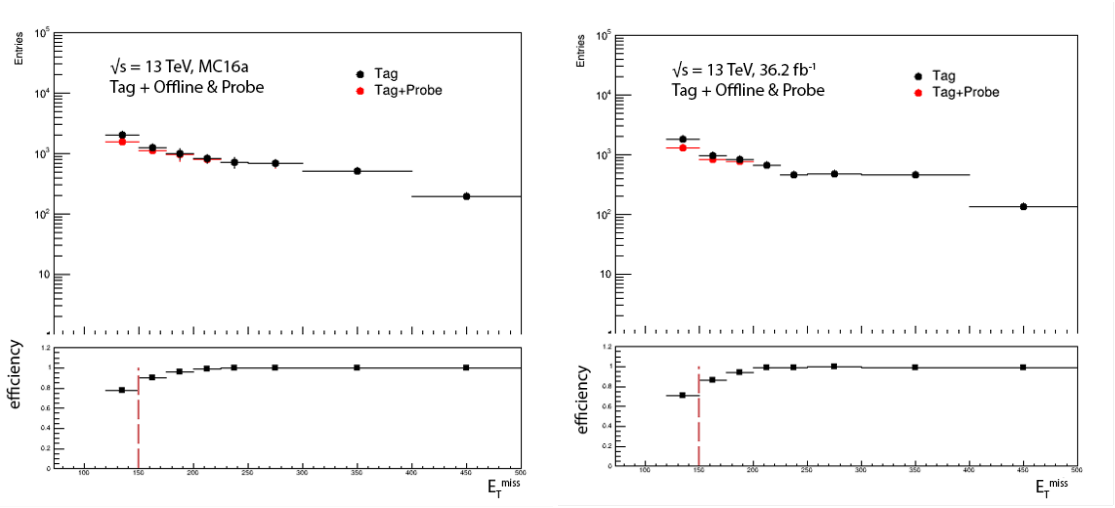

Figure 4.5: $E_{\mathrm{T}}^{\mathrm{miss}}$ distributions using Tag (black) and Probe (red) method for 50 GeV threshold $E_{\mathrm{T}}^{\mathrm{miss}}$ trigger for a combined set of MC simulated SM backgrounds (left) and 36.2 fb^{-1} of data collected in 2016 (right). Bottom plot show corresponding efficiencies.

To ensure that the combined triggers are performing at maximal efficiency offline selections cuts for the triggered objects are used to select the events that lie on the plateau of the trigger turn on curve. For the di-tau+$E_{\mathrm{T}}^{\mathrm{miss}}$ trigger, an offline 50 GeV minimum p_{T} requirement on the highest τ-lepton is used for data collected between 2015-2017, which was increased to 75 GeV in 2018 due to the change of triggers, while the second triggered τ-lepton in the event is required to have $p_{\mathrm{T}} > 40$ GeV. An offline requirement of $E_{\mathrm{T}}^{\mathrm{miss}} > 150$ GeV is used for the $E_{\mathrm{T}}^{\mathrm{miss}}$ leg of the combined trigger. For the asymmetric di-tau trigger the highest energy τ-lepton of the event is required to have an offline $p_{\mathrm{T}} > 95$ GeV, while the second highest energy τ-lepton must have $p_{\mathrm{T}} > 60$ (75) GeV for data collected between 2015-2017 (2018). The HLT online and offline thresholds used by each trigger for each trigger leg are summarised in Table 4.3.

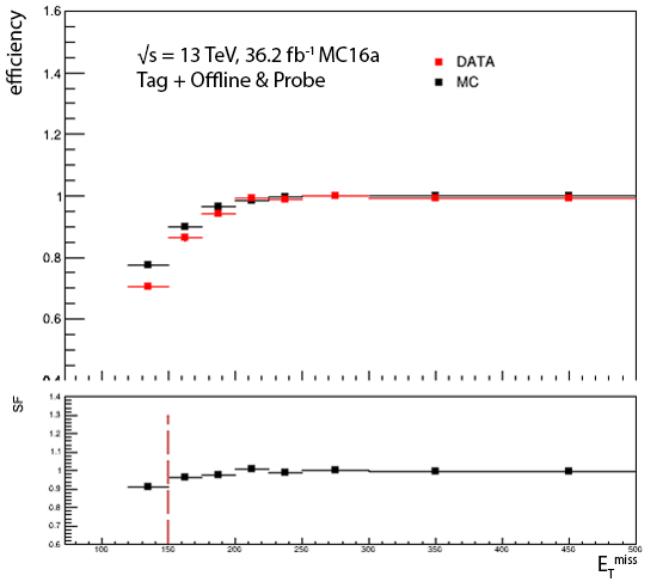

Figure 4.6: Efficiency plot of 50 GeV threshold $E_{\mathrm{T}}^{\mathrm{miss}}$ trigger for combined MC SM backgrounds (black) and collected data (red). SF values as a function of $E_{\mathrm{T}}^{\mathrm{miss}}$ are shown in the bottom plot. Online $E_{\mathrm{T}}^{\mathrm{miss}}$ thresholds shown on as vertical red dashed line.

Table 4.3: Lowest unprescaled triggers for Run-2 with two hadronic taus (asymmetric di-tau) or two hadronic taus with missing transverse momentum ($E_{\mathrm{T}}^{\mathrm{miss}}$).

Trigger	Trigger leg	Year	HLT [GeV]	Offline [GeV]
di-tau+E_T^{miss}	leading τ-lepton p_T	2015-2017	35	50
		2018	60	75
	2nd leading τ-lepton p_T	2015-2018	25	40
	E_T^{miss}	2015-2018	50	150
asymmetric di-tau	leading τ-lepton p_T	2015-2018	80	95
	2nd leading τ-lepton p_T	2015-2017	50	60
		2018	60	75

Triggers independence test

The individual trigger legs of a combined trigger are considered to be independent. The efficiency of the full trigger can, thus, be derived by combining the trigger efficiencies of the individual legs of which is constituted. This assumption is tested and proved using a *closure test*. The closure test is performed, using MC simulated samples, by comparing the product of the efficiencies of the two legs with the trigger efficiency of the full di-tau trigger. For this closure test, the asymmetric di-tau trigger as well as the combined di-tau legs of the di-tau+$E_{\mathrm{T}}^{\mathrm{miss}}$ trigger are tested with respect to their corresponding single tau trigger legs:

tau80_tau50: HLT_**tau80**_medium1_tracktwo_L1TAU60_**tau50**_medium1_tracktwo_L1TAU12

tau80_tau60: HLT_**tau80**_medium1_tracktwoEF_L1TAU60_**tau60**_medium1_tracktwoEF_L1TAU40

tau35_tau25: HLT_**tau35**_medium1_tracktwo_**tau25**_medium1_tracktwo_2TAU12IM

A simple selection of 2 medium Opposite Sign (OS) τ-leptons with no b-tagged jets, nor light leptons in the event is used. Figure 4.7 shows the resulting efficiencies, as defined by Equation 4.1 for the single legs and combined triggers using this selection. The bottom plot of the figures show the closure test, which is found to be close to unity for τ-lepton p_{T} values above 90 GeV for the asymmetric di-tau trigger. Similarly, the di-tau leg of the di-tau+$E_{\mathrm{T}}^{\mathrm{miss}}$ is also found to have a closure test value of approximately one for the full range of p_{T} values above 50 GeV. Therefore, the closure test shows that the single trigger legs can be combined to give the total efficiencies of the di-tau triggers for values above the offline trigger thresholds.

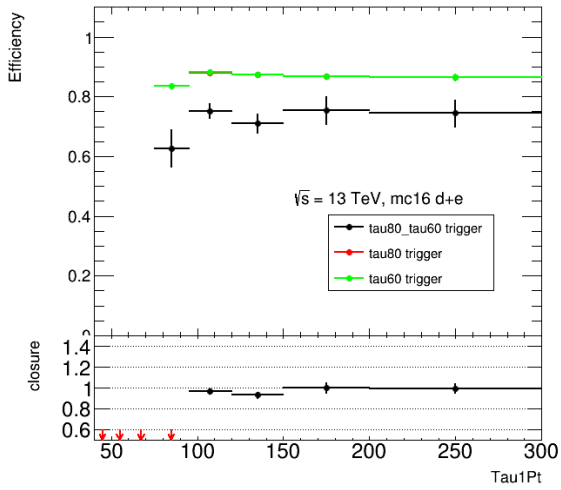

(a) tau80_tau60

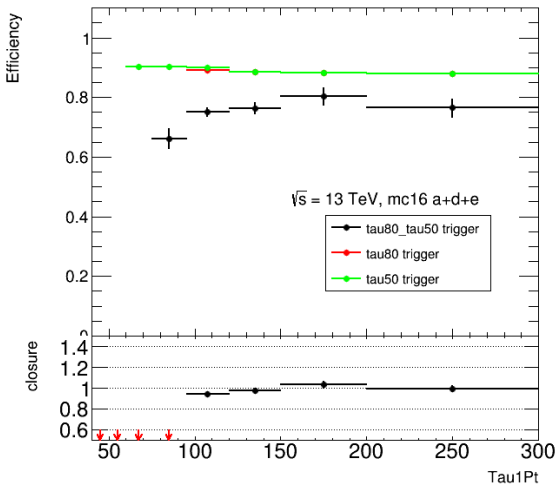

(b) tau80_tau50

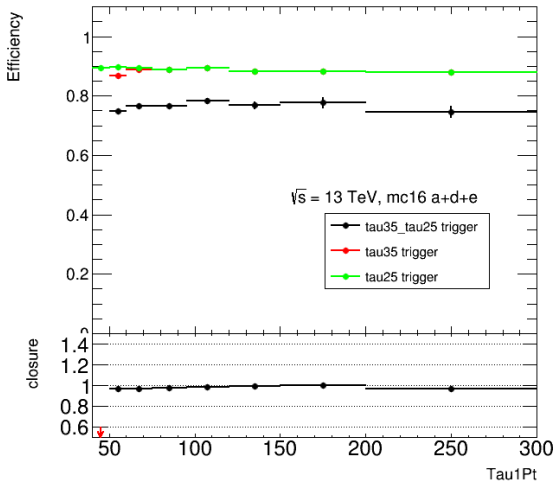

(c) tau35_tau25

Figure 4.7: Closure test for di-tau trigger efficiencies using for tau trigger legs of the asymmetric di-tau and di-tau+$E_{\mathrm{T}}^{\mathrm{miss}}$ triggers. Single tau trigger efficiencies are shown in green and red for each leg of the di-tau trigger. Combined trigger efficiency is shown in black.

4.6 Event Selection

The analysis presented utilises a cut-and-count strategy to isolate the SUSY signal from the SM background, using dedicated sets of discriminating variables. Background-enriched regions,

defined as Control Regions (CRs) are used to estimate the contribution of the most relevant background in the defined SR. MC-based or data-driven methods can be used to estimate the relative contribution of background in the SR, depending on the process that is being estimated. A detailed description of the background estimation methods used in this analysis can be found below.

Due to the different running conditions and configurations of the detector, some selection (e. g. trigger requirements or calibration parameters) are applied differently between data collected in 2015 to 2018. The different kinematic regions used for the selection of relevant events will be discussed in more detail in Sections 4.6.2 and 4.6.3. MC samples are generated for various periods of data taking, where a random number is generated and associated to the simulated MC event in order to identify any given ATLAS run. This way, simulated events can be associated with specific operation periods that reflect the parameters with which data was collected.

4.6.1 Event Cleaning

Event cleaning requirements are applied to data to ensure that only events collected when the detector was fully functional are used in the analysis. The first requirement for the event to be accepted as *"good physics"* is for the existence of a primary vertex with a minimum of two tracks, with $p_{\mathrm{T}} > 500$ MeV, associated to it. The status of the HCAL and ECAL is also checked and if any error state is returned the event is discarded. To reduce and suppress the fake-jet (*bad jet*) contamination, quality requirements on a variety of jet parameters are checked. These parameters include the fraction of energy deposited in the different layers of the calorimeters, and the fraction of jet p_{T} measured by the tracks in the ID. The impact of pileup is accounted by a technique, based on jet areas, that provides an event-by-event and jet-by-jet correction [120]. Events containing muon candidates whose relative uncertainty on their charge-to-momentum ratio ($\sigma(q/p)/|q/p|$ is larger than 0.4, or that have been identified as not originating from the pp collision (cosmic), are also discarded.

4.6.2 Signal Regions and optimization

The experimental signature expected for the signal topology described in Section 4.2 is the presence of two taus that have decayed fully hadronically and a significant amount of $E_{\mathrm{T}}^{\mathrm{miss}}$. No additional jets or light leptons (electrons or muons) in the signal event final state are expected.

As explained in Section 4.5, in order to use the tau trigger SFs and efficiencies from the individual triggers, two orthogonal SR are constructed:

Low-mass SR: Optimised to cover the low stau mass processes. The asymmetric di-τ trigger in events with $E_{\mathrm{T}}^{\mathrm{miss}} \leq 150$ GeV is used.

High-mass SR: Targets the high $\tilde{\tau}$ mass processes, using the di-τ+$E_{\mathrm{T}}^{\mathrm{miss}}$ trigger in events with $E_{\mathrm{T}}^{\mathrm{miss}} > 150$ GeV.

Preliminary selection and discriminating variables

The preliminary selection (*pre-selection*) is a basic selection common to both SRs, used as an initial step to separate the signal from the backgrounds. This selection includes the common event cleaning described in Section 4.6.1 and the trigger selection described in Section 4.5. A further selection is applied to discriminate for events that contain exactly two medium taus after OR. The two selected taus are required to be of opposite charge, generally referred to as OS taus, and to be matched to the corresponding trigger objects at HLT level. Apposite requirement on the offline $E_{\mathrm{T}}^{\mathrm{miss}}$ and tau p_{T} are applied to ensure that the triggers are in their efficiency plateau. If light leptons, a third τ-lepton, or a b-tagged jet are present, the event is rejected to ensure orthogonality from the semi-hadronic channel (where one tau decays to leptons), to suppress 3 tau background processes, and to suppress SM backgrounds originating from top quarks. Events with invariant mass of the two visible taus below 120 GeV are rejected to suppress contribution from the Z + jets and Higgs SM background events (Z/H veto). The summary of the used pre-selection is shown in Table 4.4.

Table 4.4: Preliminary selection common to both low- and high-mass SR in addition to the event cleaning.

Low-mass Preselection	High-mass Preselection
2 medium taus (OS)	
light lepton veto and 3rd tau veto	
b-jet veto	
Z/H-veto ($m(\tau_1,\tau_2) > 120$ GeV)	
asymmetric di-tau trigger	di-tau+E_T^{miss} trigger
$E_T^{miss} \leq 150$ GeV	$E_T^{miss} > 150$ GeV
τ_1 and τ_2 p_T trigger requirements	

The following event kinematic variables or global event properties, based on the decay topology of SUSY, top, and Z events are studied to further select signal events:

M_{T2} : *stranverse mass*, which can be shown to have a kinematic endpoint for events where two massive pair produced particles each decay to two objects, one of which is detected and the other escapes undetected [121, 122]. In the case of this analysis, the detected objects are the visible τ-leptons while the undetected objects are the neutralinos. The stransverse mass is defined as:

$$m_{T2} = \min_{\mathbf{q}_{\mathrm{T}}} \left[\max\left(m_{\mathrm{T},\tau_1}(\mathbf{p}_{\mathrm{T},\tau_1}, \mathbf{q}_{\mathrm{T}}), m_{\mathrm{T},\tau_2}(\mathbf{p}_{\mathrm{T},\tau_2}, \mathbf{p}_{\mathrm{T}}^{miss} - \mathbf{q}_{\mathrm{T}}) \right) \right],$$

where $\mathbf{p}_{\mathrm{T},\tau_1}$ and $\mathbf{p}_{\mathrm{T},\tau_2}$ are the transverse momenta of the two leading tau, and $\mathbf{q}_{\mathrm{T}}$ is the transverse vector that minimises the larger of the two transverse masses m_{T,τ_1} and m_{T,τ_2}. The transverse momenta is defined by:

$$m_T(\mathbf{p}_{\mathrm{T}}, \mathbf{q}_{\mathrm{T}}) = \sqrt{2(p_{\mathrm{T}} q_{\mathrm{T}} - \mathbf{p}_{\mathrm{T}} \cdot \mathbf{q}_{\mathrm{T}})};$$

$m_{\mathrm{T},\tau_1} + m_{\mathrm{T},\tau_2}$: the sum of the transverse mass values of the leading and next-to-leading taus;

M_{eff} : the *effective mass* is the scalar sum of the missing transverse energy ($E_{\mathrm{T}}^{\mathrm{miss}}$) and the transverse momenta of the leading and next-to-leading taus;

$\Delta R(\tau_1, \tau_2)$: the cone size between the leading and next-to-leading tau. An upper cut on this variable is a powerful discriminant against back-to-back events such as multi-jets;

$m(\tau_1, \tau_2)$: the invariant mass of the two reconstructed taus.

Optimization strategy

The SR optimization is fundamental for any analysis that uses the cut-and-count method. The goal is to remove as many background events as possible while retaining the largest possible number of signal events. The set of discriminating variables described above are used to this end.

To represent the discovery significance of the signal model targeted, a Figure of Merit (FoM) is employed. In this analysis the FoM used is the *significance*, which is the probability that an observed event counted in a SR could have been produced by the sole fluctuation of the background in that region. The optimization of the cuts that comprise the SR of interest is performed by maximising the value of the significance Z_n [63], which is generally implemented in the `RooStats` [123] package within the `ROOT` [124] framework, and is defined as:

$$Z_n = \frac{N_{\mathrm{sig}}}{\sqrt{N_{\mathrm{bkg}} + (N_{\mathrm{bkg}}\sigma_{\mathrm{bkg}})^2}}, \tag{4.3}$$

where N_{sig} and N_{bkg} are the signal and background yields, respectively. σ_{bkg} is the relative systematic uncertainty on the background which has been set to a flat 30% based on previous analyses. Signal statistical uncertainty is not taken into account, as it is assumed to be negligible compared to the background uncertainty.

To avoid potential bias on the part of the analysers during the SR optimization, a so-called *blinding* procedure is employed. The number of data events that fall within the SR is purposefully hidden from the analysers, until the modelling of the background falling into that SR has been solidly estimated from background-enriched CRs and tested in Validation Regions (VRs). The estimation and validation of the background is discussed in detail in Section 4.6.3.

SR definition

Based on the optimization procedure described above, the optimised signal regions are defined in Table 4.5. Values of $E_{\mathrm{T}}^{\mathrm{miss}} > 75$ GeV are required for the Low-mass SR to increase signal sensitivity. In addition the two τ-lepton candidates are required to satisfy $\Delta R(\tau_1, \tau_2) < 3.2$, $|\Delta\phi(\tau_1, \tau_2)| > 0.8$ and $m_{T2} > 70$ GeV to further suppress contributions from SM background processes.

The so-called "N-1" plots, showing the distributions of relevant kinematic variables, after the Low-mass and High-mass SRs requirements, except for the variable being evaluated, are

Table 4.5: Optimised selection for Low-mass and High-mass SRs.

Low-mass SR	High-mass SR
2 tight τ (OS)	2 medium τ (OS), $\geq$ 1 tight τ
light lepton veto and 3rd medium τ veto	
b-jet veto	
Z/H-veto ($m(\tau_1,\tau_2) > 120$ GeV)	
$\lvert\Delta\phi(\tau_1,\tau_2) > 0.8\rvert$	
$\Delta R(\tau_1,\tau_2) < 3.2$	
$m_{T2} > 70$ GeV	
asymmetric di-tau trigger	di-tau+E_T^{miss} trigger
$75 < E_T^{miss} \leq 150$ GeV	$E_T^{miss} > 150$ GeV
τ_1 and τ_2 trigger p_T requirements	

shown in Figures 4.8 and 4.9, respectively. The red arrow shows the kinematic region that is accepted by the selection, while the rest is rejected.

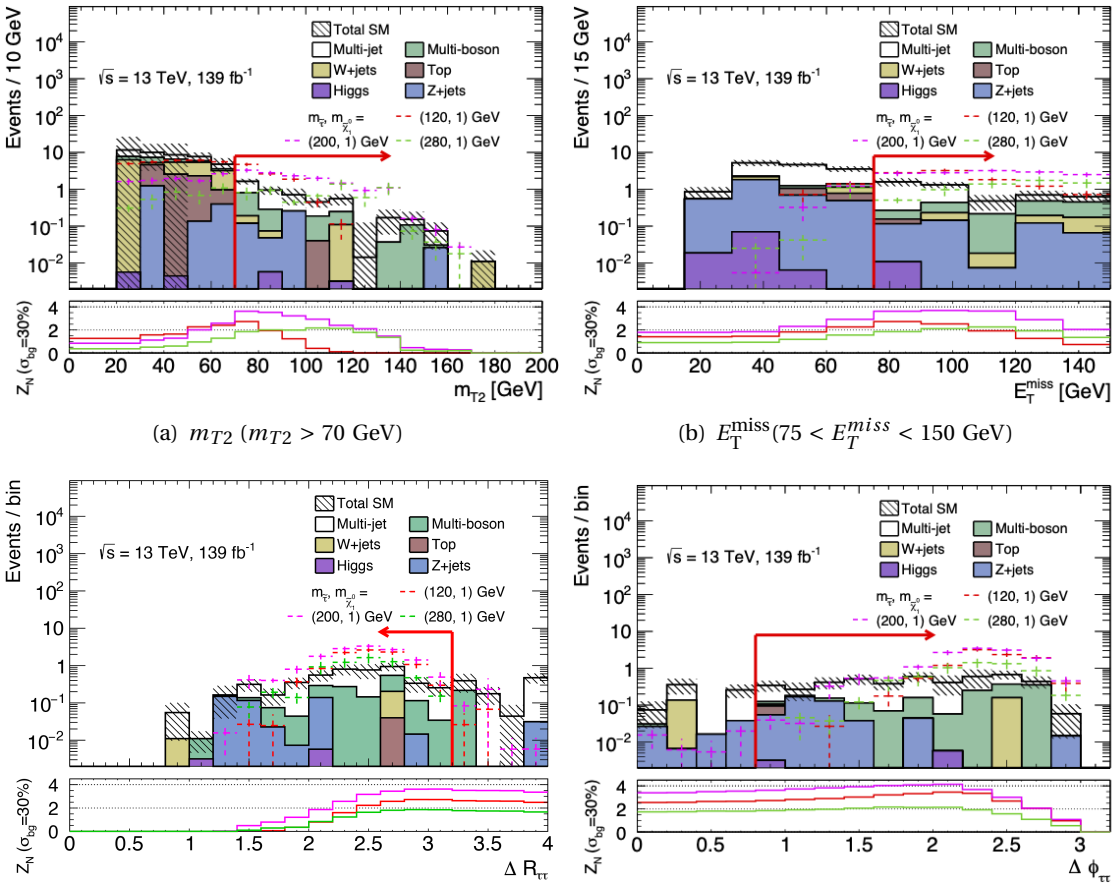

(a) m_{T2} ($m_{T2} > 70$ GeV)

(b) $E_{\mathrm{T}}^{\mathrm{miss}}$($75 < E_T^{miss} < 150$ GeV)

(c) $\Delta R(\tau_1,\tau_2)$ ($\Delta R(\tau_1,\tau_2) < 3.2$)

(d) $|\Delta\phi(\tau_1,\tau_2)|$ ($|\Delta\phi(\tau_1,\tau_2)| > 0.8$)

Figure 4.8: "N-1" distributions of relevant kinematic variables after Low-mass SR requirements, except the one on the shown variable, are applied. The stacked histogram show the expected SM background estimates from MC normalised to 139 fb^{-1}.

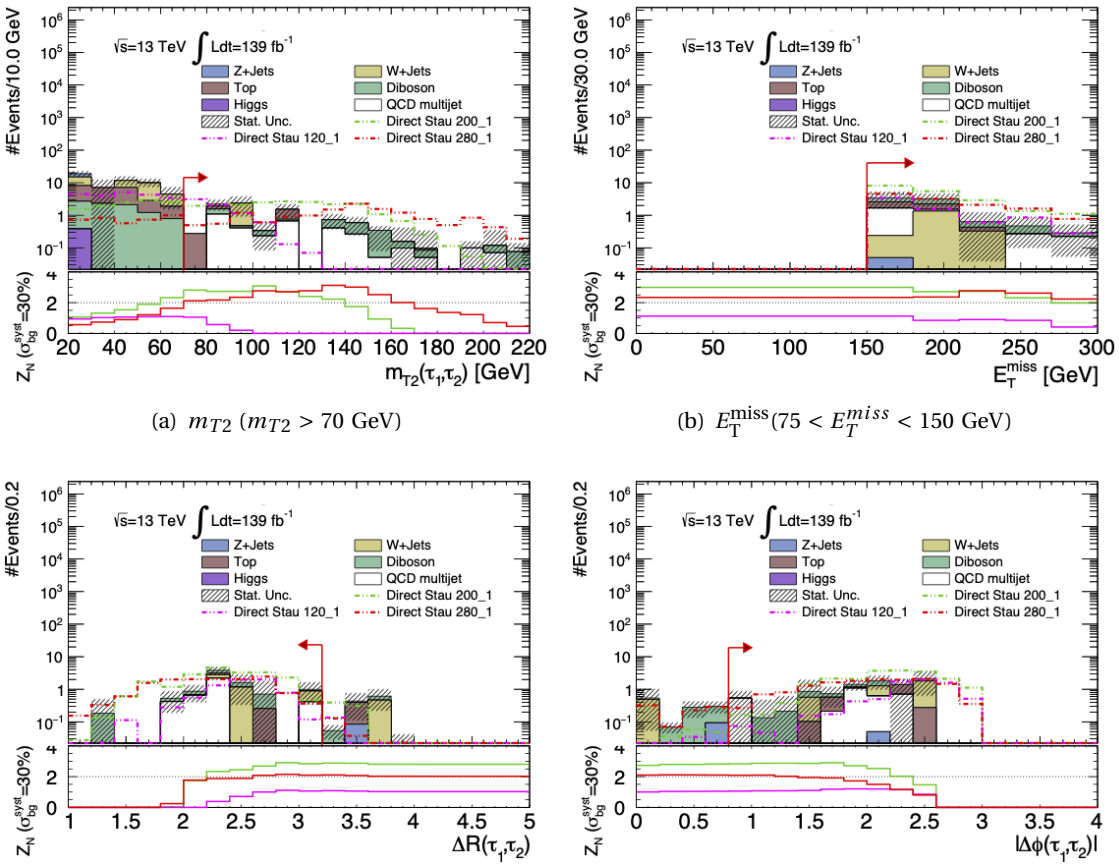

(a) m_{T2} ($m_{T2} > 70$ GeV)

(b) $E_{\mathrm{T}}^{\mathrm{miss}}$ ($75 < E_T^{miss} < 150$ GeV)

(c) $\Delta R(\tau_1,\tau_2)$ ($\Delta R(\tau_1,\tau_2) < 3.2$)

(d) $|\Delta\phi(\tau_1,\tau_2)|$ ($|\Delta\phi(\tau_1,\tau_2)| > 0.8$)

Figure 4.9: "N-1" distributions of relevant kinematic variables after High-mass SR requirements, except the one on the shown variable, are applied. The stacked histogram show the expected SM background estimates from MC normalised to 139 fb^{-1}.

4.6.3 Background estimation

The main SM backgrounds to this analysis are the multi-jet events, W + jets, and multi-boson production, as explained in Section 4.3. Background events may contain a combination of "real" τ-leptons or "fake" τ-leptons. A "real" τ-lepton is defined as a correctly identified prompt τ_{had}, while a "fake" τ-lepton is one which originates from a misidentified quark or gluon jet, an electron, or a muon.

Multi-jet and W + jets events are known as *reducible* backgrounds. These are SM processes whose final states involve either one or both final state objects to be mis-identified as τ-leptons. The contributions of the reducible background in the SRs is, therefore, estimated in data from dedicated CRs. On the other hand, the multi-boson, Z + jets, and $t\bar{t}$+V ($V = W, Z$) background processes contribute predominantly to events containing real τ-leptons and are therefore called *irreducible* backgrounds. To estimate the irreducible backgrounds, only MC simulated samples are used and validated in dedicated VRs.

Multi-jet background estimation

One of the dominant backgrounds in the SRs originates from jets mis-identified as τ-leptons in multi-jet production. It accounts for 44% (30%) of the total SM contribution in the Low-mass (High-mass) SR. This contribution is estimated using the so-called *ABCD method*.

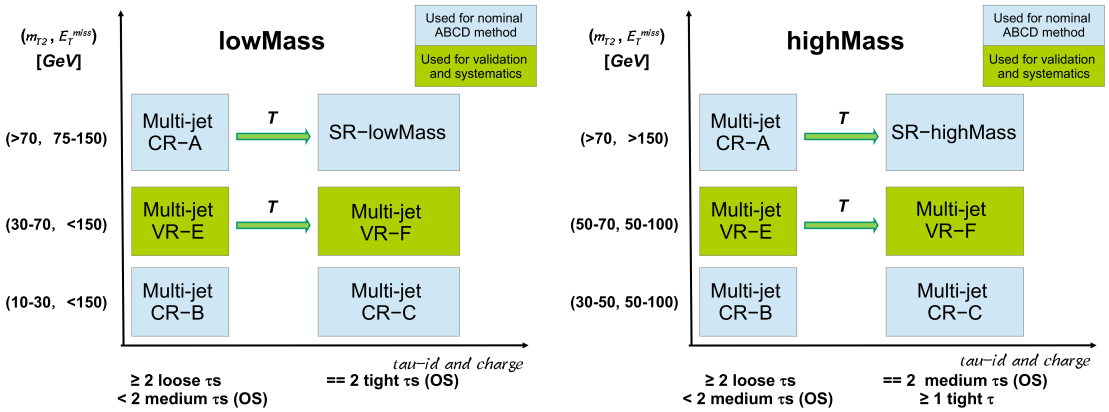

(a) (b)

Figure 4.10: Illustration of the ABCD method for the multi-jet background determination for (a) Low-mass and (b) High-mass SRs. CRs A, B, C, SR D, and VRs E, F are described in the text and are drawn as blue and green boxes, respectively. Transfer factor T used in the ABCD method is the ratio of number of multi-jet events in the regions C and B.

Four exclusive regions, labelled as A, B, C and D are defined in a two dimensional plane as a function of two (or more) uncorrelated discriminating variables. Regions A, B and C are dedicated CR while region D is the SR. Figure 4.10 shows the schematically drawn ABCD regions used in the analysis estimation of multi-jet background. The ratio of events in the regions C and B is then equal to that in the regions D and A. The number of multi-jet events in region D (N_D) can thus be calculated from the multi-jet events in region A (N_A) multiplied by the transfer factor $T = N_C/N_B$ where N_C (N_B) is the number of multi-jet events in region C (B). Regions A, B, C, D are labelled as CR-A, CR-B, CR-C, and Low-mass SR (or High-mass SR), respectively. The ABCD method only provides a first-order estimate of multi-jet background, the normalised and uncertainty being then modified by a combined fit to CR-A for both Low-mass and High-mass SR. The CR-A and SR-D are defined in the same way except that in the former the τ-leptons are required to pass the loose BDT requirement but fail the medium BDT requirement, to be orthogonal with SR-D and reduce the signal contamination in CRs. The same tau BDT identification criteria and charge requirements as in CR-A (SR-D) of the two taus is applied in CR-B (CR-C). In CR-B and CR-C, less stringent requirements on the kinematic variables M_{T2} and $E_{\mathrm{T}}^{\mathrm{miss}}$ are applied. Furthermore, two validation regions, VR-E and VR-F, are defined with similar definitions as CR-A and SR-D, respectively, except for intermediate requirements on the kinematic variables. The validation regions are used to verify the extrapolation of the ABCD estimation to the SR-D, and to estimate the systematic uncertainty from the residual correlation between the tau-identification, the charge requirement, and kinematic variables. The definitions of the control and validations regions used are summarised in Table 4.6, only for those requirements that are different in the CRs, VRs with respect to the SRs. Requirements not listed in SRs defin-

itions in Table 4.6 but present in Table 4.5 are applied to all ABCD method CRs and VRs. The *asymmetric di-tau* (*di-tau*+$E_{\mathrm{T}}^{\mathrm{miss}}$) triggers with corresponding scale factors are applied for Low-mass (High-mass) ABCD regions. The number of multi-jet events in each control region and validation region is estimated from data after subtraction of other SM contributions estimated from MC simulation. The contribution from multijet events in the Low-mass (High-mass) CR-

Table 4.6: The multi-jet CR and VR definitions for Low-mass (left) and High-mass (right) SRs. Only requirements that different in the CRs,VRs with respect to SR definitions are listed.

Low-Mass	
CR-A	**Low-mass SR (D)**
≥ 2 loose τs	$==2$ tight τs
<2 medium τs (OS)	–
$\Delta R(\tau_1,\tau_2)<3.2$	$\Delta R(\tau_1,\tau_2)<3.2$
$75<E_T^{miss}<150$ GeV	$75<E_T^{miss}<150$ GeV
$M_{T2}>70$ GeV	$M_{T2}>70$ GeV
VR-E	**VR-F**
≥ 2 loose τs	$==2$ tight τs (OS)
<2 medium τs (OS)	–
$\Delta R(\tau_1,\tau_2)<3.2$	$\Delta R(\tau_1,\tau_2)<3.2$
$E_T^{miss}<150$ GeV	$E_T^{miss}<150$ GeV
$30<M_{T2}<70$ GeV	$30<M_{T2}<70$ GeV
CR-B	**CR-C**
≥ 2 loose τs	$==2$ tight τs (OS)
<2 medium τs (OS)	–
no $\Delta R(\tau_1,\tau_2)$ cut	no $\Delta R(\tau_1,\tau_2)$ cut
$E_T^{miss}<150$ GeV	$E_T^{miss}<150$ GeV
$10<M_{T2}<30$ GeV	$10<M_{T2}<30$ GeV

High-Mass	
CR-A	**High-mass SR (D)**
≥ 2 loose τs	$==2$ medium τs
<2 medium τs (OS)	≥ 1 tight τ
$\Delta R(\tau_1,\tau_2)<3.2$	$\Delta R(\tau_1,\tau_2)<3.2$
$E_T^{miss}>150$ GeV	$E_T^{miss}>150$ GeV
$M_{T2}>70$ GeV	$M_{T2}>70$ GeV
VR-E	**VR-F**
≥ 2 loose τs	$==2$ medium τs (OS)
<2 medium τs (OS)	≥ 1 tight τ
$\Delta R(\tau_1,\tau_2)<3.2$	$\Delta R(\tau_1,\tau_2)<3.2$
$50<E_T^{miss}<100$ GeV	$50<E_T^{miss}<100$ GeV
$50<M_{T2}<70$ GeV	$50<M_{T2}<70$ GeV
CR-B	**CR-C**
≥ 2 loose τs	$==2$ medium τs (OS)
<2 medium τs (OS)	≥ 1 tight τ
no $\Delta R(\tau_1,\tau_2)$ cut	no $\Delta R(\tau_1,\tau_2)$ cut
$50<E_T^{miss}<100$ GeV	$50<E_T^{miss}<100$ GeV
$30<M_{T2}<50$ GeV	$30<M_{T2}<50$ GeV

B and VR-E is around 96% and 90% (75% and 79%), respectively. Figure 4.11 shows the prefit m_{T2} distribution in the low-Mass and High-mass VR-E. Good agreement between the data and MC is observed indicating that an appropriate estimation of the multijet contribution to this region has been derived using this procedure. The multi-jet impurity in CR-A, CR-C, and VR-F is 74%, 57%, and 51% (58%, 53%, and 51%) for the Low-mass (High-mass) region, respectively. The signal contamination is defined as the ratio of signal event multiplicity to the sum of signal and background events ($contamination = N_{sig}/(N_{sig}+N_{bkg})$). The signal contamination in multi-jet CR-A ranges from 0.4% (1.2%) to 9.4% (21.4%) for the Low-mass (High-mass) SR.

The ABCD method is validated using a different method, the *fake factor method*, which is described in detail in Chapter 5. The *universal fake factor method*, also described in Chapter 5, was not used in this analysis as it is not yet an ATLAS-approved method. The predicted multi-jet event yields from the ABCD method and Fake Factor (FF) method in both SRs and VRs agree within statistical and systematic uncertainties.

W+jets background estimation

Around 25% of the SM background in the two SRs is expected to derive from the W + jets production with at least one misidentified τ-lepton. A dedicated control region (WCR) is used to

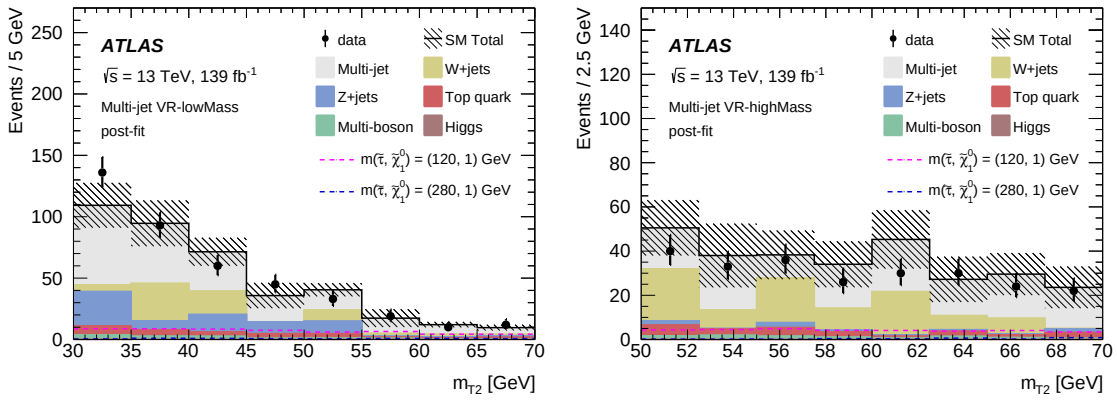

(a) (b)

Figure 4.11: The prefit M_{T2} distribution in the (a) Low-mass and (b) High-mass ABCD method defined VRs. The stacked histograms show teh expected SM backgrounds normalised to 139 fb^{-1}. The multijet contribution is estimated using the ABCD method. Hatched bands represent the combined statistical and systematic uncertainties of the total SM background. The lower panels show the ratio of data to the total SM background estimate.

normalise the W + jets MC estimate to data and another region is then used to validate the estimate (WVR). The WCR is enriched in events where the W decays leptonically to a muon and a neutrino, to suppress the contamination of multi-jet events. Therefore, events for these regions are selected with a single-muon trigger and must contain exactly one muon and one τ-lepton candidate of OS. The muon is required to have $p_{\mathrm{T}} > 50$ GeV, while the τ-lepton candidate must satisfy the *Medium* τ-lepton RNN identification criteria and have $p_{\mathrm{T}} > 60$ GeV. Top quark and $t\bar{t}$ events are suppressed by rejecting events that contain b-tagged jets, or if they are compatible with $t\bar{t}$ production (top-tagged) [125]. The transverse mass of the μ+$E_{\mathrm{T}}^{\mathrm{miss}}$system ($m_{T,\mu}$) is used to reduce the contribution from Z + jets, top-quarks, and multi-boson events. The $E_{\mathrm{T}}^{\mathrm{miss}}$ and $\Delta R(\tau,\mu)$ cut are applied to further reduce the multi-jet and Z + jets contribution, while the invariant mass and sum of transverse mass of the muon and τ-lepton ($m(\tau,\mu)$ and $m_{T,\mu}+m_{T,\tau}$) are used to improve the W + jets purity. Events in the WCR (WVR) are selected by requiring low (high) m_{T2}. The selection applied in the WCR and WVR using the cuts described above is summarised in Table 4.7.

Table 4.7: Summary of selection requirements for the W + jets control (WCR) and validation (WVR) regions.

WCR	WVR
1 medium τ and 1 isolated μ (OS)	
single-muon trigger	
$p_T(\tau) > 60$ GeV, $p_T(\mu) > 50$ GeV	
$E_T^{miss} > 60$ GeV	
b-jet veto and top-tagged events veto	
$m(\mu,\tau) > 70$ GeV	
$1 < \Delta R(\mu,\tau) < 3.5$	
$50 < m_{T,\mu} < 150$ GeV	
$m_{T,\mu} + m_{T,\tau} > 250$ GeV	
$30 < m_{T2} < 70$ GeV	$m_{T2} > 70$ GeV

The contribution of multi-jet events in the WCR (WVR) is estimated using the so-called *OS-SS method*. The OS-SS method is performed by counting the number of events in data that satisfy the same requirements as for the WCR (WVR) but with electric charge of the two leptons having the Same Sign (SS). MC processes other than multi-jet production are subtracted from the data counts in the SS region using MC simulation. This method relies on the fact that the ratio of SS to OS events in multi-jet events is close to unity while for W + jets processes it is around 0.14. This is due to the latter process having events dominated by gu/gd-initiated processes that often give rise to a jet originating from the quark with charge that is anti-correlated to the W boson charge. The systematic uncertainty assigned to the multi-jet estimate in the WCR is 100%, based on studies performed on simulated samples. The prefit m_{T2} distribution in the WCR is shown in Figure 4.12. Good agreement is observed both for the normalization and shape between data and SM prediction, and the purity of the W + jets selection is found to be around 79%. The purity in the WVR is around 69%. The contamination of signal in WCR and WVR is negligible.

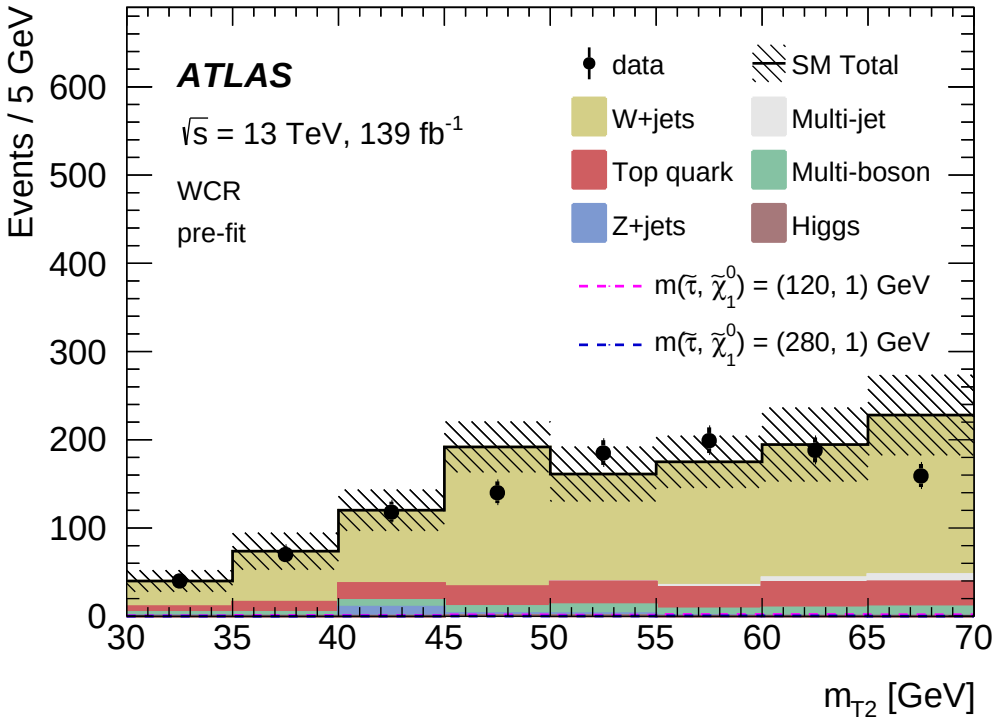

Figure 4.12: The prefit M_{T2} distribution in the WCR. The SM multi-jet production background is estimated from data using the OS-SS method, while all other backgrounds are estimated from MC simulation. Hatched bands represent the combined statistical and systematic uncertainties of the total SM background. Distributions of SUSY signal are shown but the contribution is too low to be visible.

Irreducible background estimation

Irreducible SM backgrounds arise mainly from $t\bar{t}$, single top quark, $t\bar{t}+V$, Z + jets, and multiboson processes. All other SM backgrounds are found to be negligible. These relevant irreducible backgrounds are estimated with MC simulations and validated in dedicated VRs, enriched with

events from the process to be validated. The VRs selection used to target the relevant SM background are described below.

Z+jets Validation Region (ZVR): to suppress top-quark background, b-tagged events are vetoed. To enhance the purity of Z + jets events, $\Delta R(\tau_1,\tau_2)$, $m(\tau_1,\tau_2)$, and m_{T2} requirements are applied.

Top Validation Region (TVR): to enrich the region with top-quark events a $\Delta R(\tau_1,\tau_2)$, requirement must be satisfied. There must also be at least one b-tagged jet with $p_{\mathrm{T}} > 20$ GeV. An additional requirement on the $m_{T2} > 60$ GeV is needed to be close to the SRs.

Multiboson Validation Region (VVVR): the purity of multi-boson events is enhanced via $m(\tau_1,\tau_2)$ $m_{T,\tau_1}+m_{T,\tau_2}$, and m_{T2} requirements. Top-quark background is also suppressed by rejecting events that have at least one b-tagged jet.

For all VRs events are also required to have at least two τ-leptons that satisfy the *Medium* RNN identification criteria with opposite sign charge, and at least one τ-lepton candidate must satisfy the *Tight* RNN identification criteria, in order to be close to the SR. Events must also pass either the combined di-τ+$E_{\mathrm{T}}^{\mathrm{miss}}$ trigger or the asymmetric di-τ trigger for the High-mass and Low-mass selections, respectively. Table 4.8 gives a summary of the described VRs selection criteria.

Table 4.8: Summary of selection requirements for top quark (TVR), Z + jets (ZVR) and multiboson (VVVR) validation regions.

Low-Mass		
TVR	**ZVR**	**VVVR**
≥ 2 medium τ (OS), ≥ 1 tight τ		
≥ 1 b-jet	b-jet veto	b-jet veto
—	$m(\tau_1,\tau_2) < 70$ GeV	$m(\tau_1,\tau_2) < 110$ GeV
$\Delta R(\tau_1,\tau_2) > 1.2$	$\Delta R(\tau_1,\tau_2) < 1$	—
—	—	$m_{T,\tau_1} + m_{T,\tau_2} > 250$ GeV
$m_{T2} > 60$ GeV	$m_{T2} < 60$ GeV	$m_{T2} > 60$ GeV
asymmetric di-τ trigger		
$60 < E_T^{miss} < 150$ GeV		
τ_1 and τ_2 trigger p_T requirements		

High-Mass		
TVR	**ZVR**	**VVVR**
≥ 2 medium τ (OS), ≥ 1 tight τ		
≥ 1 b-jet	b-jet veto	b-jet veto
—	$m(\tau_1,\tau_2) < 60$ GeV	$m(\tau_1,\tau_2) < 110$ GeV
$\Delta R(\tau_1,\tau_2) > 1.2$	$\Delta R(\tau_1,\tau_2) < 1$	—
—	—	$m_{T,\tau_1} + m_{T,\tau_2} > 200$ GeV
$m_{T2} > 60$ GeV	$m_{T2} < 60$ GeV	$m_{T2} > 60$ GeV
di-$\tau + E_T^{miss}$ trigger		
$E_T^{miss} > 150$ GeV		
τ_1 and τ_2 trigger p_T requirements		

The data event yields and the SM predictions are derived using a simultaneous fitting procedure based on the profile likelihood method [126], which takes as input the number of events passing the multijet and W CRs, the transfer factors, and the contribution of multijet/non-multijet and W/non-W contributions to their corresponding CR, as described in more detail in Section 4.8. The resulting data event yields and SM predictions for the WVR, TVR, and VVVR are shown in Figure 4.13. The data and SM prediction in each validation region agree within the uncertainties. The purity of the selection in Z + jets, $t\bar{t}$, and multiboson events are 83%-96%, 83%-96%, and 47%-71% in the respective VRs.

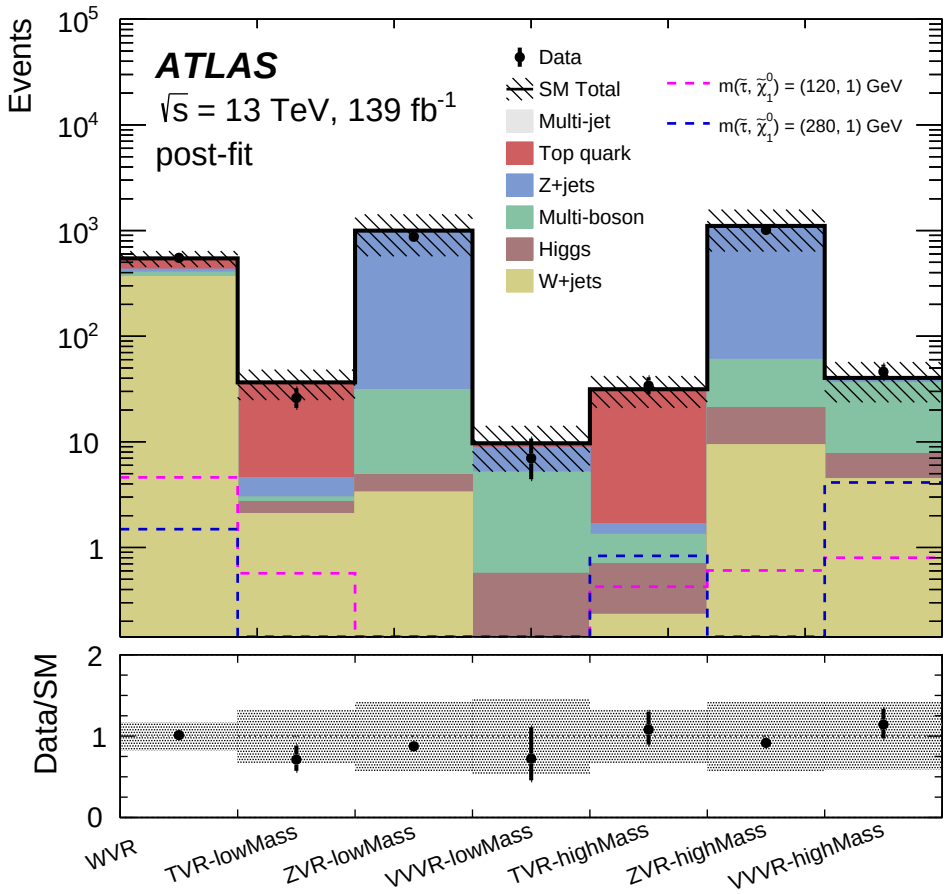

Figure 4.13: The postfit yields in the WVRs, TVRs, ZVRs and VVVRs for both High-mass and Low-mass selections. The SM multi-jet production background contribution is negligible and estimated from data using the OS-SS method, while all other backgrounds are estimated from MC simulation. Hatched bands represent the combined statistical and systematic uncertainties of the total SM background. Distributions of SUSY signal are also shown. The lower panel shows the ratio of data to the SM background estimate.

4.7 Systematic uncertainties

For this analysis several sources of systematic uncertainties are considered. These include: experimental uncertainties, which derive from the reconstruction of physics objects and the integrated luminosity of the analysed dataset used, as well as theoretical uncertainties on the modelling of the relevant SM background and SUSY signal processes.

The systematic uncertainties discussed here affect the predicted background yields in the SRs and are either used when evaluating a given background yield in the SRs, by relying on the sole MC prediction, or when computing the uncertainty on the Transfer Factor (TF). The overview of the sources of systematic uncertainties is presented in this thesis in two separate sections. One section will be dedicated to the experimental uncertainties that affect this analysis, while the other will describe the study and derivation of the theory uncertainties, including uncertainties on cross sections, choice of scales, and PDFs, primarily performed by the author.

4.7.1 Experimental uncertainties

Each reconstructed object has an assigned uncertainty. Dedicated calibrations of each physics objects (e, μ, τ_{had}, $b-$jets, and $E_{\mathrm{T}}^{\mathrm{miss}}$) are used to estimate the associated uncertainties. These calibrations are then added to the MC samples as e. g. lepton/photon reconstruction efficiencies, JES, Jet Energy Resolution (JER), b-tagging efficiencies, $E_{\mathrm{T}}^{\mathrm{miss}}$ reconstruction, etc. A list of such non-negligible uncertainties for this analysis is given here:

JES and JER: the JES and JER arise from the measured momentum of jets, which need to be calibrated to the right energy scale [127]. The uncertainty on the JES is p_{T} and pseudorapidity (η) dependent, and is evaluated in MC simulation using a set of grouped variations consisting of six Nuisance Parameters (NPs), which describe how the observed property is affected by the uncertainties. Three η intercalibration non-closure uncertainties and three additional uncertainties, the combination of all the remaining parameters ($\mathcal{O}(100)$), are used as a NP each, for a total of six NPs. The uncertainty due to the JER is evaluated by smearing the jet energy using a simple set of systematic variations with 8 NPs.

Hadronically decaying taus: τ-lepton energy scale [128], resolution, and identification are one of the main sources of experimental systematic uncertainties in the SRs because of the requirement of at least two of these objects to be present in the final selection. Uncertainties on the τ-lepton JES are evaluated using SFs and corresponding uncertainties on the efficiency of reconstructing a jet, identifying it as a tau jet, and for passing the electron OR are taken into account.

Light leptons: lepton reconstruction, identification and isolation efficiencies have contributions to the background. For electrons, uncertainties on the electron energy scale and resolution are evaluated by scaling and smearing the energies of electrons in simulated events. Similarly, muon uncertainties originating from the muon energy resolution, isolation, reconstruction and momentum scale are evaluated by modifying the energies of muons in simulated events.

***b*-Jets:** SF uncertainties in b-tagging depend on the kinematics of the jet and on the jet flavour. The efficiency of correctly identifying a jet originating from a b-quark, as well as the efficiency of incorrectly tagging a jet originating from a c or light quark are modelled using three uncertainty variations to the b-jet weight called *nominal*, *up*, and *down*, which are propagated to the SFs for b-jets.

$E_{\mathrm{T}}^{\mathrm{miss}}$: uncertainties on the missing transverse momentum are evaluated by propagating the uncertainties of the constituent objects. There is a residual uncertainty due to the "soft-term", which sums up the tracks not associated to any of the physics objects described above. Scale and resolution uncertainties for this term are evaluated by modifying it accordingly, and evaluating the effect of this change on the event selection.

Pile-up: the uncertainty on the distribution of the number of simultaneous interactions in each pp collision is performed by varying $\langle\mu\rangle$ by ±4% and using the modified parameter to perform a pile-up re-weighting procedure to match the distributions of the number of reconstructed vertices observed in data [129].

Trigger: τ-lepton trigger SFs are a source of uncertainty that is implemented using results taken from dedicated measurements [130] and are included with the τ-lepton identification uncertainty.

Luminosity: an uncertainty in the integrated luminosity of ±2.0% is applied for the combined 2015, 2016, 2017, and 2018 dataset [131].

The sources of uncertainties associated to the determination of the multijet background via the ABCD method are: the correlation among the τ-lepton identification, the charge requirement, and the kinematic variable m_{T2}, the limited number of events in the CRs, and the subtraction of the other SM backgrounds. The systematic uncertainty in the correlation is determined by comparing the transfer factor described in Section 4.6.3, between CR-B to CR-C to that of VR-E to VR-F.

Table 4.9: The postfit relative systematic uncertainty (%) in the background estimate (signal reference points) in the Low-mass and High-mass SRs from the leading sources at top (bottom). Uncertainties from different sources in the background estimates may be correlated, and do not necessarily add in quadrature to the total uncertainty.

Source of systematic uncertainty on background prediction	Low-mass SR [%]	High-mass SR [%]
Statistical uncertainty of MC samples	11	21
τ-lepton identification and energy scale	19	10
Normalization uncertainties of multijet background	12	8
Multijet estimation	4	10
Jet energy scale and resolution	5	8
E_T^{miss} soft-term resolution and scale	2	2
Source of systematic uncertainty on signal prediction	**Low-mass SR [%]**	**High-mass SR [%]**
$m(\tilde{\tau}, \tilde{\chi}_1^0)$ [GeV]	(120,1)	(280,1)
τ-lepton identification and energy scale	29	14
Statistical uncertainty of MC samples	6	10
Jet energy scale and resolution	3	2
E_T^{miss} soft-term resolution and scale	3	<1

Table 4.9 summarises the main sources of experimental systematic uncertainties in the SM background estimates for the Low-mass and High-mass SRs, where the statistical uncertainty of the event yields in the CRs is propagated to the SRs as a systematic uncertainty. The dominant uncertainties in the SRs are the statistical uncertainty of the MC prediction (11%-21%),

τ-lepton identification and energy scale (10%-19%), and multijet background normalization (8%-12%). The total uncertainty in the signal yields for the SUSY reference points is about 17%-31% and are dominated by the τ-lepton identification and energy scale (14%-29%), and the statistical uncertainty of the signal MC predictions (6%-20%).

4.7.2 Theory Uncertainties

The theoretical uncertainties are evaluated by considering variations with respect to the nominal settings and choices for the event generation. The three main sources of theoretical uncertainties considered for this analysis are: the uncertainty associated to missing higher order corrections to the cross-section, the uncertainty on PDFs, and the uncertainty on the running strong coupling constant (α_S). The *re-normalization scale* (μ_R) gives the dependence for α_S and is set to equal the momentum transfer Q of the scattering. The *factorization scale* (μ_F) refers to the separation of the hard scattering QCD effects from the PDF. A *scale variation*, i. e. a variation of the re-normalisation and factorisation scales by some fixed factors, is generally used to estimate the uncertainty associated to the missing higher order in the perturbative expansion of the partonic cross section. The uncertainty on the PDFs will change accordingly to experimental uncertainties introduced in the datasets used in the PDF fits. Two sets of PDFs are compared to the nominal PDF to check the spread between the different PDF sets and their uncertainties. The strong coupling constant is determined experimentally from the combination of different datasets and its value is quoted at the scale of the Z boson mass. The associated uncertainties are thus a combination of the experimental errors and the truncation of the theoretical value at a fixed order in perturbation theory.

Each systematic uncertainty i is described as a NP (θ_i) that parametrizes the impact on the parameter(s) of interest (i. e. rate of signal process, normalization factors, etc.). Therefore, they are described as variations from the nominal, e. g. $\theta_i = \pm 1$ for $\pm 1\sigma$, where 1σ means one standard deviation.

The recipes used for the estimation of the theoretical uncertainties for the main backgrounds are shown below.

Multiboson: The prescription used for the estimation of the uncertainties for the higher order corrections requires the usage of the factorization and re-normalization scale variations. These are implemented as seven weights in the nominal sample corresponding to the variations of the QCD factorization and re-nomalization scales in the matrix element by a factor of 2 and 0.5, avoiding variations in the opposite direction [132]. These uncertainties are then combined by taking the envelope of all the uncertainties. Uncertainties on the PDF+α_s are computed following the PDF4LHC prescriptions, that can be found in Ref. [133], and include 100 variations as well as variations in the central value of the PDF. A global 6% uncertainty due to scale and PDF should be applied to $WW/WZ/ZZ$ cross sections.

$t\bar{t}$, single top: Uncertainties associated to the parton shower, which affect the event yield of the $t\bar{t}$ background, are evaluated by comparing the predictions of POWHEG+PYTHIA8 and POWHEG+HERWIG7. The uncertainty associated to the Initial State Radiation (ISR)/Final State Radiation (FSR) are also evaluated by comparing the predictions of POWHEG+PYTHIA8 with two samples with varied radiation settings. These uncertainties are implemented as a NP for each scale variation and process; they are not constraint. The inclusive cross section uncertainty at Next-to-Next-to-Leading-Order + Next-to-Next-to-Leading Logarithm Accuracy (NNLO+NNLL) is 6%.

W,Z+jets: Similarly to the multi boson case, W/Z + jets modelling include uncertainties from the factorization and re-normalization scales, computed using different variations implemented as weights in the nominal sample. Uncertainties affecting the SHERPA event generator predictions are also estimated using the PDF sets following the PDF4LHC recommendations.

SUSY signal: signal cross sections are calculated at NLO + NLL using the resummino code from Ref. [106] with two sets of PDFs (CTEQ6.6 and MSTW2008NLO90CL). Only the cross-section uncertainty is taken into account for signal processes and it varies from 2 to 3% for the considered SUSY models.

Table 4.10: Fractional variations from nominal of theoretical uncertainties in Low-mass SR and High-mass SR.

	Low-mass SR					
	Combined $\{\mu_R,\mu_F\}$ up / down	μ_R up / down	μ_F up / down	α_S up / down	PDF up / down	alt. PDF up / down
Higgs	0.193 0.116	0.103 0.115	0.027 0.037	0.091 0.036	0.017 0.013	0.016 0.012
Multiboson	0.248 0.168	0.237 0.161	0.010 0.006	0.026 0.044	0.020 0.020	0.018 0.001
Top	0.126 0.125	0.084 0.076	0.065 0.055	0.047 0.039	0.025 0.031	0.024 0.030
W+jets	0.355 0.221	0.353 0.219	0.012 0.011	0.038 0.049	0.023 0.026	0.015 0.008
Z+jets	0.362 0.232	0.359 0.229	0.009 0.009	0.061 0.067	0.027 0.031	0.005 0.001
	High-mass SR					
	Combined $\{\mu_R,\mu_F\}$ up / down	μ_R up / down	μ_F up / down	α_S up / down	PDF up / down	alt. PDF up / down
Higgs	0.134 0.099	0.093 0.101	0.017 0.013	0.056 0.018	0.015 0.011	0.014 0.010
Multiboson	0.270 0.195	0.257 0.183	0.014 0.013	0.037 0.070	0.022 0.023	0.016 0.000
Top	0.152 0.142	0.113 0.075	0.039 0.043	0.045 0.033	0.062 0.030	0.027 0.029
Wjets	0.411 0.256	0.396 0.246	0.014 0.012	0.128 0.094	0.031 0.030	0.006 0.012
Zjets	0.391 0.246	0.375 0.233	0.016 0.013	0.058 0.053	0.031 0.028	0.011 0.002

The theoretical uncertainties determined for the Low-mass and High-mass SRs for the most relevant SM backgrounds are shown in Table 4.10. The uncertainties are shown as fractional values for the *up* and *down* variations from the nominal value of interest. The uncertainties associated to the high order corrections to the cross section are shown by the combined renormalisation and factorisation scale, as well as with the individual uncertainties to the μ_R and μ_F. The PDF uncertainties are also shown for the alternative PDF set for comparison.

In addition to the theoretical uncertainties derived for the SRs, the same uncertainties are derived for the WVR, WCR, and transfer factors from the WCR to the WVR, and from the WCR to the High-mass and Low-mass SRs. The systematic uncertainty on the transfer factor is defined as

$$\Delta TF_{Syst}^{Process} = \frac{TF_{Syst}^{Variation} - TF_{Syst}^{Nominal}}{TF_{Syst}^{Nominal}} = \frac{TF_{Syst}^{Variation}}{TF_{Syst}^{Nominal}} - 1, \tag{4.4}$$

where $TF_{Syst}^{Nominal}$ and $TF_{Syst}^{Variation}$ are the transfer factors derived using the nominal and varied property for the studied uncertainty, respectively. The full set of tables showing the fractional variations from nominal for the theoretical uncertainties for these control and validation regions, as well as corresponding transfer factors can be found in Appendix B.

The derived theoretical uncertainties are used, in combination with the experimental uncertainties described above, in the statistical interpretation of the results performed using the profile likelihood method, that will be discussed in more detail below in section 4.8.

4.8 Statistical analysis

A statistical tool able to take into account all the derived uncertainties (statistical and systematic) is required to produce quantitative results. The statistical tool used for the interpretation of the results of this analysis is performed using the profile likelihood method implementation in the HistFitter framework [134], a common framework used in ATLAS. This framework is used to implement the background-only fit with CRs described in Section 4.6.3 and statistical uncertainties to establish the compatibility of the results obtained from the data analysis to the given hypothesis.

Once the CRs and VRs are constructed and satisfactory agreement is found between the normalised background predictions and the observed data in the VRs, the background predictions can be extrapolated to the SRs. The observation of predicted background with observed data in the SRs is a process generally referred to as *unblinding*. Assuming proper background estimation has occurred, there are only two possible outcomes for the unblinding procedure: an excess of data is observed compared to the predicted background, or there is perfect agreement to the predicted SM background.

4.8.1 Likelihood Construction

Key ingredients for the fitting procedure are the transfer factors described in some detail in Section 4.6.3, for the multijet and W + jets background. The transfer factors allow for the normalization of each SM background processes between each SRs and CR. The estimated number of background events in the SR ($N_B(SR)$) is therefore given by number of observed events in the CR ($N_p^{obs.}(CR)$) and the TF, which is the ratio between the raw number MC events in the SR ($N_p^{MC}(SR)$) and CR, ($N_p^{MC}(CR)$) for process p:

$$N_B(SR) = N_p^{obs.}(CR) \times \left[\frac{N_p^{MC}(SR)}{N_p^{MC}(CR)} \right] = \mu_p \times N_p^{MC}(SR) \tag{4.5}$$

where μ_p is the ratio between the observed and estimated background yields obtained in the fit to data, and is used as a normalization factor for background. Similarly, the number of estimated signal process (s) events in the SR is given by $N_S(SR) = \mu_s \times N_s^{MC}(SR)$ where μ_s is the signal strength, while $N_s^{MC}(SR)$ is the expected signal yield in the signal region SR. The total expected number of events in signal region SR is, thus, given as:

$$N_{SR} = \mu_s N_s + \sum_i \mu_b^i N_b^i, \tag{4.6}$$

where N_s and N_b^i are the number of expected signal and background MC yields for the i^{th} background in the SR, respectively. Therefore, the background normalization factor, μ_b, is used to normalise the SM background raw un-normalised MC estimates to data in the SR, while the signal strength, μ_s, provides a scale factor associated to the theoretical strength of the signal model in the given region, determined using the profile likelihood that will be described in more detail below. The effect of systematic uncertainties on the signal and background yields are implemented in the above equation as NPs associated to the signal (θ_s^j) and i^{th} background (θ_b^{ij}), respectively:

$$N_{SR} = \mu_s N_s (1 + \sum_j \theta_s^j \sigma_s^j) + \sum_i \mu_b^i N_b^i (1 + \sum_j \theta_b^j \sigma_b^{ij}). \tag{4.7}$$

The nuisance parameters are given as variations from the nominal yields (i. e. $\theta = 0$) by some factor of a standard deviation (θ), so that when the variation from nominal is zero in both signal and background, equation 4.7 reverts to equation 4.6.

The SM background normalization factors, μ_b, signal strength μ_s and nuisance parameters θ are extracted from the analysis using a likelihood function, $\mathcal{L}$, that describes the number of events observed in the SR and/or CR as the combination of Poisson distributions and of additional distributions that implement the constraints on systematic uncertainties. The likelihood function can thus be written as:

$$\begin{aligned} \mathcal{L}\left(N_{\text{obs}}, \theta^0 | \mu_{\text{s}}, \mu_{\text{b}}, \theta\right) &= P_{\text{SR}} \times P_{\text{CR}} \times C_{\text{syst}} \\ &= P\left(N_{\text{SR}}^{\text{obs}} | N_{\text{SR}}\left(\mu_{\text{s}}, \mu_{\text{b}}, \theta\right)\right) \times \prod_{i \in \text{CR}} P\left(N_i^{\text{obs}} | N_i\left(\mu_{\text{s}}, \mu_{\text{b}}, \theta\right)\right) \times C_{\text{syst}}(\boldsymbol{\theta^0}, \boldsymbol{\theta}) \end{aligned} \tag{4.8}$$

where N_{obs} is the observed yield for a given region (denoted by the subscript). The impact of systematic uncertainties is included in the probability density function $C_{\text{syst}}(\boldsymbol{\theta^0}, \boldsymbol{\theta})$, where

$\boldsymbol{\theta}^0$ are the central values of the auxiliary measurements, which are set to zero for the fitting procedure around which $\boldsymbol{\theta}$ can be varied when, for instance, maximising the likelihood. If the systematics as assumed to be subject to Gaussian fluctuations the term take the form:

$$C_{\text{syst}}(\boldsymbol{\theta}^0, \boldsymbol{\theta}) = \prod_{j \in S} G(\theta_j^0 - \theta_j), \tag{4.9}$$

where S is the full set of systematic uncertainties considered for the auxiliary measurements (θ_j^0) by the fluctuating nuisance parameter (θ_j). More details can be found in Ref. [134, 135]. Once the likelihood equation 4.8 is constructed, it is possible to obtain the relevant SM background normalization parameters via a Maximum Likelihood Estimation (MLE), as discussed in detail in Ref. [136]. This is performed in HISTFITTER [134] interfaced with the HISTFACTORY [135] package.

4.8.2 Hypothesis testing

The BSM signal discovery or exclusion is determined using a statistical procedure known as *statistical hypothesis testing* [137]. For this type of analysis the null hypothesis H_0, i. e. the hypothesis to be tested against the alternative H_1, is chosen to be background-only, while the alternative is the signal-plus-background. The probability of an observation to be a number of Gaussian standard deviations away from the null hypothesis is given by the significance Z, given by:

$$Z = \Phi^{-1}(1 - p), \tag{4.10}$$

where Φ^{-1} is the inverse of the cumulative Gaussian distribution and p is the probability (p-value) of the observation under H_0. Equation 4.8 can be condensed by referring to the signal and background model (and associated nuisance parameters) as $\boldsymbol{\theta}$, and the likelihood as $\mathcal{L}(\mu_s, \hat{\hat{\theta}})$. In turn, a statistic test can be obtained as follows:

$$\lambda(\mu_s) = \frac{\mathcal{L}(\mu_s, \hat{\hat{\theta}})}{\mathcal{L}(\mu_s, \hat{\theta})}, \tag{4.11}$$

where the denominator is maximised over all parameters and is absolute, and the numerator is maximised for a given value of the signal strength μ_s parameter. The background-only (null hypothesis) corresponds to $\mu_s = 0$ (i. e. SM without SUSY), while $\mu_s = 1$ corresponds to alternative hypothesis which is for the presence of the SUSY model being tested. Therefore, the larger the λ values the better the agreement of the data with the hypothesis being tested (where $0 < \lambda < 1$). It is possible to redefine Equation 4.11 and assign it as our test statistic:

$$q = -\ln(\lambda(\mu_s)), \tag{4.12}$$

for the HISTFITTER software to randomly generate thousands of pseudo-data from Poisson distributions, towards the calculation of the p-value. This is done for all the models of μ_s that are being tested, which results in independent p-values for every hypothesis, including background-only.

To claim discovery (evidence) against the background-only hypothesis a value of $Z = 5$ ($Z = 3$) is required, which corresponds to a p-value of 2.87×10^{-7} (0.0013). To exclude a given signal model a significance of 1.54σ, which corresponds to $p = 0.05$ is used instead.

4.8.3 Exclusion limits

The p-values can also be defined as a CL, an alternative FoM to describe the confidence at which the measurements have been performed [138]. A signal model is excluded if the p-value between the signal hypothesis and observed data (p_{s+b}) is < 0.05. In confidence level terms, this corresponds to a 95% CL. This approach however suffers from falsely excluding models for which the analysis has little or no sensitivity to. To account for this effect, a new confidence level is used, with which, on top of the signal and background p-value (p_{s+b}), it accounts for the p-value of the background only hypothesis (p_b):

$$CL_s = \frac{p_{s+b}}{1 - p_b}. \tag{4.13}$$

Using this CL method, when the discovery and exclusion test statistic show similar distributions, the nominator and denominator of Equation 4.13 will be of the same order, which guarantees that signals are not excluded.

4.8.4 Discovery limits

Model independent limits are used to show how compatible the observed data is with the background-only hypothesis, and are generally referred to as *Discovery Limits*. These limits are particularly significant when estimating the sensitivity to new physics in regions with excess data compared to the estimated SM background. The limits include:

Background upper limit: on the number of events that can be observed before compatibility with SM breaks down.

Signal upper limit: on the visible signal cross section defined by the signal cross section, the detector acceptance, and the analysis efficiency.

A scan of μ_s in each SR is performed independently, starting with large excluded values, and reducing until p-value = 0.05, to obtain the visible signal cross sections limits. μ_s therefore acts a a dummy signal to test scenarios not included in this thesis.

4.8.5 Performing the fits

As previously discussed, the interpretation of the results is performed using a profile likelihood method implemented in the HistFitter framework [134]. The fit parameters are determined by maximising the product of the Poisson probability functions and the Gaussian probability constraints for the nuisance parameters. For the combined Low-mass and High-mass SRs, three types of fits are performed:

background-only: uses the observed events and expected SM background contributions in the CR-A and WCR as well as the TF as inputs to the fit. The normalizations of the W + jets and multijet contributions are used as free parameters in the fit. The signal is assumed to be absent.

model-independent: data event yields and SM background estimates with associated uncertainties are combined in the *model-independent limit* fit in a given SR, to test whether any new physics contributes to the SR. The background yields and uncertainties are taken from the background only fit results.

model-dependent SUSY signal is allowed to populate both the SRs and CRs, and is scaled by a freely floating signal normalization factor in the fit. Background normalization factors are also determined at the same time in the fit. If the upper limit on the signal normalization factor obtained in the fit is smaller than unity then the SUSY model is rejected at 95% CL.

The result of the background only fit is presented in Table 4.11, which shows a summary of the observed, expected, and fitted events in the High-mass and Low-mass multijet CRs as well as the CR and VR used for W + jets SM background estimation. The fitting shows comparable results with the observed event multiplicity in all the CRs as well as in the WVR, which gives great confidence in the modelling of the relevant backgrounds and their estimations. The SRs can therefore be unblinded, and the data yields in the SRs can be compared to the prediction.

Table 4.11: Observed, expected, and fitted event yields of SM processes in the multijet CRs and W + jets CR and VR. The fitted event yields are given after the background-only fit. Uncertainties correspond to the sum in quadrature of statistical and systematic uncertainties.

	Multijet CR-A Low-mass	**Multijet CR-A High-mass**	**WCR**	**WVR**
Observed	72	27	1099	552
Total SM (fit)	72.05 ± 8.41	26.97 ± 4.92	1099.10 ± 33.14	545.46 ± 134.13
Multiboson	1.43 ± 0.56	1.88 ± 0.98	63.19 ± 20.80	36.55 ± 12.00
W+jets	12.96 ± 4.31	$4.31^{+7.26}_{-4.31}$	853.86 ± 67.29	365.60 ± 130.02
Top	2.65 ± 0.92	3.31 ± 1.61	167.28 ± 41.34	115.78 ± 32.18
Z+jets	$0.25^{+1.41}_{-0.25}$	1.47 ± 0.69	12.78 ± 7.26	27.04 ± 20.43
Higgs	$0.01^{+0.34}_{-0.01}$	0.01 ± 0.01	$1.05^{+1.77}_{-1.05}$	$0.48^{+1.01}_{-0.48}$
Multijet	54.74 ± 9.86	15.99 ± 6.28	0.93 ± 0.93	0.00 ± 0.00
Total SM (exp.)	72.00	27.00	1184.34	581.27

4.9 Results

In this section the results for the search of direct production of $\tilde{\tau}$ particles in final states with two hadronically decaying τ-leptons and $E_{\mathrm{T}}^{\mathrm{miss}}$ are presented using 139 fb^{-1} of data collected with the ATLAS experiment at the LHC, at a centre-of-mass energy of $\sqrt{s} = 13$ TeV. The CRs and VRs used for the estimation SM background, as well as the SRs used to isolate the SUSY signal of

interest have been previously discussed in Sections 4.6.3 and 4.6.2, respectively. The statistical strategies adopted have also been discussed in Section 4.8.

The fitted, expected, and observed event yields in the Low-mass and High-mass SRs are summarised in Table 4.12. In both signal regions, observation and background predictions are found to be compatible within uncertainties. The most dominant background contribution is found to be from the multijet background process, which contributes to ~ 50% (~ 30%) of all background processes in the Low-mass (High-mass) SR. This is further illustrated by Figure 4.14, which shows the m_{T2} distributions for data, expected SM backgrounds, and the SUSY reference signal points defined in Section 4.2. The background distributions in these plots have been scaled to the values determined from the simultaneous fit. It is clear that the distributions show no statistically significant excess in the data compared to the SM background in either SRs. The observations and predictions are thus fully compatible within uncertainties.

Table 4.12: Observed, expected, and fitted event yields of SM processes in the Low-mass and High-mass SRs. The fitted event yields are given after the background-only fit. Uncertainties correspond to the sum in quadrature of statistical and systematic uncertainties.

	SR Low-mass	**SR High-mass**
Observed	10	7
Total SM (fit)	5.97 ± 1.67	10.17 ± 3.47
Multiboson	1.36 ± 0.78	2.57 ± 1.23
W+jets	1.49 ± 0.69	2.51 ± 2.25
Top	$0.04^{+0.80}_{-0.04}$	1.96 ± 0.54
Z+jets	$0.44^{+0.49}_{-0.44}$	$0.04^{+0.13}_{-0.04}$
Higgs	$0.01^{+0.02}_{-0.01}$	0.00 ± 0.00
Multijet	2.63 ± 0.74	3.09 ± 1.40
Total SM (exp.)	6.06	10.34

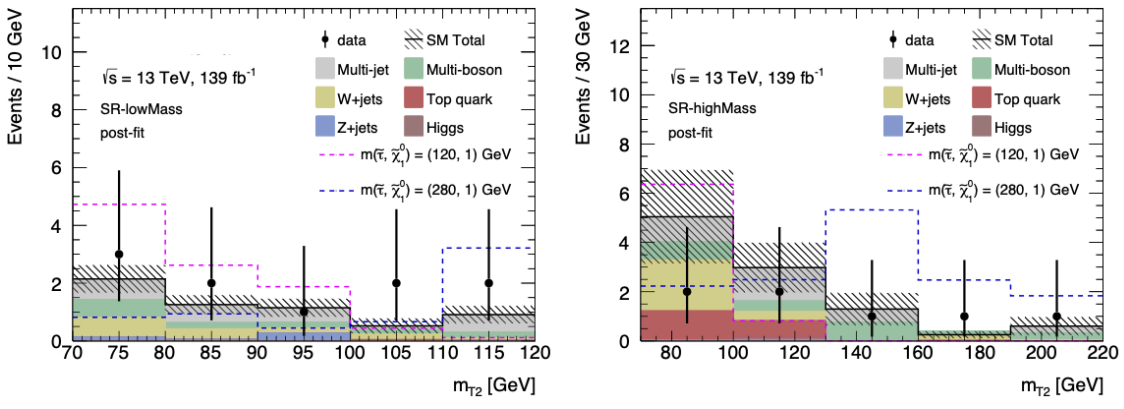

(a) (b)

Figure 4.14: Post-fit m_{T2} distribution for Low-mass SR (left) and High-mass SR (right). The stacked histograms show the expected SM background. Contribution from W + jets and multijet background events are scaled with the corresponding normalization factors derived from the background-only fit. The SUSY signal point distributions are shown, for reference, as dashed lines.

Individual model-independent fits of the Low-mass SR and High-mass SR on the visible BSM cross section are used to derive the p-value for the background to fluctuate to the observed yields if no signal is present $p(s = 0)$ (p_0) and are reported in Table 4.13. No significant excess is observed for either the High-mass or Low-mass SRs, with only a small ($< 2\sigma$) over-fluctuation in the Low-mass SR corresponding to a p_0-value of 0.11. In case of an under-fluctuation, the p-value is defaulted at 0.5. The observed and expected 95% CL upper limits on the visible BSM cross section (σ^{95}_{vis}) derived from the same model-independent fits are also presented. Signal models are excluded if the CL is less then 0.05

Table 4.13: Observed and expected event yields for the SUSY $m(\tilde{\tau})$ 120 GeV and 280 GeV with $m(\tilde{\chi}^0_1)$ =1 GeV for all SRs considered in this analysis. The uncertainties include experimental, theoretical and statistical uncertainties. Table also reports the observed and expected 95% CL: upper limits on the visible BSM cross-section (σ^{95}_{vis}) and the number of signal events (S^{95}). The discovery p-value (p_0) is also reported. Values of $p_0 > 0.5$ are truncated at $p_0 = 0.5$.

	SR Low-mass	**SR High-mass**
$m(\tilde{\tau}, \tilde{\chi}^0_1) = (120, 1)$ GeV	9.8 ± 4.0	7.2 ± 2.2
$m(\tilde{\tau}, \tilde{\chi}^0_1) = (280, 1)$ GeV	6.1 ± 1.5	14.4 ± 2.5
p_0-value (Z)	0.11 (1.23)	0.50 (0.00)
S^{95}_{exp}	$7.7^{+3.5}_{-2.0}$	$0.9^{+3.5}_{-2.7}$
S^{95}_{obs}	11.6	7.3
Expected σ^{95}_{vis} [fb]	$0.055^{+0.025}_{-0.014}$	$0.065^{+0.025}_{-0.019}$
Observed σ^{95}_{vis} [fb]	0.08	0.05

4.10 Interpretation

In the absence of any significant excess over the expected SM background, exclusion limits at 95% CL are set on the masses of the $\tilde{\tau}$ and $\tilde{\chi}^0_1$ using the model-dependent limit fit. The exclusion limits are set using the observed and expected number of events in the signal regions derived in the analysis. Figure 4.15 shows the exclusion limits for the combined Low-mass and High-mass SRs for the simplified SUSY model mentioned in Section 4.2, using a step size of 10 GeV to scan the full parameter space. The solid lines show the observed exclusion contours, while the dash lines represent the expected exclusion limits. The yellow band around the expected limit is used to represent the $\pm 1\sigma$ variations, which include all uncertainties except for theoretical uncertainties in the signal cross-section. The sensitivity to $\pm 1\sigma$ variations of the theoretical uncertainties in the signal cross-section are shown by the dotted lines around the observed limit. Stau masses from 120 GeV to 390 GeV are excluded for a massless lightest neutralino in the scenario of combined $\tilde{\tau}_{\text{L}}$ and $\tilde{\tau}_{\text{R}}$ ($\tilde{\tau}_{L+R}\tilde{\tau}_{L+R}$). The exclusion limits for the individual left-handed and right-handed $\tilde{\tau}$ production have also been derived and are shown in Figure 4.16. For $\tilde{\tau}_{\text{L}}$ pair production only ($\tilde{\tau}_{\text{L}}\tilde{\tau}_{\text{L}}$), the exclusion limit extends from 155 GeV to 310 GeV. For the counterpart $\tilde{\tau}_{\text{R}}$ pair production ($\tilde{\tau}_{\text{R}}\tilde{\tau}_{\text{R}}$) no significant observed exclusion limit was set. While the $\tilde{\tau}_{\text{L}}$ pairs have a higher production cross-section, the $\tilde{\tau}_{\text{R}}$ have a higher efficiency times acceptance due to kinematic differences in the resulting decay products. These limits

extend significantly beyond the previous found results in the high $\tilde{\tau}$ mass regions, shown in References [54, 139–141].

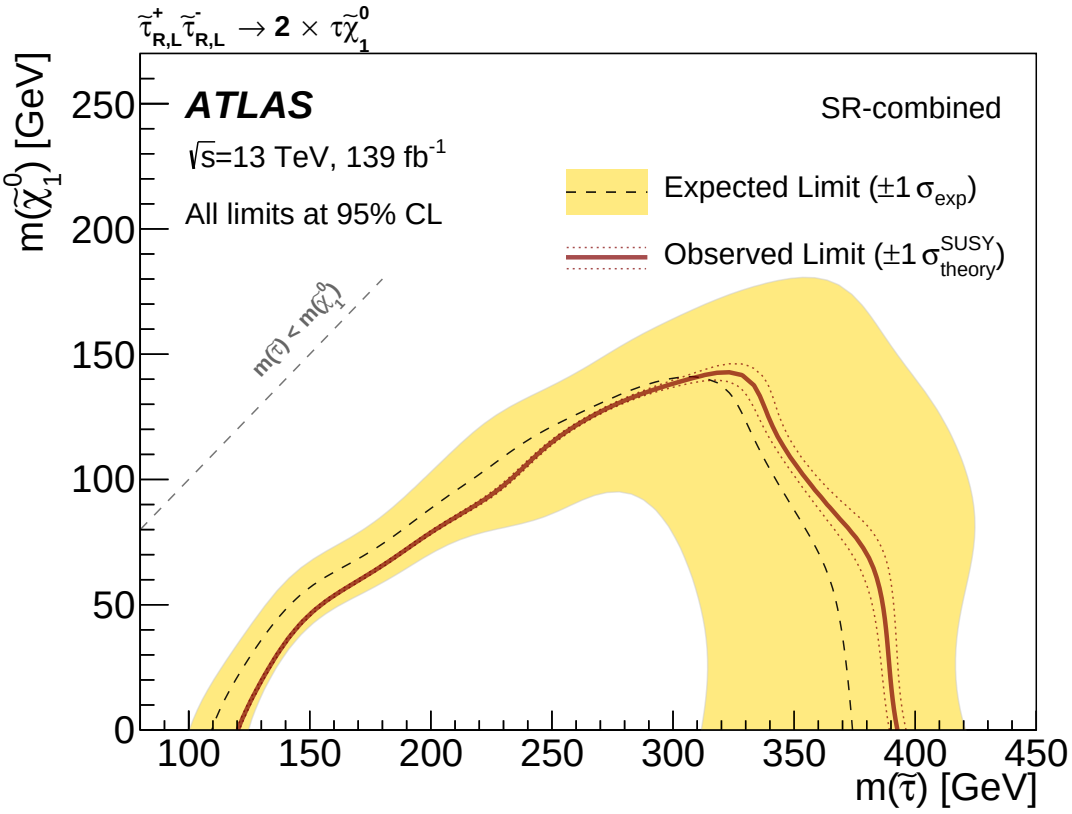

Figure 4.15: 95% CL exclusion limits for simplified models with direct $\tilde{\tau}$ pair production in the combined High-mass and Low-mass SRs.

4.11 Summary

In this chapter the strategy and methodology used for the search for the direct production of the supersymmetric partner of the τ-lepton ($\tilde{\tau}$) from pp collisions at the LHC is presented. The final state signature of the SUSY process studied by this analysis is composed of two hadronically decaying τ-leptons and two $\tilde{\chi}^0_1$ ($pp \rightarrow \tilde{\tau}\tilde{\tau}$, ($\tilde{\tau} \rightarrow \tau\tilde{\chi}^0_1$)), which is not visible in the ATLAS detector and is, thus, considered as $E_{\mathrm{T}}^{\mathrm{miss}}$. The construction and optimization of the two orthogonal signal regions used to tackle high and low SUSY signal mass points, via the application of two different di-tau triggers (*asymmetric di-tau* and *di-tau*+$E_{\mathrm{T}}^{\mathrm{miss}}$) whose performance studies and SFs derivation was done by the author, is presented. This is followed by a description of the main sources of SM backgrounds that pollute the SRs, as well as the methods and CRs used to estimate their contributions to number of events observed in the SRs. The main sources of SM background processes with corresponding CRs and VRs employed is summarised below;

***W*+jets:** the source of this background is derived from the mis-identification of one τ-lepton. The W + jets contribution is estimated using a dedicated WCR enriched in W boson decay events, which is in turn validated in an orthogonal WVR.

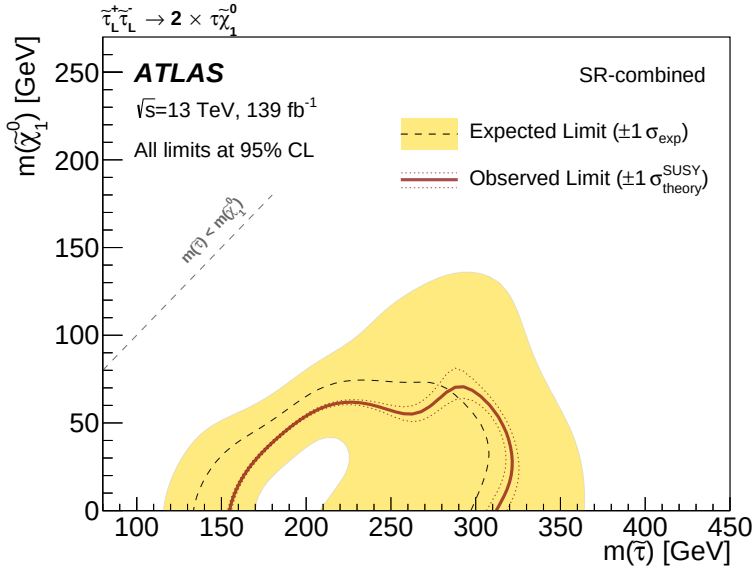

(a)

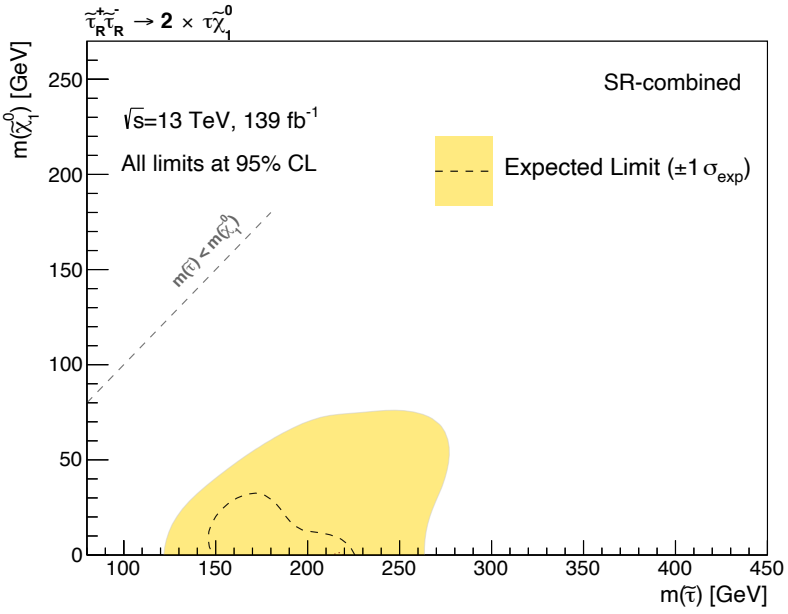

(b)

Figure 4.16: 95% CL exclusion limits for simplified models with direct (a) $\tilde{\tau}_L\tilde{\tau}_L$ and (b) $\tilde{\tau}_R\tilde{\tau}_R$ pair production in the combined High-mass and Low-mass SRs.

Multijet: these events produce the highest background multiplicity in the constructed SR, from jets being mis-identified as τ-leptons, due to the process's high cross-section. The contribution to the SR is estimated from a set of *transfer factors* derived using a combination of CRs and VRs named the *ABCD method*.

Irreducible: these are the SM background processes which produce final states identical to the SUSY process final states. These include processes such as Z + jets, $t\bar{t}$, single top, $t\bar{t}$+V, and multiboson production. The contribution of these SM background to the SR event yields is estimated using MC simulated samples in dedicated VRs.

Systematic uncertainties are separated into experimental and theory uncertainties, the latter of which have been studied and derived by the author, and are implemented into the fitting procedures used to retrieve the background scale factors and discovery limits. No statistically significant excess in data collected was found in either High-mass or Low-mass SRs. Therefore, exclusion limits on the mass of the $\tilde{\tau}$ and $\tilde{\chi}_1^0$ have been extracted. This analysis has been presented at several conferences and has been published in the *Physical Review D* journal, see Reference [2].

FAKE TAU ESTIMATION

5

Standing at the crossroads trying to read the signs, to tell me which way I should go, to find the answer.

Eric Clapton

In this chapter the identification and object reconstruction efficiency of hadronically decaying tau particles (τ_{had}) will be presented. A brief introduction to the τ_{had} object and the motivation for its accurate reconstruction in the ATLAS detector, together with the expected challenges, is discussed in Section 5.1. An in depth explanation of the Fake Factor (FF) method – one of the methods used for the estimation of the τ_{had} faking objects – will be presented in Section 5.2. Section 5.3 describes a new method currently being developed within the ATLAS collaboration that uses the principles of the FF method, described in the former section, to estimate the number of fake τ_{had} objects for any given τ_{had}-abundant selection region, and the tool under development that uses this method to derive the corresponding FF values for this arbitrary region. In Section 5.4 the derivation of the different data regions used by the tool for interpolation is discussed. Sections 5.5 and 5.6 discuss the MC FF tool inputs and jet width templates derivation used for proof of concept, respectively. In Section 5.7, a significant portion of the author work on the derivation of the inputs for the Tau Fake Factor Tool (TFFT) and jet width distribution studies is presented. The author has had a leading contribution in these studies, in particular in the MC inputs, the derivation of the sample structures, the jet width distributions, and of the derived FF values. In Section 5.8, a brief description of the fitting procedure used by the tool and the expected future developments is given. Finally, Section 5.9 gives a summary of the discussed project, and concludes this chapter by highlighting the main points of interest investigated.

5.1 Fake taus

As discussed in Section 2.4, τ-leptons can decay hadronically into one or three charged pions 72% and 22% of the times, respectively. Jets originating from other background processes can

often be mis-identified as τ-leptons in the ATLAS experiment.

The main background to hadronic τ-lepton decay comes from jets of energetic hadrons produced from the fragmentation of quarks and gluons, present both at trigger level as well as during the event reconstruction. The narrow shower in the calorimeter, the distinct number of tracks, and displaced τ-lepton decay vertex are the variables used to discriminate τ_{had} lepton candidates from jets.

Final states with hadronic τ-lepton decays are very important to the ATLAS physics program, as well as to the analysis discussed in Chapter 4. The reconstruction and identification algorithms discussed in Chapter 4 will have a direct and significant impact on the quark to gluon ratio that populate the reconstructed fake-τ objects.

5.2 Fake Factor method

After the τ_{had} identification with either BDT or RNN techniques, there are still large numbers of misidentified τ_{had} objects (fake-τ) remaining. MC simulations are insufficient to properly model the fake-τ background with large enough statistics. This is due to the large cross section of jet production at the LHC relative to the τ production and the subsequent difficulty in modelling jet shower shape and track multiplicity to match that of a true τ jet.

Data-driven methods, such as the FF method described here, are therefore a very powerful tool towards the estimation of fake-τ multiplicities. In the FF method, a correction factor is applied to data in a particular SR, in order to estimate the fake-τ background in that region. This correction factor, normally referred to as the Fake Factor value, is measured in a dedicated CR that is abundant in fake-τ, and is defined as:

$$\mathrm{FF}(i) = \frac{N^{CR\text{-data}}_{\tau_{had}}(i)}{N^{CR\text{-data}}_{\text{anti}-\tau_{had}}(i)}, \tag{5.1}$$

where $N^{CR}_{\tau_{had}}$ is the number of visible τ_{had} objects in data that pass the identifier algorithm working point of interest (BDT or RNN) in the given CR and $N^{CR}_{\text{anti}-\tau_{had}}$ is the number that fail the same working point of interest, also in data. The index, i, refers to the bin where the FF is calculated. Typical choices of binning are in p_{T}, η and number of prongs. Assuming that the SR of interest requires the visible τ_{had} objects to pass a given identification work point, the number of fake-τ leptons in that region is then calculated by:

$$N^{\tau_{had}}_{fakes}(i) = N_{\text{anti}-\tau_{had}}(i) \times FF(i), \tag{5.2}$$

where $N_{\text{anti}-\tau_{had}}$ is the number of visible τ_{had} objects in data that fail the identification working point in the SR. It is important to note that $N^{CR}_{\tau_{had}}$, $N^{CR}_{\text{anti}-\tau_{had}}$, and $N_{\text{anti}-\tau_{had}}$ have the visible τ_{had} truth-matched to a true τ-lepton performed in MC samples and subtracted from the τ_{had} multiplicity. The truth matching procedure used to perform this step will be described in more detail in the next section. This results in the transformation of Equation 5.1 to:

$$\mathrm{FF}(i) = \frac{N^{CR}_{\tau_{had}}(\mathrm{Data})(i) - N^{CR}_{\text{truth }\tau_{had}}(\mathrm{MC})(i)}{N^{CR}_{\text{anti}-\tau_{had}}(\mathrm{Data})(i) - N^{CR}_{\text{truth anti}-\tau_{had}}(\mathrm{MC})(i)}, \tag{5.3}$$

where $N^{CR}_{\text{truth } \tau_{had}}$ and $N^{CR}_{\text{truth anti}-\tau_{had}}$ is the number of truth matched τ_{had} object in MC simulations that pass or fail the identification criteria, respectively. Therefore, contribution of true τ events in either category is subtracted in the CR. Consequently equation 5.2 can also be redefined as:

$$N^{\tau_{had}}_{fakes}(i) = (N_{\text{anti}-\tau_{had}}(\text{Data})(i) - N_{\text{anti}-\tau_{had}}(\text{MC})(i)) \times FF(i), \tag{5.4}$$

when subtracting the contribution of real τ's estimated in MC simulations ($N_{\text{anti}-\tau_{had}}(\text{MC})$).

Truth Matching

The τ_{had} truth-matching procedure is performed by comparing the path of a true τ to that of the visible τ_{had}. If the path coincides, i. e.the ΔR[1] between the truth object and the reconstructed visible τ_{had} is < 0.2, then the τ_{had} is considered truth matched to that object. In the case of multiple truth objects being within a cone of $\Delta R < 0.2$, the object with the highest p_{T} is chosen. Figure 5.1 shows a schematic representation of the cones constructed for the τ-lepton truth matching-procedure.

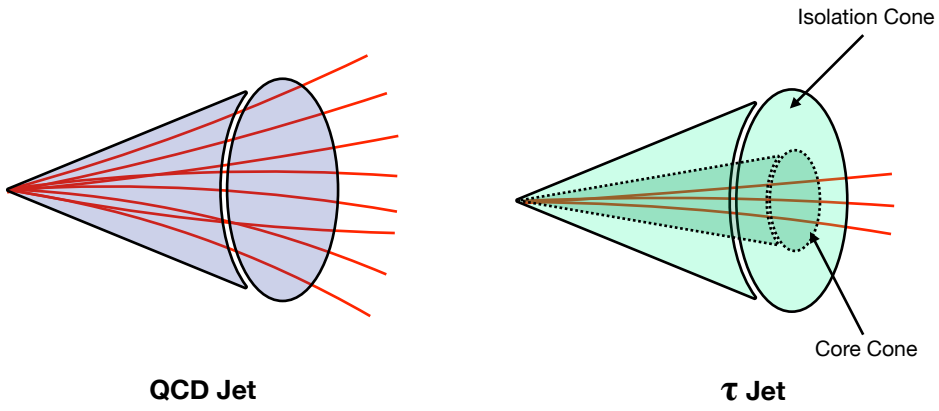

Figure 5.1: Diagram illustrating the difference in QCD and τ jet cones. τ jets tend to have one or three charged tracks inside a "core cone" ($\Delta R < 0.2$) and an absence of particles inside a larger "isolation cone" ($0.2 < \Delta R < 0.4$). QCD jets, on the other hand, generally tend to have more charged tracks in relatively wide cone.

As shown by this figure, jets are associated to the decay of a visible τ_{had} if there are either one or three charged tracks that are within a tight "core cone" of $\Delta R \lesssim 0.2$ inside a larger and relatively void "isolation cone" of $\Delta R \lesssim 0.4$. QCD jets tend to have more particles in a relatively wide cone compared to those initiated by τ-decays. It is also important to note that quark-initiated jets tend to be more narrow and contain less particles than jets initiated by gluons.

The implication of this is that quark- and gluon-initiated jets have different probabilities of being reconstructed as τ_{had}. Therefore, different background processes tend to have different

[1] $\Delta R = \sqrt{(\Delta\eta)^2 + (\Delta\phi)^2}$

quark/gluon compositions. Thus, the FF value generally needs to be derived as a combination of FF values from different backgrounds processes:

$$\mathrm{FF}_{comb} = f_W \mathrm{FF}_W + f_Z \mathrm{FF}_Z + f_{t\bar{t}} \mathrm{FF}_{t\bar{t}} + f_{QCD} \mathrm{FF}_{QCD} + \cdots, \tag{5.5}$$

where f_X represent the fraction of background source ($X = W, Z, t\bar{t}, QCD, \ldots$) in the given region of interest and FF_X is the corresponding FF value for that background in the same region. Therefore, the combined FF value (FF_{comb}) is derived by combining all the FF values from the different sources of backgrounds.

5.3 Universal Fake Factor method

The FFs should be measured in a CR with similar quark/gluon compositions to the SR. This is quite difficult to achieve in practice, although it is necessary to correctly apply FFs to any particular SR. The dependence of the quark- and gluon-initiated jet composition in an arbitrary region can be studied by considering the FF of pure quark and pure gluon samples. In this case, jets initiated from quarks and gluons would be defined as misidentified visible τ_{had}'s that fail a particular identification criteria working point. If we assume there are no other objects that can initiate a jet (and neglecting the difference in light and heavy flavoured quark-initiated jets), the FF can be written as a function of the quark fraction:

$$\mathrm{FF}(q_f) = q_f \mathrm{FF}_q + (1 - q_f)\mathrm{FF}_g, \tag{5.6}$$

where q_f is the fraction of quark-initiated jets in the sample, FF_q is the FF associated to the quarks, and FF_g is the FF associated to the gluons in the sample. If it is assumed that jets can only be initiated by quarks or gluons then:

$$1 = q_f + g_f, \tag{5.7}$$

where g_f is the fraction of gluon-initiated jets in the sample.

Figure 5.2 shows an illustration representing the FF as a function of q_f. It is clear that any pure quark or pure gluon region will have fixed values of FF, represented in the illustration by FF_q and FF_g, respectively. However, the pure quark and gluon FFs are not directly measurable quantities in data, but the functional relationship between of the FF and q_f can be determined in data by interpolation.

If two arbitrary regions are considered, where the FFs are written as:

$$\mathrm{FF}_1 = q_1 \mathrm{FF}_q + (1 - q_1)\mathrm{FF}_g, \tag{5.8}$$

$$\mathrm{FF}_2 = q_2 \mathrm{FF}_q + (1 - q_2)\mathrm{FF}_g, \tag{5.9}$$

then FF_q and FF_g can be expresses analytically using the above system of equations:

$$\mathrm{FF}_q = \frac{(1 - q_2)\mathrm{FF}_1 - (1 - q_1)\mathrm{FF}_2}{q_2 - q1}, \tag{5.10}$$

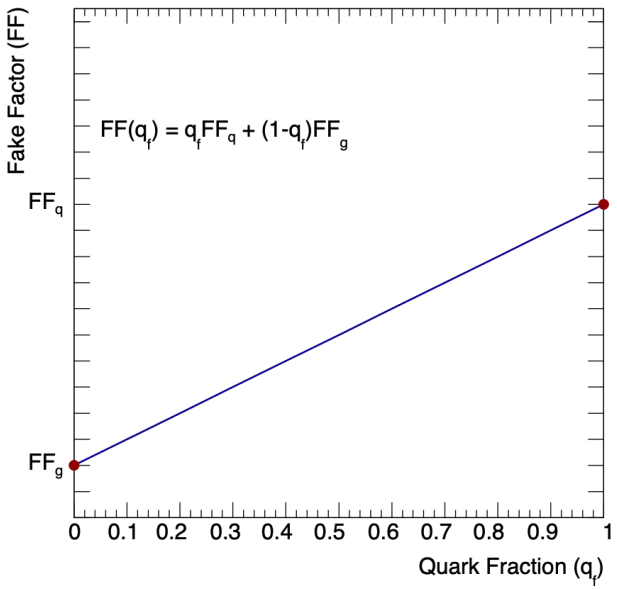

Figure 5.2: Illustration of linear dependence of FF on the quark fraction, q_f, given the relationship FF = $q_f \mathrm{FF}_q$ + $(1-q_f)\mathrm{FF}_g$. The points at the extremes show the FF for a pure quark or pure gluon sample (FF_q FF_g respectively).

and

$$\mathrm{FF}_g = \frac{q_2\mathrm{FF}_1 - q_1\mathrm{FF}_2}{q_2 - q1}, \tag{5.11}$$

where FF_1 and FF_2 are measured as described in Section 5.2 using equation 5.1:

$$\mathrm{FF}_1 = \frac{N^{CR_1}_{\tau_{had}}}{N^{CR_1}_{\text{anti}-\tau_{had}}}, \tag{5.12}$$

and

$$\mathrm{FF}_2 = \frac{N^{CR_2}_{\tau_{had}}}{N^{CR_2}_{\text{anti}-\tau_{had}}}. \tag{5.13}$$

For any arbitrary SR the corresponding anti-ID region (i. e. the same SR selection but with the τ_{had} identification criteria flipped so that only the events for which the τ_{had} fails the identification criteria pass) can be used to derive the appropriate FF. Thus, the FF can be defined as:

$$\mathrm{FF}_{SR} = q_{SR}\mathrm{FF}_q + (1-q_{SR})\mathrm{FF}_g, \tag{5.14}$$

where FF_{SR} is the FF value for this SR-like region and FF_q and FF_g are given by equations 5.10 and 5.11, respectively. Therefore, FF of the SR-like region can be re-written in terms of the FF for the two arbitrary regions FF_1 and FF_2:

$$\mathrm{FF}_{SR} = q_{SR}\frac{(1-q_2)\mathrm{FF}_1 - (1-q_1)\mathrm{FF}_2}{q_2 - q1} + (1-q_{SR})\frac{q_2\mathrm{FF}_1 - q_1\mathrm{FF}_2}{q_2 - q1}, \tag{5.15}$$

making the FF_{SR} value dependent only on three unknown quantities: q_1, q_2 and q_{SR}, which are the quark fractions for the arbitrary regions 1, 2, and SR, respectively. Therefore, by deriving the FF values of two regions (one gluon and one quark abundant), as well as their corresponding quark fraction it is possible, in turn, to determine the FF value for any given SR. Figure 5.3 illustrates this procedure along the linear dependence of the FF to the q_f for arbitrary regions 1, 2, and SR. The SR quark fraction (q_{SR}) is determined by a fit to quark and gluon fractions derived in MC template to data. This procedure is explained in more detail in Section 5.8.

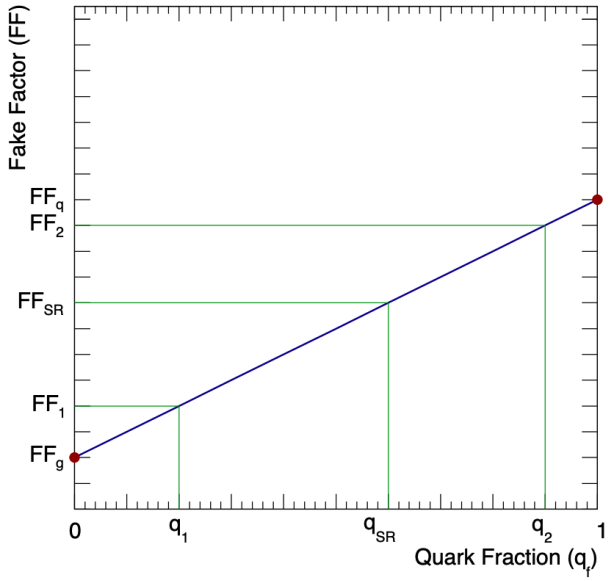

Figure 5.3: Illustration of the interpolation of FF_{SR} using pure quark/gluon FF, thus allowing the determination of FF uniquely by analytically calculating FF_q and FF_g.

Jet Width

The quark fraction cannot be calculated directly from data, as individual partons are not seen or reconstructed by the ATLAS detector. Therefore, the quark fraction must be derived in MC using a template method, i. e. where a *discriminating variable* is used to discriminate between different types of partons. The truth-matching method is used to identify the τ_{had} objects that are truth-matched to quark and gluon-initiated jets. These objects are then parametrised using a variable with good quark/gluon separation.

A variable found to have well-suited separation between quarks and gluons is the jet width. The jet width is a p_{T}-weighed ΔR of the objects associated to the jet:

$$j = \frac{\Sigma_i \Delta R^i \, p_T^i}{\Sigma_i \, p_T^i}, \tag{5.16}$$

where i is the number of objects that constitute the reconstructed jet. The jet width can be calculated from the calorimeter-based LC topo-cluster [142] jets that seed the visible τ_{had}, which in the text will be referred to as *calo-based jet width*.

This definition is quite sensitive to proton-proton interactions per bunch crossings (referred to in text as pile-up and denoted by μ) [143]. It was found that the calo-jet based track width was suffering from significant mis-modelling in the MC due to the incorrect modelling of pileup jets in the samples. Therefore, it became impossible to use this particular variable for discrimination, despite it having such good sensitivity to quark and gluon-initiated jets.

Because of this, a *track-based jet width* was explored instead. The track-based jet width is calculated using the same jet width equation described above (equation 5.16), but it only considers tracks associated to the seeded jet that:

- Have $p_{\mathrm{T}} > 1000$ MeV

- Are associated to the primary vertex

If no tracks fulfil these two requirements, then the jet width value is set to -1. Therefore, track-based jet width values of -1 tend to be associated to pileup jets, which do not come from the interaction's primary vertex.

Some examples of jet width distributions are shown in Figure 5.4 for several different MC samples. These plots show the normalised quark and gluon calo-based (top) and track-based (bottom) jet widths for Z+jets (left) and Dijets (right) samples simulated for the 2015-2016 data collection period. To produce these distributions the reconstructed jet-faking τ_{had} was truth-matched to its corresponding parton. The templates use τ_{had} candidates that fail the *Medium* BDT working point and have a minimum BDT score of 0.005. As mentioned above, there is reasonable quark gluon separation in both samples for both calo-based and track-based jet widths. The relatively lower number of gluons observed in the track-based jet width distribution compared to what is found when looking at the calo-based distribution is due to the higher number of gluons that have a track-based jet width value of -1, shown in the plot by the first bin (underflow).

Some mis-modelling present in both the calo-based and track-based jet width, as shown in Figure 5.5. The track-based (a) and calo-based (b) jet width shown in this figure are for the 1-prong visible τ_{had} in a Z boson abundant region of phase space derived using the following selection:

- A single muon trigger
- A leading muon $p_{\mathrm{T}} > 27$ GeV which is matched to the trigger
- The sub-leading muon has $p_{\mathrm{T}} > 10$ GeV
- Two muons of opposite-sign charge that pass the *Tight* isolation working point[2]
- M(μ,μ) $\in$ (81,101) GeV
- No electrons present
- At least one visible τ_{had} candidate with:
  - $p_{\mathrm{T}} > 20$ GeV
  - Absolute charge of 1
  - 1 or 3 tracks associated with its vertex
  - Failed *Medium* BDT identification working point and no minimum score requirement

[2] as defined in Reference [98]

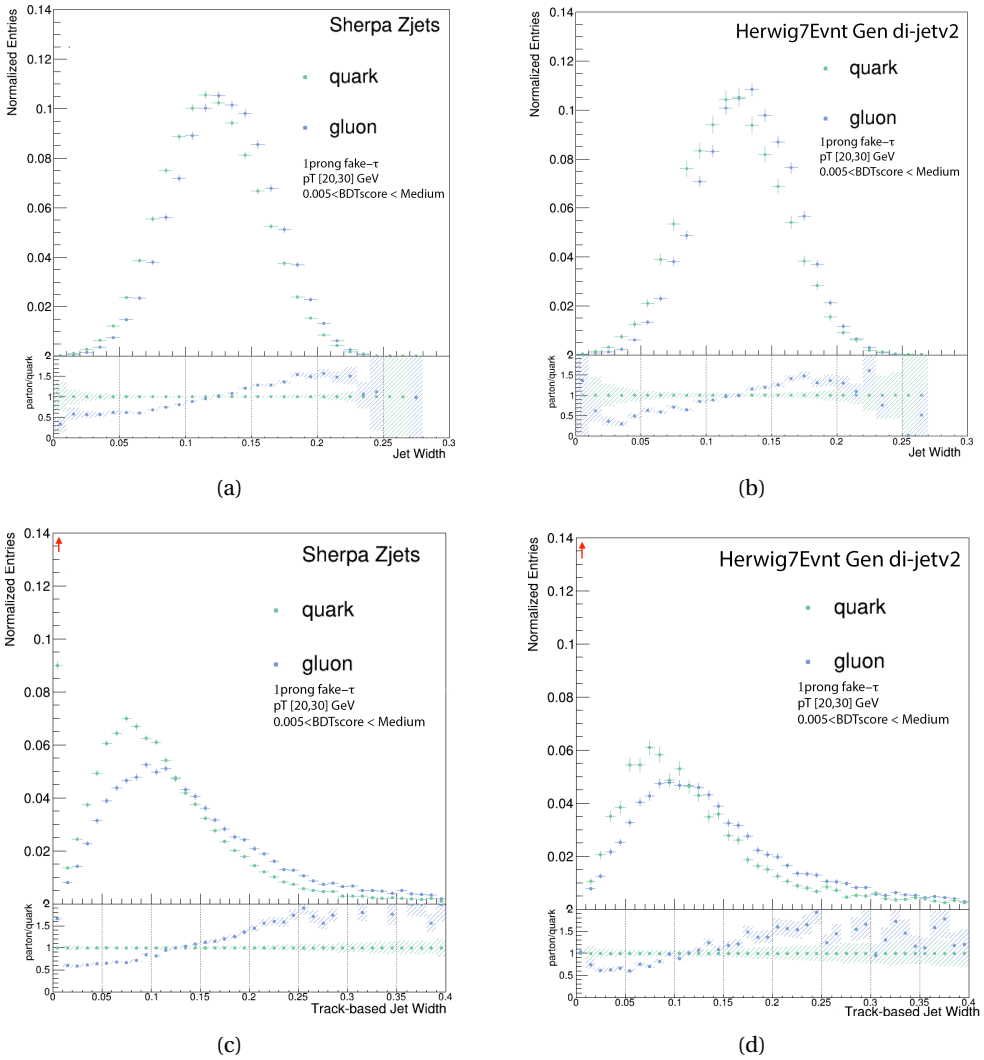

Figure 5.4: Unit-normalised quark and gluon distributions of calo-based (top) and track-based (bottom) jet widths, in the p_{T} bin [20,30] GeV, derived from MC samples of Z+jets (left) and Dijet (right) events are shown in the top half of each plot. Underneath each template the ratio of parton to quarks (chosen as reference) is shown. τ_{had} candidates that fail the *Medium* BDT identification working point and have a minimum BDT score of 0.005 are truth-matched to the corresponding parton. Red arrows indicate a point that is outside the range of the graph.

The calo-based mis-modelling is caused by the poor modelling of pileup jets in the sample, which causes a difference in the shape, as well as a shift, of the MC calo-based jet width distribution compared to data. The track-based jet width template also shows some mis-modelling of the jet width. Because the ratio of data to MC for the track-based jet width in the bulk of the distribution is approximately flat, then the shape can be assumed to be well simulated, albeit poorly normalized. The inaccurate normalisation is caused by the large number of jet width entries with values equal to -1, which for a 1-prong p_{T} inclusive visible τ_{had} candidate, corresponds to $\sim$ 30% of the cases, and by the presence of pile-up jets that still pass the stricter selection of the track-based jet width. The flat ratio of data to MC allows for the track-based jet width to be used as discriminating variable for quark and gluon-initiated jets.

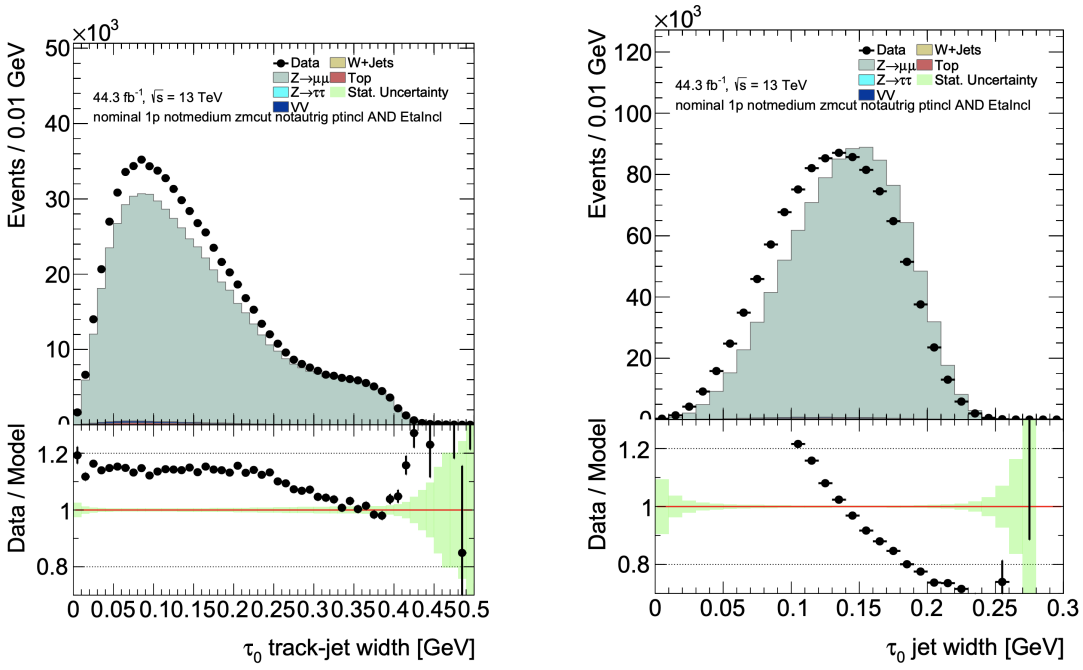

(a) (b)

Figure 5.5: Distributions of visible τ_{had} candidates jet width in Data and MC using a track-based (a) and calo-based (b) jet width. Top plots show the jet width distributions for different MC processes and 44.3 fb^{-1} of collected data. Bottom plots show the Data/MC ratio, where 1 represents perfect agreement.

5.4 Data regions

This section describes the two FF regions used to derive FF_1 and FF_2 defined above, for interpolation. The quark abundant region is dominated by Z boson production in association with jets (Z + jets) with Z→ $\mu\mu$ events selected using a single μ trigger [144]. The corresponding derived FF values will be referred to as FF_Z from here on. The second region is a multi-jet gluon-enriched region, consisting of di-jet events triggered using a single jet trigger. The resulting FF value corresponding to this region will be referred to as FF_{MJ}.

5.4.1 Quark abundant region

The Z + jets region was isolated in data using the following selection:

- Events are accepted if any of the the following single muon triggers are fired:
  - For data collected in 2015:
    - HLT_mu20_iloose_L1MU15
    - HLT_mu50
  - For data collected in 2016 onwards:
    - HLT_mu26_ivarmedium

    * HLT_mu50

- Events are accepted if there are no electrons that pass the *Loose* identification criteria[3] and with $p_{\mathrm{T}} > 15$ GeV
- There are exactly two reconstructed muons with:
  - Muon passes the *Tight* track-based isolation working point [98]
  - Leading $p_{\mathrm{T}} > 27.3$ GeV and matched to trigger
  - Sub-leading $p_{\mathrm{T}} > 10.0$ GeV
  - *Medium* quality [98]
  - $M(\mu,\mu) \in (70,100)$ GeV
- There is exactly one reconstructed τ-lepton with:
  - $p_{\mathrm{T}} > 18.0$ GeV
  - Absolute charge of 1
  - 1 or 3 tracks associated with its vertex
  - RNN efficiency score > 0.01

Using the above selection, a region predominately dominated by Z + jets and, thus, abundant with quark-initiated tau-faking jets, is obtained. Therefore, using the method described in Section 5.2 the values for the FFs can be derived for any given region or anti-region of identification working point.

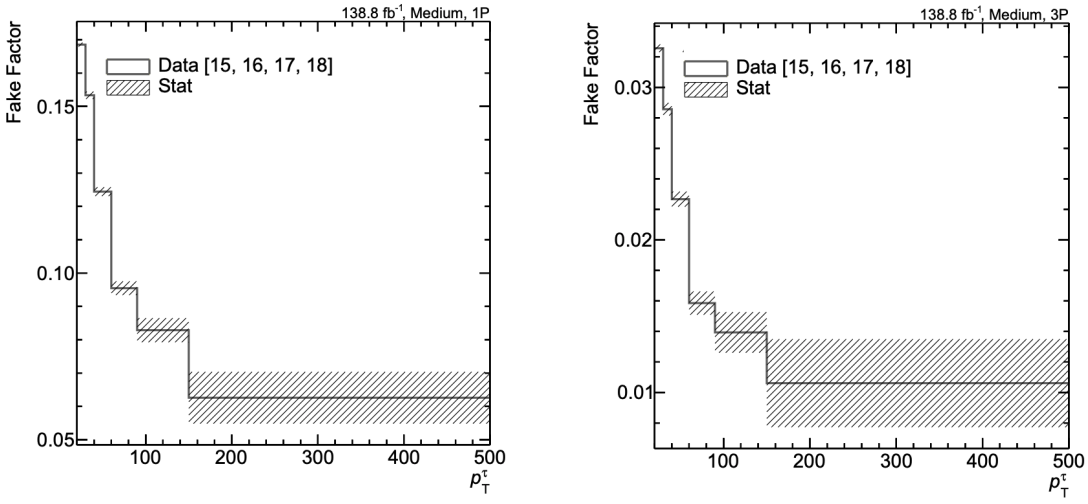

(a) (b)

Figure 5.6: Distributions of FF values as a function of the leading visible τ_{had} object in the Z+jets quark-initiated tau-faking-jets abundant data region for the one prong (left) and three prong (right) case using *Medium* RNN working point and full Run-2 data

[3] Likelihood (LH) based electron identification criteria is described in detail in References [145, 146]

Figure 5.6 shows the visible τ_{had} FF values with respect to the leading tau p_{T} (denoted by p_T^{τ} in the figure) derived from data using the selection above. Real τ are subtracted using MC simulations, for a *Medium* RNN working point for 1 prong (a) and 3 prong (b) case, as defined by equation 5.12. The FF values seem to have a strong dependence with p_{T}. These plots show that the FF values decrease as the visible τ_{had}object p_{T} increases. The FFs for the 3 prong τ-leptons are also found to be lower in value then for 1 prong τ-leptons.

As discussed in Section 2.4, the rejection power of both RNN and BDT classifiers increases with increasing p_{T}. In a fake-τ dominated sample, as the p_{T} increases the probability for the classifier to identify and reject fake-τ also increases. This will, in turn, decrease the number of τ_{had} objects that populate the pass-ID region (nominator of equation 5.12), whilst simultaneously increasing the fail-ID region (denominator of equation 5.12). The FF as a function of τ_{had} p_{T} in a region that is abundant in fake-τcandidates, such as the one described above, is thus expected to decrease with increasing p_{T}.

The lower FF values of the 3 prong τ-leptons, compared to the 1 prong, are due to the higher rejection power of the RNN/BDT classifier for the 3 prong taus. This results in a relatively higher multiplicity of taus which fail the identification working point compared to the 1 prong scenario.

5.4.2 Gluon abundant region

The Multi-jet production was isolated in data to derive a gluon abundant region to derive FF values as in Section 5.4.1. To achieve this, the following selection was used:

- Event are accepted if any of the the following single jet triggers are fired:
  - HLT_j15 with offline $p_{\mathrm{T}} > 20$ GeV
  - HLT_j25 with offline $p_{\mathrm{T}} > 35$ GeV
  - HLT_j35 with offline $p_{\mathrm{T}} > 45$ GeV
  - HLT_j85 with offline $p_{\mathrm{T}} > 110$ GeV
  - HLT_j110 with offline $p_{\mathrm{T}} > 120$ GeV
  - HLT_j175 with offline $p_{\mathrm{T}} > 216$ GeV
  - HLT_j260 with offline $p_{\mathrm{T}} > 300$ GeV
  - HLT_j360 with offline $p_{\mathrm{T}} > 400$ GeV
  - HLT_j400 with offline $p_{\mathrm{T}} > 440$ GeV
  - HLT_j420 with offline $p_{\mathrm{T}} > 460$ GeV
- No electrons that pass *Loose* identification criteria[4] with $p_{\mathrm{T}} > 15$ GeV
- No *Loose* quality muon with $p_{\mathrm{T}} > 7$ GeV

[4] LH based electron identification criteria is described in detail in References [145, 146]

- No photon that passes the *Loose* identification criteria [145, 146] with $p_{\mathrm{T}} > 10$ GeV
- At least one jet
  - $p_{\mathrm{T}} > 20$ GeV
  - $\eta < 4.5$
  - No JVT[5] requirement
- Loose jet cleaning
- OR[6] procedure is performed
  - With loosely selected electrons, muons, taus, photons, and jets
  - Where tau selection before OR: $p_{\mathrm{T}} > 20$ GeV, RNN > 0.01

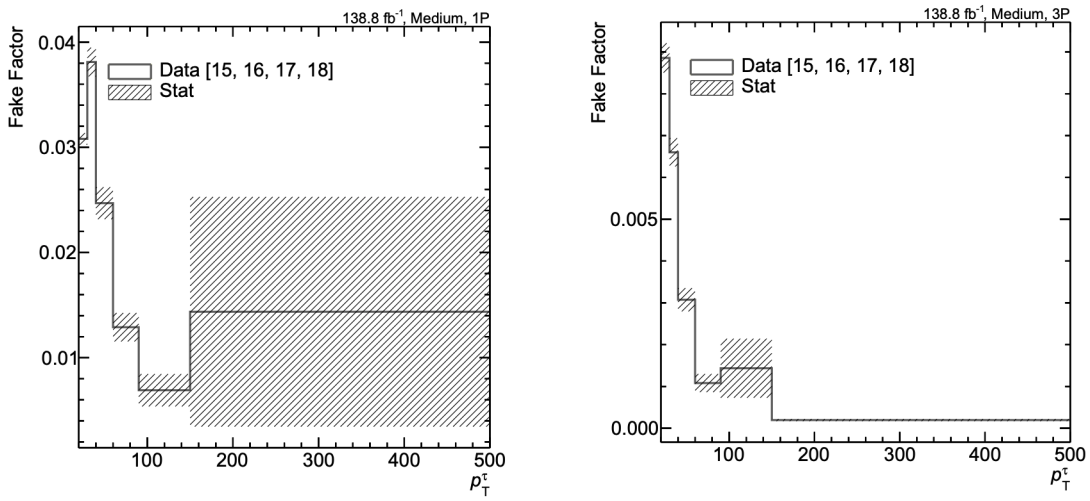

(a) (b)

Figure 5.7: Distributions of FF values as a function of the leading visible τ_{had} object in the di-jets gluon-initiated tau-faking-jets abundant data region for the one prong (left) and three prong (right) case using "Medium RNN" working point and full Run-2 data. Truth tau subtraction has not been applied to these results.

Figure 5.7 shows the FF values derived for this region for the 1 prong (a) and 3 prong (b) cases, as a function of the leading visible τ_{had} p_{T} for the *Medium* RNN working point. Similarly to the Z + jets region, the FF values for the di-jet region are found to be dependent on the leading τ_{had} p_{T} but with slightly lower overall values. This is due to the high multiplicity of jets in this region, which have a higher probability of being mis-identified as taus. This results in a larger multiplicity of τ-leptons failing the RNN working point, thus translating to overall lower FF values. It is worth noting that the large uncertainty band shown in the highest p_{T} bin for the 1 prong case is due to low statistics in that bin from the data collected in 2017. In the 3 prong case there are no τ-leptons above 150 GeV that pass the required selection, resulting in the last bin of the distribution not being populated.

[5] The JVT is a multivariate combination of track-based variables used to suppress pileup jets [147]
[6] OR procedure discussed in detail in Section 5.5.3

5.5 MC Inputs

In this section the MC samples, generators, selections, and required calibrations, used to produce the track based jet width and FF distributions needed to determine the quark fraction and for the estimation of the FF values, are discussed. Section 5.3 describes how, through the derivation of pure quark and pure gluon track based jet width templates, it is possible to calculate the relative abundance of quarks (quark fraction) in a given sample using a fitting procedure (to be discussed in more detail in Section 5.8). The track based jet width, and τ_{had} transverse momentum distributions derived from MC samples used for the quark fraction fitting will be referred as templates from here on.

5.5.1 Samples and generators

Parton kinematics can differ slightly depending on the generator used due to the different methods and prescriptions used for the Matrix Element PS matching. To account for this systematic effect, a set of MC samples generated using different generators have been studied. The samples studied are separated into two categories: High Priority (HP) and Low Priority (LP) samples. HP samples include only Z + jets, W + jets and di-jets processes that have been produced using similar generator with significant statistics. LP samples include a wider range of processes produced with different generators, and can be used to study the generator effects and boost the overall statistics.

The HP Z + jets and W + jets samples have been generated using POWHEG-BOX v1 [148] interfaced to the PYTHIA V8.186 [149](referred as PYTHIA 8 from now on) PS and hadronisation model, except for the heavy-flavour decays which are modelled using the EVTGEN V1.2.0 [150] program. The CTEQ6L1 PDF [151] is used for the parton shower along with the AZNLO [152] set of tuned parameters. The HP di-jet samples are generated using the PYHTIA 8 and EVTGEN combination as above, but using the A14 set [104] of tune parameters with the NNPDF2.3 LO PDF [105] set instead and are separated into several slices of different generator-level jet p_{T} thresholds, generally referred to as "JZx" (with x running from 0 to the number of slices) [153]. JZxW is the same as JZx slicing but filtered based on the p_{T} spectrum such that there are equal numbers of events at each p_{T}.

Table 5.1 summarises the samples and generators as well as any filtering or slicing that were applied to each sets of samples. As mentioned previously, HP samples are used as the main samples for comparison, while LP samples have been used for further studies of generator and process driven effects.

5.5.2 Analysis Object Data Samples selection

Analysis Objects Data (AOD) samples are the baseline MC samples produced by the ATLAS collaboration. AOD samples are not skimmed or slimmed for any particular type of analysis and instead are composed of the full collections of reconstructed objects. This makes these type of

Table 5.1: Samples and generators used for FF studies. Generators for each samples are shown with corresponding PDF sets, selections and filters. Sample names shown in bold text represent HP samples, the rest are considered LP samples.

Processes	Generators	PDF	veto / filter	selection / comments
Z+jets W+jets	SHERPA v2.2.1	NNPDF3.0 NNLO	c-jet veto and b-jet veto OR c-jet filter and b-jet veto OR b-jet filter	$m(\ell,\ell) > 40$ GeV $\max(\text{HT}, p_T^V) \in [0,70,140,280,500,1000,\text{inf}]$
			b-jet veto OR b-jet filter	10 GeV $< m(\ell,\ell) < 40$ GeV, $\max(\text{HT}, p_T^V) \in [0,70,140,280,\text{inf}]$
	MADGRAPH5_AMC@NLO v2.2.3.p4 + PYTHIA 8 + EVTGEN v1.2.0	A14 NNPDF2.3 LO	c-jet veto and b-jet veto OR c-jet filter and b-jet veto OR b-jet filter	$m(\ell,\ell) > 40$ GeV HT $\in [0,70,140,280,500,1000,2000,\text{inf}]$
				$N_p \in [0,1,2,3,4]$ (*only for some $Z \to \tau\tau$ samples)
	POWHEG v1 + PYTHIA 8 + EVTGEN v1.2.0	**AZNLO CTEQ6L1**		$m(\ell,\ell) > 60$ GeV
Multiboson	SHERPA v2.2.1	NNPDF3.0 NNLO		on shell diboson production with factorised decays
	SHERPA v2.2.2			$m(\ell,\ell)_{SFOS} > 4$ GeV $p_T(\ell_1) > 5$ GeV $p_T(\ell_2) > 5$ GeV
				$m(\ell,\ell) > 2 \times m_\ell + 250$ MeV $(p_T(\ell_1) > 20$ GeV OR $p_T(\ell_2) > 50$ GeV) AND $(p_T(\ell_2) < 5$ GeV OR $m(\ell_{SFOS==1}) < 4$ GeV)
	POWHEG v2 + PYTHIA 8 + EVTGEN v1.2.0	AZNLO CTEQ6L1		$m(\ell,\ell)_{min} > 4$ GeV
Dijets	Herwig v7.0.4 + EvtGen v1.6.0	NNPDF3.0 NLO (ME) MMHT2014 (shower/MPI)		JZx with x $\in [1,2,3,4,5,6,7,8,9,10,11]$
	PYTHIA 8 + EVTGEN v1.2.0	**A14 NNPDF23LO**		JZxW with x $\in [1,2,3,4,5,6,7,8,9,10,11,12]$
single top + $t\bar{t}$	POWHEG + PYTHIA 8 + EVTGEN v1.6.0	A14 NNPDF23LO	non-hadronic decays hadronic decays inclusive leptonic decay	$h_{damp} = 258.75$ GeV (1.5 × top mass)
	POWHEG + HERWIG v7.0.4 + EVTGEN v1.6.0	NNPDF3.0 NLO (ME) MMHT2014 (shower/MPI)	single lepton di-lepton all hadronic leptonic decay inclusive	$h_{damp} = 258.75$ GeV (1.5 × top mass)

samples very useful to use for an initial proof of concept as the samples wont be affected by any bias introduced though the application of selections, calibrations or derivations. To maintain the unbiased property of the AOD samples, only a very loose selection is used to construct a region abundant with fake τ_{had} objects. The following selection cuts are thus applied:

- At least one tau:
  - $p_{\text{T}} > 20$ GeV
  - BDT background rejection efficiency score > 0.005

Where the BDT was later changed to the better performing RNN identifier, following the recommendations for the appropriate reconstruction of the visible τ_{had}, and thus changing the BDT score selection to RNN background rejection efficiency score > 0.01. The τ_{had} are categorised accoring to their Particle Databook Group Identification (PDG ID)s [111] from the results of the truth matching procedure. To truth match the visible τ_{had} to their corresponding τ_{had}-faking parton, the jet seeding the τ_{had} object is identified and is used for the truth-matching. Table 5.2 shows the categories used to describe the truth-matched visible τ_{had} objects using the variables: CONETRUTHLABELID for identifying the τ_{had} faking jets and PARTONTRUTHLABELID to identify τ_{had}candidates truth-matched to parton jets. Both variables use the absolute value of PDG ID values to describe the appropriate truth-matched object.

Table 5.2: Truth table for selection of quark, gluon and un-matched candidates from jet-faking τ_{had}objects identified via the truth matching method.

Parton / Object	Cone Truth Label ID	Parton Truth Label ID
Fake-tau	!|15|, !|13|, !|11|, !|22|	-
Quark	Fake-tau	$\in [0,7]$
Gluon	Fake-tau	21
Un-Matched	Fake-tau	-1, 0

Un-matched objects are defined as the candidates that fail the truth-matching procedure. Figure 5.8 shows the distribution of highest visible fake-taus p_{T} per event for matched (i.e. quark and gluon) objects against the same distribution for the un-matched objects for all MC campaigns. The ratio plot below the p_{T} distributions shows that the un-matched objects have a higher multiplicity in the low τ_{had} p_{T} region and decrease with increasing transverse momentum. Furthermore, the fraction of of un-matched candidates seems to increase with increasing mean number of interaction per bunch-crossing ($\langle\mu\rangle$). The different MC samples shown in Figure 5.8 are generated with the different pileup conditions associated to the different data collection periods (2015-2016, 2017, and 2018), where MC16a, MC16d, and MC16e correspond to $\langle\mu\rangle = 24.5$, $\langle\mu\rangle = 37.8$, and $\langle\mu\rangle = 36.1$ with luminosities of 36.2 fb^{-1}, 44.3 fb^{-1}, and 58.4 fb^{-1}, respectively. The relative higher number of un-matched candidates present in the samples with higher $\langle\mu\rangle$ implies a direct correlation between un-matched candidates and $\langle\mu\rangle$. A considerably significant number of un-matched candidates can, thus, be attributed to fake-τ pile-up jets.

$\mathbf{p}_T$ dependence

The left and right plots of Figure 5.9 show the p_{T} distributions extracted from Z + jets, W + jets, and di-jet samples for the jet-initiated fake-tau objects matched to MC quarks and gluons, respectively. Different samples are found to possess different kinematic distributions for these tau-faking objects, which in turn affects their corresponding jet width distributions. A boosted visible τ_{had} object can have a narrower jet width compared to a lower p_{T} object since the tracks from the boosted object will tend to be closer. Furthermore, when comparing the data samples to MC samples for FF interpolation the $Z \to \mu\mu$ region will match more closely the $Z \to ee$ sample's kinematic properties then the W + jets or di-jets MC samples, for instance. However, all samples described in the previous section (both HP and LP) are needed to construct the resulting templates. The dependence (or bias) caused by the different p_{T} distributions between the samples on the jet widths must therefore be isolated and removed. There are two main effects that need to be addressed.

The first effect to consider is the direct dependence of p_{T} on the jet width of the τ_{had} object. To that end, the p_{T} of the fake-τ_{had} candidates is separated into bins, as shown by Table 5.3. The jet width templates and FF values need to, thus, be derived for each p_{T} bin. This ensures

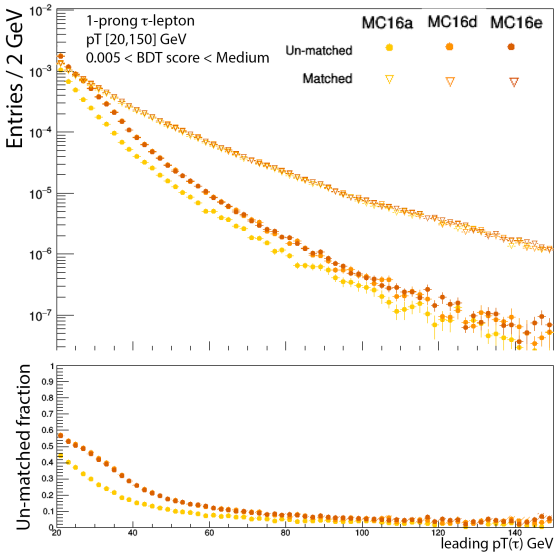

(a)

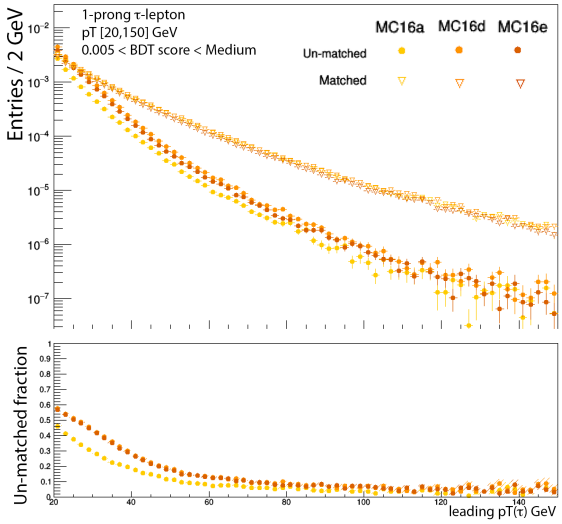

(b)

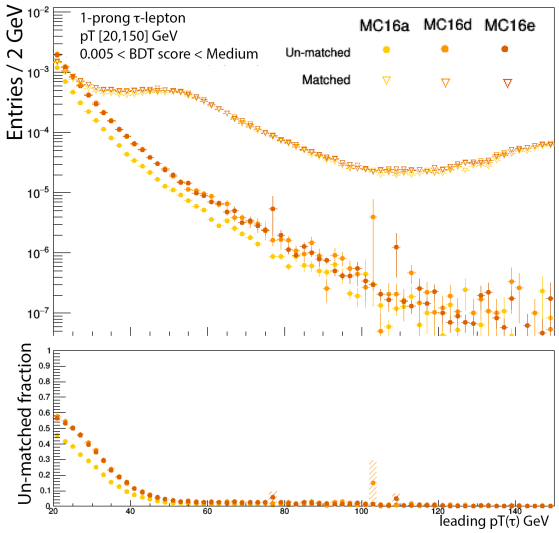

(c)

Figure 5.8: Figures showing the p_{T} distribution for leading τ_{had} candidates for matched (quark+gluon) and un-matched candidates in the (a) Z+jets, (b) W+jets and (c) di-jet samples for MC16a, MC16d and MC16e campaigns. The bottom plots shows the ratio of matched to un-matched candidates for each campaign for the respective samples.

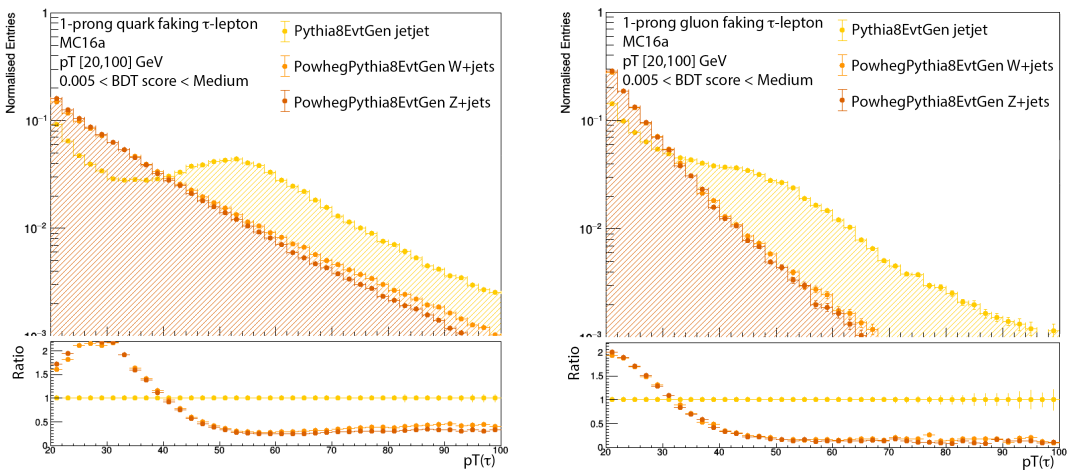

(a) (b)

Figure 5.9: τ_{had} p_{T} distribution plots for truth matched fake-tau candidates,i. e. to quarks (left) and gluons (right) in dijet, Z+jet and W+jet samples. Histograms have been normalised to unity to show differences in shape. Bottom plot shows the ratio between the dijet and the other sample's p_{T} distribution.

that regions of different kinematic properties are treated and evaluated separately. Each p_{T} bin is then "fine-binned" in intervals of 1 GeV, while the jet width should have bin widths of 0.01.

Table 5.3: visible τ_{had} p_{T} binning used for derivation of templates and FF values.

Min [GeV]	Max [GeV]
20	30
30	40
40	60
60	90
90	150
150	inf

Further dependences of notice are taken considered and are isolated into further bins, as shown by Table 5.4. "Prong" refers to the number of charge tracks associated with the studied τ_{had} vertex, and can either be 1 or 3 prong. "BDT WP" and "RNN WP" correspond to the the BDT and RNN identifier algorithm working points, respectively, and can be either *Loose*, *Medium* or *Tight* as defined in Table 2.1. The "BDT min" and "RNN min", corresponds to the minimum background rejection efficiency scores of the BDT and RNN identifier algorithms at which a τ_{had} candidate is accepted. The "JVT cut" selects for objects that have passed the JVT algorithm [147], which is primarily used to suppress pileup jets. Finally, the last possible selection displayed in the column "Trigger requirement" applies when a trigger requirement is requested to be passed by the τ_{had} object.

The second effect that needs to be considered is the different p_{T} distributions shapes between different samples. The procedure used to minimise this effect is called "p_{T} re-weighing" and is performed differently for MC-to-MC compared to MC-to-data, as follows.

Table 5.4: Further available requirements for further isolation of jet width dependence. Any combination of these requirements can be done and studied, where each combination would result in corresponding set of FF values and jet width templates. Note "*" corresponds to the options that have so far been studied.

Prong	BDT min	BDT WP	RNN min	RNN WP	WP region	JVT cut	Trigger Pass
1*	0.00	Loose	0.00	Loose	pass	no JVT cut*	no requirement*
	0.05*	Medium*	0.01*	Medium*			
3*	0.50	Tight	0.05*	Tight	fail*	some JVT cut	passed

For the MC-to-MC re-weighing, the MC samples are separated into two categories, one sample is used as "reference", while the rest are considered "variable" samples. The "reference" sample p_{T} distribution is used as the distribution to which the other ("variable") samples are re-weighed to. Because the different parton p_{T} distributions (quark, gluon, un-matched...) need to be independently re-weighed, the procedure must be performed for each parton. Each sample's parton full p_{T} distribution can thus be derived and plotted in histograms of 1 GeV p_{T} bins. The distributions are normalised to unity before the re-weighing is performed, as to be independent of any scaling factors applied to the distribution. By comparing the "reference sample" distribution to the "variable sample," a weight for each p_{T} bin can be derived for each sample. This event weight is then be used to re-weigh the "variable sample" p_{T} distribution to the "reference sample".

In contrast, when comparing the MC samples (di-jet, W + jets and Z + jets) to the FF interpolation data regions (multijet and $Z \rightarrow \mu\mu$), the quark, gluon and un-matched candidates are independently re-weighed to the p_{T} distribution of the FF interpolation regions as well as to the region of interest.

An example of p_{T} re-weighing is shown for the quark template p_{T} in Figure 5.10. Plot (a) shows the quark and gluon p_{T} distributions between the different samples in the p_{T} bin $\in [20,30]$ before re-weighing. As described above, the distributions have been normalised to unity to clearly show the differences in the p_{T} distribution between samples. In Plot (b), the same distributions, with the p_{T} re-weighing procedure applied are shown. The p_{T} re-weighing changes the distribution shape to make it coincide with the appropriate parton distribution.

Figure 5.11 shows the effect of p_{T} re-weighing on the jet width distributions for quarks (a), gluons (b) and un-matched (c) MC templates. For all templates the p_{T} re-weighing results in only a very small shift of the jet width distribution. This indicates that the p_{T} distribution shape between processes only has a small effect for these samples.

5.5.3 Derived Analysis Object Data samples

The concepts described above for the derivation and application of FF are intended to be developed for use in many different types of analyses. To that end, it is important to ensure that general analyses selections and object calibrations, or any other tools applied at analysis level, do not unexpectedly affect the quark fraction or jet width templates. If so they must be studied

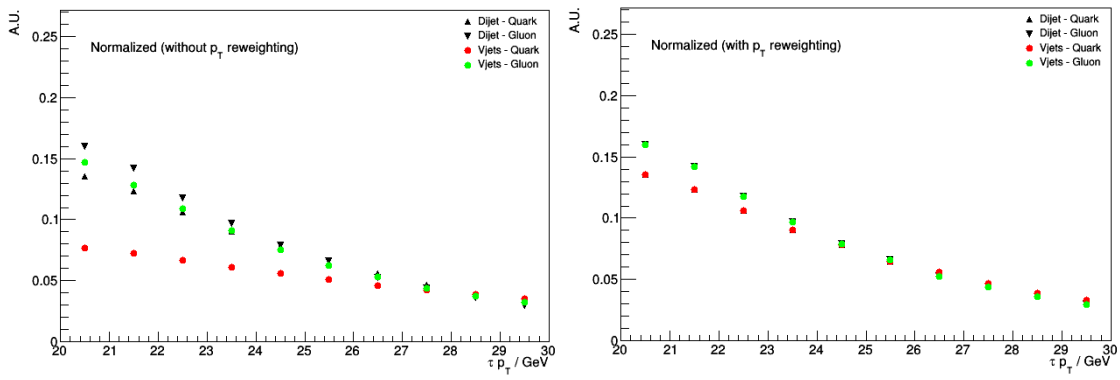

(a) (b)

Figure 5.10: Top plot shows the distribution of τ_{had} p_{T} of truth matched τ_{had} to quark (black) and gluon (red) for dijet and V+jets (W+jets and Z+jets merged). Bottom plot shows the same distributions after implementing the re-weighing procedure with respect to the dijet sample.

and understood for the proper application of the universal FF method.

Figure 5.12 shows the track based jet width distributions between the same MC samples that have undergone two different calibration processes. The distributions have been produced using fake-τ objects in the anti-*Medium* working point BDT region (i. e. accepting events which fail the *Medium* BDT τ_{had} requirement), with 1-prong, and in the p_{T} bin $\in$ [20,30] GeV. One of the samples shown is an AOD (blue), while the second is a Derived Analysis Object Data (DAOD) sample (red). DAOD (also called "derivation") is the name given to AOD samples that have also been processed through "derivation selections." Significant discrepancies in the track based jet width distributions are observed, indicating that the selections applied to the DAOD sample result in biases to the τ-lepton kinematics, that needs to be fully understood.

The samples used for ATLAS physics analyses are DAOD. This is because DAOD samples include selections and calibrations that are essential for the accurate reconstruction of particle objects. The most relevant and common processing procedures applied to DAOD samples are the τ_{had} object calibration, the overlap removal procedure, and implementation of tighter selection cuts. All of these procedures are discussed in more detail below.

Object calibration

An important step of the visible τ_{had} object reconstruction is the calibration. After the reconstruction of a τ_{had} following the prescription described in Ref. [78], the energy of the tau candidate is calibrated at the LC scale, which corrects for calorimeter non-compensation and for the energy deposited in dead material or outside topological clusters of calorimeter cells. The correction of the tau energy back to the true visible energy, via the application of the Tau Energy Scale (TES) can have significant effects on the kinematic properties of the reconstructed τ_{had}. These effects must be taken into consideration when deriving templates of the τ_{had} jet track-based jet width. The TES calibration is generally performed when generating a "deriva-

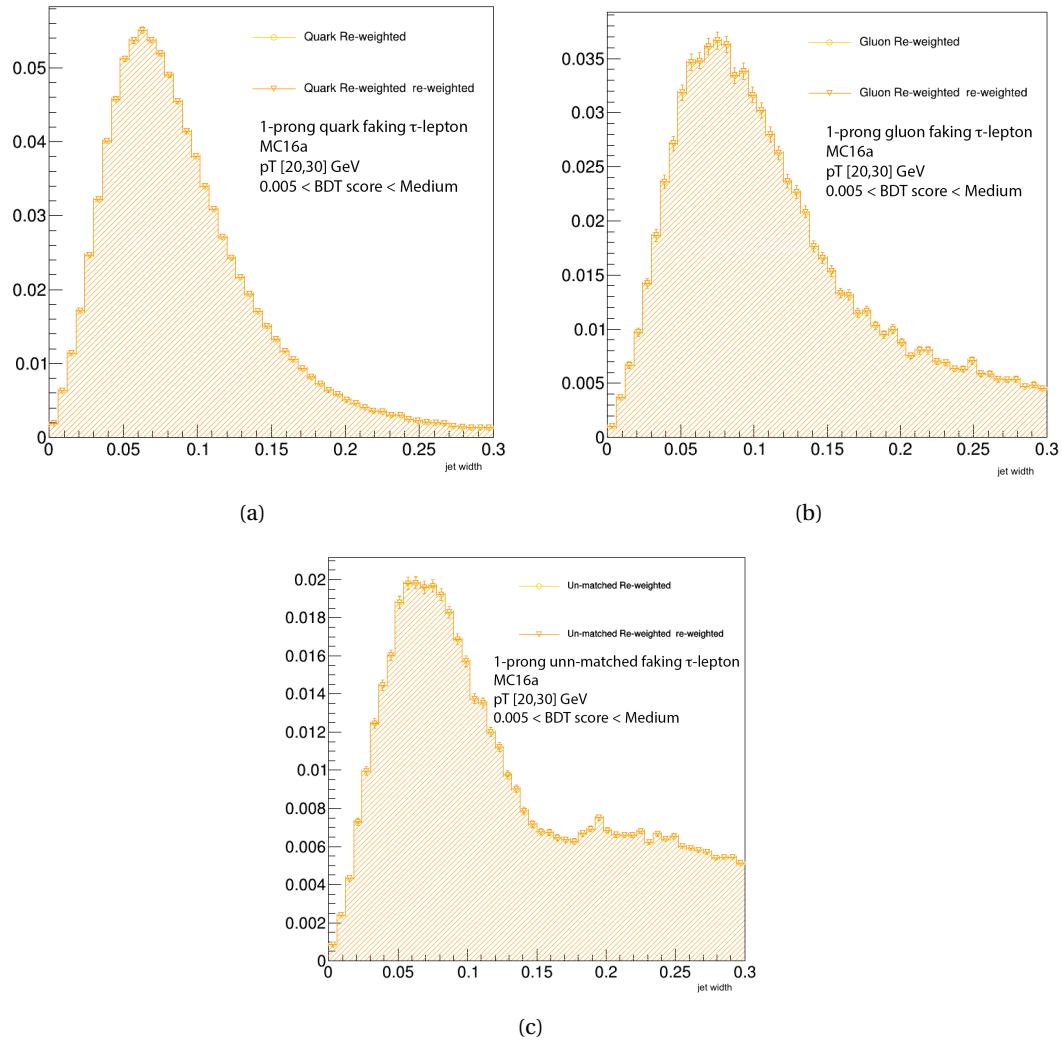

Figure 5.11: The effect of p_{T} re-weighing on MC16a Z+jet sample using dijet sample as "reference" on the track-based jet width templates of quark, gluon and un-matched candidates are shown in plots (a), (b) and (c), respectively. All plots correspond to one prong 20-30 GeV τ_{had} candidates which fail the "Medium" BDT working point.

tion" sample. Hence, the τ_{had} objects contained in AOD samples are not calibrated. The effect of TES calibration on the tau objects can be seen in Figure 5.13 where the quark (a), gluon (b) and un-matched (c) track-based jet width templates are shown for calibrated and un-calibrated τ_{had} objects. The figure shows the track based jet width templates for the different partons in the p_{T} bin $\in [20,30]$ in the Z$\rightarrow \mu\mu$ process. The large discrepancy observed in the parton's templates is due to the larger number of candidates with a track-based jet width value of -1, which when normalised to unity results in a relatively smaller distribution for the calibrated objects compared to the non-calibrated.

Overlap removal procedure

A common procedure employed when running an analysis is to remove potentially overlapping objects, i. e. a lepton that falls within the same "cone" of a jet. An OR procedure, where the

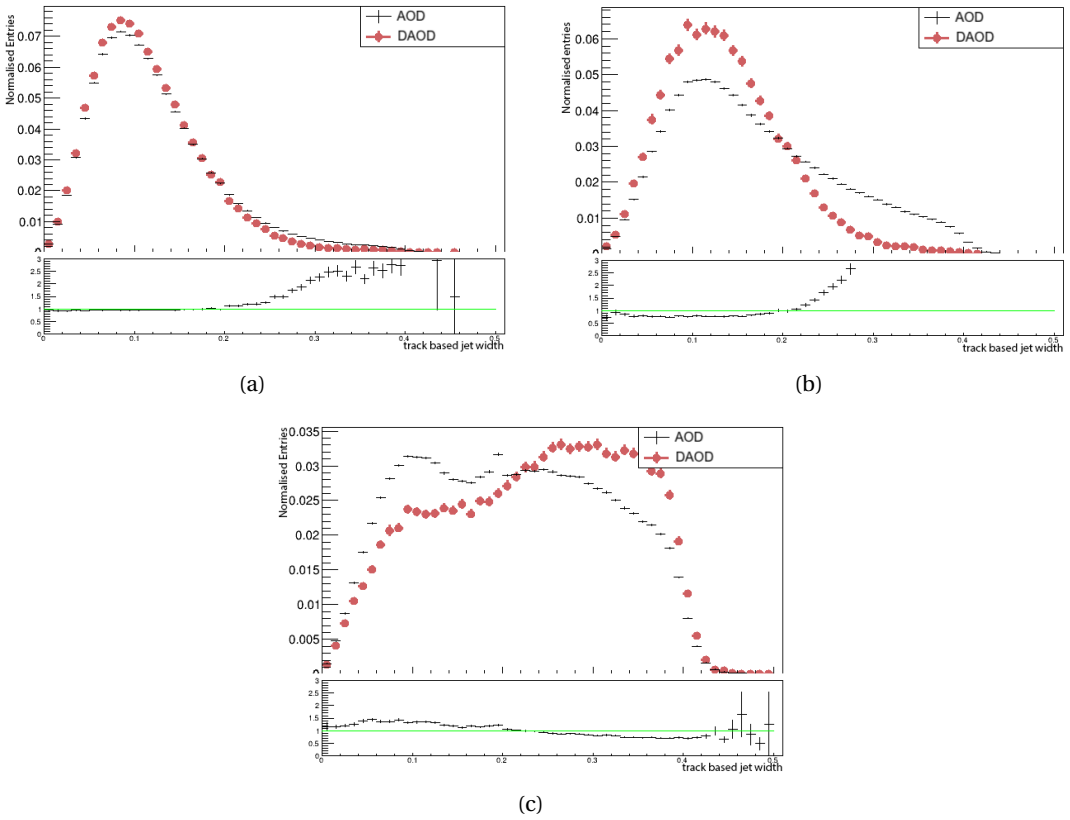

Figure 5.12: Comparison between AOD and DAOD samples for quark (a), gluon (b) and un-matched (b) track-based jet width templates. The bottom plot shows the ratio between the AOD and DAOD distribution.

inputs are two objects that have been loosely selected, is performed to resolve the ambiguity and discard one of the two objects. This is done by looking angular distance ΔR between the two reconstructed objects in the detector. Table 5.5 shows the standard selection applied using ΔR to resolve ambiguity between the different objects. The OR procedure can, thus, have a large effect on the multiplicity of tau-faking objects in the observed events.

Figure 5.14 shows the effect of the OR procedure on the track-based jet width distribution for a $Z \rightarrow \mu\mu$ sample 1 prong tau-faking quarks. The reconstructed fake-τ_{had} objects are shown in the plot by green points when the TES calibration is applied but without OR, in blue when the TES calibration is not applied and neither is the OR, and in yellow when both TES calibration and OR are applied. It is important to note that the OR procedure should only be implemented after applying the TES calibration to the reconstructed τ_{had} objects as the kinematic properties of all the objects in the event need to be properly modelled before any candidate is rejected, hence why the "applied OR but no TES calibration" combination is not shown.

In this plot, the distributions have been normalised to unity only for values of track-based jet width above 0. This is to better display the differences in template shape between the calibrated and un-calibrated distributions since, as shown in the previous section, have significantly different scales when normalised to unity while taking into account the values of track-based jet width of -1. The calibration of the reconstructed tau objects cause a decrease in the of the

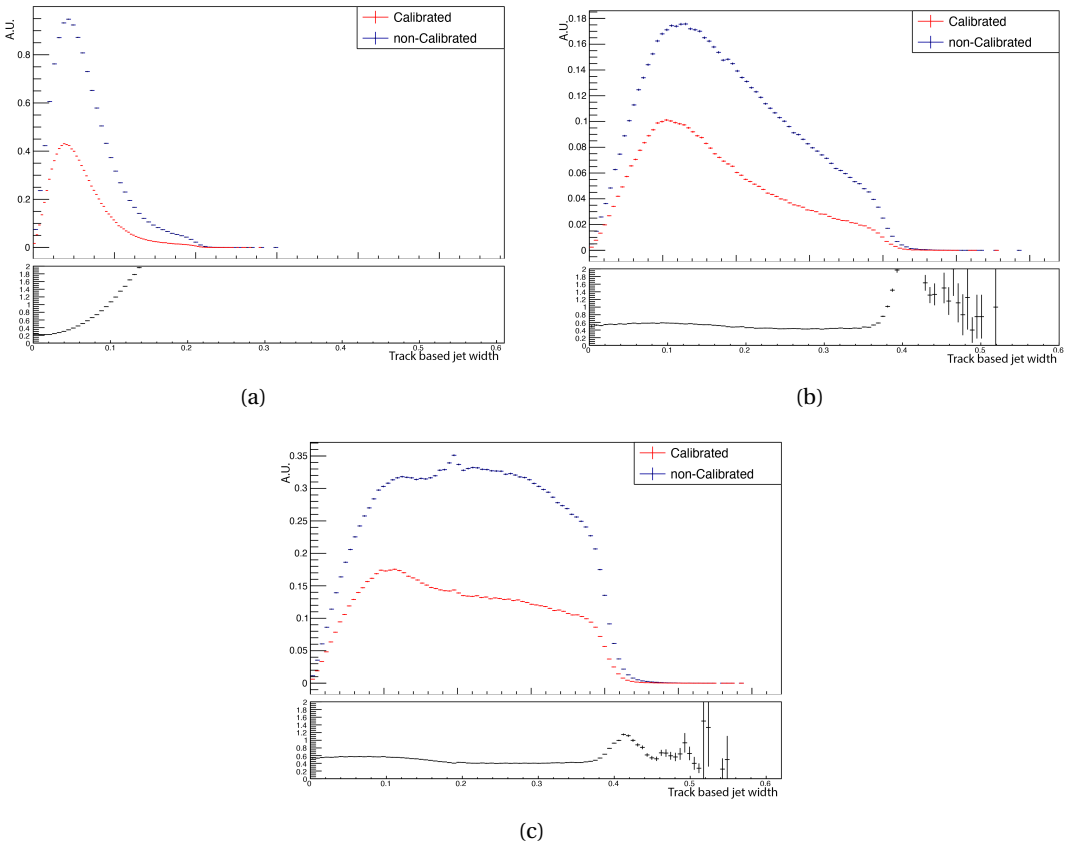

Figure 5.13: Comparison of track-based jet width distribution of 1-prong fake-τ (a) quarks, (b) gluons, and (c) unmatched candidates between an un-calibrated and calibrated $Z \to \mu\mu$ sample.

Table 5.5: Steps are performed in the listed order. Only surviving objects participate in the subsequent steps.

Reject Object	Against	Criteria
electron	electron	shared track, $p_{T_1} < p_{T_2}$
tau	electron	$\Delta R < 0.2$
tau	muon	$\Delta R < 0.2$
muon	electron	is a calo-muon, shares ID track
electron	muon	shares ID track
photon	electron	$\Delta R < 0.4$
photon	muon	$\Delta R < 0.4$
jet	electron	$\Delta R < 0.2$
electron	jet	$\Delta R < 0.4$
jet	muon	N. Tracks < 3, $\Delta R < 0.2$
muon	jet	$\Delta R < 0.4$
jet	tau	$\Delta R < 0.2$
photon	jet	$\Delta R < 0.4$
large-R jet	electron	$\Delta R < 1.0$
jet	large-R jet	$\Delta R < 1.0$

tail of the distribution, as shown by comparing the green and the blue histograms. This seems to be due to the fact that by applying the TES calibration a significant number of low-p_{T} τ_{had}

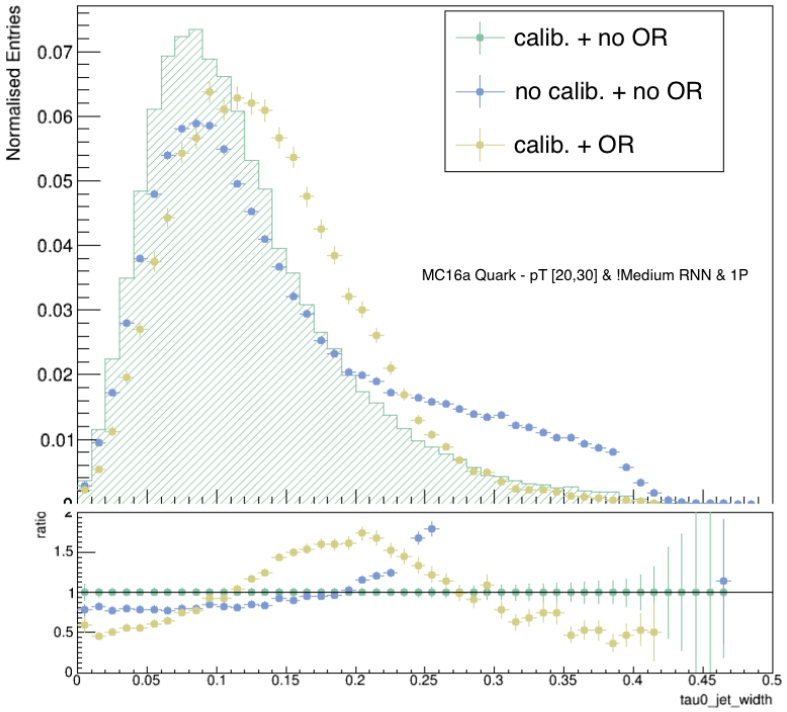

Figure 5.14: Distributions of track based jet width for quark faking 1-prong τ_{had} objects using no calibration and no OR (blue), calibrated and no OR (green), calibrated and OR (yellow). Distributions have been derived using MC simulations for the 2015-2016 running conditions, for $p_T \in [20,30]$ GeV and RNN score between 0.01 and the Medium working point.

that normally populate the tail of the distribution are renormalised in a way that now allows them to fail the track-based jet width requirements, thus also explaining the large increase in track-based jet width values of -1. Therefore, the ratio between the two histograms is approximately flat in the bulk of the distributions, with the large shape discrepancy being observed primarily in the tail. By comparing the green and yellow histogram shapes, it is clear that the OR procedure introduces a shift in the track-based jet width distribution towards higher-p_{T} values. This is due to the fact that lower-p_{T} tracks will generally have "larger cones" and thus have a higher probability of overlapping with other objects.

DAOD Selection

The ATLAS experiment has produced many different analysis derivations to cover the full ATLAS physics program. For this study only a small specific subset of the available derivations are considered. These are the TAUP3, SUSY11 and HIGG4D2 derivations. These derivations have been specifically chosen because the "derivation selections" applied in them do not affect the kinematic properties of the tau leptons, via direct skimming or slimming of the tau containers nor by requesting a minimum BDT or RNN identification algorithm score requirement. This results in DAOD samples, whose τ-lepton kinematics should be completely unbiased by the derivation used.

Table 5.6 shows the skimming used within each derivation and the derived samples. Different samples have been processed using different derivation because the selection applied in

the DAODs limit the possible samples whose events pass the specified selection. For example, TAUP3 DAOD can be applied to W + jets samples but will be less efficient on di-jet samples due to the requirement of having at least one tau and one muon present in the event which, due to low multiplicity of real muons in this type of decay, would reduce the statistics of the latter sample significantly.

Table 5.6: Derived AOD selections and samples used. LP samples have all been produced using the TAUP3 derivation with the exception of LP di-jets.

Derivation	Samples	Selection
SUSY11	HP Di-jet	single-jet trigger skim and τ $p_T > 15$ GeV with 1 or 3 charged tracks
HIGG4D2	HP Z+jets	at least one τ with $p_T > 18$ GeV and $\Delta R < 0.6$, non-cosmic ("good") muon [98] with $p_T > 12$ GeV, electron with $p_T > 15$ GeV passes: the electromagnetic calorimeter-based isolation [154] *Medium* working point OR the likelyhood-based identification [145] *Medium* working point and there is a jet with $p_T > 18$ GeV
TAUP3	HP W+jets LP samples*	at least one non-cosmic muon [98] with $p_T < 20$ GeV, at least one τ with $p_T > 18$ GeV with 1 or 3 charged tracks and at least one primary vertex in event with more than 3 associated tracks

The effect of the different DAODs to the same sample is is shown by Figure 5.15, where the HP $Z \rightarrow \mu\mu$ and $Z \rightarrow ee$ are derived using both TAUP3 and HIGG4D2 derivations and are subsequently merged into a unique Z + jets sample, for each derivation. The track-based jet width distribution for gluon-faking 1 prong τ_{had} are derived and plotted against each other using these two different samples in the anti-*Medium* RNN region, for p_{T} bin $\in [20,30]$. The distributions show very good agreement, indicating that that there is no apparent bias on the τ_{had} reconstructed objects kinematics introduced with the implementation of the DAOD selection.

5.6 Proof of concept

Section 5.3 describes how pure quark or pure gluon regions with (i. e. regions with $q_f = 1$ or $g_f = 1$) will have the same respective FF_q and FF_g values, independent of the sample used. In turn, this indicates that different sample's quark and gluon track based jet width distributions should also be very similar, yet not necessarily identical if we take into account statistical and systematic variations. This property of universality between pure quark and pure gluon regions is referred to as the FF and template universality and is a key property required towards achieving proof of concept for the universal FF method.

5.6.1 Template universality

Figure 5.16 shows the track based jet width templates, separated into the different p_{T} bins (as described in Section 5.5.2) for the 1 prong (left) and 3 prong (right) gluon fake-τ jets with BDT score ranging from 0.05 up to the *Medium* BDT working point, without JVT or trigger requirements for the di-jet (black), W + jets (red) and Z + jets (green) samples. Only samples that

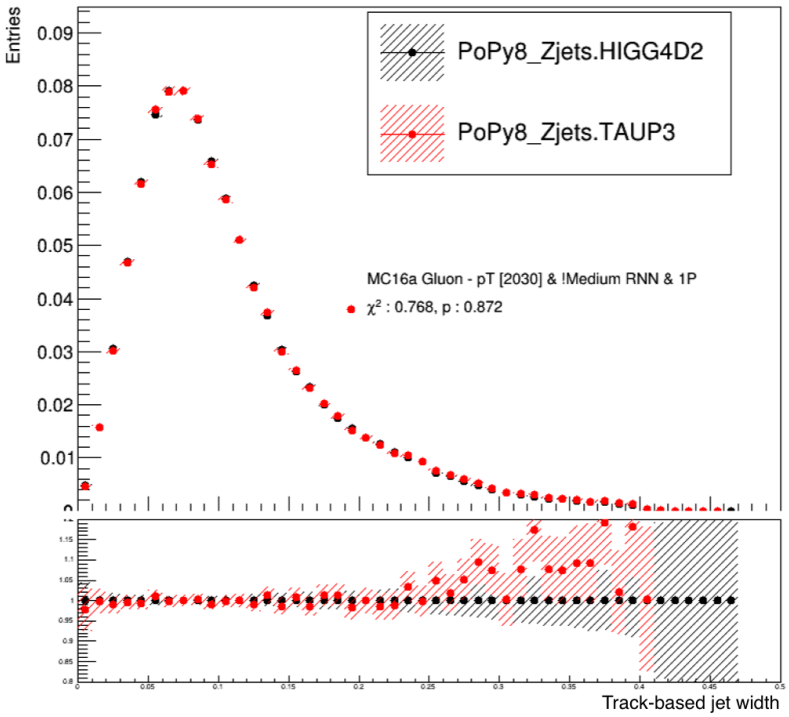

Figure 5.15: MC16a tau-faaking gluon initiated jet track based jet width template between HIGG4D2 (black) and TAUP3 (red) Z+jets derivation samples. The χ^2 value with corresponding p-value is shown on plot, indicating a statistical correlation between the two distributions at 95% CL.

simulate the pileup conditions during 2016 data taking are shown[7], normalised to unity. The templates have very similar shapes up to the high p_{T} bins where more discrepancies are observed. In these high-p_{T} bins the sample statistics are very low, which allows the event weight to be more significant and thus translate into uneven distributions with large jumps in the data points. Figure 5.17 shows the same track-based jet width templates for the quark initiated fake-τ jet objects. The same selection used for the gluon templates is used. These distributions show regions of pure quark and gluon fake-τ jets, that have been identified and selected using the truth-matching procedure. Because of the consistent shapes of the distributions observed across samples and p_{T} bins, the templates indicate a track-based jet width universality between samples. Some differences are observed in the higher p_{T} bin distributions due to the lower statistics of the samples, making the distribution more susceptible to event weight variations.

Figure 5.18 shows the track based jet width template for the quark, gluon and un-matched tau-faking jets. A good separation is observed between the quark and gluon templates, as expected. However, very similar templates are observed in the lower p_{T} bins of the di-jet sample between the gluon and un-matched candidates. This suggests that the un-matched candidates could be used as a statistical supplement to the gluon template for some of the samples where the templates match. As explained in Section 5.5.2, the different pileup condition, simulated to reflect the Run-2 data taking period run conditions, have a direct effect on the jet width templates of the tau-faking partons. In particular, the un-matched candidates are heavily affected

[7] The full set of templates for all p_{T} bins, and all average pileup conditions (2016, 2017, and 2018) can be found in Appendix C.1

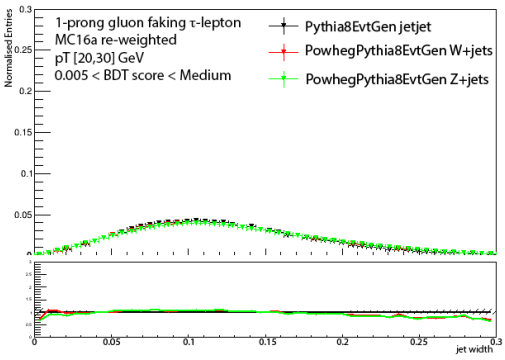

(a) 1 prong τ_{had} - $20 < p_T < 30$ GeV

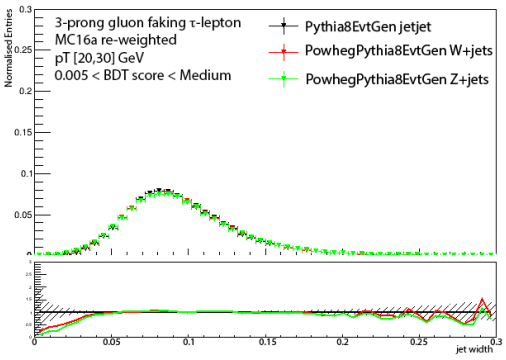

(b) 3 prong τ_{had} - $20 < p_T < 30$ GeV

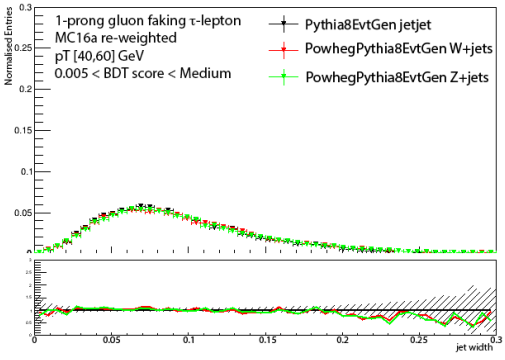

(c) 1 prong τ_{had} - $40 < p_T < 60$ GeV

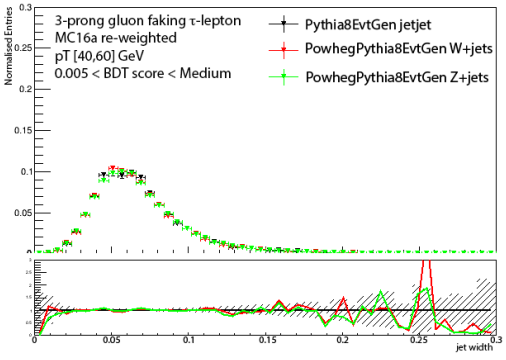

(d) 3 prong τ_{had} - $40 < p_T < 60$ GeV

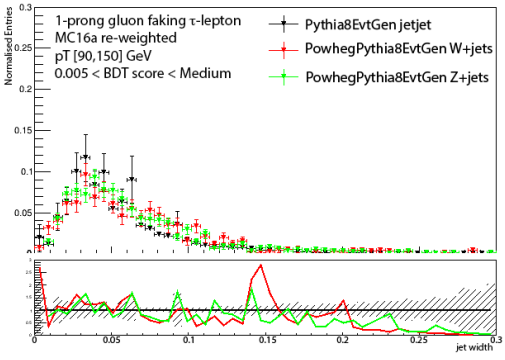

(e) 1 prong τ_{had} - $90 < p_T < 150$ GeV

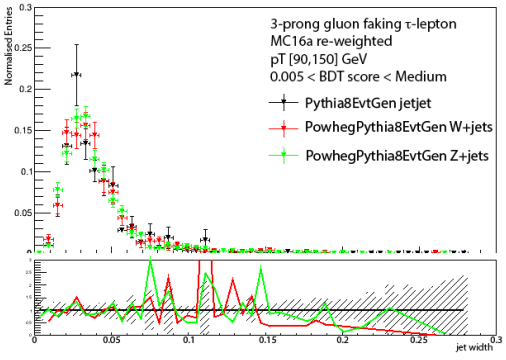

(f) 3 prong τ_{had} - $90 < p_T < 150$ GeV

Figure 5.16: Track based jet width templates of gluon initiated fake-τ jets for the multijet (balck), W + jets (red), and Z + jets (green) MC simulated samples. Separated into p_{T} bins of 20-30 GeV, 40-60 GeV and 90-150 GeV going from top to bottom. Left column row shows templates for 1 prong tau, and right column for the 3 prong tau.

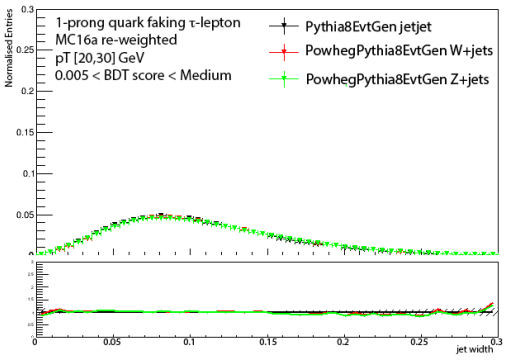

(a) 1 prong τ_{had} - $20 < p_T < 30$ GeV

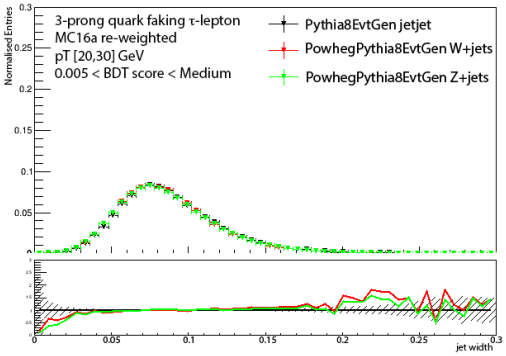

(b) 3 prong τ_{had} - $20 < p_T < 30$ GeV

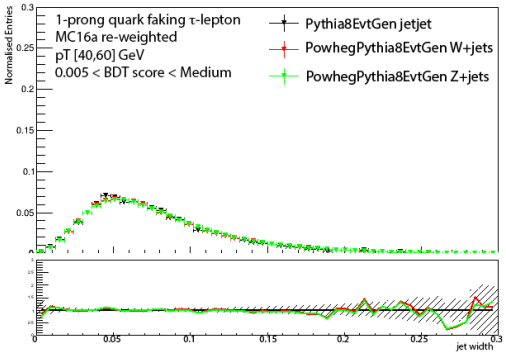

(c) 1 prong τ_{had} - $40 < p_T < 60$ GeV

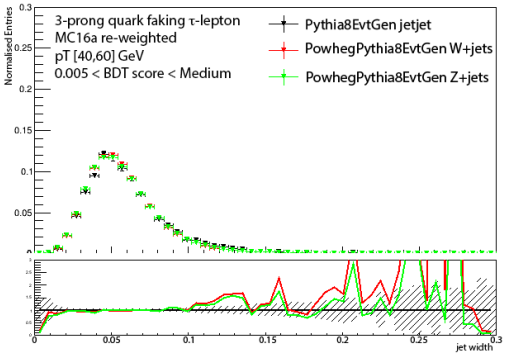

(d) 3 prong τ_{had} - $40 < p_T < 60$ GeV

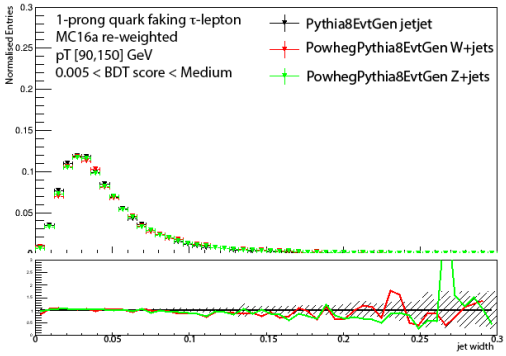

(e) 1 prong τ_{had} - $90 < p_T < 150$ GeV

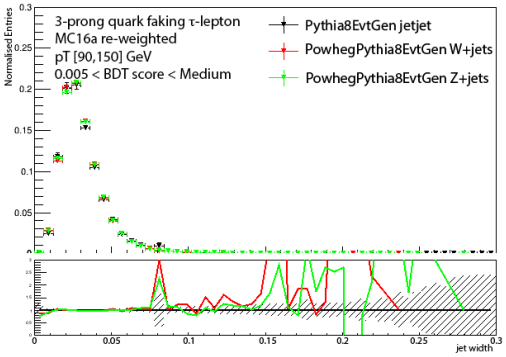

(f) 3 prong τ_{had} - $90 < p_T < 150$ GeV

Figure 5.17: Track based jet width templates of quark initiated fake-τ jets for the multijet (balck), W + jets (red), and Z + jets (green) MC simulated samples. Separated into p_{T} bins of 20-30 GeV, 40-60 GeV and 90-150 GeV going from top to bottom. Left column row shows templates for 1 prong tau, and right column for the 3 prong tau.

by the pileup conditions and multiplicity of the studied sample. This is particularly evident in the different track based jet width distributions of the un-matched candidates between the Z + jets and di-jet sample. The effect of pileup on the shape of the un-matched candidates track based jet width templates will be discussed in more details in Section 5.7.

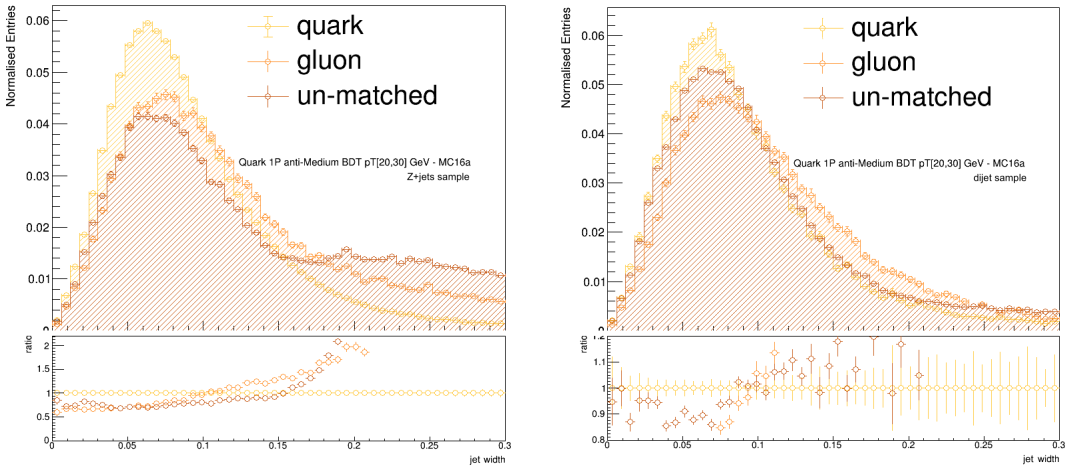

(a) (b)

Figure 5.18: Distributions of track-based jet width for quark, gluon and un-matched candidates in Z+jet (left) and dijet (right) samples. Ratio plot between the quark and other samples partons is shown in the bottom plot of the diagrams.

5.6.2 FF universality

Using the same selections as in the previous section, the p_{T} distributions for the quark, gluon, and un-matched candidates in the Z + jets, W + jets, and di-jet samples have derived, as well as the corresponding FF values as a function of leading τ_{had} p_{T}, as shown in Figure 5.19.

In these plots the binned p_{T} distributions for the leading τ_{had} faking quark, gluon, and un-matched jet initiated fake-τ candidates that pass (solid line) and fail (dotted line) the *Medium* BDT identifier working point, with corresponding FF values binned into the appropriate p_{T} bins for each sample, are shown. The FF values are found to consistent between samples, albeit with some small differences due to kinematic and statistical effects, and dependent on p_{T}. This shows that FF universality seems to be present between the different samples, as predicted by the universal FF method.

5.7 DAOD Templates

For the fitting procedure the quark, gluon, and un-matched candidate templates are needed from different processes and samples. To account for the τ_{had} biases introduced by derivations, the parton templates have also been derived using DAOD samples.

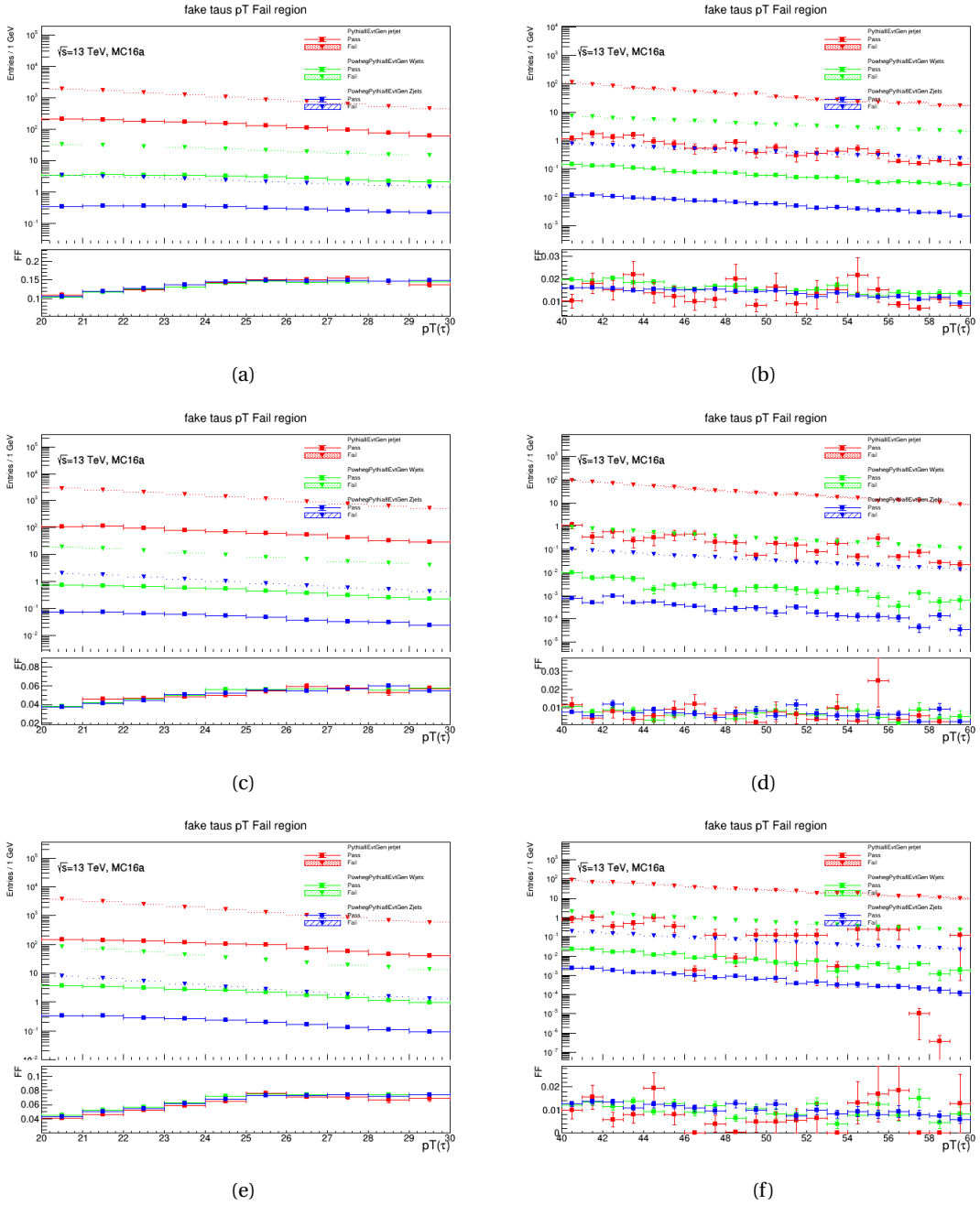

Figure 5.19: Distribution of visible τ_{had} p_{T} for quark (top) and gluon (middle) and un-matched (bottom) tau-faking jet candidates pass and fail region for the "Medium" BDT working point in p_{T} bins 20-30 GeV (left) and 40-60 GeV (right). Bottom plots show corresponding FF values.

5.7.1 Quark templates

Figure 5.20(a) shows the quark distribution between di-jet, Z + jets, and $t\bar{t}$ samples for the 1 prong τ_{had} candidates that fail the RNN identification working point, with p_{T} bin $\in$ [20,30] GeV. Significant agreement is observed between the di-jet and Z + jets templates but a large shift in the track-based jet width distribution is observed in the $t\bar{t}$ sample.

Upon closer inspection of the quark initiated fake-τ jets, the track-based jet width distribution was found to be directly dependent on quark-type, where the mean value of track-based jet width increases for increasingly heavier quarks. For a b-jet abundant sample such as the $t\bar{t}$, this translates to a general shift of the track-based jet width distribution towards larger values for all p_{T} bins. Figure 5.20(b) shows the track-based jet width templates for quark-initiated fake-τ jets in the di-jet, Z + jets, and $t\bar{t}$ samples using the same selection used in Figure 5.20(a), but now rejecting track-based jet width values deriving from fake-τs truth matched to a b-jet quark. The resulting templates show good agreement, with little change observed in the Z + jets and di-jet templates (which is expected), while a large shift towards smaller values of track-based jet widths is observed in the $t\bar{t}$ template that allows for better agreement with the di-jet and Z + jets templates.

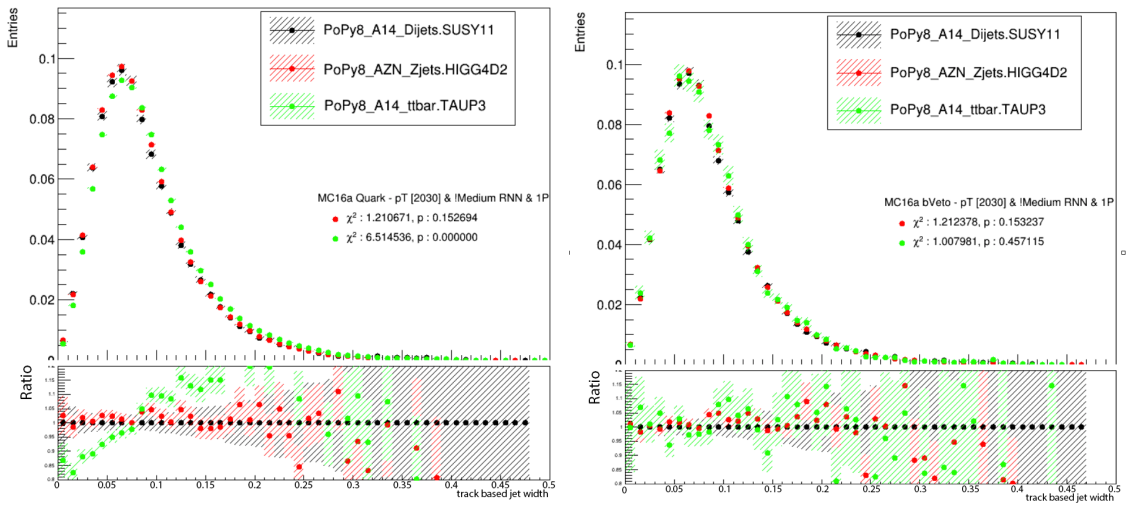

(a) (b)

Figure 5.20: Quark initiated tau-faking jets track-based jet width distribution between di-jet (black), Z + jets (red) and $t\bar{t}$ (green) samples. All histograms have been normalised to unity and have been re-weighed to the di-jet Quark p_{T} distribution. The χ^2 value with corresponding p-values (with respect to the di-jet distribution) are shown for each histogram.

5.7.2 Gluon templates

Similarly to the previous section the gluon templates have been studied in closer detail. Figure 5.21 left-hand side plot (a) shows the track-based jet width distributions between the PYTHIA 8 di-jet, POWHEG+PYTHIA 8 Z+jet and SHERPA 221 W/Z + jets samples. A significant shift

is observed between the templates, with the SHERPA 221 (POWHEG+PYTHIA 8) sample being shifted towards lower (higher) track-based jet width average values. This effect is caused by the different generator used to simulate the parton level objects. Depending on the PDF set and parton showering used at generator level, different kinematic distributions for the parton objects are obtained, which in turn affect the kinematic properties of the partons themselves. This translates to a slight change in the shape of the track-based jet width distribution observed. To account for this effect a "shift factor" is derived. By shifting the template of the Z + jets template by some fractional amount (which will be referred to as the "shift factor") it is possible to obtain an optimised track-based jet width distribution that minimises the χ^2 value between the di-jet and Z + jets samples template shapes, as shown in Figure 5.21(b). Therefore, the derived "shift factor" can be used as a systematic error to account for the different generators that have been used to produce the different set of samples. This systematic error should be included when evaluating the errors associated with the fitting procedure, described in detail in Section 5.8.

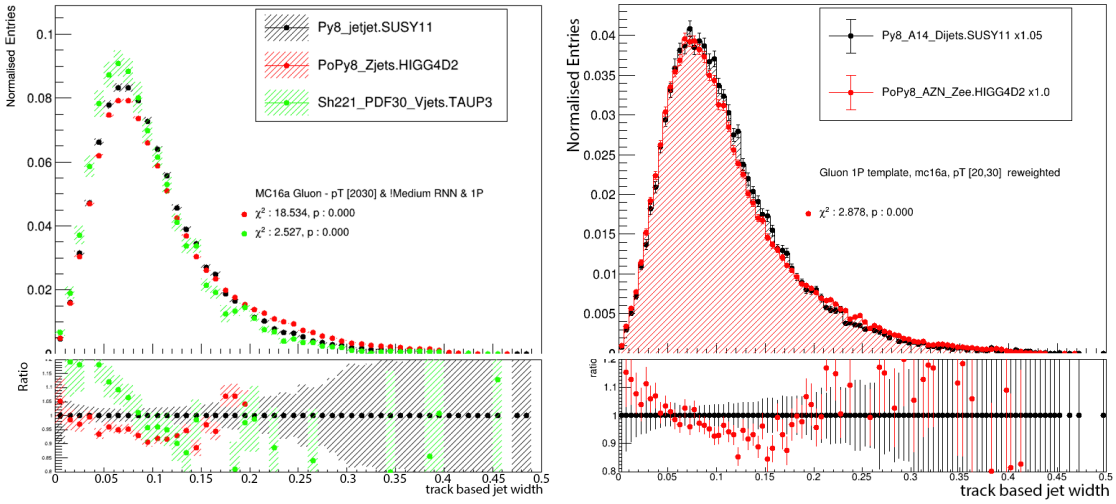

(a) (b)

Figure 5.21: Gluon-initiated tau-faking jets, track-based jet width distribution between di-jet (black), Z+jets (red) and W/Z + jets (green) samples. All histograms have been normalised to unity and have been re-weighed to the di-jet Gluon p_{T} distribution. The χ^2 value with corresponding p-values (with respect to the di-jet distribution) are shown for each histogram.

5.7.3 Un-matched jet templates

As defined in Section 5.5.2, the un-matched candidates are fake-τ jet objects which either fail the truth matching procedure or for which no seeding jet is found. The un-matched candidates have also been found to be primarily composed of pile-up jets. The kinematic distributions of the un-matched candidates should, thus, be heavily affected by the selection used on the derivation sample. The derivation selection used on the di-jet sample will by construction, due to the low threshold requirement of having to pass a single-jet trigger and have a reconstructed τ_{had} for it to be accepted, be more prone to contain pile-up jets in its events. Inversely, the derivation selections used for the Z + jets and $t\bar{t}$ samples, which only require one muon and

one τ_{had} for the event to be accepted, will have a lower probability of containing pile-up jets in the final stored events. This effect is clearly shown in Figure 5.22, which shows the track-based jet width distributions between the SUSY11 di-jet, HIGG4D2 Z + jets and TAUP3 $t\bar{t}$ samples by the black, red and green points respectively. The plot shows a large discrepancy in the shape of the distributions between the di-jet and Z + jets. This clearly indicates the effect that pile-up jets have on the shape of the un-matched candidates track-based jet width templates. The derivation used has a clear impact on the track based jet width template shape of the un-matched candidates, and must therefore be taken into account in the fit. The un-matched candidates' shape will differ significantly depending on the selection used and must thus be taken into account when fitting the MC templates to a data region to derive the appropriate quark fraction.

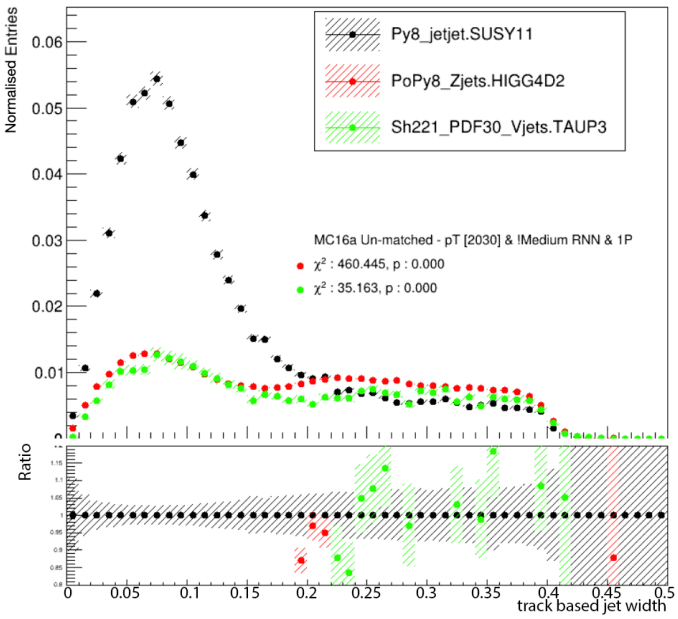

Figure 5.22: Un-matched candidate-initiated tau-faking jets track-based jet width distribution between di-jet (black), Z + jets (red) and $t\bar{t}$ (green) samples. All histograms have been normalised to unity and have been re-weighed to the di-jet un-matched p_{T} distribution. The χ^2 value with corresponding p-values (with respect to the di-jet distribution) are shown for each histogram.

5.8 Fitting Procedure and Tool development

The ATLAS collaboration is currently developing the TFFT [155] as a single executable in the ATLAS analysis program ATHENA 21.2 [156]. The aim of the tool is to perform "on-the-fly" interpolation for any user-given SR that fails the identification classifier working point of interest, to derive the corresponding τ-lepton FF values with associated uncertainties. The workflow of the TFFT, as well as the required inputs and output are shown in Figure 5.23. The TFFT requires the user to provide the p_{T} and jet width histograms for the relevant SR. The ATLAS dedicated task-force in charge of providing methods components and tools for the determination of the fake-τ background, which has also been developing the TFFT, has been working towards the preparation of the other required inputs for the tool. The provided inputs include the data re-

gion, and MC parton p_{T} and jet widths templates. The TFFT performs the p_{T} re-weighing on given jet width templates as discussed in Section 5.7, determines the quark fraction of the input sample, and derives the FF by interpolation with systematic error calculation.

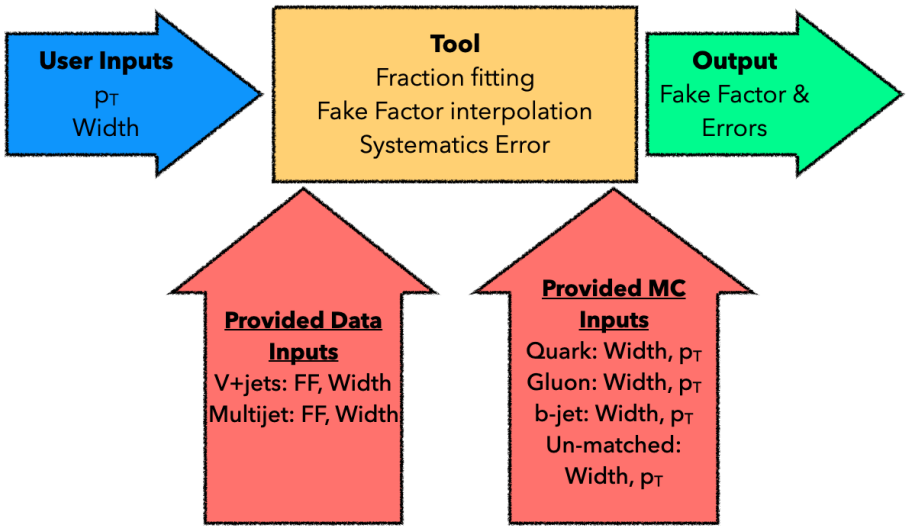

Figure 5.23: Illustration of general workflow of TFFT. The TFFT requires histograms of p_{T} and jet widths from the user as inputs to the tool. The dedicated ATLAS task-force provides the p_{T} and jet width histograms for data-region and MC partons inputs required for the interpolation and quark fraction fitting.

Quark Fraction determination

The quark fraction is determined by a fit to data using the quark, b-jet, gluon, and un-matched MC templates as parameters. The discriminating variable used is the track based jet width are described in Section 5.3. The fitting procedure is performed using a minimum log-likelihood method, implemented using HISTFACTORY [135] for the likelyhood building and MINUIT [157] for minimization.

To test the fitting procedure a known mixture of Z→ $\mu\mu$ and multi-jet events was used to derive the fraction of multi-jet events (α_{MJ}) in the sample using the tool. The two samples used for this test have been normalised to the number of Z→ $\mu\mu$ events. The mixture has been set to 60% Z→ $\mu\mu$ events and 40% multi-jet events. Figure 5.24 shows the result of the TFFT fitting procedure using this sample mixture, not considering systematic constraints or the effect of statistical uncertainty. The fit is able to reproduce the fraction of multi-jet events ($\alpha_{MJ} = 0.4$) with a very small χ^2 value, indicating a perfect reconstruction of the known mixture of the two samples. The black dots indicate the template of the mixture, while the green and red markers indicate the Z→ $\mu\mu$ and multi-jet events templates, respectively, that have been used to produce the fit, which is shown as the solid blue line on the plot. The ratio of the fitted template and the mixed template is shown in the bottom plot, which is found to be 1 across the whole range of jet width values. This validates the fitting procedure's ability to reproduce the correct fraction of multi-jet events in the sample.

In order to model the fit results with the addition of systematic uncertainties, the following

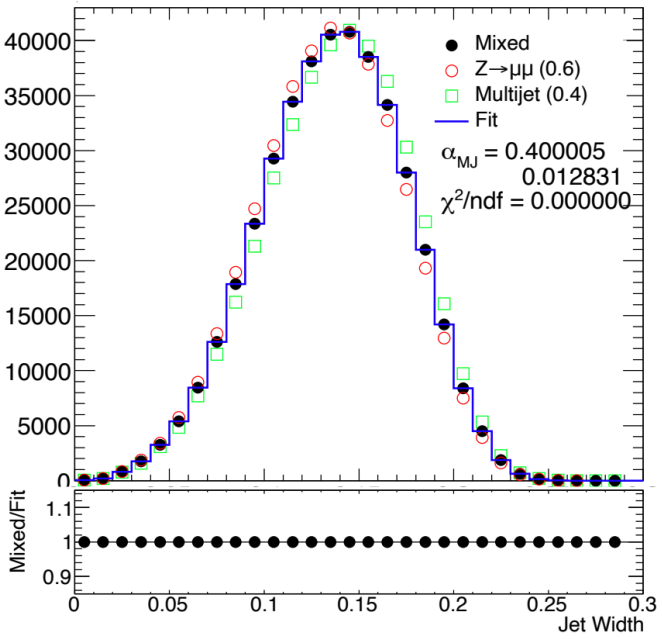

Figure 5.24: Fit of Z→ $\mu\mu$ and multi-jet data templates to a known mixture of the two. Fit does not consider any constraint terms describing systematic variations. Templates correspond to one prong, 20-30 GeV τ_{had} candidates that fail the *Medium* BDT working point.

constraint terms have been tested:

Flat Systematic Uncertainty: log-normal constraint of ±5% of the bin content of each sample. For this type of systematic ±5% represents ±1σ.

Shape Shift Uncertainty: log-normal constraint of Gaussian variation for each bin centred at 0 with σ of 1 for both "up" and "down" variation.

Template Statistical Uncertainty: Gaussian constraint that uses a modified version of the Barlow-Beeston method [158], which considers the relative statistical uncertainty for all samples combined.

By implementing the aforementioned constraints simultaneously in the fitting procedure, in order to mimic the inclusion of systematic and statistical uncertainties, the templates and fitting can be re-performed for the mixed samples as shown by Figure 5.25. On the left, the result of the fit is shown with both Z→ $\mu\mu$ and multi-jet templates. The right plot shows the pull plot of the included systematic variations. The fit shows a slight increase in error from 1.3% to 2.5% with $\chi^2 << 1$, which is indicative of an "Asimov" type fit to a precisely know data sample. The "pull" plot indicates that the fit result is consistent with the expectation that the templates are precise, given the known mixture of the data sample. The exception is "fraction multi-jet," which corresponds to the fraction of multi-jet events in the sample. This is due to starting point for both templates being declared as 50%, making this kind of pull expected.

Since the FF interpolation contains three unknowns, α_Z, α_{MJ} and α_{SR}, the fraction fitting procedure is the most important part of the TFFT. The fitting procedure performed for the

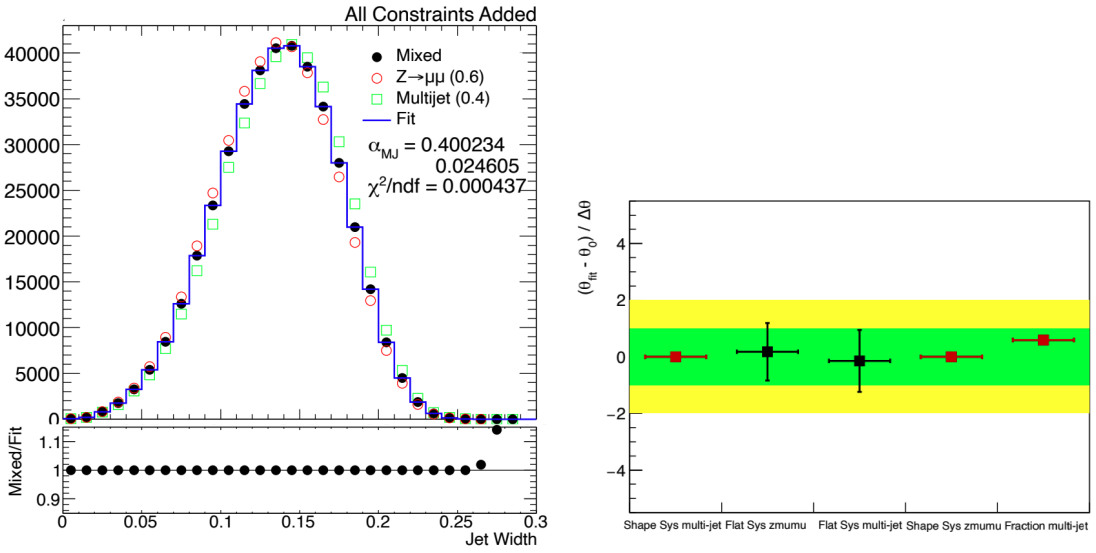

(a) (b)

Figure 5.25: Left hand plot shows fit of Z→ $\mu\mu$ and multi-jet data templates to a known mixture of the two. Systematic variations constraint terms have been taken into account when performing fit. Templates correspond to one prong, 20-30 GeV τ_{had} candidates that fail the *Medium* BDT working point. Right hand plot shows "pull" plot of the relevant systematics included in the fitting procedure performed in the left plot.

determination of the quark-fraction of a given sample using the calibrated quark, b-jet, gluon, and un-matched τ_{had}-faking jet candidate templates is shown in Figure 5.26. The 20-30 GeV p_{T} bin is shown for the candidates that fail the *Medium* RNN identification criteria working point. The mixed sample used in this case has a quark fraction (α_q) of 50%. The fit has improved significantly with the inclusion of the un-matched and b-jet templates as parameters to the fit, resulting in a $\chi^2 < 5$ and a α_q=0.512±0.004. It is important to note that appropriate systematic uncertainties need to be identified and implemented into the quark fraction fitting procedure for a proper estimate of the quark fraction and fit to be derived.

The TFFT is therefore showing promising results towards the derivation of FF values via template fitting and interpolation. The use of track based jet width as the discriminating variable shows some promise in its ability to correctly identify the true quark fraction in a given sample when using the 4 parameter fit derived from MC: the quark, gluon, un-matched, and b-jet fake-τ_{had} candidate jets, as well as the MC pileup template in the form of un-matched candidates. There are still aspects that need further investigation such as ambiguities in the definition of the τ_{had} candidates, including non-uniformity across different object selection frameworks, that are required to test to the robustness of the fit. Furthermore, all systematic uncertainties described in the previous sections need to be fully identified and implemented in the quark fraction fitting procedure.

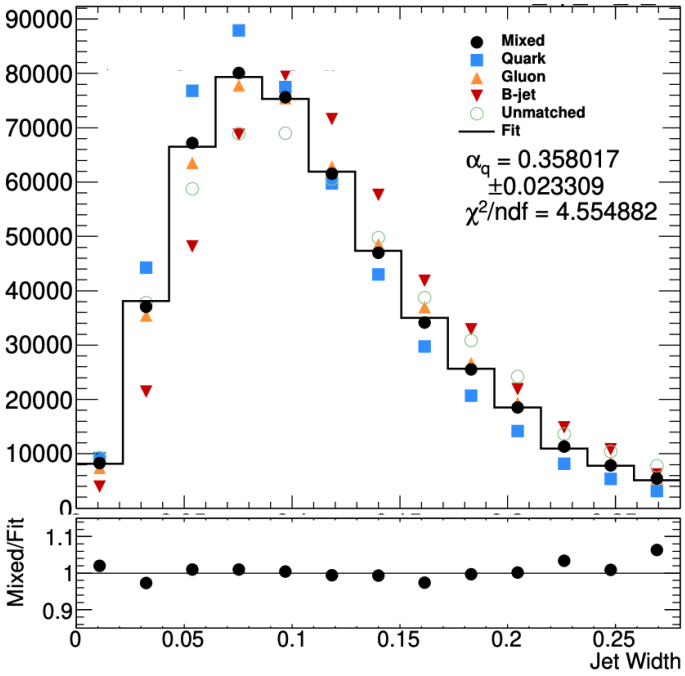

Figure 5.26: Fit of Z→ $\mu\mu$ and multi-jet data templates to a known mixture of the two. Fit does not consider any constraint terms describing systematic variations. Templates correspond to one prong, 20-30 GeV τ_{had} candidates that fail the *Medium* RNN working point.

5.9 Summary

This chapter presented the strategy and implementation of the universal fake factor method for the estimation of the number of fake tau objects present in any SR of interest. The studies and tests done towards the ongoing development of the TFFT are also presented, including the currently available inputs provided by the dedicated ATLAS task force. The work presented in this chapter has been proposed for presentation at several national conferences, including the Sussex Student Conference 2020[8], and is expected to be summarised in a paper by the analysis group conveners.

[8] Link to abstract: https://docs.google.com/document/d/1B4myu9WOYEt-N_h1xjHOJLjrfHtg734BpJhSb0jal_0

FUTURE SEARCHES

6

You can't always get what you want. But if you try sometime, yeah. You just might find, you get what you need.

The Rolling Stones

In this chapter a discussion of the plans for future searches for the SUSY τ-lepton spartner in the third data collection run of the LHC are presented. A strong emphasis is given towards the study of SUSY signals with $\tilde{\tau}$ production in association with Vector Boson Fusion (VBF) for the exploration of the compressed mass regions and the development of a new trigger strategy for the efficient selection of events of interest to the general ATLAS $\tilde{\tau}$ analysis strategy. In Section 6.1, a summary of the current status of the direct-$\tilde{\tau}$ production analysis is provided, along with the current obstacles that are expected to be overcome with the collection of additional data during the third data-collection run of the LHC and the planned High Luminosity LHC described in Section 6.2. A study performed by the author, for the use of low-threshold triggers, that will be introduced for the High Luminosity LHC to improve the selection of di-$\tilde{\tau}$ production events, is given in Section 6.3. In Section 6.4, a description of some interesting topologies for the exploration of the $\tilde{\tau}$ mass compressed region via the production of $\tilde{\tau}$ sparticles in association with jets via VBF, along with the MC simulation process and the preliminary selection strategy used to isolate these SUSY samples is presented. Section 6.5 will show an initial study performed by the author to observe the kinematic properties of the simulated VBF SUSY topologies compared to the SM background. The author has also had significant involvement in the study comparing the achievable signal acceptance using a VBF trigger available during Run-2 to the di-tau+$E_{\mathrm{T}}^{\mathrm{miss}}$ trigger used in the analysis described in Chapter 4, with the goal of understanding the possible sensitivity gain achievable when using dedicated VBF triggers in the third data-collection run of the LHC and beyond. The results of this study are presented in Section 6.6. Finally, in Section 6.7 a summary of the discussed studies and foreseen obstacles for future experiments in the search of SUSY sparticles is given, along with concluding remarks that highlight the main points of interest investigated within the chapter.

6.1 The compressed mass region

In Chapter 4, the most up to date limits on the mass of the $\tilde{\tau}$ particle are presented. These limits, however, show a large un-explored region for relatively small mass difference ($\Delta m = m_{\tilde{\tau}} - m_{\tilde{\chi}_1^0}$), which is generally referred to as the *compressed region*. In the direct $\tilde{\tau}$ production scenario, small Δm topologies would generally result in final states containing τ-leptons with very low p_T values ("soft"), that are below the current threshold at which τ-lepton objects can be reconstructed by the ATLAS detector. This makes the exploration of these compressed regions very experimentally challenging, but worth investigating nonetheless.

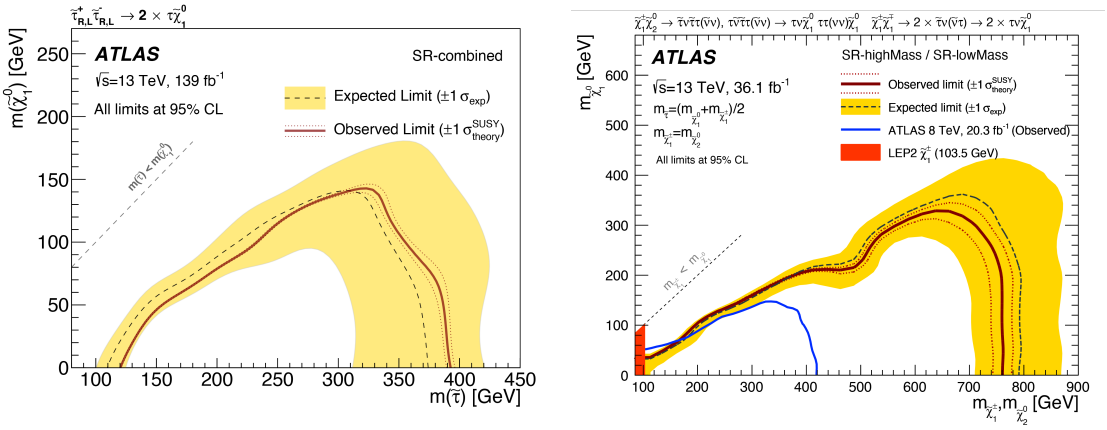

(a) (b)

Figure 6.1: Observed and expected 95% exclusion limits for simplified models with (a) direct $\tilde{\tau}$ pair production, and (b) $\tilde{\chi}_1^{\pm}$ and $\tilde{\chi}_1^0$ production with $\tilde{\tau}$. Plots are produced using 139 fb^{-1} and 36.1 fb^{-1} of proton-proton collisions data collected at $\sqrt{s}$= 13 TeV at the LHC by the ATLAS experiment and ATLAS+LEP, respectively.

Figure 6.1(a) shows the available exclusion limits for the mass of the $\tilde{\chi}_1^0$ candidate as function of the $\tilde{\tau}$ mass. The results shown in this figure have been derived using 139 fb^{-1} of data collected by ATLAS at the LHC with 13 TeV of proton-proton collisions, and are the result of the analysis described in Chapter 4. Similarly, the $\tilde{\chi}_1^0$ exclusion limits have been derived for $\tilde{\tau}$ channels mediated by other winos, such as the Chargino-Chargino and Chargino-Neutralino productions. The combined exclusion limits for these channels is shown in Figure 6.1(b). These limits have been derived using 36.1 fb^{-1} of data collected at 13 TeV by ATLAS at the LHC using proton-proton collisions at centre-of-mass energies $\sqrt{s}$= 13 TeV [159].

6.2 LHC Run-3 and beyond

Currently, the LHC is in the middle of its Long Shut-down 2 (LS2) during which the ATLAS detector is undergoing some required maintenance and upgrades to a few of the existing systems and sub-detector. Some of the most significant upgrades expected to be completed by the end of LS2 are the introduction of the New Small Wheel (NSW) to help the MS system towards the detection and precise measurement of muon leptons, a significant improvement to the current

L1 trigger system, and the implementation of a new multi-threaded based software framework (ATHENAMT). All these upgrades are expected to be of great importance for the successful performance of the third data-collection run of the LHC (Run-3). Run-3 is expected to begin in 2022 with a commissioning year, collecting 10-20 fb^{-1} of data. The following two years (2023-2024) are planned to be the main production years, aiming to collect $\sim 80\ \text{fb}^{-1}$ of pp collision data per year with the ATLAS detector. The goal for the beam energy is to achieve a centre-of-mass energy of $\sqrt{s}$= 14 TeV, although due to slow progress in magnet training, the $\sqrt{s}$ may be limited to 13.5 or even 13 TeV. In any case, during the production years the mean number of interactions per bunch crossing is expected to be $\langle\mu\rangle \approx 55$ for about 80% of the time, which is significantly higher than the previously measured $\langle\mu\rangle$ in Run-1 and Run-2 (refer to Figure 2.1). Run-3, therefore, provides many interesting challenges but also opportunities for further SUSY studies. The increase of luminosity could potentially permit for more "exotic" (i. e. lower production cross-section) channels to gain enough statistics to become relevant towards the study of the compressed mass regions not accessible to standard electroweak SUSY searches.

High Luminosity LHC

Plans for a High Luminosity LHC (HL-LHC) are already under way. The HL-LHC is expected to begin colliding protons soon after the end of Run-3. The aim of the HL-LHC is to deliver $\sim 2500\ \text{fb}^{-1}$ of pp collision data at around 5 times the nominal LHC luminosity ($5 \times 10^{34}\,\text{cm}^{-2}\text{s}^{-1}$) to the ATLAS experiment over ten years [160]. The increased luminosity will significantly enhance the capabilities of searches for new physics at the LHC, extending the reach for SUSY sparticle searches in the multi-TeV region. This is particularly exciting for the low production cross-section SUSY searches, which will benefit from the luminosity increase and the higher statistics. Furthermore, the potential increase of centre-of-mass energy to $\sqrt{s}$= 14 TeV will allow for searches in higher mass regions.

6.3 Low-threshold triggers

One of the main limiting factors to the study of the compressed regions are the triggers. As discussed in Section 6.1, the compressed $\tilde{\tau}$ mass region is largely populated by low-p_{T} τ-leptons. Currently, these soft objects are not being efficiently selected by the τ-lepton triggers used by ATLAS [130]. Therefore, it is important to study and understand the possible gain in sensitivity achievable by upgrading the ATLAS triggers to select lower-p_{T} τ-leptons for future analyses.

In this study, low offline p_{T} thresholds are compared to the *asymmetric di-tau* trigger described in Section 4.5 to study the possible achievable gain in sensitivity that a hypothetical low-threshold trigger could achieve. This new low-threshold di-τ trigger is currently under development within the ATLAS collaboration and planned to be implemented for the HL-LHC. To quantify the signal acceptance to background rejection a simplified version for the sensitivity

is defined:

$$\frac{S}{\sqrt{B}} = \frac{N_{signal}}{\sqrt{N_{background}}}, \tag{6.1}$$

where N_{signal} and $N_{background}$ are the number of signal and background events that pass the selection, respectively [161].

The lowered p_{T} thresholds to be studied for this proposed di-τ trigger are 40 GeV for the highest-p_{T} (*leading*) τ-lepton of the event and 30 GeV for the second highest p_{T} (*sub-leading*) τ-lepton. The even lower 20 GeV and 30 GeV thresholds for the leading- and sub-leading τ-leptons are also studied in this section. This study has been performed using similar MC simulated SM background samples as the ones described in Chapter 4, with the exception of the multijet background samples which have not been included. All available samples are combined and normalised to total of 139.0 fb^{-1}. A representative sub-set of the direct-$\tilde{\tau}$ signal samples used in the analysis described in the aforementioned Chapter have been used in this study. The signal samples have been simulated to have $\tilde{\chi}_1^0$ and $\tilde{\tau}$ masses of:

- 1 GeV and 100 GeV
- 1 GeV and 200 GeV
- 60 GeV and 100 GeV
- 100 GeV and 160 GeV
- 160 GeV and 280 GeV

and $\tilde{q}$ masses of 1.5 TeV, respectively. These signal points have been chosen to have a representative range of masses along the diagonal ([60,100] GeV, [100,160] GeV, and [160,280] GeV) and two points well contained within the already excluded mass region ([100,1] GeV and [200,1] GeV) for validation.

A basic set of pre-selection cuts are used to ensure the selection of relevant events for the study. For an event to pass this pre-selection, it is required to have 2 OS Tight τ-leptons that pass the asymmetric di-tau trigger along with its offline trigger requirements[1], or that pass the low offline p_{T} thresholds for the proposed di-tau trigger.

Figure 6.2 shows the resulting τ-lepton and $E_{\mathrm{T}}^{\mathrm{miss}}$ kinematic distributions for the simulated MC SUSY signal and SM background samples, when requesting that the asymmetric di-tau trigger has been fired in the event and matched a di-τ-lepton pair. Figures 6.3 and 6.4 show the same distributions, using the same selection but for the lowered offline p_{T} thresholds of $p_{\mathrm{T}}(\tau_1) = 40$ GeV and $p_{\mathrm{T}}(\tau_2) = 30$ GeV (will be shortened to "(40,30) GeV" for ease), and $p_{\mathrm{T}}(\tau_1) = 30$ GeV and $p_{\mathrm{T}}(\tau_2) = 20$ GeV (will be shortened to "(30,20) GeV" for ease), respectively.

As shown by these kinematic distributions, the asymmetric trigger is able to significantly reduce the background while also rejecting a significant amount of small Δm signal. On the other hand, the lower p_{T}-thresholds allow for more compressed signal events to pass but also

[1] Refer to Section 4.5 for asymmetric di-tau trigger offline requirements

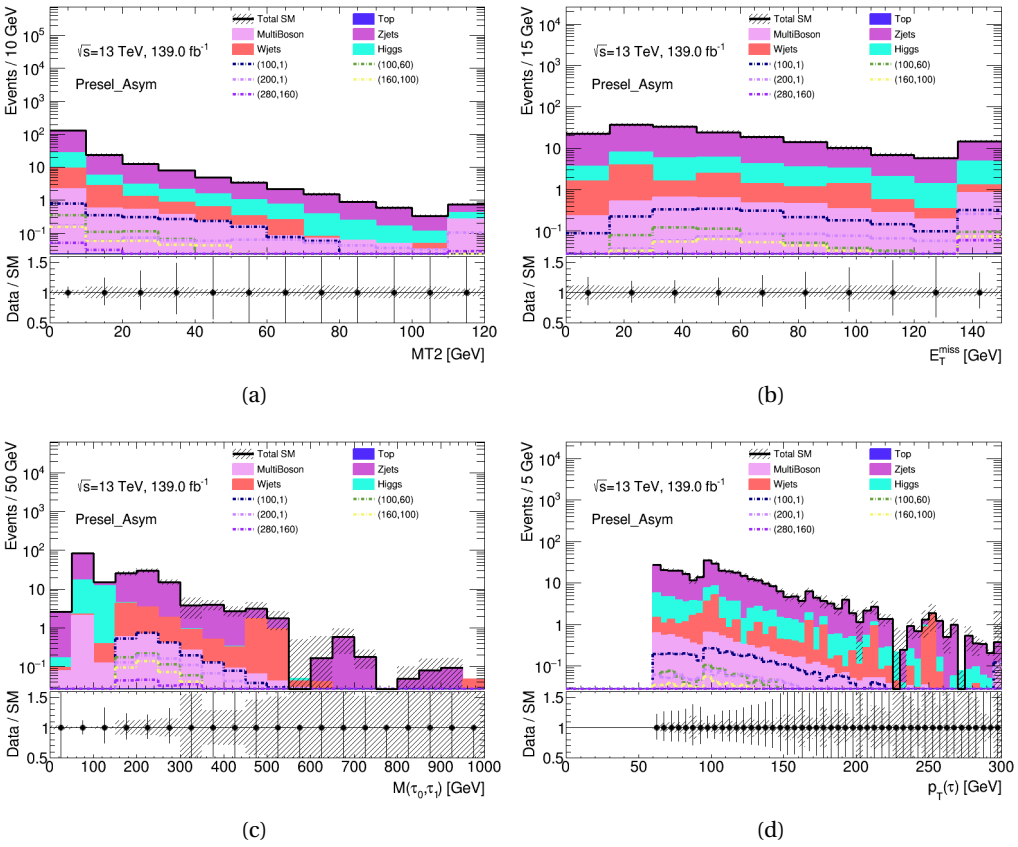

Figure 6.2: Distributions of (a) MT2, (b) $E_{\mathrm{T}}^{\mathrm{miss}}$, (c) $M(\tau_0,\tau_1)$, and (d) $p_{\mathrm{T}}(\tau)$ in the preselection region using the asymmetric di-tau trigger to select relevant events. Signal scenarios are shown by the dotted lines while SM MC samples displayed as stacked histogram. The shaded band include only systematic uncertainties in the background prediction.

have a very poor background rejection. The overall multiplicity of each background and signal in the given region is shown in Table 6.1, with the resulting sensitivity values shown in Table 6.2. The asymmetric di-tau trigger has significantly higher sensitivity to signal events with large Δm compared to the lowered thresholds selection. The compressed scenario mass signal points' sensitivities are observed to be of comparable values between the asymmetric trigger and lower thresholds, showing that there seems to be no significant improvement to the sensitivity when using these lower p_{T} thresholds.

However, unlike the asymmetric di-tau trigger that tends to reject a large portion of the compressed region signal point events, the lack of sensitivity of the lower-thresholds triggers is derived from the poor background rejection caused by the higher acceptance of events containing low momentum objects. A stricter event selection aimed at reducing some of the more prominent backgrounds, such as the W, Z, and Higgs boson production in association with jets, could help reduce background contribution to a level such that an improved significance for the compressed mass signals is observed. A dedicated SR created to take advantage of the lowered thresholds and target the compressed signal points should be considered for optimal results. Due to time limitation such region has not been derived and instead a version of the Low-mass SR described in Table 4.5 has been used in this study. The $MT2$ requirement

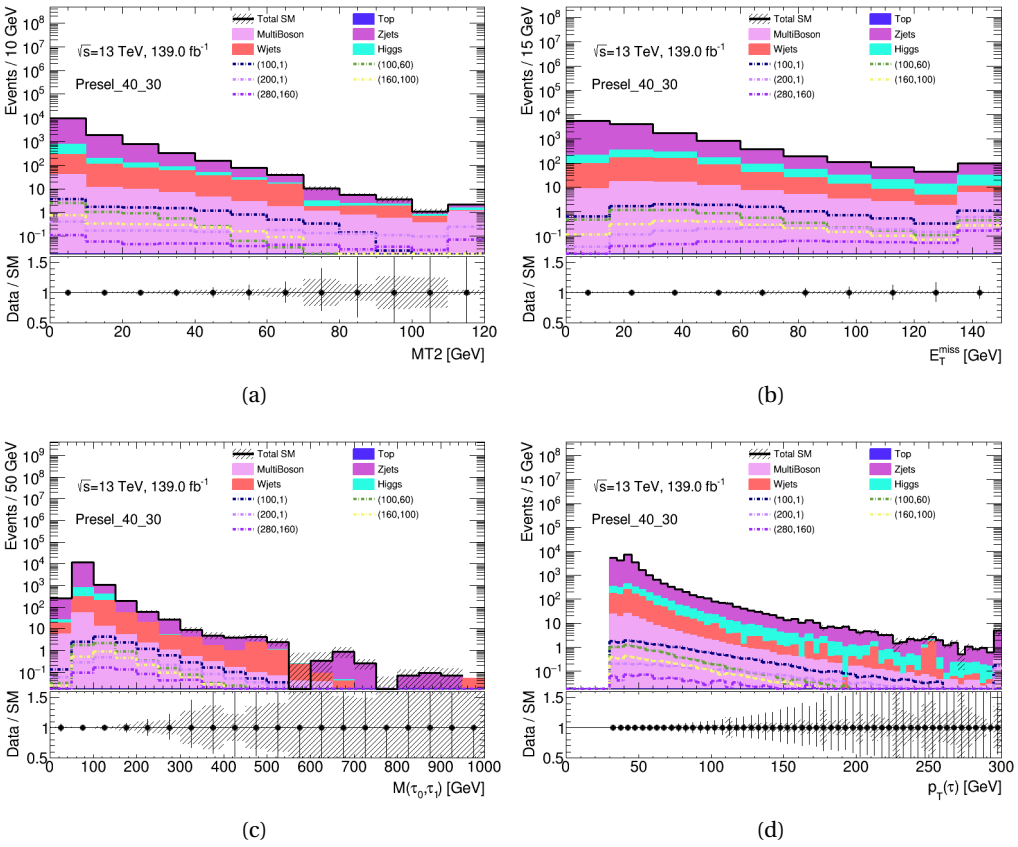

Figure 6.3: Distributions of (a) MT2, (b) $E_{\mathrm{T}}^{\mathrm{miss}}$, (c) $M(\tau_0,\tau_1)$, and (d) $p_{\mathrm{T}}(\tau)$ in the preselection region using the lowered $p_{\mathrm{T}}(\tau_0) > 40$ GeV and $p_{\mathrm{T}}(\tau_1) > 30$ GeV offline thresholds to select relevant events. Signal scenarios are shown by the dotted lines while SM MC samples displayed as stacked histogram. The shaded band include only systematic uncertainties in the background prediction.

($MT2 > 70$ GeV) has been lifted from the original set of selection cuts for this region in order to obtain slightly higher statistics.

The $E_{\mathrm{T}}^{\mathrm{miss}}$ and τ-lepton kinematic distributions for events that pass the asymmetric di-tau trigger in loosened Low-mass SR are shown in Figure 6.5. Similarly, Figures 6.6 and 6.7 show the same kinematic distributions for the lowered p_{T} thresholds (40,30) GeV and (30,20) GeV, respectively. The implementation of a tighter event selection, via the use of the Low-mass SR, has caused a significant reduction of SM background events with comparable event multiplicities for SUSY signals at high values of $MT2$. The overall multiplicity of events passing this loosened Low-mass SR selection for both signal and background processes is shown in Table 6.3. The multiplicities are shown for events passing the asymmetric di-tau trigger, or have leading and sub-leading τ-leptons with p_{T} of (40,30) GeV or (30,20) GeV.

Compared to the preselection, the implementation of the SR results in the number of accepted SM background events that pass the asymmetric di-tau trigger to decreases on average by a factor of ~20. For the lower p_{T} thresholds the SM background multiplicity reduces by around ~400-1500, with the Higgs background decreasing by $\mathcal{O}(1000)$ in magnitude. Similarly to the results observed when applying the preselection, when events are required to pass

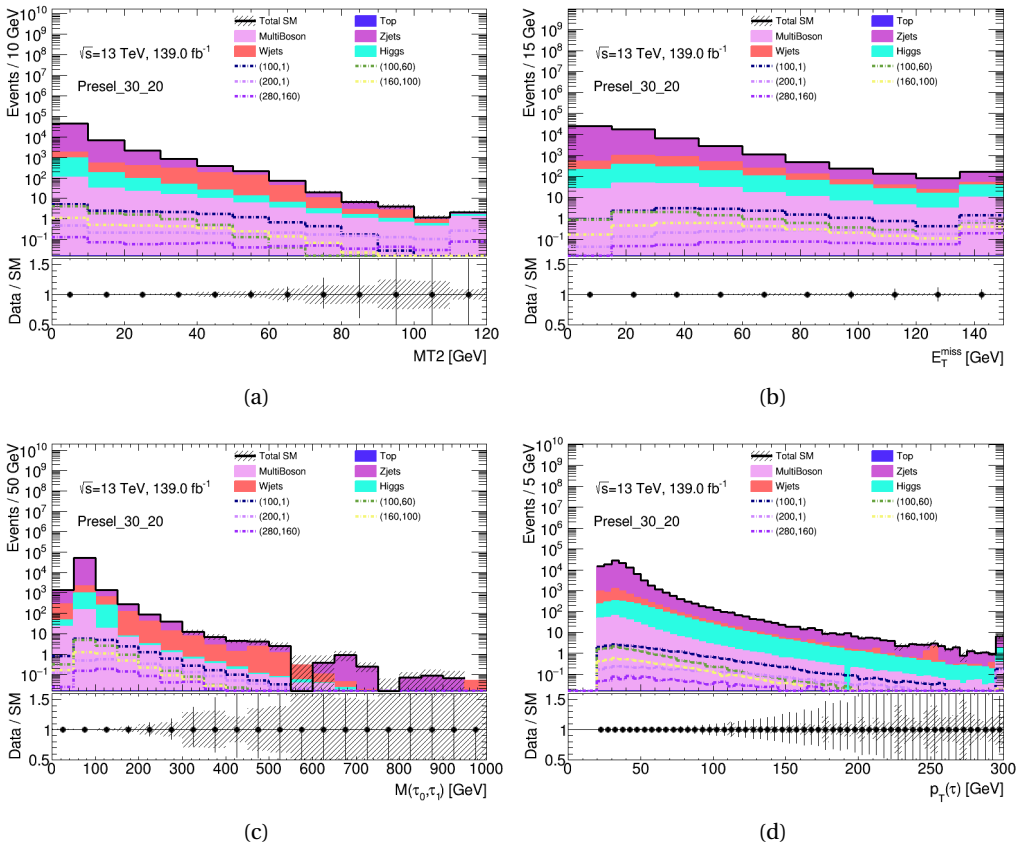

Figure 6.4: Distributions of (a) MT2, (b) $E_{\mathrm{T}}^{\mathrm{miss}}$, (c) $M(\tau_0,\tau_1)$, and (d) $p_{\mathrm{T}}(\tau)$ in the preselection region using the lowered $p_{\mathrm{T}}(\tau_0) > 30$ GeV and $p_{\mathrm{T}}(\tau_1) > 20$ GeV offline thresholds to select relevant events. Signal scenarios are shown by the dotted lines while SM MC samples displayed as stacked histogram. The shaded band include only systematic uncertainties in the background prediction.

the asymmetric di-tau trigger, a better background discrimination is achieved compared to when they are required to pass the lower p_{T} thresholds. This higher background discrimination comes at the cost of fewer signal events being accepted by the trigger, particularly for the compressed mass scenarios. On the other hand, the looser low-thresholds p_{T} requirements allow for enough signal events to pass the selection to make the resulting sensitivities comparable to the ones achieved by the asymmetric di-tau trigger and sometimes even greater, as shown by Table 6.4. For all signal points, the sensitivity increases with the implementation of the SR selections. The 40-30 GeV combination of low threshold selection shows the highest achievable sensitivity for the (100,1) GeV, (200,1) GeV, (100,60) GeV, and (280,160) GeV mass, while the 30-20 GeV combination achieves the highest sensitivity for the (160,100) GeV and (100,60) GeV mass points, albeit by a small margin.

This investigation shows some promising preliminary results towards lowering the trigger thresholds. The lowering of the trigger thresholds results in an initial drop in sensitivity achieved when no selection is applied, due to more background events being accepted by the trigger. However, this effect is counterbalanced by the higher signal acceptance which results in overall higher sensitivity values for the compressed mass points after the application of SR selections. It is also worth noting that a dedicated SR targeted to select for compressed SUSY

Table 6.1: Number of expected MC events corresponding to the signal and background prediction passing the preselection. Multiplicities are shown for the asymmetric trigger, leading and sub-leading tau p_{T} of 40 GeV and 30 GeV and leading and sub-leading tau p_{T} of 30 GeV and 20 GeV.

	Asym. Trigger	$p_T(\tau_1) > 40$ GeV $p_T(\tau_2) > 30$ GeV	$p_T(\tau_1) > 30$ GeV $p_T(\tau_2) > 20$ GeV
Background			
Multiboson	4.64	78.58	192.69
Wjets	11.05	510.08	1993.41
Top	0.00	0.00	0.00
Zjets	145.05	11881.93	52052.14
Higgs	26.71	639.67	1101.29
Total	187.45	13110.26	55339.53
$(\tilde{\tau},\tilde{\chi}_1^0)$ [GeV]			
(100,1)	2.24	11.29	15.94
(200,1)	0.81	2.09	2.49
(160,100)	0.40	2.26	3.28
(100,60)	0.65	5.34	9.07
(280,160)	0.20	0.59	0.70

Table 6.2: Signal sensitivity after application of preselection selection for the asymmetric trigger, leading and sub-leading tau p_{T} of 40 GeV and 30 GeV and leading and sub-leading tau p_{T} of 30 GeV and 20 GeV.

$(\tilde{\tau},\tilde{\chi}_1^0)$ [GeV]	Asym. Trigger	$p_T(\tau_1) > 40$ GeV $p_T(\tau_2) > 30$ GeV	$p_T(\tau_1) > 30$ GeV $p_T(\tau_2) > 20$ GeV
(100,1)	0.163	0.099	0.068
(200,1)	0.059	0.018	0.011
(160,100)	0.030	0.020	0.014
(100,60)	0.047	0.047	0.039
(280,160)	0.015	0.005	0.003

mass points would provide even better discrimination between background and signal events and thus yield even better sensitivity.

This is a preliminary study that does not take into account several aspects relating to the trigger objects and selections used in ATLAS. In this study, the lower thresholds were performed on offline reconstructed objects, rather than the online trigger object, like it is performed for the asymmetric di-tau trigger requirements. However, due to the current limitation of τ_{had} reconstruction within ATLAS, the study of the lower p_{T} threshold on trigger objects would have been non-trivial and beyond the scope of this project which was an initial proof of concept. Currently, the limiting factor for lowering the thresholds triggers is due to the challenges that arise from the reconstruction of low momentum τ-leptons. A significant amount of work is currently being conducted within ATLAS to address these challenges, making the possibility of low-threshold di-tau triggers in the future worth investigating further.

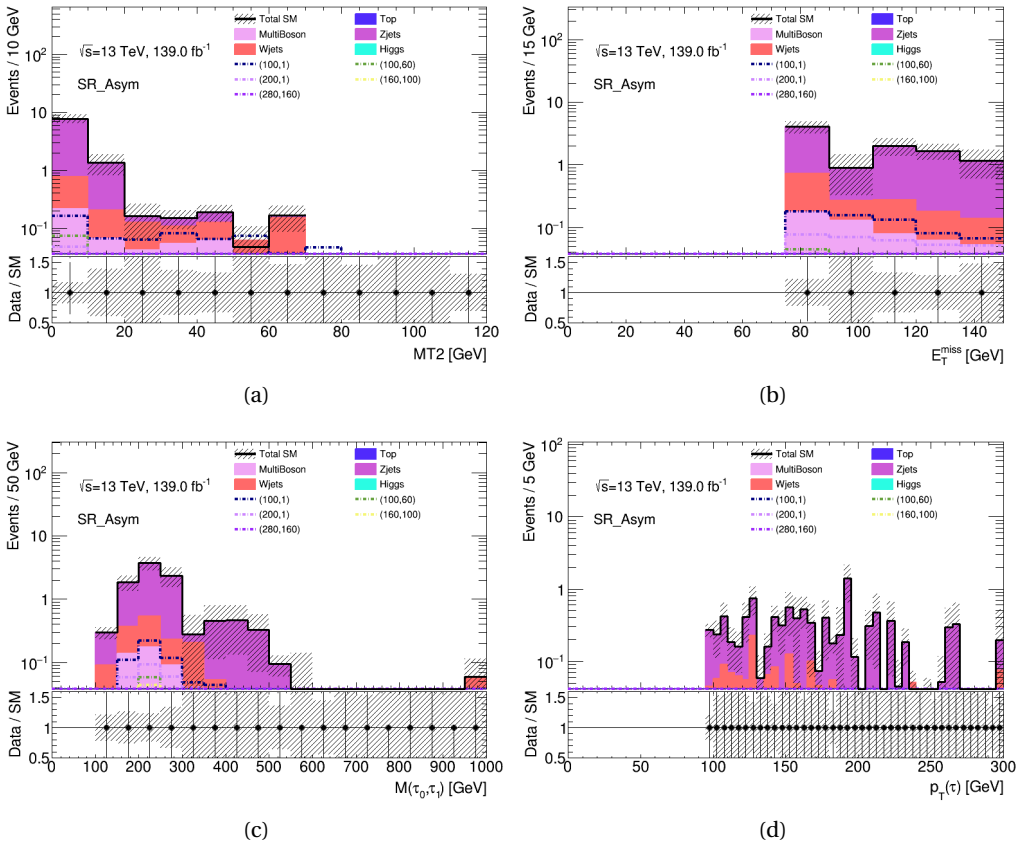

Figure 6.5: Distributions of (a) MT2, (b) $E_{\mathrm{T}}^{\mathrm{miss}}$, (c) $M(\tau_0,\tau_1)$, and (d) $p_{\mathrm{T}}(\tau)$ in the SR using the asymmetric di-tau trigger to select relevant events. Signal scenarios are shown by the dotted lines while SM MC samples displayed as stacked histogram. The shaded band include only systematic uncertainties in the background prediction.

6.4 Vector Boson Fusion Strategy

A possible complimentary study towards the exploration of the compressed $\tilde{\tau}$ mass region is via the search for $\tilde{\tau}$ production in association with VBF scenarios [162]. As stated above, traditional $\tilde{\tau}$ searches have lower sensitivities in the compressed mass spectrum region due to the experimental difficulties present when reconstructing low momentum SM particles, in particular for hadronically decaying τ-leptons. In contrast, in VBF processes the electroweak SUSY particles are pair-produced in association with two high-p_{T} jets that are close to the beam axis (*forward*) and are travelling in opposite directions, which result in a large di-jet invariant mass (m_{jj}). The presence of these two additional high-p_{T} VBF jets in the event topology provide an extra level of background discrimination available to the analysis, while simultaneously creating a "recoil" effect that facilitates the detection of the $E_{\mathrm{T}}^{\mathrm{miss}}$ in the event and aids in the identification of the "soft" τ-leptons, because of this natural kinematic boost [163, 164]. Figure 6.8 shows the Feynman diagrams of $\tilde{\tau}$ production via the following VBF processes that are addressed in this chapter: direct production, via Chargino-Neutralino, and via Chargino-Chargino. A summary of the individual processes' topology and expected final states are described below.

VBF di-$\tilde{\tau}$: the production of a $\tilde{\tau}$ pair via VBF is the most analogous process to the signal ex-

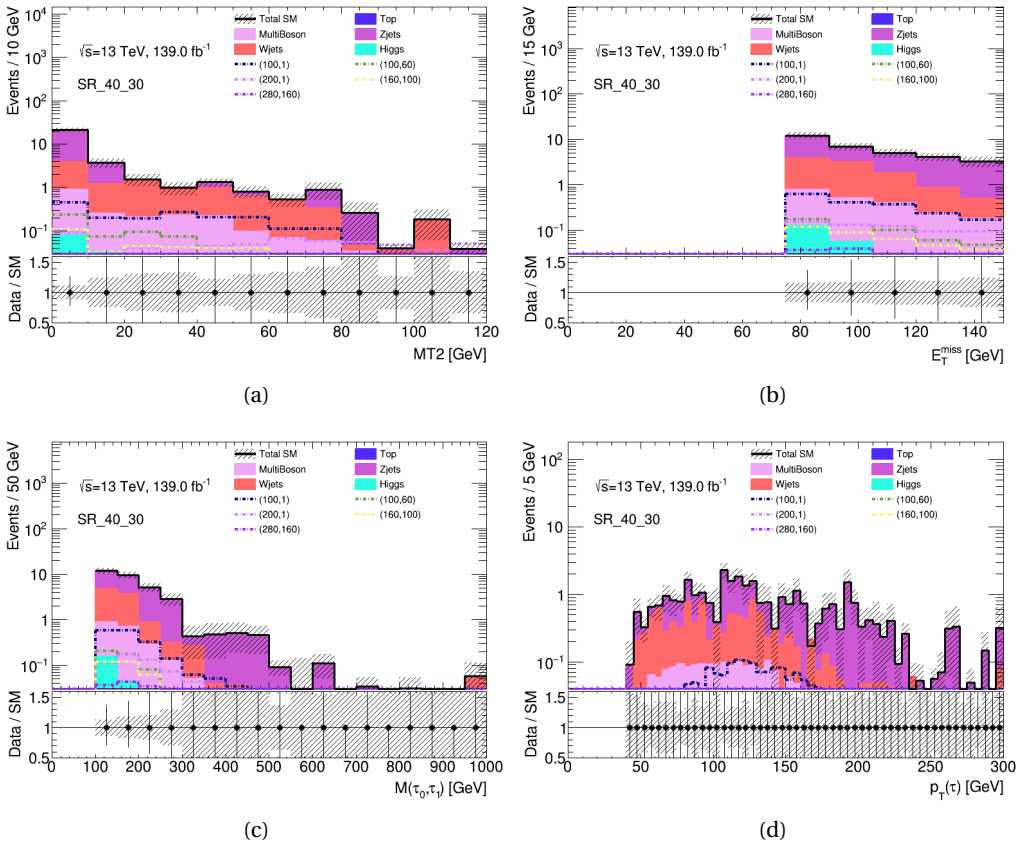

Figure 6.6: Distributions of (a) MT2, (b) $E_{\mathrm{T}}^{\mathrm{miss}}$, (c) $M(\tau_0,\tau_1)$, and (d) $p_{\mathrm{T}}(\tau)$ in the SR using the lowered $p_{\mathrm{T}}(\tau_0) > 40$ GeV and $p_{\mathrm{T}}(\tau_1) > 30$ GeV offline thresholds to select relevant events. Signal scenarios are shown by the dotted lines while SM MC samples displayed as stacked histogram. The shaded band include only systematic uncertainties in the background prediction.

plored by the analysis described in Chapter 4. The highest order topology of this VBF process is shown in Figure 6.8(a), where two W bosons exchange a $\tilde{\chi}_2^0$ and produce $\tilde{\tau}$ particle. Each $\tilde{\tau}$ in turn decays into a τ-lepton and $\tilde{\chi}_1^0$. Similarly to the direct $\tilde{\tau}$ production, this process also contains two hadronically decaying τ-leptons and large $E_{\mathrm{T}}^{\mathrm{miss}}$ in the final state. However, unlike the direct $\tilde{\tau}$ production the two τ-leptons have no opposite charge requirement since they are produced independently via VBF production process and there are two high-p_{T} jets in opposite hemispheres and with large m_{jj} value that are also expected in the final state.

VBF Chargino-Chargino: Figure 6.8(b) shows the highest order process for the VBF production of two $\tilde{\chi}_1^{\pm}$ via the exchange of $\tilde{\chi}_2^0$. The $\tilde{\chi}_1^{\pm}$ further decays to a τ-neutrino and $\tilde{\tau}$, which in turn produces a τ-lepton and $\tilde{\chi}_1^0$. This results in a final state consisting of two τ-leptons, a large amount of $E_{\mathrm{T}}^{\mathrm{miss}}$ originating from the invisible $\tilde{\chi}_1^0$ and neutrinos, and two high-p_{T} jets from the VBF interaction. Although the final state topology is very similar to the VBF direct-$\tilde{\tau}$ production, the presence of the additional charginos in the process significantly increases the amount of $E_{\mathrm{T}}^{\mathrm{miss}}$ expected in the final states, which may be extremely useful when constructing a dedicated trigger to target these types of scenarios.

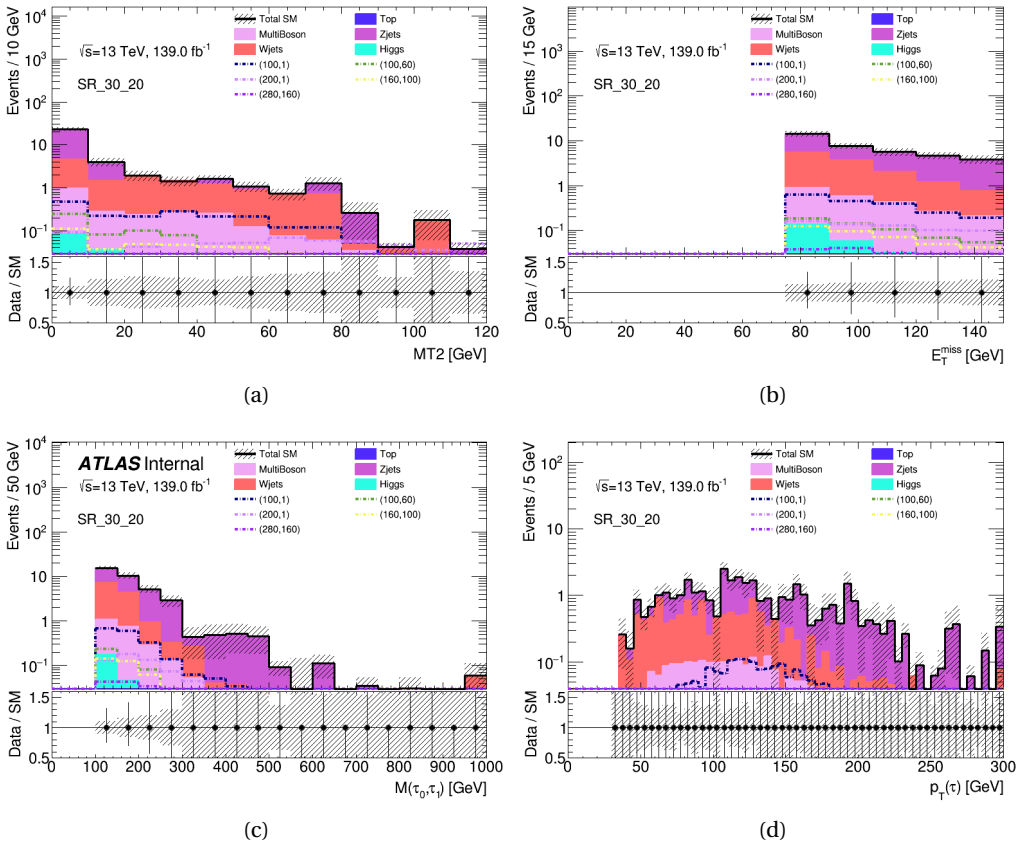

Figure 6.7: Distributions of (a) MT2, (b) $E_{\mathrm{T}}^{\mathrm{miss}}$, (c) $M(\tau_0,\tau_1)$, and (d) $p_{\mathrm{T}}(\tau)$ in the SR using the lowered $p_{\mathrm{T}}(\tau_0) > 30$ GeV and $p_{\mathrm{T}}(\tau_1) > 20$ GeV offline thresholds to select relevant events. Signal scenarios are shown by the dotted lines while SM MC samples displayed as stacked histogram. The shaded band include only systematic uncertainties in the background prediction.

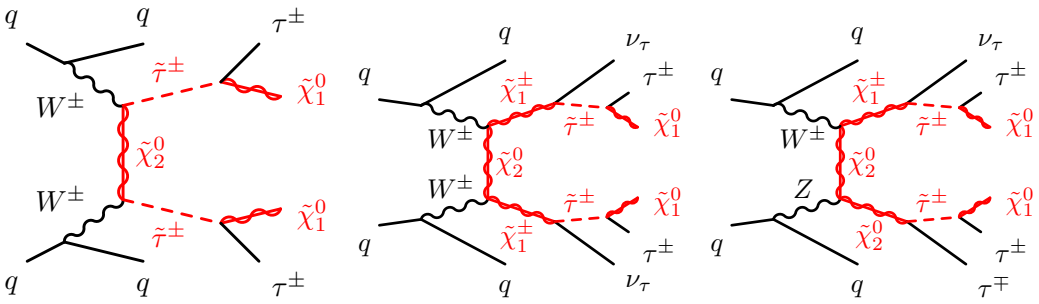

Figure 6.8: Diagrams of the decay topology of the signal models considered in this chapter. Displayed processes show (a) the VBF production of charged $\tilde{\tau}$ with at least two associated jets, (b) the production of two $\tilde{\chi}_1^{\pm}$ that further decay into $\tilde{\tau}$, and (c) the production of $\tilde{\chi}_1^{\pm}$ and $\tilde{\chi}_2^0$ that further decay into $\tilde{\tau}$.

VBF Chargino-Neutralino: the production of a Chargino-Neutralino pair via VBF is shown by Figure 6.8(c). The W and Z boson exchange a $\tilde{\chi}_2^0$ while also producing a $\tilde{\chi}_1^{\pm}$ and $\tilde{\chi}_2^0$, respectively. The $\tilde{\chi}_1^{\pm}$ decays into a $\tilde{\tau}$ and τ-neutrino, while the $\tilde{\chi}_2^0$ decays into a $\tilde{\tau}$ and τ-lepton. The $\tilde{\tau}$ sleptons further decay into τ-leptons and $\tilde{\chi}_1^0$ which is observed by the ATLAS detector as $E_{\mathrm{T}}^{\mathrm{miss}}$. Therefore, the final state for the VBF Chargino-Neutralino scen-

Table 6.3: Number of expected MC events corresponding to the signal and background prediction passing the SR. Multiplicities are shown for the asymmetric trigger, leading and sub-leading tau p_{T} of 40 GeV and 30 GeV and leading and sub-leading tau p_{T} of 30 GeV and 20 GeV.

	Asym. Trigger	$p_T(\tau_1) > 40$ GeV $p_T(\tau_2) > 30$ GeV	$p_T(\tau_1) > 30$ GeV $p_T(\tau_2) > 20$ GeV
Background			
Multiboson	0.46	1.88	2.10
Wjets	1.08	8.12	10.78
Top	0.00	0.00	0.00
Zjets	8.21	21.27	22.92
Higgs	0.04	0.23	0.25
Total	9.79	31.50	36.05
$(\tilde{\tau},\tilde{\chi}_1^0)$ [GeV]			
(100,1)	0.61	1.80	1.92
(200,1)	0.31	0.60	0.62
(160,100)	0.12	0.35	0.38
(100,60)	0.13	0.51	0.55
(280,160)	0.08	0.16	0.17

Table 6.4: Signal sensitivity after application of the SR selection for the asymmetric trigger, leading and sub-leading tau p_{T} of 40 GeV and 30 GeV and leading and sub-leading tau p_{T} of 30 GeV and 20 GeV.

$(\tilde{\tau},\tilde{\chi}_1^0)$ [GeV]	Asym. Trigger	$p_T(\tau_1) > 40$ GeV $p_T(\tau_2) > 30$ GeV	$p_T(\tau_1) > 30$ GeV $p_T(\tau_2) > 20$ GeV
(100,1)	0.196	0.321	0.320
(200,1)	0.099	0.107	0.103
(160,100)	0.037	0.062	0.063
(100,60)	0.042	0.091	0.092
(280,160)	0.025	0.029	0.028

ario is unique compared to the other processes described above due to the presence of an additional τ-lepton in the final state, for a total of 3 τ-leptons, in addition to the expected large $E_{\mathrm{T}}^{\mathrm{miss}}$ and two high-p_{T} jets.

6.4.1 Sample generation

Simulated samples for the signals events described above have been generated using MC event generators. The pair production of $\tilde{\chi}_1^{\pm}$, $\tilde{\chi}_2^0$ gauginos, and $\tilde{\tau}$ ($\tilde{\chi}_1^{\pm}\tilde{\chi}_1^{\pm}$, $\tilde{\chi}_1^{\pm}\tilde{\chi}_2^0$, and $\tilde{\tau}\tilde{\tau}$) with associated partons for the respective signal samples are generated with the MADGRAPH program (v2.6.2) [103]. The PS and hadronisation processes modelling is performed by the PYTHIA8 program [149], while the decays of the τ-leptons are described using the EVTGEN program [165]. The signal cross sections are calculated at Leading Order (LO) using the MADGRAPH generator and are found to be 10 – 20 fb for VBF di-$\tilde{\tau}$ production, $\mathcal{O}(10^{-2})$ – 5 fb for VBF $\tilde{\chi}_1^{\pm}\tilde{\chi}_1^{\pm}$ production, and $\mathcal{O}(80)$ fb for VBF $\tilde{\chi}_1^{\pm}\tilde{\chi}_2^0$ production. The cross section of the signal is strongly dependent

on the simulated process and SUSY sparticle masses. Therefore, there can be significant differences in cross sections within each process depending on the mass of the simulated sparticles.

A reduced set of mass points for the gauginos and $\tilde{\tau}$ masses that cover both the unexplored "compressed-region" and the "excluded-region" have been simulated. The mass points which overlap with the excluded mass region have been simulated for validation purposes. The *average mass* assumption ($m_{\tilde{\tau}} = 0.5(m_{\tilde{\chi}_1^\pm} + m_{\tilde{\chi}_1^0})$) is used for the calculation of the $\tilde{\tau}$ mass for the $\tilde{\chi}_1^\pm\tilde{\chi}_1^\pm$ and $\tilde{\chi}_1^\pm\tilde{\chi}_2^0$ VBF scenarios. The mass of the $\tilde{\tau}$ is instead predefined for the di-$\tilde{\tau}$ VBF scenario simulation. In all scenarios the $\tilde{\chi}_1^\pm$ and $\tilde{\chi}_2^0$ are assumed to be mass degenerate.

The di-$\tilde{\tau}$ VBF signal samples have been fully simulated by previous ATLAS analysts and have thus undergone all steps of offline reconstruction and object identification, with associated inefficiencies and calibrations applied. The Chargino-Chargino and Chargino-Neutralino VBF signal samples, however, have not been previously simulated within ATLAS. Therefore, the author began the simulation production process for these samples, but due to time restrictions was not able undergo all steps of the objects' reconstruction and identification required. A more detailed description of the simulation process for these signal processes, along with the resulting kinematic distributions and accessible sensitivities is provided in Section 6.5. Due to the incomplete processing of the Chargino-Chargino and Chargino-Neutralino VBF samples, the kinematic information available in these samples is the "real" (i. e. MC simulated) information, rather than the more realistic offline reconstructed information that takes into account reconstruction inefficiencies and energy calibrations. Table 6.5 provides a summary of the MC simulated mass points for the different VBF scenarios studied in this chapter. The generation processes for the backgrounds samples has already been described in depth in Chapter 4.

Table 6.5: VBF signal samples simulated $\tilde{\tau}$, $\tilde{\chi}_1^\pm/\tilde{\chi}_2^0$, and $\tilde{\chi}_1^0$ mass points. In the simulation of the Chargino-Chargino and Chargino-Neutralino scenarios the average mass assumption ($m_{\tilde{\tau}} = ¡(m_{\tilde{\chi}_1^\pm} + m_{\tilde{\chi}_1^0})$) was adopted for derivation of the $\tilde{\tau}$ mass.

VBF scenario	$\tilde{\chi}_1^\pm/\tilde{\chi}_2^0$ [GeV]	$\tilde{\chi}_1^0$ [GeV]	$\tilde{\tau}$ [GeV]
di-$\tilde{\tau}$	—	100.0	50.0
	—	100.0	60.0
	—	100.0	70.0
	—	100.0	90.0
	—	100.0	95.0
	—	90.0	40.0
	—	90.0	60.0
	—	90.0	80.0
	—	90.0	85.0
$\tilde{\chi}_1^\pm\tilde{\chi}_1^\pm$	450.0	0.0	225.0
	400.0	250.0	125.0
	250.0	200.0	225.0
	150.0	100.0	125.0
	100.0	65.0	82.5
$\tilde{\chi}_1^\pm\tilde{\chi}_2^0$	200.0	0.0	100.0
	200.0	150.0	175.0

6.4.2 VBF selection

In order to discriminate signal VBF events from the SM background a set of selection cuts, based on previously published results by CMS in Reference [166] are used to construct a custom VBF-SR. In this VBF-SR, the τ-leptons in the events are required to have $|\eta| < 2.1$ and $\Delta R > 1.5$ in order to select high quality and well isolated candidates. Events with $E_{\mathrm{T}}^{\mathrm{miss}} < 30$ GeV containing a b-tagged jet, or containing a light lepton are rejected to reduce the SM background contamination from $t\bar{t}$, multiboson, and V+jets ($V = Z, W$) events. To select for VBF topology, at least two jets in the event are required to be in opposite hemispheres ($\eta_1\eta_2 < 0$) and with large separation ($|\Delta\eta(j,j)| > 4.2$). Events are also selected if the jets have $p_{\mathrm{T}} > 50$ GeV, $|\eta| < 5.0$, and a combined dijet mass of $m_{jj} > 250$ GeV. Table 6.6 shows a summary of the selection cuts used to construct the described VBF-SR.

Table 6.6: Summary of selection requirements for the VBF-SR.

VBF-SR
2 medium τ with $p_{\mathrm{T}} > 35$ GeV and $\|\eta\| < 2.1$
light lepton veto
b-jet veto
at least 2 jets with $p_T > 50$ GeV and $\|\eta\| < 5$
$\eta_j\eta_j < 0$
$\|\Delta\eta(j,j)\| > 2.8$
$\Delta R(\tau,\tau) > 1.5$
$m_{jj} > 250$ GeV
$E_T^{miss} > 85$ GeV

6.5 Simulation study of VBF $\tilde{\chi}_1^{\pm}\tilde{\chi}_1^{\pm}$ and $\tilde{\chi}_1^{\pm}\tilde{\chi}_2^0$

In order to study the kinematic properties of the signal samples described above, the Chargino-Chargino and Chargino-Neutralino VBF topologies had to be simulated. This was done using MADGRAPH simulator interfaced with PYTHIA8 and EVTGEN, similarly to what had been previously done for the di-$\tilde{\tau}$ VBF signal samples. All samples were simulated to be inclusive in QCD and with only a simple generator filter. A generator filter is used to accept only the simulated events that fit with the wanted selection of final state objects. In order to be as inclusive as possible when simulating these samples, a very loose generator filter selection was applied which required at least two τ-leptons in the final state that are allowed to decay either leptonically or hadronically. The τ-leptons are also required to have at least $p_{\mathrm{T}} > 15$ GeV and $|\eta| < 2.8$, since τ-leptons outside these values cannot currently be accurately reconstructed by the ATLAS detector. The efficiency associated with the generator filter is taken into account as a systematic weight associated to the generated events, along with the expected cross-section and the sum of all weighted events. All samples have been simulated with 10^4 events to ensure a quick sim-

ulation process. This, however, results in the signal samples possessing low statistics and large event weights.

Figures 6.9 and 6.10 show the Chargino-Chargino, and Figures 6.11 and 6.12 the Chargino--Neutralino VBF signal samples kinematic distributions compared to the SM background processes. All samples are normalised to 54.8 fb^{-1}. As previously predicted, it is possible to observe from these plots that the more "compressed" signal points tend to have overall lower momentum τ-lepton and jet objects. The production of more massive sparticles also results in overall softer final state kinematics. The kinematic variables shown in these plots are inclusive for all decay channels of the signal samples. This is particularly evident in the distribution of number of τ_{had} leptons, which shows that the majority of the events contain a single τ_{had}. This is a result of the τ-lepton ability to decay either hadronically to pions ($\pi^{\pm}, \pi^0$) or leptonically to light leptons (e, μ), making it statistically more likely to have a semi-leptonic, where at least one τ-lepton has decayed to lepton. This results in the majority of events containing only one (two) τ_{had} for the Chargino-Chargino (Chargino-Neutralino) VBF scenario. As mentioned previously, these plots should only be used for a preliminary observation of the kinematic properties of the signal samples compared to the SM background. They have not undergone the full simulation and reconstruction process required by the ATLAS MC samples and thus cannot be used to reach any final conclusion on expected sensitivity.

To further study the effects of the kinematic properties of these signal samples compared to the SM backgrounds, a loosened selection based on the VBF-SR described in Section 6.4.2 has been derived. Due to the incomplete nature of the simulated signal samples under study, some of the selection cuts present in the VBF-SR could not be applied and have thus been discarded. For this loosened VBF-SR , events are accepted if they pass the following set of selection cuts:

- Exactly (at least) 2 τ_{had} with $p_{\mathrm{T}} > 35$ GeV and $|\eta| < 2.1$ when studying the $\tilde{\chi}_1^{\pm}\tilde{\chi}_1^{\pm}$ ($\tilde{\chi}_1^{\pm}\tilde{\chi}_2^0$) VBF scenario
- Light leptons veto
- $\Delta R(\tau, \tau) > 1.5$
- $E_{\mathrm{T}}^{\mathrm{miss}} > 85$ GeV
- At least 2 jets with $p_T > 50$ GeV and $|\eta| < 5$
- $|\Delta\eta(j, j)| > 2.8$
- $m_{jj} > 250$ GeV

Figures 6.13 and 6.14 show the Chargino-Chargino, and Figures 6.15 and 6.16 the Chargino--Neutralino VBF signal samples kinematic distributions compared to the SM background processes using this loosened VBF-SR. The selection applied to the Chargino-Chargino VBF signal and SM backgrounds seem to be allow for some signal excesses at high $MT2$, $E_{\mathrm{T}}^{\mathrm{miss}}$, and m_{jj}

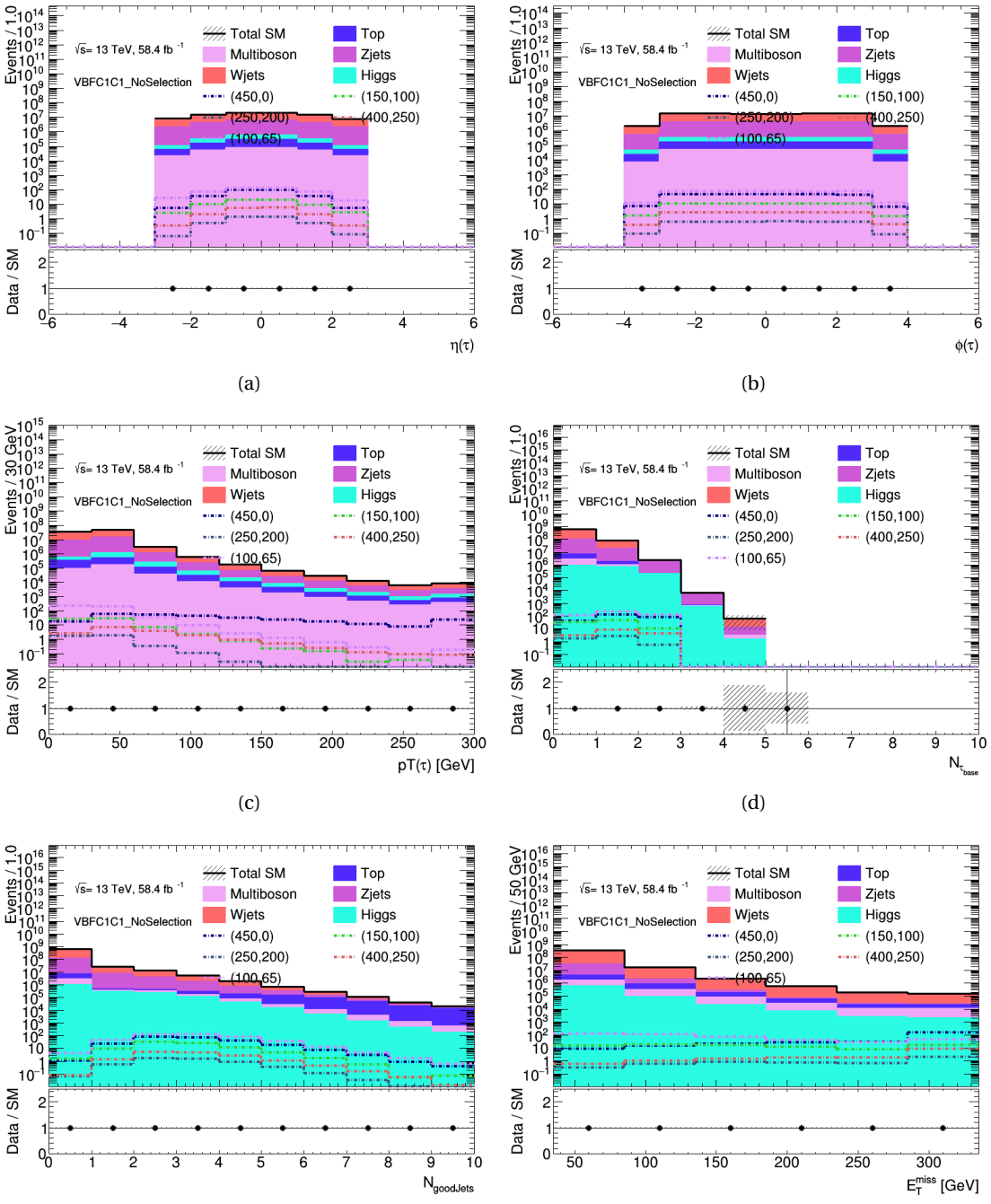

Figure 6.9: Set of kinematic distributions for τ-leptons, and jets objects for VBF SUSY $\tilde{\chi}_1^{\pm}\tilde{\chi}_1^{\pm}$ signal and SM background MC simulated samples. Shaded areas represent the statistical uncertainties only.

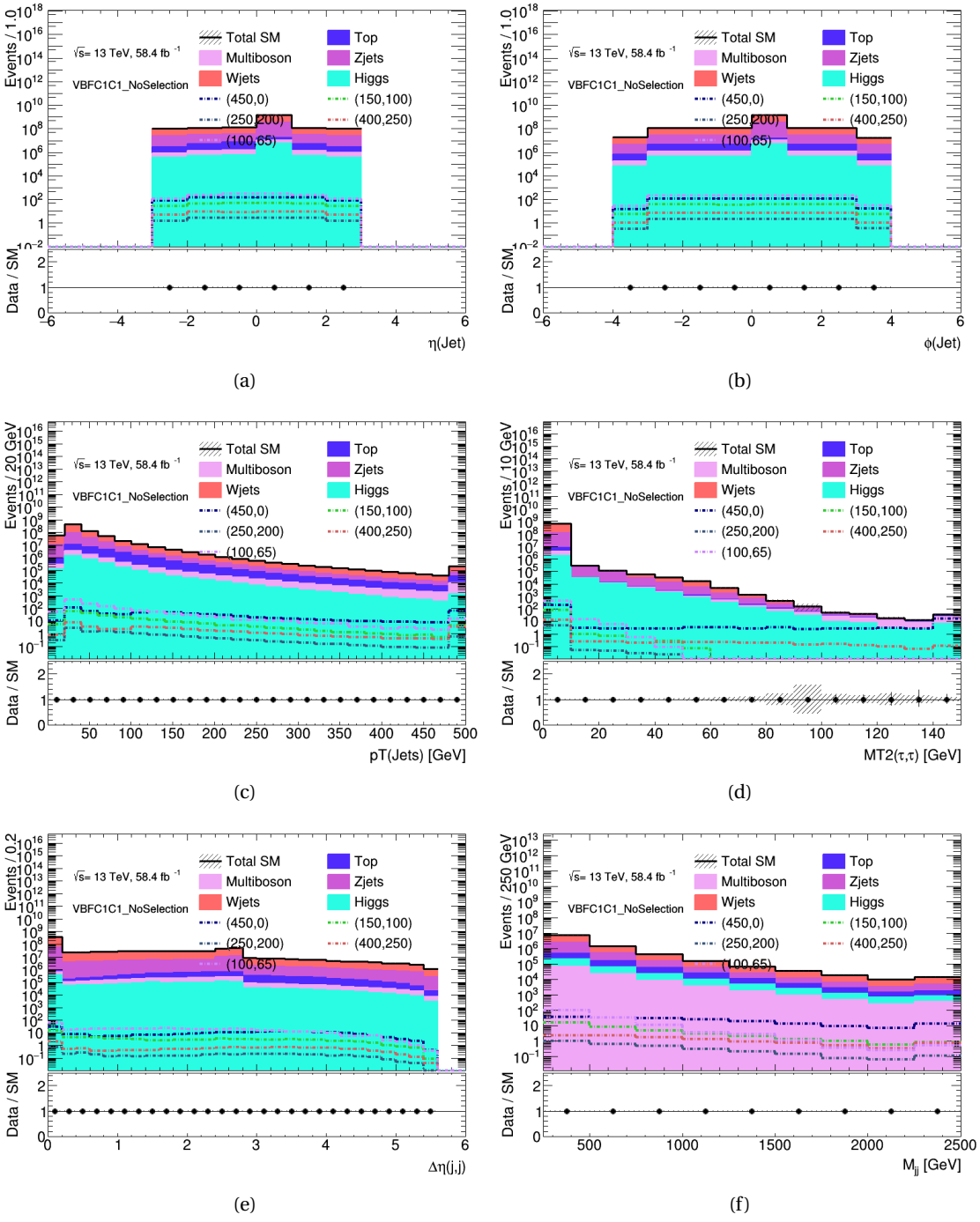

Figure 6.10: Set of kinematic distributions for τ-leptons, and jets objects for VBF SUSY $\tilde{\chi}_1^{\pm}\tilde{\chi}_1^{\pm}$ signal and SM background MC simulated samples. Shaded areas represent the statistical uncertainties only.

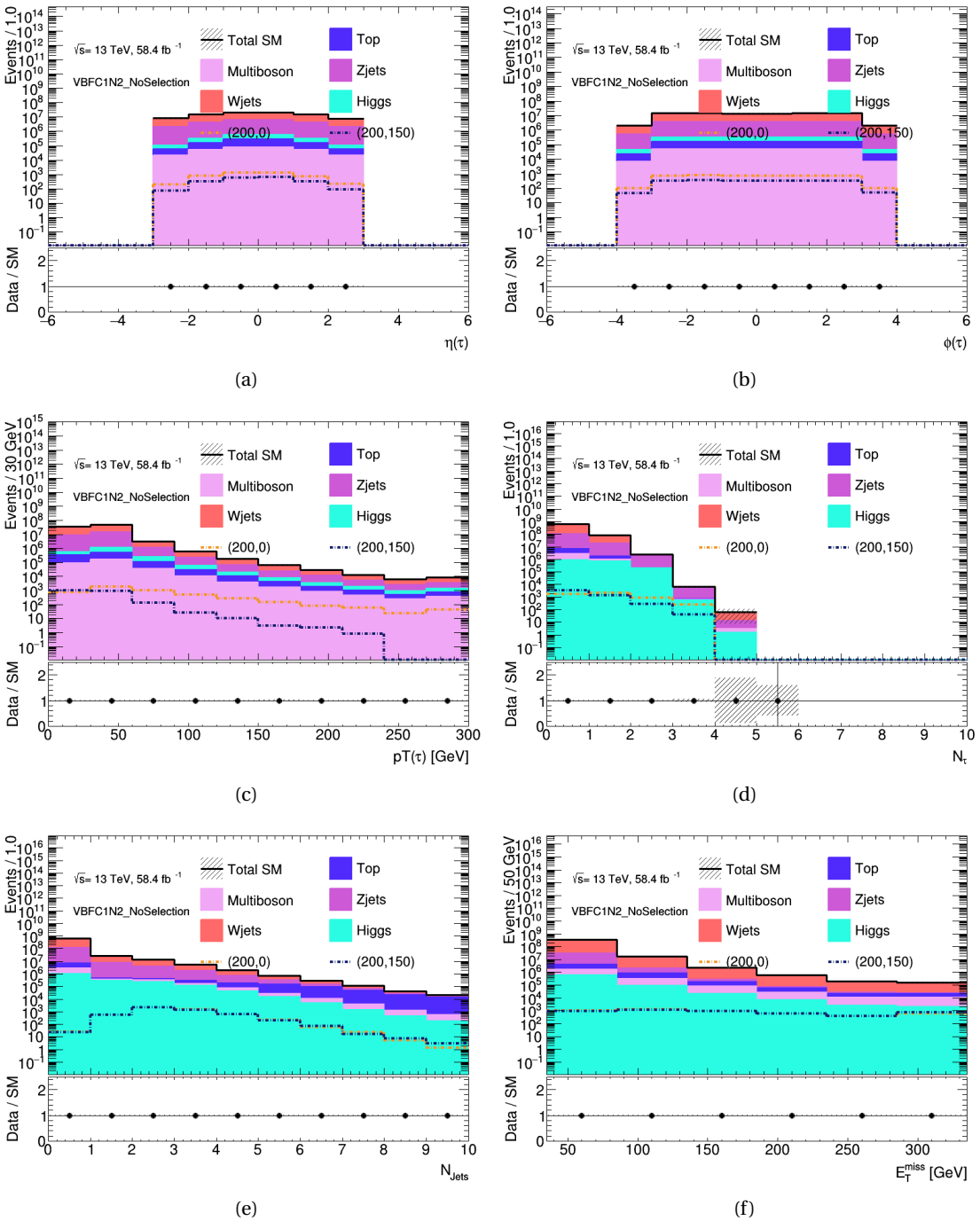

Figure 6.11: Set of kinematic distributions for τ-leptons, and jets objects for VBF SUSY $\tilde{\chi}_1^{\pm}\tilde{\chi}_2^{0}$ signal and SM background MC simulated samples. Shaded areas represent the statistical uncertainties only.

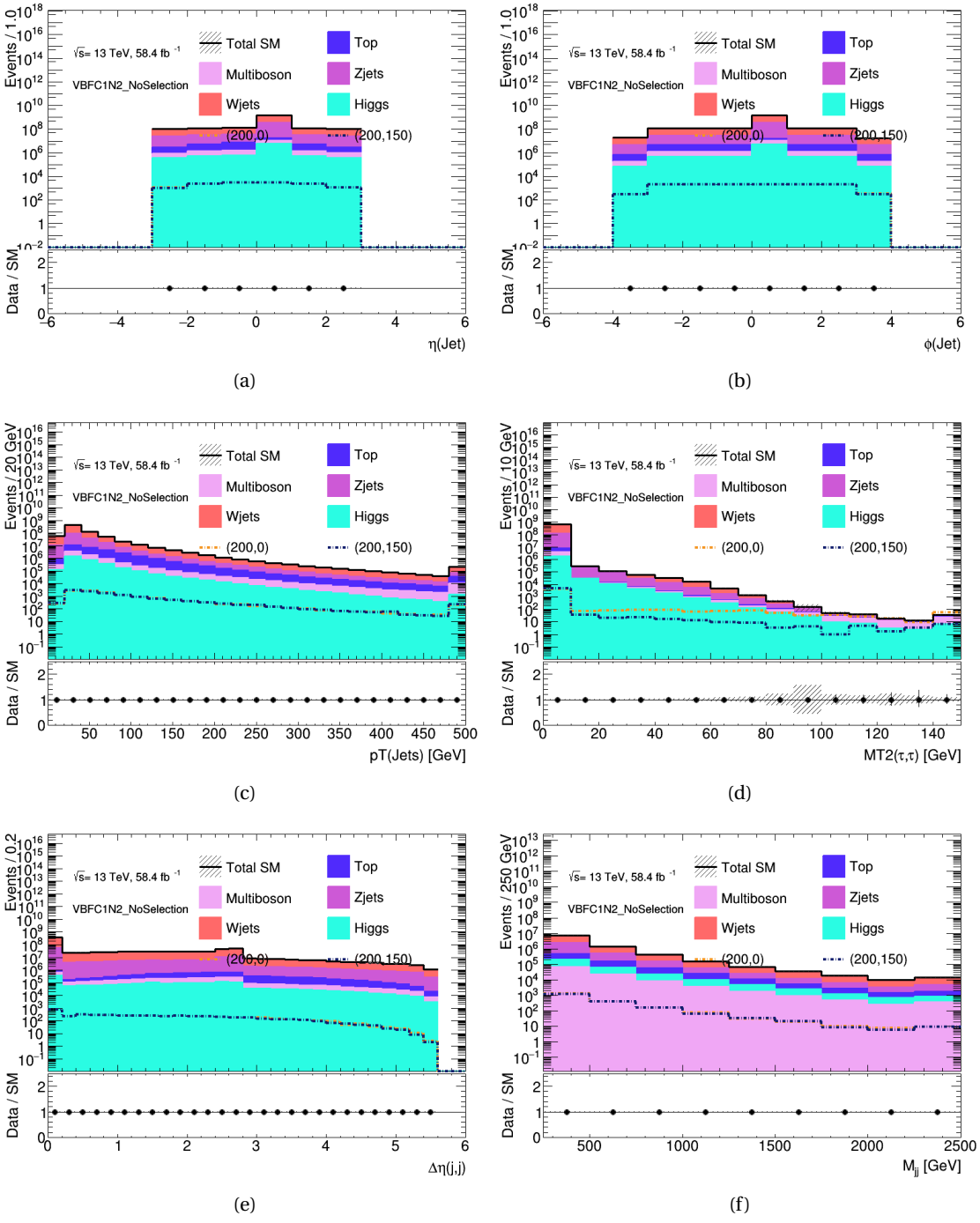

Figure 6.12: Set of kinematic distributions for τ-leptons, and jets objects for VBF SUSY $\tilde{\chi}_1^{\pm}\tilde{\chi}_2^{0}$ signal and SM background MC simulated samples. Shaded areas represent the statistical uncertainties only.

values, for the large Δm signal points. The more compressed signals are found to be heavily suppressed by this selection. This is due to the fact that in these scenarios the simulated particles tend to populate the lower end of the kinematic regime (low p_{T} τ-leptons), making high τ-lepton p_{T} cuts result in very high signal rejection. Unlike the Chargino-Chargino scenario, the Chargino-Neutralino samples are found to have an overall higher signal acceptance and some excess in signal events in the high $MT2$, $E_{\mathrm{T}}^{\mathrm{miss}}$, and m_{jj} regions, even for the compressed mass point with $m_{\tilde{\chi}_1^{\pm}}$ = 200 GeV and $m_{\tilde{\chi}_1^0}$ = 150 GeV. This could be attributed to the higher overall cross-section of the samples and the more unique 3 τ_{had} final state signature, which provides a higher multiplicity of events with at least 2 τ_{had}leptons.

This initial study shows some promising results towards the possibility of using these VBF SUSY signals to study the unexplored compressed mass regions. These preliminary results are showing that to achieve the best signal sensitivity it will become increasingly important to improve the τ_{had} identification and reconstruction and thus enable the selection of "softer" τ-leptons by the ATLAS trigger. Nonetheless, the $\tilde{\chi}_1^{\pm}$-$\tilde{\chi}_2^0$ VBF samples show that even with higher p_{T} thresholds these samples could achieve significant signal excesses in key discriminating variables, if appropriate selection regions are derived to exploit their unique kinematics signatures.

6.6 VBF trigger

During the last year of the Run-2 data collection period a single di-τ+jets un-prescaled trigger was made operational to target VBF scenarios with two τ-leptons and jets in the final states. The trigger was named:

$$HLT\_tau25\_mediumRNN\_tracktwoMVA\_tau20\_mediumRNN\_tracktwoMVA\_ j70\_j50\_0eta490\_invm900j50\_L1MJJ\_500\_NFF$$

and was dedicated to the selection of VBF events containing a Higgs boson decaying to a two τ_{had} final state ($H \rightarrow \tau\tau$). It requires at least two τ-leptons in the event with $p_{\mathrm{T}}(\tau_1) > 25$ GeV and $p_{\mathrm{T}}(\tau_2) > 20$ GeV, that pass the *medium* RNN identification working point criteria, and have between 1 and 3 tracks identified using a MVA [78, 167]. It also requires there to be two HLT jet objects with $p_{\mathrm{T}} > 70$ GeV and $p_{\mathrm{T}} > 50$ GeV, respectively, and with $0 < \eta < 4.9$. The trigger also requires the jets to have a combined invariant mass (m_{jj}) value above 900 GeV in the HLT and above 500 GeV at L1. An event is only accepted by this trigger if all these conditions are met by both the HLT and L1.

As mentioned in Section 6.3, the understanding and development of current and new triggers towards the study more complex and exotic scenarios becomes increasingly important as more data is collected by the ATLAS experiment. As of yet, there has been no study performed on the efficacy of the currently available di-τ_{had} VBF trigger for triggering VBF SUSY scenarios. In this section, the kinematic variable distributions and yields resulting from from the selection of VBF di-$\tilde{\tau}$ events using the aforementioned VBF di-τ_{had} trigger compared to the simulated SM

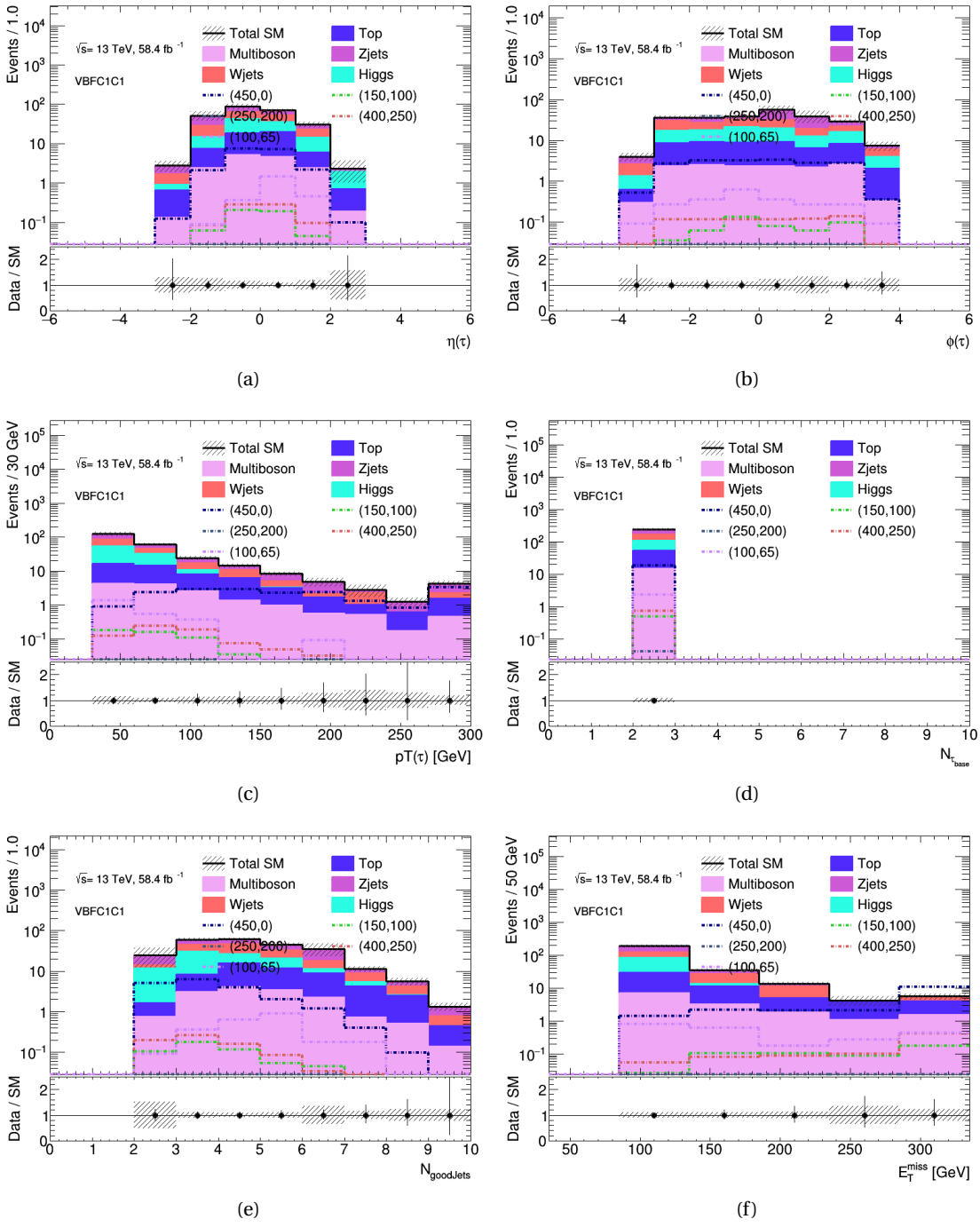

Figure 6.13: Set of kinematic distributions for τ-leptons, and jets objects for VBF SUSY $\tilde{\chi}_1^{\pm}\tilde{\chi}_1^{\pm}$ signal and SM background MC simulated samples that pass the VBF SR. Shaded areas represent the statistical uncertainties only.

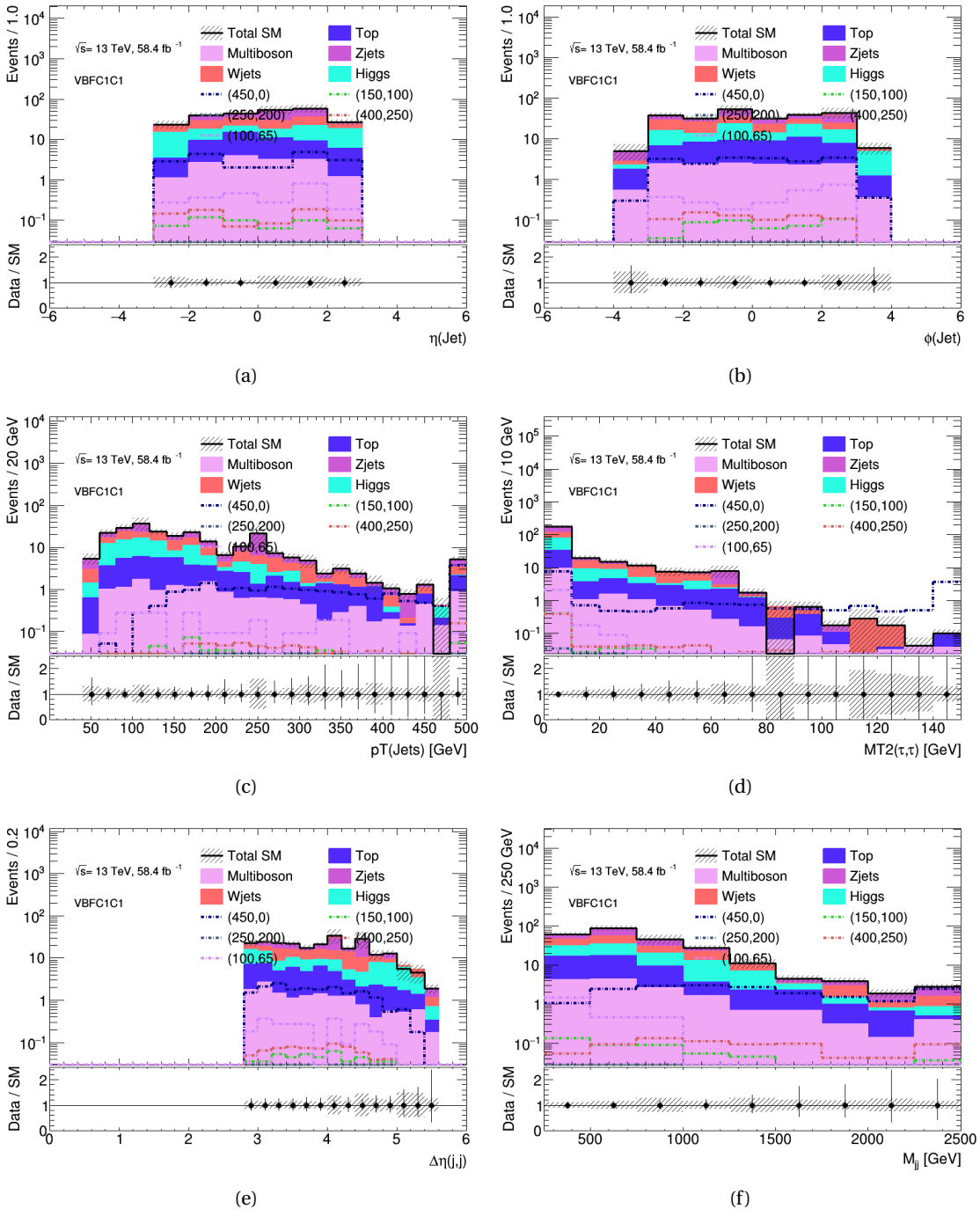

Figure 6.14: Set of kinematic distributions for τ-leptons, and jets objects for VBF SUSY $\tilde{\chi}_1^{\pm}\tilde{\chi}_1^{\pm}$ signal and SM background MC simulated samples that pass the VBF SR. Shaded areas represent the statistical uncertainties only.

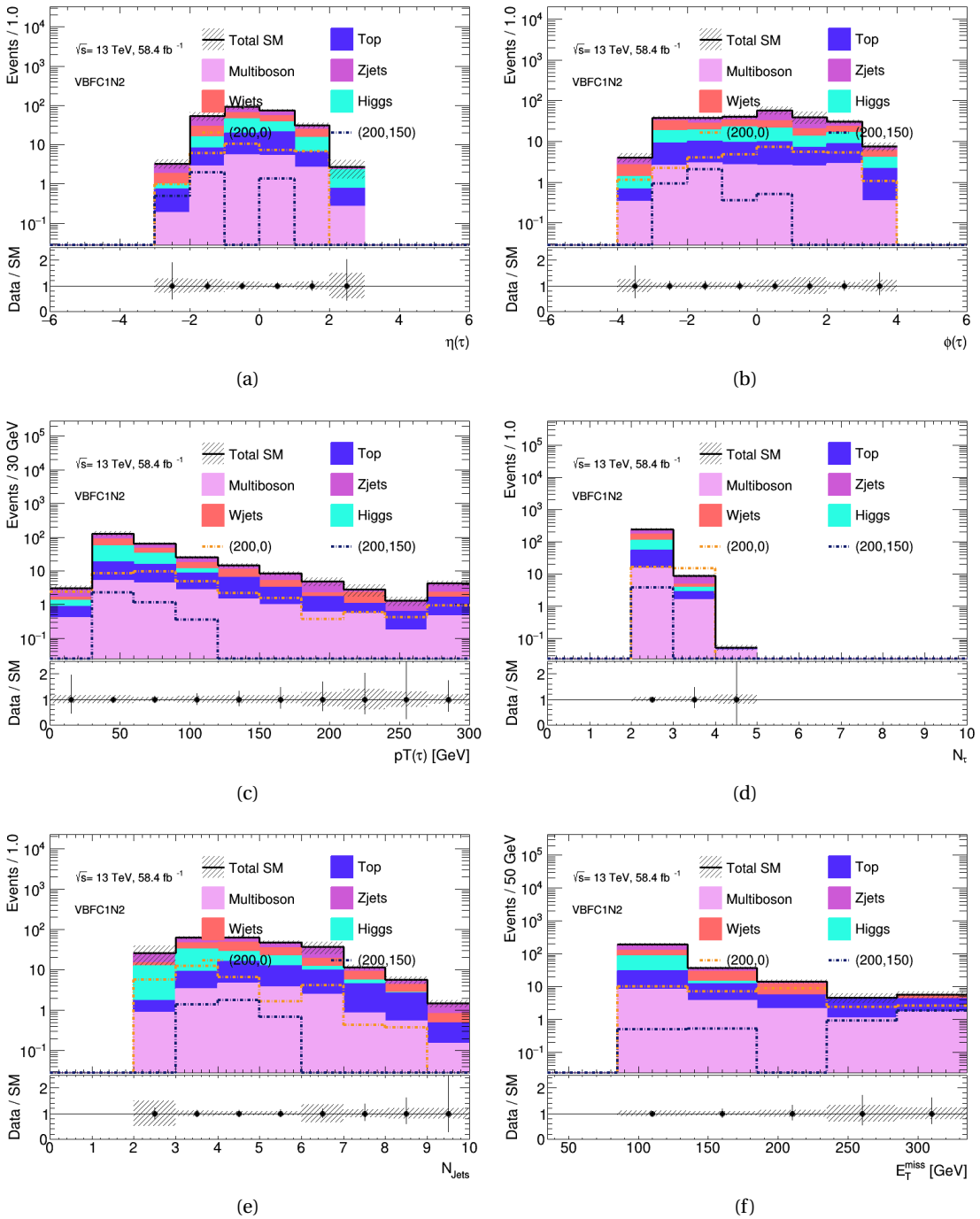

Figure 6.15: Set of kinematic distributions for τ-leptons, and jets objects for VBF SUSY $\tilde{\chi}_1^{\pm}\tilde{\chi}_2^0$ signal and SM background MC simulated samples that pass the VBF SR. Shaded areas represent the statistical uncertainties only.

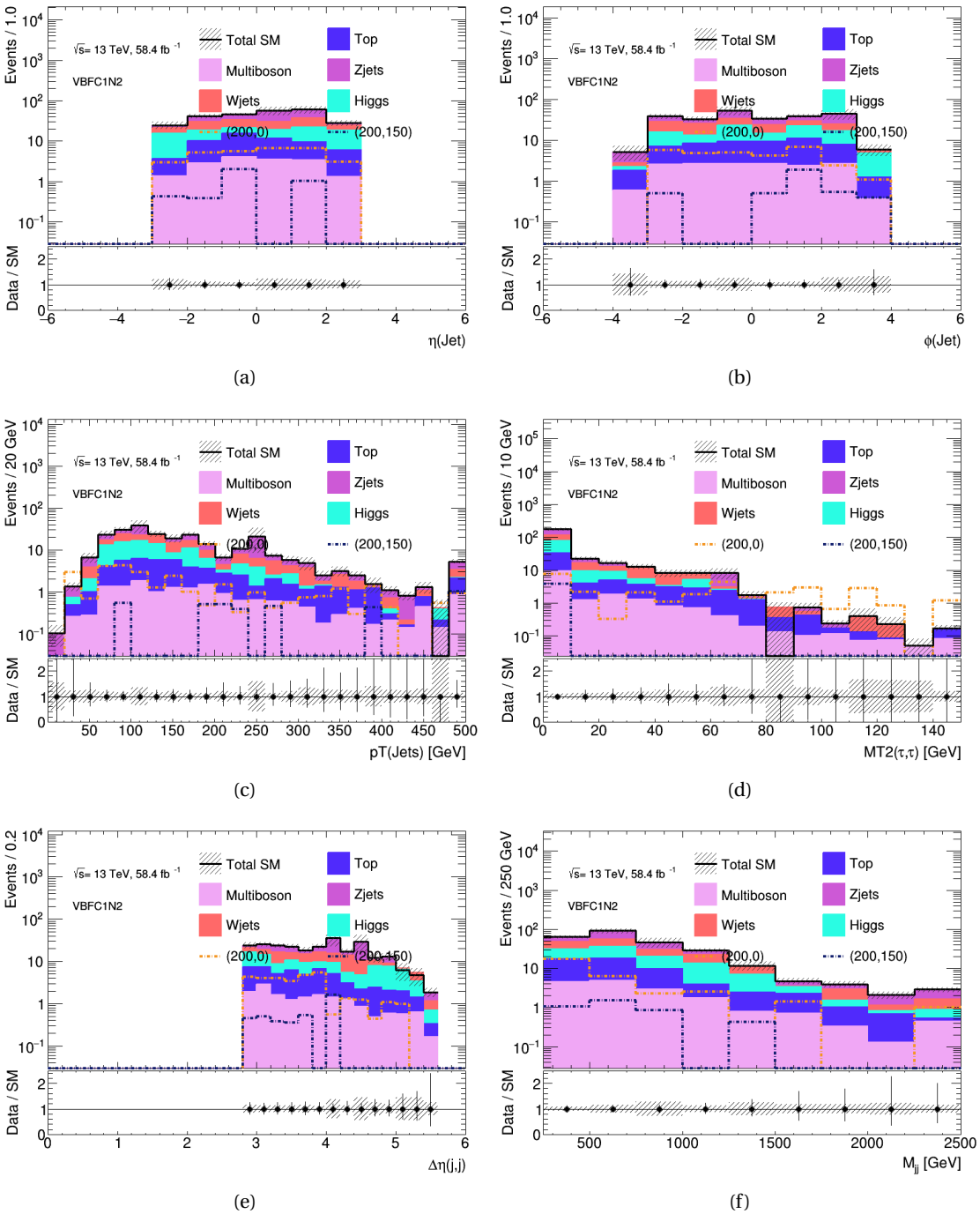

Figure 6.16: Set of kinematic distributions for τ-leptons, and jets objects for VBF SUSY $\tilde{\chi}_1^{\pm}\tilde{\chi}_2^0$ signal and SM background MC simulated samples that pass the VBF SR. Shaded areas represent the statistical uncertainties only.

background will be presented. MC simulated signal and SM background processes are used, normalised to an integrated luminosity of 54.8 fb^{-1} (only data collected in 2018 is simulated since the trigger was not operational before hand). The VBF di-$\tilde{\tau}$ signal scenario mass points described in Table 6.5 have been used in this study.

The VBF-SR selection shown in Table 6.6 is used to reject SM background events in combination with the studied VBF trigger along with its associated offline thresholds. To ensure that the trigger is performing at maximal efficiency, both τ-leptons that pass the di-τ VBF trigger are required to have offline $p_{\mathrm{T}} > 35$ GeV. Similarly, for the jet legs of the VBF trigger to be performing at maximal efficiency a requirement of two jets with offline $p_{\mathrm{T}} > 80$ GeV and $p_{\mathrm{T}} > 60$ GeV is enforced. The di-tau+$E_{\mathrm{T}}^{\mathrm{miss}}$ trigger described in Section 4.5 is used as a reference in this study to compare the efficacy of the VBF trigger at selecting VBF signal events. To ensure high trigger performance for the di-tau+$E_{\mathrm{T}}^{\mathrm{miss}}$ trigger, the offline τ-lepton p_{T} requirements have been changed appropriately, while the $E_{\mathrm{T}}^{\mathrm{miss}}$ requirement is increased to 150 GeV, following the prescription described in Section 4.5. A summary of the additional selection to the VBF-SR introduced by the di-tau VBF and di-tau+$E_{\mathrm{T}}^{\mathrm{miss}}$ triggers is shown in Table 6.7

Table 6.7: Summary of offline selection requirements for the di-tau VBF and di-tau+$E_{\mathrm{T}}^{\mathrm{miss}}$ triggers in addition to the VBF-SR.

di-τ VBF trigger	di-τ+E_T^{miss} trigger
$p_T(\tau) > 35$ GeV	$p_T(\tau_0) > 75$ GeV, $p_T(\tau_1) > 40$ GeV
$p_T(j_0) > 80$ GeV, $p_T(j_1) > 60$ GeV	$p_T(j) > 50$ GeV
$E_T^{miss} > 30$ GeV	$E_T^{miss} > 150$ GeV

The kinematic distributions of τ-lepton and jet MC simulated objects resulting from the events passing the VBF-SR for the di-tau VBF and di-tau+$E_{\mathrm{T}}^{\mathrm{miss}}$ triggers are shown in Figures 6.17 and 6.18, and Figures 6.19 and 6.20, respectively. The kinematic variables found to have the most discriminating power for both trigger strategies are the m_{jj} and $E_{\mathrm{T}}^{\mathrm{miss}}$, as the signal becomes more dominant over the SM background with increasing value of m_{jj} and $E_{\mathrm{T}}^{\mathrm{miss}}$. Nonetheless, no appreciable signal excess is achieved using the combination of these triggers and this selection, suggesting that further optimisation is required.

Using the di-tau VBF trigger to select for relevant events seems to have comparable background rejection compared to the di-tau+$E_{\mathrm{T}}^{\mathrm{miss}}$ trigger, as shown by the event multiplicities separated for each SM background and SUSY processes in Table 6.8. The most predominant background that passes the di-tau VBF trigger is found to be the Z + jets background, which results in ~ 56% of the total background multiplicity, while W + jets and mutliboson backgrounds contribute to ~ 17% of the total background each. For the di-tau+$E_{\mathrm{T}}^{\mathrm{miss}}$ trigger the most predominant background contribution instead comes from the multiboson processes (~ 40%), followed by the Z + jets processes (~ 36%), with W + jets contributing to ~ 17% of the total SM background. For both di-tau+$E_{\mathrm{T}}^{\mathrm{miss}}$and di-tau VBF triggers, both Top and Higgs processes

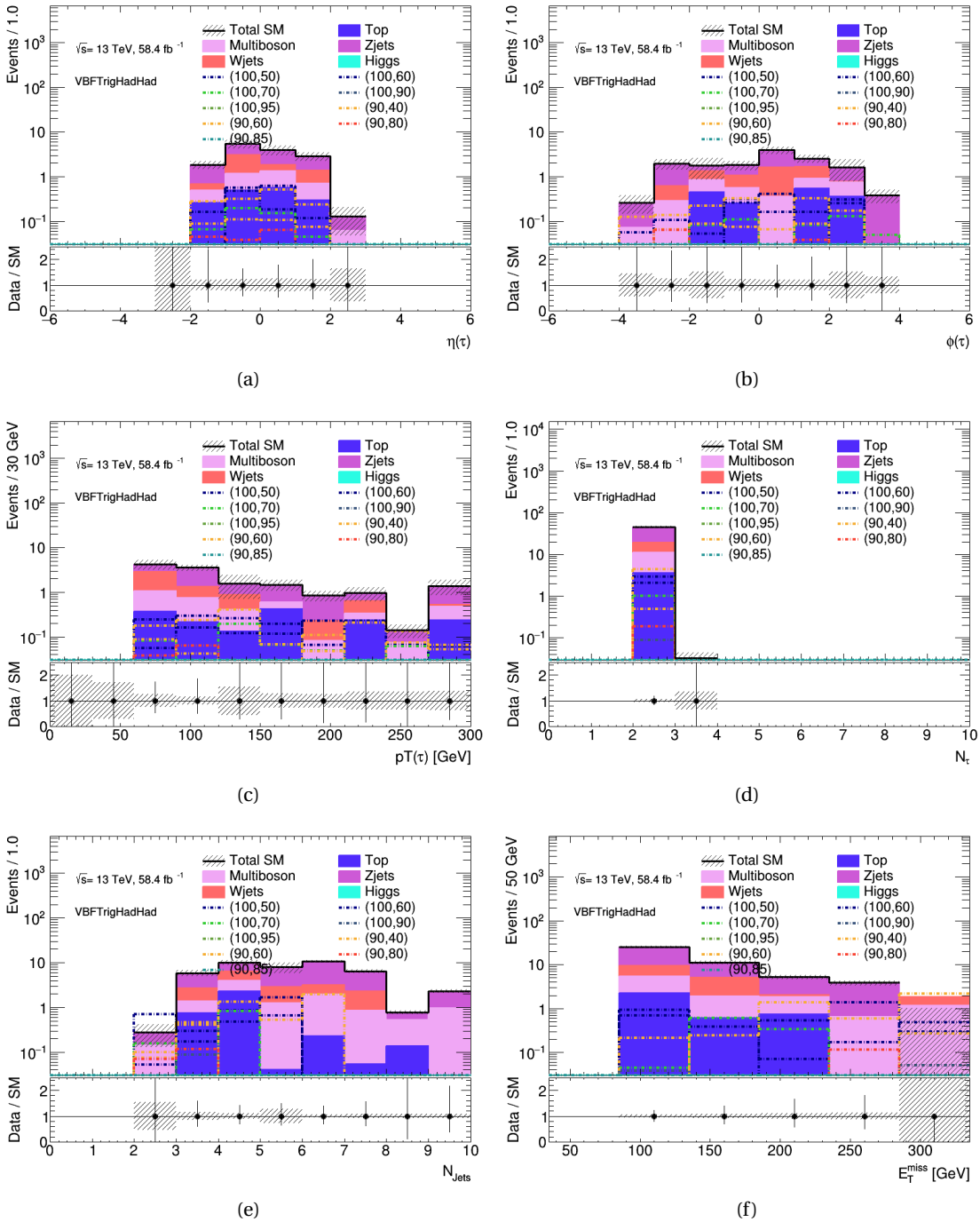

Figure 6.17: Set of kinematic distributions for τ-leptons, and jets objects for VBF SUSY di-$\tilde{\tau}$ signal and SM background MC simulated samples that are accepted by the di-tau VBF trigger. Shaded areas represent the statistical uncertainties only.

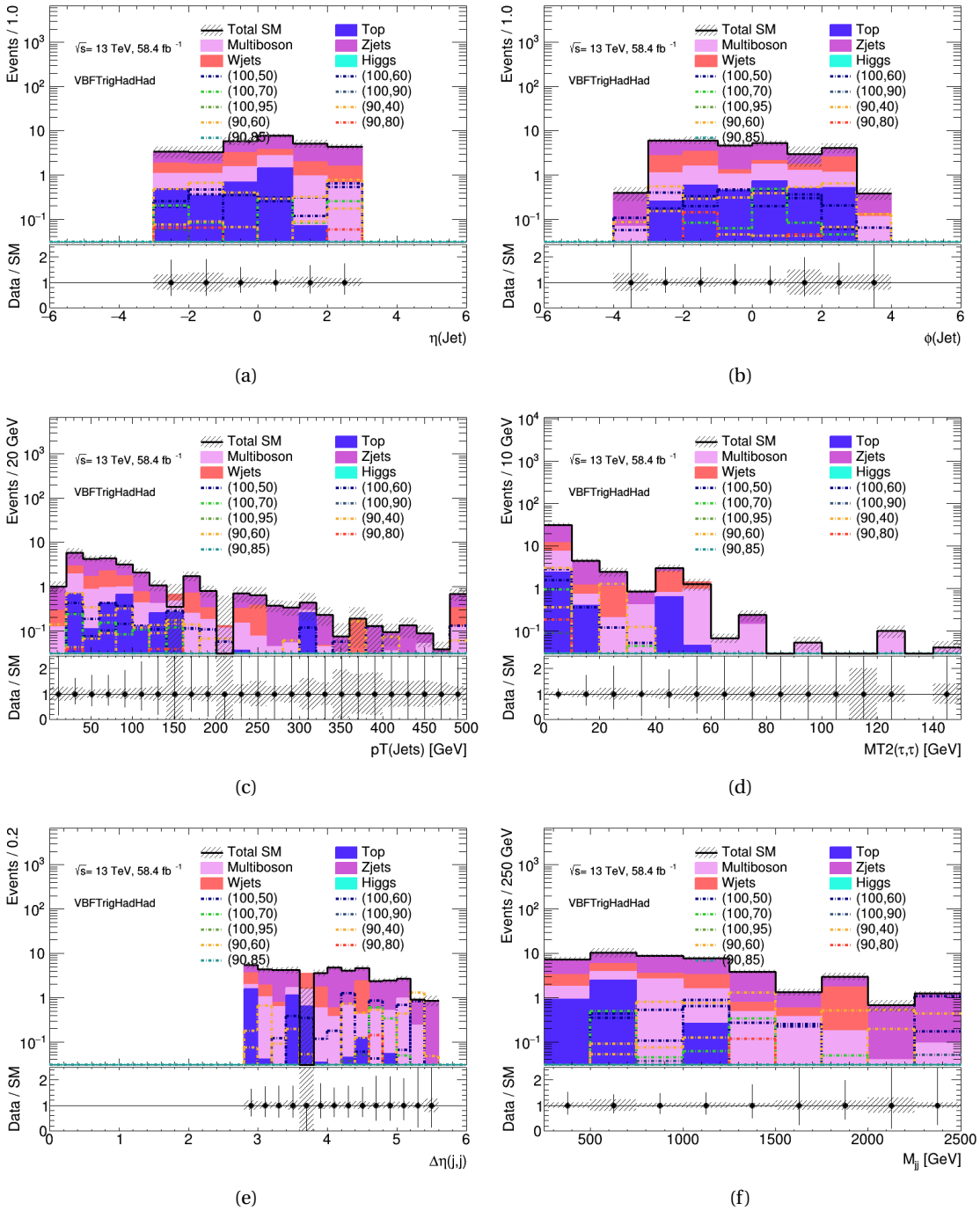

Figure 6.18: Set of kinematic distributions for τ-leptons, and jets objects for VBF SUSY di-$\tilde{\tau}$ signal and SM background MC simulated samples that are accepted by the di-tau VBF trigger. Shaded areas represent the statistical uncertainties only.

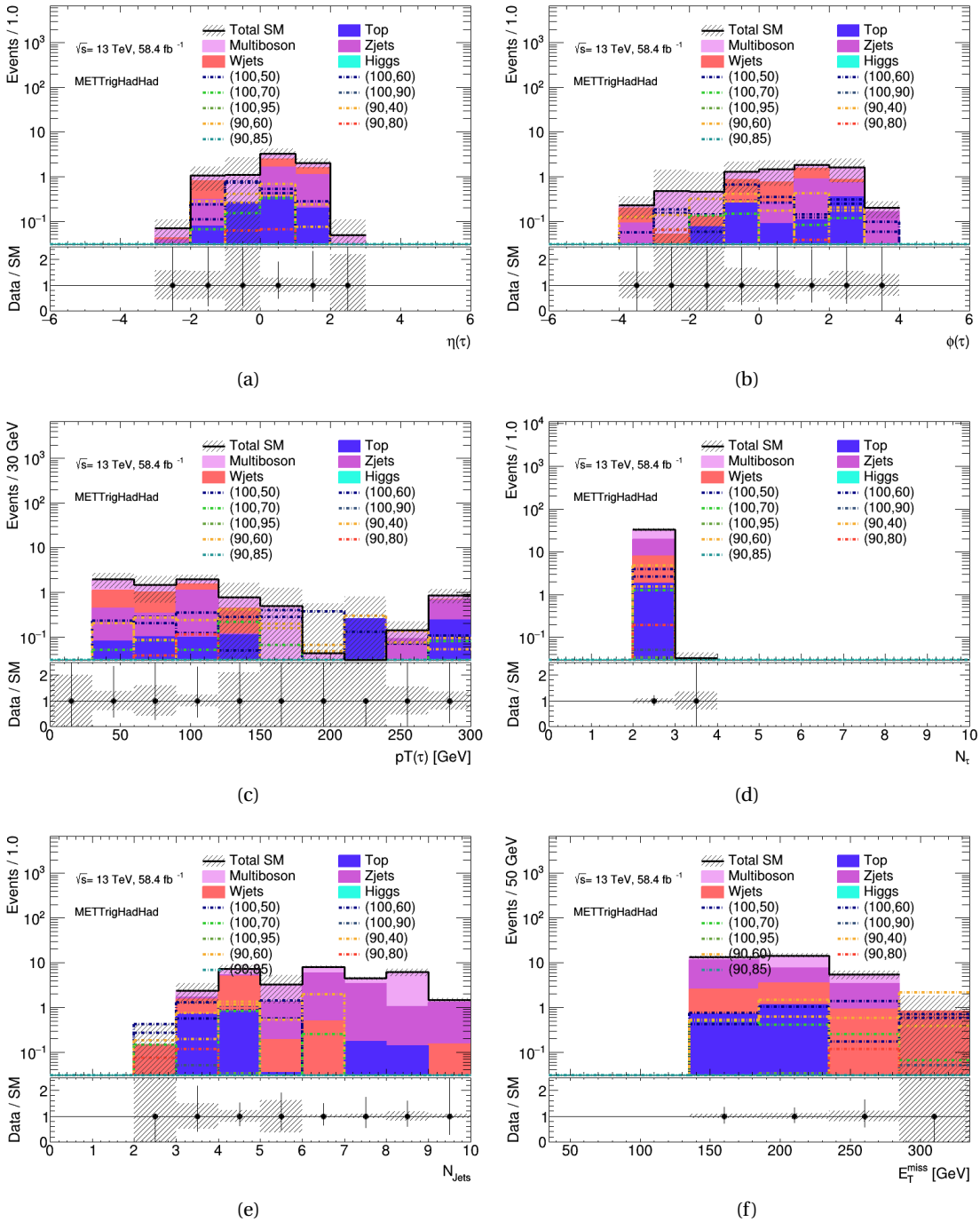

Figure 6.19: Set of kinematic distributions for τ-leptons, and jets objects for VBF SUSY di-$\tilde{\tau}$ signal and SM background MC simulated samples that are accepted by the di-tau+$E_{\mathrm{T}}^{\mathrm{miss}}$ trigger. Shaded areas represent the statistical uncertainties only.

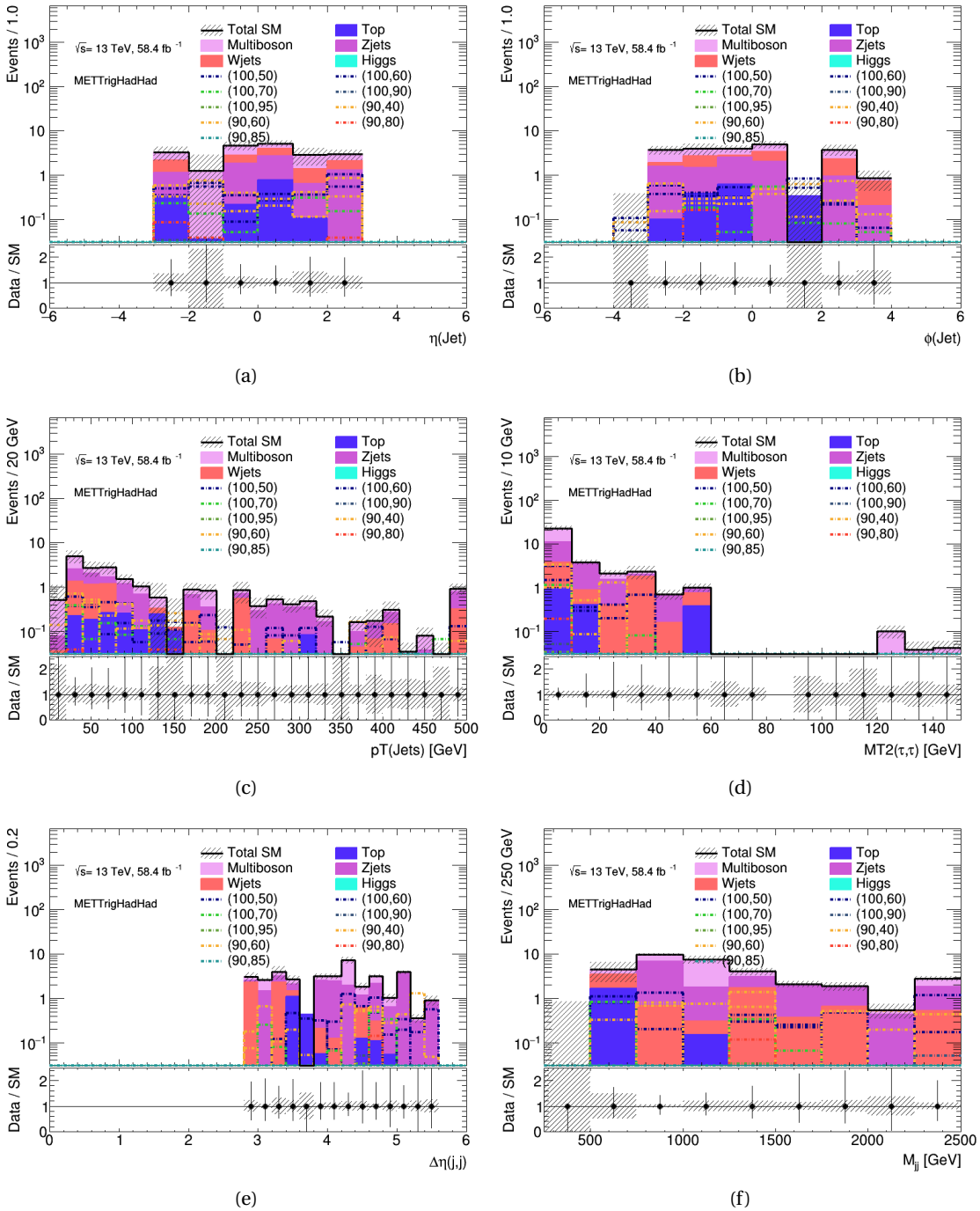

Figure 6.20: Set of kinematic distributions for τ-leptons, and jets objects for VBF SUSY di-$\tilde{\tau}$ signal and SM background MC simulated samples that are accepted by the di-tau+$E_{\mathrm{T}}^{\mathrm{miss}}$ trigger. Shaded areas represent the statistical uncertainties only.

Table 6.8: Number of expected MC events corresponding to the signal and background prediction passing the VBF-SR. Multiplicities are shown for the di-tau VBF and di-tau+$E_{\mathrm{T}}^{\mathrm{miss}}$ triggers.

	di-tau VBF trigger	di-tau+E_T^{miss} trigger
Background		
Multiboson	7.53	13.20
Wjets	8.02	5.96
Top	3.53	1.79
Zjets	25.31	11.80
Higgs	0.00	0.00
Total	44.39	32.75
$(\tilde{\tau},\tilde{\chi}_1^0)$[GeV]		
(100,50)	2.03	2.64
(100,60)	2.88	3.83
(100,70)	0.99	1.23
(100,90)	0.09	0.05
(100,95)	0.00	0.03
(90,40)	4.36	4.72
(90,60)	0.48	1.51
(90,80)	0.18	0.19
(90,85)	0.00	0.00

contribute to < 10% of the total accepted background. Accepted signal multiplicity is similar for both triggers, with the di-tau+$E_{\mathrm{T}}^{\mathrm{miss}}$ trigger having a slightly higher acceptance overall.

The di-tau VBF trigger is, thus, observed to have lower signal event acceptance across all signal mass points, as shown in Table 6.9. The di-tau+$E_{\mathrm{T}}^{\mathrm{miss}}$ trigger is found to have on average ~ 1.5 times the sensitivity to VBF SUSY signals that the currently available VBF trigger. This suggest the need for a custom trigger dedicated to the selection of VBF events that possess a SUSY process topology, to target these signals and explore the compressed region.

Table 6.9: Signal event acceptance after application of VBF-SR selection using di-tau VBF and di-tau+$E_{\mathrm{T}}^{\mathrm{miss}}$ triggers.

$(\tilde{\tau},\tilde{\chi}_1^0)$ [GeV]	di-tau VBF trigger	di-tau+E_T^{miss} trigger
(100,50)	0.30	0.46
(100,60)	0.43	0.67
(100,70)	0.15	0.21
(100,90)	0.01	0.01
(100,95)	0.00	0.01
(90,40)	0.65	0.82
(90,60)	0.07	0.26
(90,80)	0.03	0.03
(90,85)	0.00	0.00

As demonstrated in Section 6.5, VBF signals have strong potential for investigating the compressed regions of the $\tilde{\chi}_1^{\pm}$ $\tilde{\chi}_1^0$ and $\tilde{\tau}$ mass regions and would thus strongly benefit from the in-

troduction of a trigger dedicated to the selection of such events. No such trigger currently exists but there is a large amount of work ongoing in the ATLAS collaboration towards the development and testing of such triggers in preparation of Run-3 and beyond.

6.7 Summary

In this chapter several studies aimed at providing new avenues for further SUSY searches into $\tilde{\tau}$ production are presented. These studies are important for the continued development of the ATLAS physics program as it prepares to begin the next stages of data collection at the LHC. An initial study towards the understanding of the achievable sensitivity gain from lowered τ-lepton p_{T} threshold is presented and has shown some promising preliminary results. MC VBF signals samples have been simulated by the author and are described in detail in this chapter. A study on the kinematic properties of these samples at simulation level is presented and has been found to posses some promise towards the exploration of the compressed $\tilde{\tau}$ mass region. The performance of a currently available VBF trigger is presented compared to the di-tau+$E_{\mathrm{T}}^{\mathrm{miss}}$ trigger used in previous searches of di-$\tilde{\tau}$ production. The VBF trigger is found not to be as effective in selecting VBF SUSY signals as the di-tau+$E_{\mathrm{T}}^{\mathrm{miss}}$ trigger suggesting the need for such a dedicated trigger in order to more effectively search the unexplored compressed mass region.

CONCLUSIONS

All in all, you're just another brick in the wall.

Pink Floyd

In this thesis the best results to date for the search of the direct production of the supersymmetric partner of the τ-lepton, from pp collisions delivered by the LHC with a centre-of-mass energy $\sqrt{s} = 13$ TeV, are presented. Data collected by the ATLAS experiment between 2015 and 2018, corresponding to 139 fb^{-1}, is used to search for the $\tilde{\tau}$ particle that decays to two hadronically decaying τ-leptons and transverse missing energy, $E_{\mathrm{T}}^{\mathrm{miss}}$. Two SRs are derived and optimised to tackle the high and low $\tilde{\tau}$ signal masses separately. The author had leading involvement in the study of the performance of the tau triggers both in the inner detector, and as a full trigger chain used for the definition of the SRs. The $t\bar{t}$, $t\bar{t}$+V, Z + jets, single top, and multiboson irreducible SM backgrounds are estimated using dedicated VRs derived using MC simulated samples. The reducible SM backgrounds derived from the mis-identification of τ-lepton from the multijet and W + jets processes are estimated from data using the *ABCD method* and a dedicated WCR, respectively.

The theory uncertainties have been estimated by the author for the main SM background processes, which combined with the experimental uncertainties, are used by the fitting procedure as the total systematic uncertainties associated with the analysis. No significant deviation from the expected SM background events is observed in the constructed VRs, indicating an accurate estimation of background contributions.

Statistical fits have been used to extract the normalization factors used to derive the expected SM event yield in the defined SRs. In the absence of any significant excess over the expected SM background, the observed and expected numbers of events are used to set 95% CL exclusion limits on the parameters of the simplified electroweak supersymmetry models. Stau masses from 120 GeV to 390 GeV are excluded for a massless lightest neutralino, for this scenario. Limits on the simplified model production of left-handed-staus ($\tilde{\tau}_{\mathrm{L}}$), with masses between 155 GeV and 310 GeV for a massless lightest neutralino, have also been set .

A novel technique, named *Universal Fake Factor* method, currently under development for

the estimation of mis-identified τ_{had} objects in any arbitrary SR is also described in detail in Chapter 5. Once fully developed, this method will be able to produce *transfer factors* that can be used for the estimation of the main sources of reducible backgrounds for any analysis involving τ-leptons. This method is currently being validated in ATLAS and it is expected to be used by the collaboration in all analyses involving τ-leptons.

A description of possible future SUSY searched at ATLAS to target currently unexplored regions of $\tilde{\tau}$ masses is provided in Chapter 6. Several studies targeting low momentum τ-leptons and VBF SUSY topologies have been performed. The results yielded from these studies show the need for further improvements in the ATLAS trigger strategy and in the reconstruction of low energy hadronically decaying τ-leptons for future searches.

ANALYSIS TRIGGER STUDIES

A.1 Turn on curves

Different selection regions have been derived to create the turn on curves required for the estimation of the trigger efficiency described in Chapter 4. In addition to the region defined in the aforementioned chapter, two additional regions targeting Z boson production in association with jets and Top production have been derived as follows:

Z region: exactly 1 signal muon and at least one signal τ-lepton with OS to muon candidate. The muon must pass a single muon trigger and have $p_{\mathrm{T}} > 30$ GeV. The calculated invariant mass between the muon and τ-lepton must be $65 < M(\mu,\tau) < 95$ GeV. Only events without any b-tagged jets and with $M_{T2} < 20$ GeV are accepted.

Top region: exactly 1 signal muon and at least one signal τ-lepton with OS to muon candidate. The muon must pass a single muon trigger and have $p_{\mathrm{T}} > 30$ GeV. Events must contain at least 2 baseline jets and at least one b-tagged jet. At least of the jets must have $p_{\mathrm{T}} > 100$ GeV.

Using these selection the resulting turn on curves for the studied single leg tau triggers have been derived and are shown in Figures A.1 and A.2 for the Z region and top region, respectively.

The resulting offline thresholds are consistent with the ones derived using the W boson abundant regions described in Chapter 4.

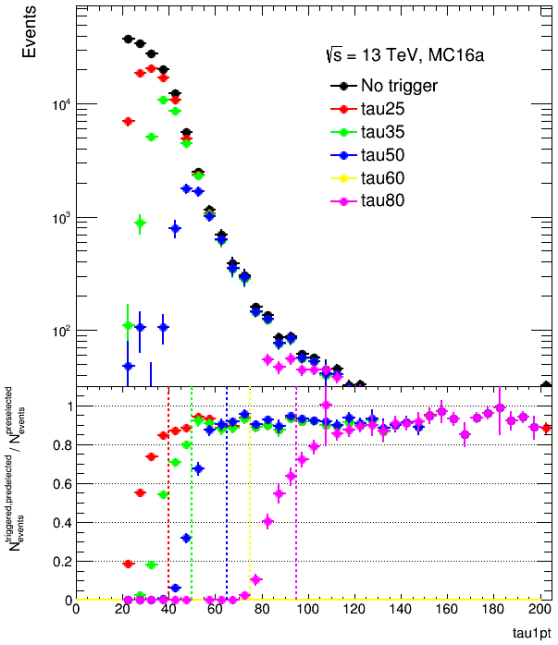

(a) Z region 2015-2016

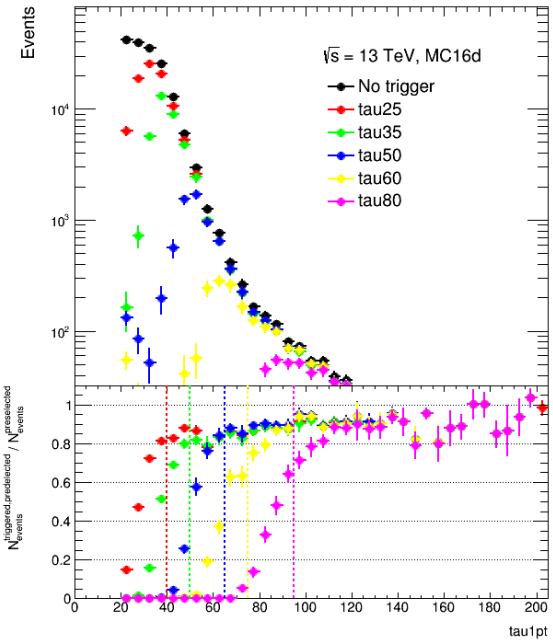

(b) Z region 2017

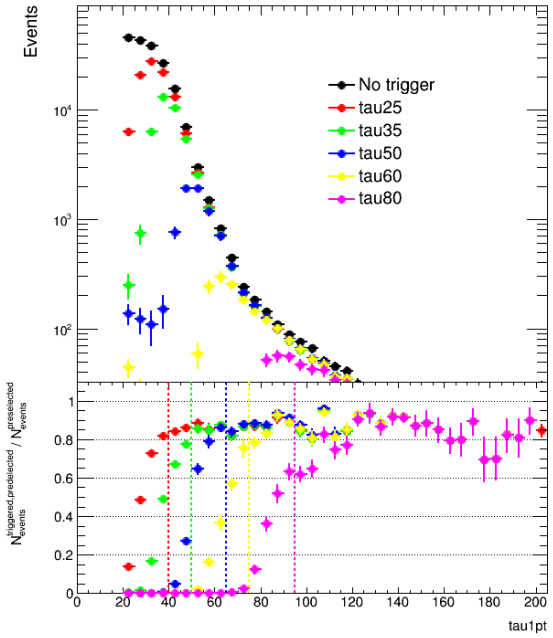

(c) Z region 2018

Figure A.1: Turn-on curves of single tau triggers using the Z region selection cuts on SM background samples, simulated in MC for 2015-2016, 2017, and 2018 data. Dashed line represents estimated turn-on thresholds.

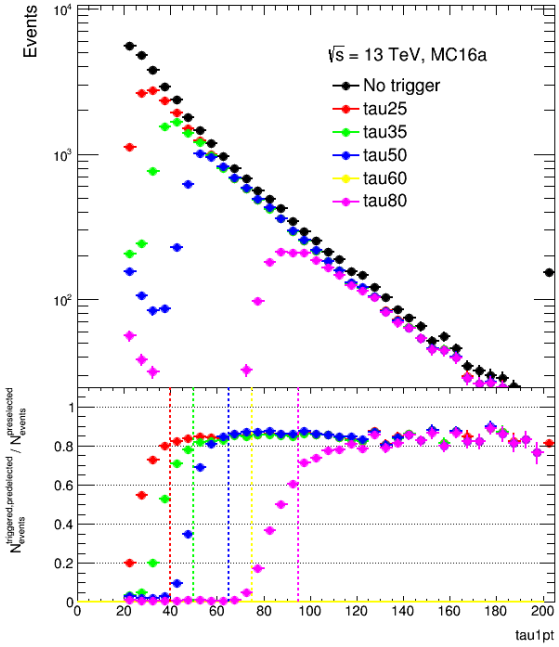

(a) Top region 2015-2016

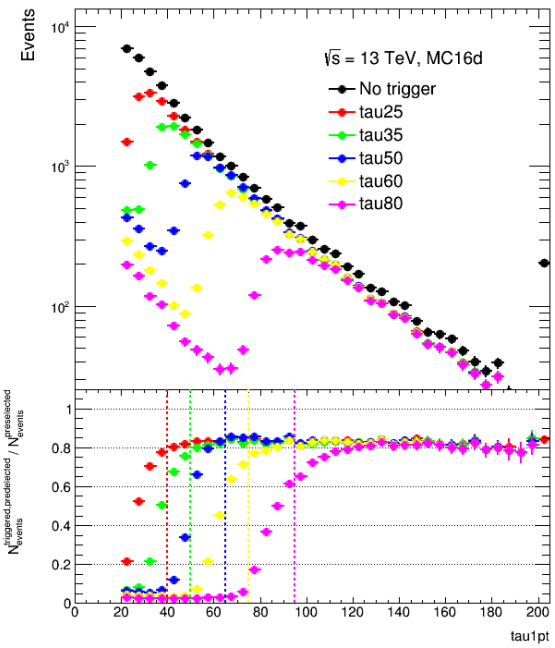

(b) Top region 2017

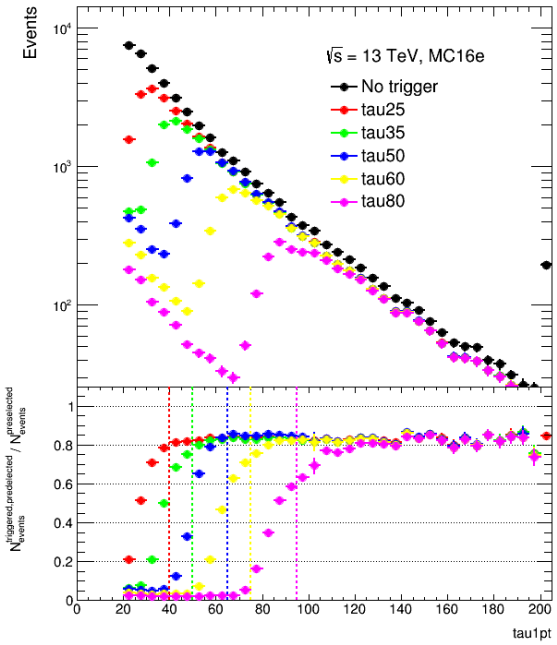

(c) Top region 2018

Figure A.2: Turn-on curves of single tau triggers using the top region selection cuts on SM background samples, simulated in MC for 2015-2016, 2017, and 2018 data. Dashed line represents estimated turn-on thresholds.

THEORETICAL UNCERTAINTIES

B

The theoretical uncertainties derived for the WCR, and WVR defined in 4.6.3 for all relevant SM backgrounds. To extrapolate the estimation of W + jets background events in the WVR, and SRs a transfer factor between these regions can be defined as $T = N_R/N_{WCR}$, where N_R and N_{WCR} are the number of events that pass the region that pass some region (R =WCR, High-mass SR, or Low-mass SR) and the WVR, respectively. The relevant systematic uncertainties are thus calculated using equation 4.4($\Delta TF_{Syst}^{Process} = \frac{TF_{Syst}^{Variation}}{TF_{Syst}^{Nominal}} - 1$), for the W + jets background alone, since these transfer factors are only relevant to the estimation of W + jets background events.

Table B.1: Table containing theoretical uncertainties for all relevant backgrounds using the WCR selection.

	WCR					
	Combined $\{\mu_R,\mu_F\}$ up / down	μ_R up / down	μ_F up / down	α_S up / down	PDF up / down	alt. PDF up / down
Higgs	0.101	0.001	0.098	0.071	0.025	0.022
	0.077	0.062	0.077	0.026	0.017	0.015
Multiboson	0.174	0.164	0.007	0.025	0.016	0.019
	0.129	0.123	0.007	0.048	0.017	0.002
Top	0.064	0.012	0.030	0.030	0.036	0.042
	0.085	0.041	0.014	0.041	0.039	0.046
Wjets	0.249	0.232	0.014	0.025	0.017	0.014
	0.165	0.154	0.013	0.054	0.020	0.006
Zjets	0.232	0.205	0.023	0.027	0.016	0.012
	0.155	0.137	0.020	0.050	0.017	0.010

Table B.2: Table containing theoretical uncertainties for all relevant backgrounds using the WVR selection.

	WVR					
	Combined $\{\mu_R,\mu_F\}$ up / down	μ_R up / down	μ_F up / down	α_S up / down	PDF up / down	alt. PDF up / down
Higgs	0.110	0.008	0.109	0.063	0.021	0.023
	0.077	0.053	0.077	0.024	0.016	0.014
Multiboson	0.172	0.159	0.011	0.034	0.016	0.019
	0.128	0.119	0.011	0.039	0.017	0.003
Top	0.104	0.064	0.032	0.044	0.052	0.035
	0.095	0.064	0.027	0.037	0.039	0.041
Wjets	0.278	0.255	0.020	0.021	0.020	0.014
	0.184	0.169	0.017	0.043	0.021	0.004
Zjets	0.207	0.195	0.012	0.034	0.019	0.016
	0.145	0.137	0.011	0.044	0.018	0.003

Table B.3: Table containing theoretical uncertainties for W + jets background estimation transfer factors from the WCR to: the WVR (TF_{WVR}), the Low-mass SR ($TF_{\text{Low-mass SR}}$), and to the High-mass SR ($TF_{\text{High-mass SR}}$) for W + jets background only.

	Combined $\{\mu_R,\mu_F\}$ up / down	μ_R up / down	μ_F up / down	α_S up / down	PDF up / down	alt. PDF up / down
TF_{WVR}	0.024	0.019	0.006	0.003	0.002	0.0002
	0.022	0.017	0.005	0.012	0.001	0.003
$TF_{\text{Low-mass SR}}$	0.086	0.099	0.002	0.013	0.005	0.002
	0.067	0.077	0.001	0.005	0.006	0.015
$TF_{\text{High-mass SR}}$	0.130	0.134	0.0003	0.101	0.013	0.019
	0.109	0.108	0.001	0.042	0.010	0.018

FAKE TAU ESTIMATION ADDITIONAL MATERIAL

C

C.1 MC templates

In this section, the track based jet width distributions derived using the base selection samples described in Section 5.5.2 of Chapter 5 are shown. The shown distributions have been made using the following selection requirements:

- τ_{had} $p_{\mathrm{T}} > 20$ GeV
- τ_{had} minimum BDT score > 0.05
- τ_{had} fails the *Medium* BDT working point
- No JVT requirement
- No trigger requirements

The distributions of the track based jets width have been produced for the full set of available p_{T} bins and for both 1 prong and 3 prong fake-τ candidates.

2015-2016

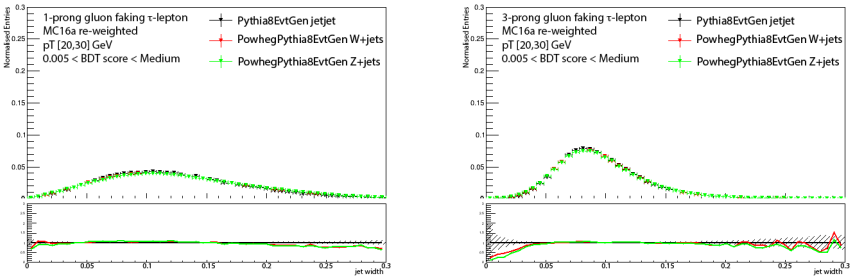

(a)

(b)

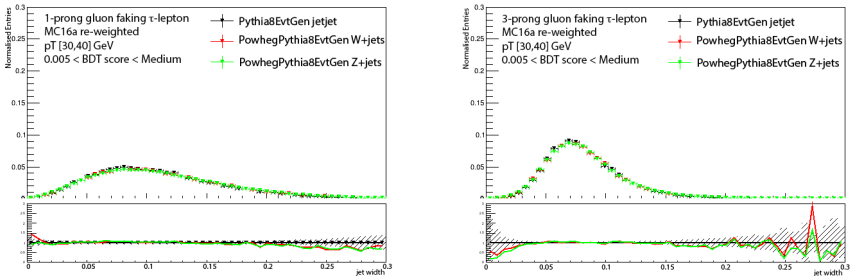

(c)

(d)

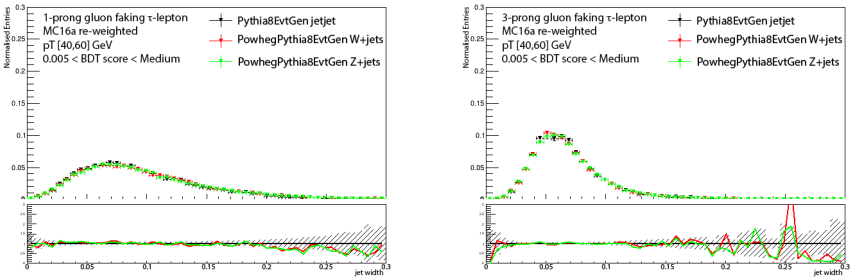

(e)

(f)

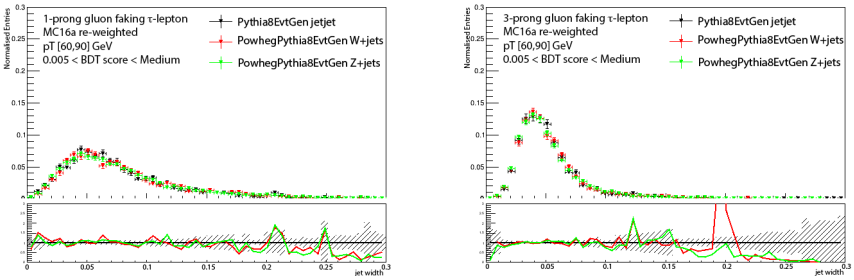

(g)

(h)

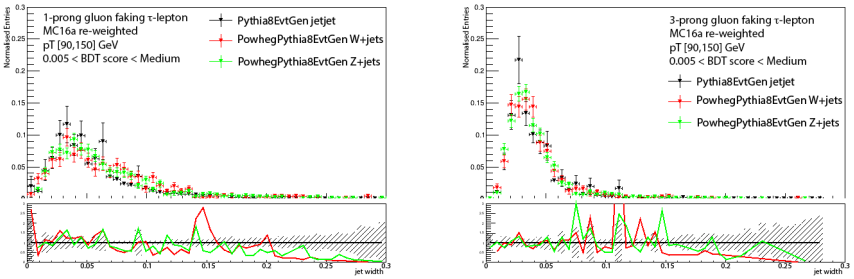

(i)

(j)

Figure C.1: Jet Width templates of gluon tau-faking jets separated into p_{T} bins, going from top as the lowest p_{T} bin to bottom being the highest. Left column shows templates for 1 prong tau, while right columns shows 3 prong tau templates. Samples shown have been produced for the 2015-2016 data collection period pile-up conditions.

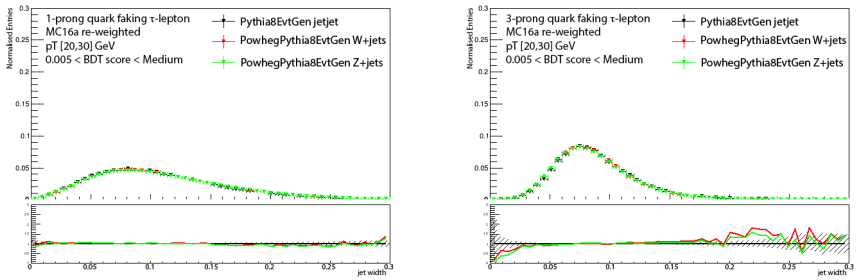

(a)

(b)

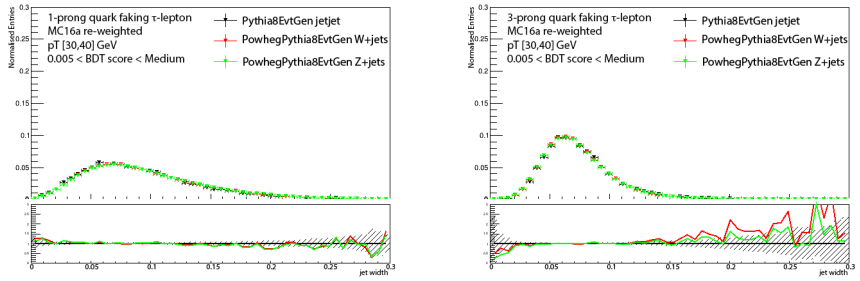

(c)

(d)

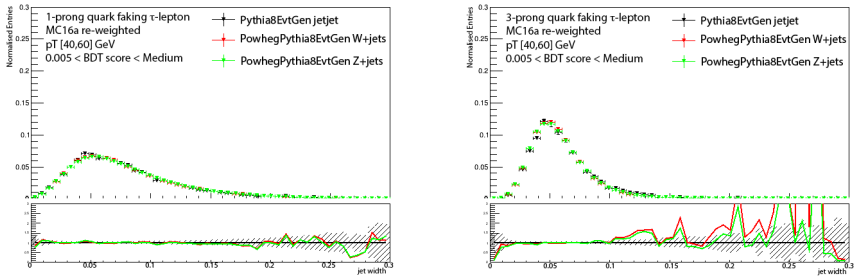

(e)

(f)

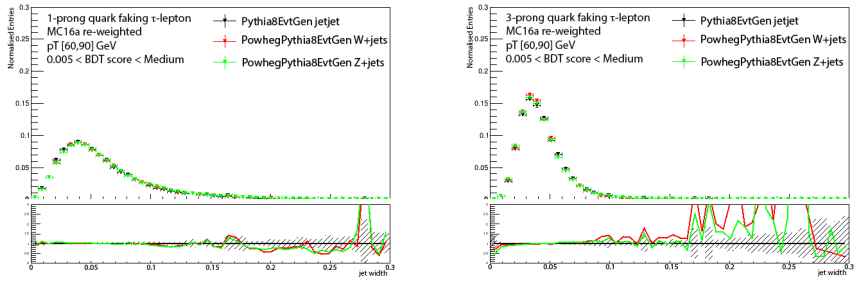

(g)

(h)

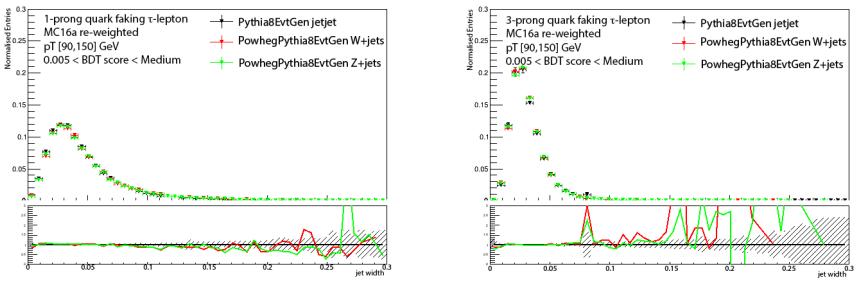

(i)

(j)

Figure C.2: Jet Width templates of quark tau-faking jets separated into p_{T} bins, going from top as the lowest p_{T} bin to bottom being the highest. Left column shows templates for 1 prong tau, while right columns shows 3 prong tau templates. Samples shown have been produced for the 2015-2016 data collection period pile-up conditions.

2017

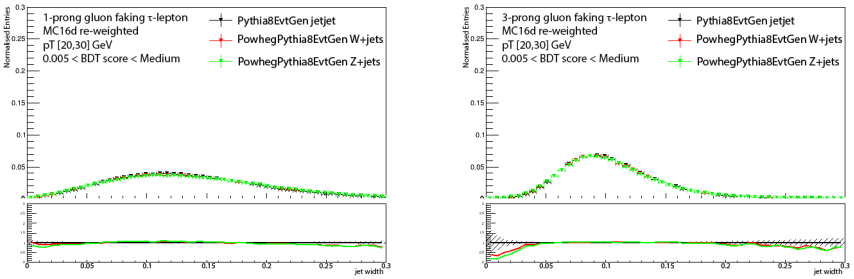

(a)

(b)

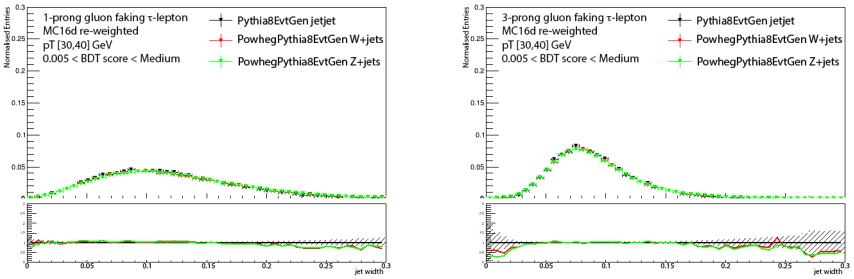

(c)

(d)

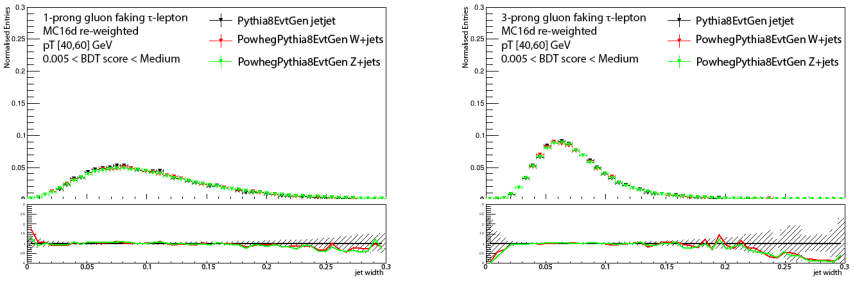

(e)

(f)

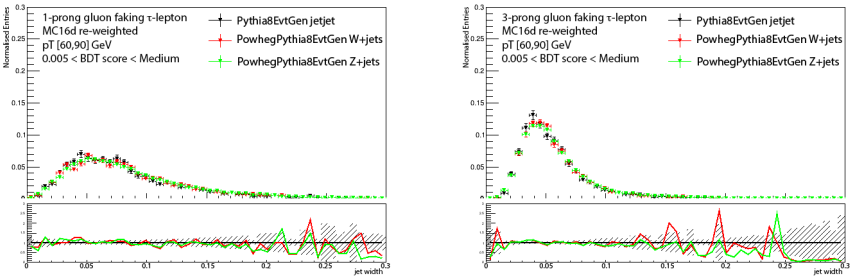

(g)

(h)

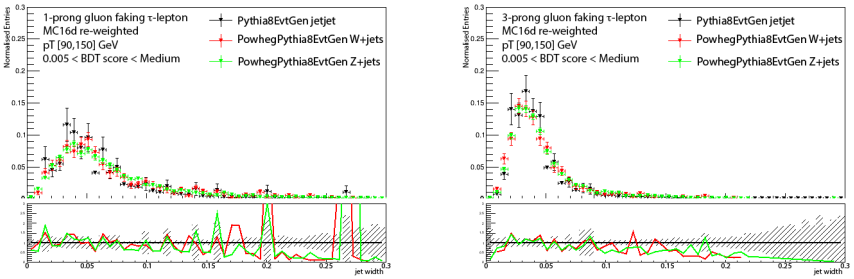

(i)

(j)

Figure C.3: Jet Width templates of gluon tau-faking jets separated into p_{T} bins, going from top as the lowest p_{T} bin to bottom being the highest. Left column shows templates for 1 prong tau, while right columns shows 3 prong tau templates. Samples shown have been produced for the 2017 data collection period pile-up conditions.

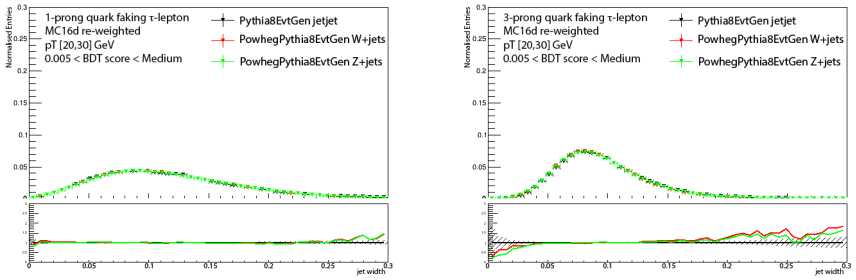

(a)

(b)

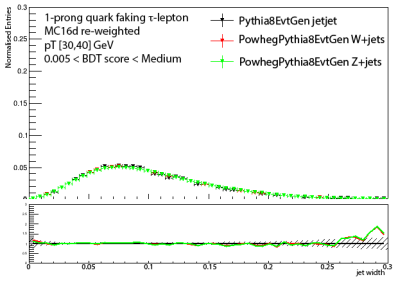

(c)

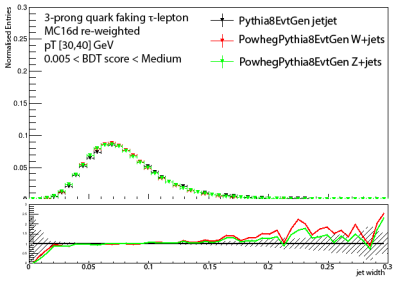

(d)

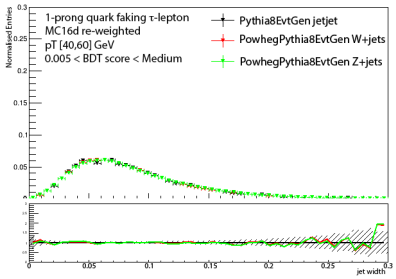

(e)

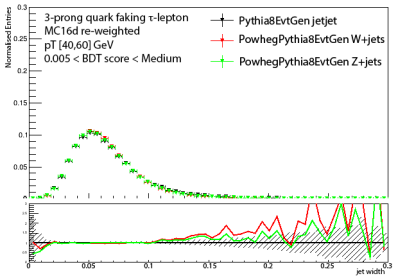

(f)

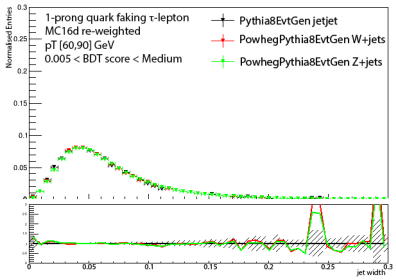

(g)

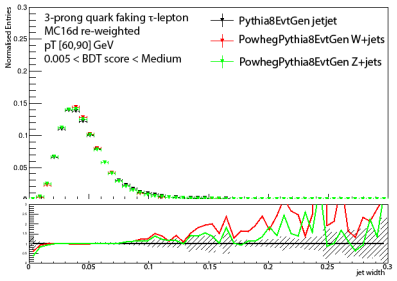

(h)

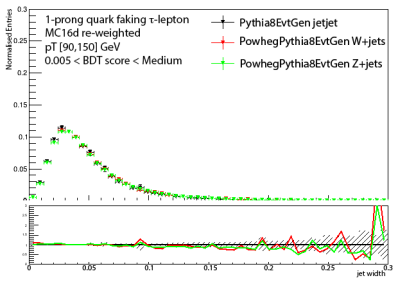

(i)

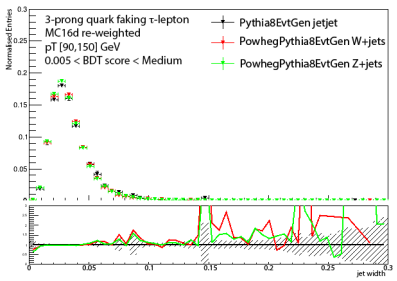

(j)

Figure C.4: Jet Width templates of quark tau-faking jets separated into p_{T} bins, going from top as the lowest p_{T} bin to bottom being the highest. Left column shows templates for 1 prong tau, while right columns shows 3 prong tau templates. Samples shown have been produced for the 2017 data collection period pile-up conditions.

GLOSSARY

ALICE A Large Ion Collider Experiment 25

AOD Analysis Objects Data 107

ATLAS A Toroidal LHC ApparatuS 10

BDT Boosted Decision Tree 36

BR Branching Ratio 59

BSM Beyond Standard Model 3

CERN European Organization for Nuclear Research 4

CKM Cabibbo-Kobayashi-Maskawa 12

CL Confidence Level 20

CMBR Cosmic Microwave Background Radiation 12

CMS Compact Muon Solenoid 10

CPU Central Processing Unit 44

CR Control Region 70

CSC Cathode Strip Chamber 33

CTP Central Trigger Processor 41

DAOD Derived Analysis Object Data 113

DM Dark Matter 12

ECAL Electromagnetic Calorimeter 28

EM electromagnetic 5

FCal Forward Calorimeter 33

FCNC Flavour Changing Neutral Currents 17

FF Fake Factor 76

FoM Figure of Merit 72

FSR Final State Radiation 84

FTF Fast Track Finder . . . 43

FTK Fast Tracker . . . 41

GUT Grand Unification Theory . . . 11

HCAL Hadronic Calorimeter

HL-LHC High Luminosity LHC . . . 133

HLT High Level Trigger . . . 34

HP High Priority . . . 107

IBL Insertable B-Layer . . . 29

ID Inner Detector . . . 26

ISR Initial State Radiation . . . 84

JES Jet Energy Scale . . . 61

JER Jet Energy Resolution . . . 81

JVT Jet Vertex Tagger . . . 61

L1 Level-1 . . . 34

L1Calo L1 Calorimeter . . . 41

L1Muon L1 Muon . . . 41

LAr Liquid Argon . . . 32

LC Local hadronic Calibration . . . 36

LEIR Low Energy Ion Ring . . . 25

LEP Large Electron-Positron Collider . . . 10

LH Likelihood . . . 104

LHC Large Hadron Collider . . . 3

LHCb Large Hadron Collider beauty . . . 25

LINAC2 Linear Accelerator 2 . . . 25

LINAC3 Linear Accelerator 3 . . . 25

LO Leading Order . . . 142

LP Low Priority . . . 107

LS1 Long Shut-down 1 . . . 24

LS2 Long Shut-down 2 . . . 132

LSP Lightest Supersymmetric Particle . . . 17

MC Monte Carlo . . . 57

ME Matrix Element . . . 59

MDT Monitored Drift Tube . . . 33

MLE Maximum Likelihood Estimation . . . 87

MS Muon Spectrometer . . . 27

MSSM Minimal Supersymmetric Standard Model . . . 14

MVA Multivariate Algorithm . . . 38

NbTi Niobium-Titanium . . . 28

NLO Next-to-Leading Order

NNLO Next-to-Next-to-Leading Order

NLO + NLL Next-to-Leading-Logarithm Accuracy . . . 59

NNLO+NNLL Next-to-Next-to-Leading-Order + Next-to-Next-to-Leading Logarithm Accuracy . . . 84

NNLL Next-to-Next-to-Leading Logarithm

NP Nuisance Parameter . . . 81

NSW New Small Wheel . . . 132

OR Overlap Removal . . . 60

OS Opposite Sign . . . 69

Pb lead . . . 32

PhD Doctor of Philosophy . . . 2

Pixel Silicon Pixel Tracker . . . 26

PDF Parton Distribution Function . . . 59

PDG ID Particle Databook Group Identification . . . 108

pMSSM Phenomenological MSSM . . . 18

PS Parton Shower . . . 25

PSB Proton Synchrotron Booster . . . 25

PV Primary Vertex . . . 60

QCD Quantum Chromodynamics . . . 7

QED Quantum Electrodynamics . . . 6

QFT Quantum Field Theory . . . 4

RF Radiofrequency . . . 24

RNN Recursive Neural Network . . . 37

RoI Region of Interest . . . 34

ROS Read-Out System . . . 41

RPC R-Parity Conserving . . . 33

RPC Resistive-Plate Chamber . . . 33

BIBLIOGRAPHY

[1] B. R. Martin and S. Graham, *Particle physics*. The Manchester physics series. Wiley, Chichester, 2nd ed.. ed., 1997.

[2] ATLAS Collaboration, *Search for direct stau production in events with two hadronic τ-leptons in $\sqrt{s} = 13$ TeV pp collisions with the ATLAS detector*, Phys. Rev. D **101** (2020) 032009. https://link.aps.org/doi/10.1103/PhysRevD.101.032009.

[3] G. Arnison et al., *Experimental observation of isolated large transverse energy electrons with associated missing energy at s=540 GeV*, Physics Letters B **122** no. 1, (1983) 103 – 116. http://www.sciencedirect.com/science/article/pii/0370269383911772.

[4] UA1 Collaboration, *Experimental Observation of Lepton Pairs of Invariant Mass Around 95-GeV/c^2 at the CERN SPS Collider*, Phys. Lett. **B126** (1983) 398–410. [,7.55(1983)].

[5] M. L. Perl and et.al., *Evidence for Anomalous Lepton Production in $e^+ - e^-$ Annihilation*, Phys. Rev. Lett. **35** (1975) 1489–1492. https://link.aps.org/doi/10.1103/PhysRevLett.35.1489.

[6] ATLAS Collaboration, *Observation of a New Particle in the Search for the Standard Model Higgs Boson with the ATLAS Detector at the LHC*, Phys.Lett. **B716** (2012), arXiv:1207.7214 [hep-ex].

[7] CMS Collaboration, *Observation of a new boson at a mass of 125 GeV with the CMS experiment at the LHC*, Phys.Lett. **B716** (2012), arXiv:1207.7235 [hep-ex].

[8] M. E. Peskin, D. V. Schroeder, *An Introduction to Quantum Field Theory*. Westview Press, 1995.

[9] E. Noether, *Invariant variation problems*, Transport Theory and Statistical Physics **1** no. 3, (1971) 186–207, https://doi.org/10.1080/00411457108231446. https://doi.org/10.1080/00411457108231446.

[10] L. Lederman and C. Hill, *Symmetry and the Beautiful Universe*. Prometheus Books, 2004. https://books.google.co.uk/books?id=X2QPAQAAMAAJ.

[11] M. Gell-Mann, *The interpretation of the new particles as displaced charge multiplets*, Il Nuovo Cimento (1955-1965) **4** no. 2, (1956) 848–866. https://doi.org/10.1007/BF02748000.

[12] T. Nakano and K. Nishijima, *Charge Independence for V-particles*, Progress of Theoretical Physics **10** no. 5, (1953) 581–582, https://academic.oup.com/ptp/article-pdf/10/5/581/5364926/10-5-581.pdf. https://doi.org/10.1143/PTP.10.581.

[13] A. Pich, *The Standard Model of Electroweak Interactions*, arXiv:1201.0537 [hep-ph].

[14] S. Weinberg, *The quantum theory of fields. Vol. 2: Modern applications*. Cambridge University Press, 2013.

[15] S. L. Glashow, *Partial Symmetries of Weak Interactions*, Nucl. Phys. **22** (1961) 579–588.

[16] A. Salam and J. Ward, *Electromagnetic and weak interactions*, Physics Letters **13** no. 2, (1964) 168 – 171. http://www.sciencedirect.com/science/article/pii/0031916364907115.

[17] S. Weinberg, *A Model of Leptons*, Phys. Rev. Lett. **19** (1967) 1264–1266. https://link.aps.org/doi/10.1103/PhysRevLett.19.1264.

[18] P. W. Higgs, *Broken Symmetries and the Masses of Gauge Bosons*, Phys. Rev. Lett. **13** (1964) 508–509.

[19] F. Englert and R. Brout, *Broken Symmetry and the Mass of Gauge Vector Bosons*, Phys. Rev. Lett. **13** (1964) 321–323.

[20] J. Ellis, M. K. Gaillard, and D. V. Nanopoulos, *A Historical Profile of the Higgs Boson. An Updated Historical Profile of the Higgs Boson,*. https://cds.cern.ch/record/2012465.

[21] ATLAS Collaboration, *Combined measurements of Higgs boson production and decay using up to* 80 fb^{-1} *of proton-proton collision data at* $\sqrt{s} = 13$ TeV *collected with the ATLAS experiment*, Phys. Rev. D **101** (2020) 012002. https://link.aps.org/doi/10.1103/PhysRevD.101.012002.

[22] ATLAS Collaboration, *Measurement of the Higgs boson mass in the* $H \to ZZ* \to 4\ell$ *and* $H \to \gamma\gamma$ *channels with s=13 TeV pp collisions using the ATLAS detector*, Physics Letters B **784** (2018) 345–366. https://www.sciencedirect.com/science/article/pii/S0370269318305884.

[23] S. Weinberg, *Implications of Dynamical Symmetry Breaking*, Phys. Rev. **D19** (1976) 1277–1280.

[24] K. L. Chan, U. Chattopadhyay, and P. Nath, *Naturalness, weak scale supersymmetry, and the prospect for the observation of supersymmetry at the Fermilab Tevatron and at the CERN LHC*, Physical Review D **58** no. 9, (1998). http://dx.doi.org/10.1103/PhysRevD.58.096004.

[25] L. J. Hall, D. Pinner, and J. T. Ruderman, *A natural SUSY Higgs near 125 GeV*, Journal of High Energy Physics **2012** no. 4, (2012) 1–25. http://dx.doi.org/10.1007/JHEP04(2012)131.

[26] G. Ross and B. P. Company, *Grand Unified Theories*. Benjamin/Cummings Series in the Life Sciences. Benjamin/Cummings Publishing Company, 1984. https://books.google.co.uk/books?id=cfbvAAAAMAAJ.

[27] A. D. Sakharov, *Violation of CP Invariance, C asymmetry, and baryon asymmetry of the universe*, Pisma Zh. Eksp. Teor. Fiz. **5** (1967) 32–35.

[28] V. Kuzmin, V. Rubakov, and M. Shaposhnikov, *On anomalous electroweak baryon-number non-conservation in the early universe*, Physics Letters B **155** no. 1, (1985) 36–42. https://www.sciencedirect.com/science/article/pii/0370269385910287.

[29] N. Jarosik, C. L. Bennett, J. Dunkley, B. Gold, M. R. Greason, M. Halpern, R. S. Hill, G. Hinshaw, A. Kogut, E. Komatsu, D. Larson, M. Limon, S. S. Meyer, M. R. Nolta, N. Odegard, L. Page, K. M. Smith, D. N. Spergel, G. S. Tucker, J. L. Weiland, E. Wollack, and E. L. Wright, *Seven-year Wilkinson Microwave Anisotropy Probe (WMAP) Observations: Sky Maps, Systematic Errors, and Basic Results*, The Astrophysical Journal Supplement Series **192** no. 2, (2011) 14. http://dx.doi.org/10.1088/0067-0049/192/2/14.

[30] M. Carena, J. Moreno, M. Quirós, M. Seco, and C. Wagner, *Supersymmetric CP-violating currents and electroweak baryogenesis*, Nuclear Physics B **599** no. 1, (2001) 158–184. https://www.sciencedirect.com/science/article/pii/S0550321301000323.

[31] V. C. Rubin and W. K. Ford, Jr., *Rotation of the Andromeda Nebula from a Spectroscopic Survey of Emission Regions*, Astrophysical Journal **159** (1970) 379.

[32] M. Bradac, S. W. Allen, T. Treu, H. Ebeling, R. Massey, R. G. Morris, A. von der Linden, and D. Applegate, *Revealing the properties of dark matter in the merging cluster MACSJ0025.4-1222*, Astrophys. J. **687** (2008) 959, arXiv:0806.2320 [astro-ph].

[33] Planck Collaboration, P. A. R. Ade et al., *Planck 2013 results. XVI. Cosmological parameters*, Astron. Astrophys. **571** (2014) A16, arXiv:1303.5076 [astro-ph.CO].

[34] M. H. Jones, R. J. A. Lambourne, and S. Serjeant, *An Introduction to Galaxies and Cosmology (2nd ed)*. Cambridge University Press/Open University, Cambridge, January, 2015. http://oro.open.ac.uk/44361/.

[35] G. Gentile, G. I. G. Józsa, P. Serra, G. H. Heald, W. J. G. de Blok, F. Fraternali, M. T. Patterson, R. A. M. Walterbos, and T. Oosterloo, *HALOGAS: Extraplanar gas in NGC 3198*, Astronomy and Astrophysics **554** (2013) A125, arXiv:1304.4232 [astro-ph.CO].

[36] S. P. Martin, *A Supersymmetry primer*, arXiv:hep-ph/9709356 [hep-ph]. [Adv. Ser. Direct. High Energy Phys.18,1(1998)].

[37] R. Barbieri and G. F. Giudice, *Upper Bounds on Supersymmetric Particle Masses*, Nucl. Phys. **B306** (1988) 63–76.

[38] F. Jegerlehner, *The hierarchy problem of the electroweak Standard Model revisited*, arXiv:1305.6652 [hep-ph].

[39] C. CSÁKI, *The minimal supersymmetric standard model*, Modern Physics Letters A **11** no. 08, (1996) 599–613. http://dx.doi.org/10.1142/S021773239600062X.

[40] J. Ellis, J. Hagelin, D. Nanopoulos, K. Olive, and M. Srednicki, *Supersymmetric relics from the big bang*, Nuclear Physics B **238** no. 2, (1984) 453–476. https://www.sciencedirect.com/science/article/pii/0550321384904619.

[41] M. Bona, M. Ciuchini, E. Franco, V. Lubicz, G. Martinelli, F. Parodi, M. Pierini, P. Roudeau, C. Schiavi, L. Silvestrini, V. Sordini, A. Stocchi, and V. Vagnoni, *Model-independent constraints on $\Delta F=2$ operators and the scale of new physics*, Journal of High Energy Physics **2008** no. 03, (2008) 049–049. https://doi.org/10.1088/1126-6708/2008/03/049.

[42] ATLAS Collaboration, *Search for squarks and gluinos in final states with jets and missing transverse momentum using 36 fb^{-1} of $\sqrt{s} = 13$ TeV pp collision data with the ATLAS detector*, Phys. Rev. D **97** (2018) 112001. https://link.aps.org/doi/10.1103/PhysRevD.97.112001.

[43] ATLAS Collaboration, *Search for new phenomena in final states with large jet multiplicities and missing transverse momentum using $\sqrt{s}$ = 13 TeV proton-proton collisions recorded by ATLAS in Run 2 of the LHC*, Journal of High Energy Physics **2020** no. 10, (2020) 62. https://doi.org/10.1007/JHEP10(2020)062.

[44] W. Beenakker, C. Borschensky, M. Krämer, A. Kulesza, and E. Laenen, *NNLL-fast: predictions for coloured supersymmetric particle production at the LHC with threshold and Coulomb resummation*, Journal of High Energy Physics **2016** no. 12, (2016). http://dx.doi.org/10.1007/JHEP12(2016)133.

[45] ATLAS Collaboration, M. Aaboud et al., *Search for a scalar partner of the top quark in the jets plus missing transverse momentum final state at $\sqrt{s}$=13 TeV with the ATLAS detector*, JHEP **12** (2017) 085, arXiv:1709.04183 [hep-ex].

[46] ATLAS Collaboration, *Search for direct pair production of the top squark in all-hadronic final states in proton-proton collisions at $\sqrt{s} = 8$ TeV with the ATLAS detector*, JHEP **09** (2014) 015, arXiv:1406.1122 [hep-ex].

[47] ATLAS Collaboration, *Search for new phenomena with top quark pairs in final states with one lepton, jets, and missing transverse momentum in pp collisions at $\sqrt{s}$= 13 TeV with the ATLAS detector*, tech. rep., 2020. arXiv:2012.03799 [hep-ex].

[48] A. M. Sirunyan, A. Tumasyan, W. Adam, F. Ambrogi, T. Bergauer, J. Brandstetter, M. Dragicevic, J. Erö, A. Escalante Del Valle, and et al., *Search for top squark pair production in a final state with two tau leptons in proton-proton collisions at $\sqrt{s}$ = 13 TeV*, Journal of High Energy Physics **2020** no. 2, (2020). http://dx.doi.org/10.1007/JHEP02(2020)015.

[49] A. M. Sirunyan, A. Tumasyan, W. Adam, F. Ambrogi, T. Bergauer, J. Brandstetter, M. Dragicevic, J. Erö, A. Escalante Del Valle, and et al., *Search for direct top squark pair production in events with one lepton, jets, and missing transverse momentum at 13 TeV with the CMS experiment*, Journal of High Energy Physics **2020** no. 5, (2020). http://dx.doi.org/10.1007/JHEP05(2020)032.

[50] ATLAS Collaboration, *SUSY March 2021 Summary Plot Update*, Tech. Rep. ATL-PHYS-PUB-2021-007, CERN, Geneva, Mar, 2021. http://cds.cern.ch/record/2758782.

[51] L3 Collaboration, *Search for scalar leptons and scalar quarks at LEP*, Physics Letters B **580** no. 1-2, (2004) 37–49. http://dx.doi.org/10.1016/j.physletb.2003.10.010.

[52] ATLAS Collaboration, *Search for the electroweak production of supersymmetric particles in $\sqrt{s} = 8$ TeV pp collisions with the ATLAS detector*, Phys. Rev. D **93** (2016) 052002. https://link.aps.org/doi/10.1103/PhysRevD.93.052002.

[53] CMS Collaboration, *Search for electroweak production of charginos in final states with two τ leptons in pp collisions at $\sqrt{s} = 8$ TeV*, Journal of High Energy Physics **2017** no. 4, (2017) 18. https://doi.org/10.1007/JHEP04(2017)018.

[54] A. M. Sirunyan, A. Tumasyan, W. Adam, F. Ambrogi, T. Bergauer, J. Brandstetter, M. Dragicevic, J. Erö, A. E. Del Valle, and et al., *Search for direct pair production of supersymmetric partners to the τ lepton in proton–proton collisions at $\sqrt{s} = 13$ TeV*, The European Physical Journal C **80** no. 3, (2020). http://dx.doi.org/10.1140/epjc/s10052-020-7739-7.

[55] O. S. Brüuning, P. Collier, P. Lebrun, S. Myers, R. Ostojic, J. Poole and P. Proudlock, *LHC Design Report,*. https://cds.cern.ch/record/782076.

[56] K. Wille, *The physics of particle accelerators: an introduction.* Oxford Univ. Press, Oxford, 2000. https://cds.cern.ch/record/560708.

[57] D. Brandt, *CAS - CERN Accelerator School: Intermediate Accelerator Physics: Zeuthen, Germany 15 - 26 Sep 2003. CAS - CERN Accelerator School: Intermediate Course on Accelerator Physics,*. http://cds.cern.ch/record/603056.

[58] ATLAS Collaboration, Z. Marshall, *Simulation of Pile-up in the ATLAS Experiment*, J. Phys. Conf. Ser. **513** (2014) 022024.

[59] C. Lefèvre, *The CERN accelerator complex,*. http://cds.cern.ch/record/1260465.

[60] LHCb Collaboration, *The LHCb Detector at the LHC*, JINST (2008).

[61] ALICE Collaboration, *The ALICE experiment at the CERN LHC*, Journal of Instrumentation **3** no. 08, (2008) S08002. http://stacks.iop.org/1748-0221/3/i=08/a=S08002.

[62] CMS Collaboration, *The CMS experiment at the CERN LHC*, Journal of Instrumentation **3** no. 08, (2008) S08004. http://stacks.iop.org/1748-0221/3/i=08/a=S08004.

[63] R. D. Cousins, J. T. Linnemann, and J. Tucker, *Evaluation of three methods for calculating statistical significance when incorporating a systematic uncertainty into a test of the background-only hypothesis for a Poisson process*, Nuclear Instruments and Methods in Physics Research Section A: Accelerators, Spectrometers, Detectors and Associated Equipment **595** no. 2, (2008) 480 – 501. http://www.sciencedirect.com/science/article/pii/S0168900208010255.

[64] A. Yamamoto, Y. Makida, R. Ruber, Y. Doi, T. Haruyama, F. Haug, H. ten Kate, M. Kawai, T. Kondo, Y. Kondo, J. Metselaar, S. Mizumaki, G. Olesen, O. Pavlov, S. Ravat, E. Sbrissa, K. Tanaka, T. Taylor, and H. Yamaoka, *The ATLAS central solenoid*, Nuclear Instruments and Methods in Physics Research Section A: Accelerators, Spectrometers, Detectors and Associated Equipment **584** no. 1, (2008) 53 – 74. http://www.sciencedirect.com/science/article/pii/S0168900207020414.

[65] ATLAS Collaboration, *The ATLAS experiment at the CERN Large Hadron Collider*, Journal of Instrumentation **3** no. 08, (2008) S08003. http://stacks.iop.org/1748-0221/3/i=08/a=S08003.

[66] ATLAS Collaboration, "Atlas experiment - photos." http://atlasexperiment.org/photos/inner-detector-combined.html.

[67] ATLAS Collaboration, *ATLAS pixel detector electronics and sensors*, Journal of Instrumentation **3** no. 07, (2008) P07007–P07007. https://doi.org/10.1088/1748-0221/3/07/p07007.

[68] ATLAS Collaboration, *ATLAS pixel detector electronics and sensors*, Journal of Instrumentation **3** no. 07, (2008) P07007. http://stacks.iop.org/1748-0221/3/i=07/a=P07007.

[69] ATLAS Collaboration, *ATLAS Insertable B-Layer Technical Design Report,*. https://cds.cern.ch/record/1291633.

[70] ATLAS Collaboration, *The silicon microstrip sensors of the ATLAS semiconductor tracker*, Nuclear Instruments and Methods in Physics Research Section A: Accelerators, Spectrometers, Detectors and Associated Equipment **578** no. 1, (2007) 98–118. https://www.sciencedirect.com/science/article/pii/S0168900207007644.

[71] A. Bingül, *The ATLAS TRT and its Performance at LHC*, Journal of Physics: Conference Series **347** no. 1, (2012) 012025. http://iopscience.iop.org/article/10.1088/1742-6596/347/1/012025/meta.

[72] ATLAS Collaboration, *ATLAS liquid-argon calorimeter: Technical Design Report,*. https://cds.cern.ch/record/331061.

[73] ATLAS Collaboration, *Technical Design Report for the Phase-II Upgrade of the ATLAS Tile Calorimeter*, Tech. Rep. CERN-LHCC-2017-019. ATLAS-TDR-028, CERN, Geneva, Sep, 2017. https://cds.cern.ch/record/2285583.

[74] ATLAS Collaboration, *ATLAS muon spectrometer: Technical design report,*. https://cds.cern.ch/record/331068.

[75] ATLAS TDAQ Collaboration, M. Abolins et al., *The ATLAS Data Acquisition and High Level Trigger system*, JINST **11** no. 06, (2016) P06008.

[76] ATLAS Collaboration, W. Panduro Vazquez, *The ATLAS Data Acquisition system in LHC Run 2*, J. Phys. Conf. Ser. **898** no. 3, (2017) 032017.

[77] K. Olive, *Review of Particle Physics*, Chinese Physics C **38** no. 9, (2014) 090001. https://doi.org/10.1088%2F1674-1137%2F38%2F9%2F090001.

[78] ATLAS Collaboration, *Reconstruction, Energy Calibration, and Identification of Hadronically Decaying Tau Leptons in the ATLAS Experiment for Run-2 of the LHC*, Tech. Rep. ATL-PHYS-PUB-2015-045, CERN, Geneva, Nov, 2015. https://cds.cern.ch/record/2064383.

[79] ATLAS Collaboration, *Identification of hadronic tau lepton decays using neural networks in the ATLAS experiment*, Tech. Rep. ATL-PHYS-PUB-2019-033, CERN, Geneva, Aug, 2019. https://cds.cern.ch/record/2688062.

[80] ATLAS Collaboration, *Performance of the ATLAS Trigger System in 2015*, Eur. Phys. J. **C77** (2017), arXiv:1611.09661 [hep-ex].

[81] ATLAS Collaboration, G. Aad et al., *The ATLAS Inner Detector Trigger performance in pp collisions at 13 TeV during LHC Run 2*, arXiv:2107.02485 [hep-ex].

[82] ATLAS Collaboration, P. Jenni, M. Nessi, M. Nordberg, and K. Smith, *ATLAS high-level trigger, data-acquisition and controls: Technical Design Report.* Technical Design Report ATLAS. CERN, Geneva, 2003. https://cds.cern.ch/record/616089.

[83] ATLAS Collaboration, *Performance of the ATLAS muon trigger in pp collisions at* $\sqrt{s} = 8$ *TeV*, Eur. Phys. J. C **75** no. 3, (2015).

[84] ATLAS Collaboration, *The ATLAS Level-1 Calorimeter Trigger*, Journal of Instrumentation **3** no. 03, (2008) P03001. http://stacks.iop.org/1748-0221/3/i=03/a=P03001.

[85] ATLAS Collaboration, *Operation of the ATLAS trigger system in Run 2*, Journal of Instrumentation **15** no. 10, (2020) P10004–P10004. http://dx.doi.org/10.1088/1748-0221/15/10/P10004.

[86] ATLAS Collaboration, *Studies for the development of the Inner Detector trigger algorithms at ATLAS*, Tech. Rep. ATL-DAQ-PUB-2013-002, CERN, Geneva, Sep, 2013. https://cds.cern.ch/record/1602918.

[87] P. Yepes, *A fast track pattern recognition*, Nuclear Instruments and Methods in Physics Research Section A: Accelerators, Spectrometers, Detectors and Associated Equipment **380** no. 3, (1996) 582 – 585. http://www.sciencedirect.com/science/article/pii/0168900296007267.

[88] M. Sutton, *Tracking at level 2 for the ATLAS high level trigger*, Nuclear Instruments and Methods in Physics Research Section A: Accelerators, Spectrometers, Detectors and Associated Equipment **582** no. 3, (2007) 761 – 765. http://www.sciencedirect.com/science/article/pii/S0168900207021122. VERTEX 2006.

[89] R. Frühwirth, *Application of Kalman filtering to track and vertex filtering*, Nucl.Instrum.Meth. **A262** (1987).

[90] T. Cornelissen, M. Elsing, I. Gavrilenko, W. Liebig, E. Moyse, and A. Salzburger, *The new ATLAS track reconstruction (NEWT)*, Journal of Physics: Conference Series **119** no. 3, (2008) 032014. https://doi.org/10.1088/1742-6596/119/3/032014.

[91] ATLAS Collaboration, *Performance of the ATLAS Silicon Pattern Recognition Algorithm in Data and Simulation at* $\sqrt{s} = 7$ *TeV*, Tech. Rep. ATLAS-CONF-2010-072, CERN, Geneva, Jul, 2010. https://cds.cern.ch/record/1281363.

[92] ATLAS Collaboration, *ATLAS inner detector: Technical Design Report, 1.* Technical Design Report ATLAS. CERN, Geneva, 1997. https://cds.cern.ch/record/331063.

[93] ATLAS Collaboration, S. Haywood, L. Rossi, R. Nickerson, and A. Romaniouk, *ATLAS inner detector: Technical Design Report, 2.* Technical Design Report ATLAS. CERN, Geneva, 1997. https://cds.cern.ch/record/331064.

[94] T. G. Cornelissen, M. Elsing, I. Gavrilenko, J.-F. Laporte, W. Liebig, M. Limper, K. Nikolopoulos, A. Poppleton, and A. Salzburger, *The global χ^2 track fitter in ATLAS*, Journal of Physics: Conference Series **119** no. 3, (2008) 032013. https://doi.org/10.1088/1742-6596/119/3/032013.

[95] ATLAS Collaboration, K. Choi, *Tracking and Vertexing with the ATLAS Inner Detector in the LHC Run-2*, Jun, 2017. https://cds.cern.ch/record/2271033.

[96] ATLAS Collaboration, *Performance of the ATLAS Inner Detector Track and Vertex Reconstruction in the High Pile-Up LHC Environment*, Tech. Rep. ATLAS-CONF-2012-042, CERN, Geneva, Mar, 2012. https://cds.cern.ch/record/1435196.

[97] F. Meloni, *Primary vertex reconstruction with the ATLAS detector*, Journal of Instrumentation **11** no. 12, (2016) C12060–C12060. https://doi.org/10.1088/1748-0221/11/12/c12060.

[98] ATLAS Collaboration, *Muon reconstruction performance of the ATLAS detector in proton–proton collision data at $$\sqrt{s}$$=13 TeV*, The European Physical Journal C **76** no. 5, (2016) 292. https://doi.org/10.1140/epjc/s10052-016-4120-y.

[99] ATLAS Collaboration, *Performance of the ATLAS muon trigger in 2011*, Tech. Rep. ATLAS-CONF-2012-099, CERN, Geneva, Jul, 2012. https://cds.cern.ch/record/1462601.

[100] M. Aaboud, G. Aad, B. Abbott, D. C. Abbott, O. Abdinov, B. Abeloos, D. K. Abhayasinghe, S. H. Abidi, O. S. AbouZeid, and et al., *Electron reconstruction and identification in the ATLAS experiment using the 2015 and 2016 LHC proton–proton collision data at $\sqrt{s} = 13$ TeV*, The European Physical Journal C **79** no. 8, (2019). http://dx.doi.org/10.1140/epjc/s10052-019-7140-6.

[101] G. Jungman, M. Kamionkowski, and K. Griest, *Supersymmetric dark matter*, Physics Reports **267** no. 5, (1996) 195 – 373. http://www.sciencedirect.com/science/article/pii/0370157395000585.

[102] D. Albornoz Vásquez, G. Bélanger, and C. Bœhm, *Revisiting light neutralino scenarios in the MSSM*, Physical Review D **84** no. 9, (2011). http://dx.doi.org/10.1103/PhysRevD.84.095015.

[103] J. Alwall, R. Frederix, S. Frixione, V. Hirschi, F. Maltoni, O. Mattelaer, H. S. Shao, T. Stelzer, P. Torrielli, and M. Zaro, *The automated computation of tree-level and next-to-leading order differential cross sections, and their matching to parton shower simulations*, JHEP **07** (2014) 079, arXiv:1405.0301 [hep-ph].

[104] ATLAS Collaboration, *ATLAS Pythia 8 tunes to 7 TeV data*, tech. rep., 2014. https://bib-pubdb1.desy.de/record/193122. OA.

[105] R. D. Ball, V. Bertone, S. Carrazza, C. S. Deans, L. Del Debbio, S. Forte, A. Guffanti, N. P. Hartland, J. I. Latorre, J. Rojo, and M. Ubiali, *Parton distributions with LHC data*, Nuclear Physics B **867** no. 2, (2013) 244 – 289. http://www.sciencedirect.com/science/article/pii/S0550321312005500.

[106] B. Fuks, M. Klasen, D. R. Lamprea, and M. Rothering, *Precision predictions for electroweak superpartner production at hadron colliders with Resummino*, The European Physical Journal C **73** no. 7, (2013) 2480.

[107] W. Beenakker, M. Klasen, M. Kramer, T. Plehn, M. Spira, and P. Zerwas, *The Production of charginos / neutralinos and sleptons at hadron colliders*, Phys. Rev. Lett. **83** (1999) 3780–3783, arXiv:hep-ph/9906298. [Erratum: Phys.Rev.Lett. 100, 029901 (2008)].

[108] G. Bozzi, B. Fuks, and M. Klasen, *Threshold resummation for slepton-pair production at hadron colliders*, Nuclear Physics B **777** no. 1-2, (2007) 157–181. http://dx.doi.org/10.1016/j.nuclphysb.2007.03.052.

[109] B. Fuks, M. Klasen, D. R. Lamprea, and M. Rothering, *Revisiting slepton pair production at the Large Hadron Collider*, Journal of High Energy Physics **2014** no. 1, (2014). http://dx.doi.org/10.1007/JHEP01(2014)168.

[110] J. Fiaschi and M. Klasen, *Slepton pair production at the LHC in NLO+NLL with resummation-improved parton densities*, Journal of High Energy Physics **2018** no. 3, (2018). http://dx.doi.org/10.1007/JHEP03(2018)094.

[111] Particle Data Group Collaboration, C. Patrignani et al., *Review of Particle Physics*, Chin. Phys. **C40** no. 10, (2016) 100001.

[112] ATLAS Collaboration, *Muon reconstruction performance in early $\sqrt{s}$ = 13 TeV data*,. https://cds.cern.ch/record/2047831.

[113] ATLAS Collaboration, *Jet Calibration and Systematic Uncertainties for Jets Reconstructed in the ATLAS Detector at $\sqrt{s}$ = 13 TeV*, Tech. Rep. ATL-PHYS-PUB-2015-015, CERN, Geneva, Jul, 2015. https://cds.cern.ch/record/2037613.

[114] ATLAS Collaboration, *Monte Carlo Calibration and Combination of In-situ Measurements of Jet Energy Scale, Jet Energy Resolution and Jet Mass in ATLAS*, Tech. Rep. ATLAS-CONF-2015-037, CERN, Geneva, Aug, 2015. http://cds.cern.ch/record/2044941.

[115] ATLAS Collaboration, M. Aaboud et al., *Determination of jet calibration and energy resolution in proton-proton collisions at $\sqrt{s}$ = 8 TeV using the ATLAS detector*, Eur. Phys. J. C **80** no. 12, (2020) 1104, arXiv:1910.04482 [hep-ex].

[116] ATLAS Collaboration, *Selection of jets produced in 13TeV proton-proton collisions with the ATLAS detector*, Tech. Rep. ATLAS-CONF-2015-029, CERN, Geneva, Jul, 2015. http://cds.cern.ch/record/2037702.

[117] M. Aaboud, G. Aad, B. Abbott, O. Abdinov, B. Abeloos, D. K. Abhayasinghe, S. H. Abidi, O. S. AbouZeid, N. L. Abraham, and et al., *Measurements of b-jet tagging efficiency with the ATLAS detector using $t\bar{t}$ events at $\sqrt{s}$=13 TeV*, Journal of High Energy Physics **2018** no. 8, (2018). http://dx.doi.org/10.1007/JHEP08(2018)089.

[118] ATLAS Collaboration, *Performance of missing transverse momentum reconstruction for the ATLAS detector in the first proton-proton collisions at at $\sqrt{s}$= 13 TeV*, Tech. Rep. ATL-PHYS-PUB-2015-027, CERN, Geneva, Jul, 2015. http://cds.cern.ch/record/2037904.

[119] ATLAS Collaboration, *Performance of missing transverse momentum reconstruction in proton-proton collisions at $\sqrt{s}$ = 7 TeV with ATLAS*, Eur. Phys. J. C **75** no. 1844, (2012).

[120] M. Cacciari and G. P. Salam, *Pileup subtraction using jet areas*, Physics Letters B **659** no. 1, (2008) 119–126. https://www.sciencedirect.com/science/article/pii/S0370269307011094.

[121] C. Lester and D. Summers, *Measuring masses of semi-invisibly decaying particle pairs produced at hadron colliders*, Physics Letters B **463** no. 1, (1999) 99 – 103. http://www.sciencedirect.com/science/article/pii/S0370269399009454.

[122] A. Barr, C. Lester, and P. Stephens, *m(T2): The Truth behind the glamour*, J. Phys. **G29** (2003) 2343–2363, arXiv:hep-ph/0304226 [hep-ph].

[123] L. Moneta, K. Belasco, K. Cranmer, S. Kreiss, A. Lazzaro, D. Piparo, G. Schott, W. Verkerke, and M. Wolf, *The RooStats Project*, 2011. arXiv:1009.1003 [physics.data-an].

[124] R. Brun and F. Rademakers, *ROOT: An object oriented data analysis framework*, Nucl. Instrum. Meth. **A389** (1997) 81–86.

[125] D. R. Tovey, *On measuring the masses of pair-produced semi-invisibly decaying particles at hadron colliders*, Journal of High Energy Physics **2008** no. 04, (2008) 034–034. https://doi.org/10.1088/1126-6708/2008/04/034.

[126] G. Cowan, K. Cranmer, E. Gross, and O. Vitells, *Asymptotic formulae for likelihood-based tests of new physics*, Eur. Phys. J. **C71** (2011) 1554, arXiv:1007.1727 [physics.data-an]. [Erratum: Eur. Phys. J.C73,2501(2013)].

[127] ATLAS Collaboration, *Jet energy scale measurements and their systematic uncertainties in proton-proton collisions at $\sqrt{s}$ = 13 TeV with the ATLAS detector*, Phys. Rev. **D96** no. 7, (2017) 072002, arXiv:1703.09665 [hep-ex].

[128] T. Mitani, M. A. Pickering, and et.al., *Measurement of the tau lepton reconstruction and identification performance in the ATLAS experiment using pp collisions at $\sqrt{s}$ = 13 TeV*, Tech. Rep. ATL-COM-PHYS-2016-929, CERN, Geneva, Jul, 2016. https://cds.cern.ch/record/2199788.

[129] ATLAS Collaboration, *Measurement of the Inelastic Proton-Proton Cross Section at $\sqrt{s} = 13$ TeV with the ATLAS Detector at the LHC*, Phys. Rev. Lett. **117** (2016) 182002. https://link.aps.org/doi/10.1103/PhysRevLett.117.182002.

[130] ATLAS Collaboration, *The ATLAS Tau Trigger in Run 2*, Tech. Rep. ATLAS-CONF-2017-061, CERN, Geneva, Jul, 2017. http://cds.cern.ch/record/2274201.

[131] ATLAS Collaboration, *Luminosity determination in pp collisions at $\sqrt{s} = 13$ TeV using the ATLAS detector at the LHC*, Tech. Rep. ATLAS-CONF-2019-021, CERN, Geneva, Jun, 2019. https://cds.cern.ch/record/2677054.

[132] E. Bothmann, M. Schönherr, and S. Schumann, *Reweighting QCD matrix-element and parton-shower calculations*, The European Physical Journal C **76** no. 11, (2016) 590. https://doi.org/10.1140/epjc/s10052-016-4430-0.

[133] J. Butterworth, S. Carrazza, A. Cooper-Sarkar, A. D. Roeck, J. Feltesse, S. Forte, J. Gao, S. Glazov, J. Huston, Z. Kassabov, and et al., *PDF4LHC recommendations for LHC Run II*, Jan, 2016. http://dx.doi.org/10.1088/0954-3899/43/2/023001.

[134] M. Baak, G. J. Besjes, D. Côte, A. Koutsman, J. Lorenz, and D. Short, *HistFitter software framework for statistical data analysis*, Eur. Phys. J. **C75** (2015) 153, arXiv:1410.1280 [hep-ex].

[135] ROOT Collaboration, K. Cranmer, G. Lewis, L. Moneta, A. Shibata, and W. Verkerke, *HistFactory: A tool for creating statistical models for use with RooFit and RooStats*, Tech. Rep. CERN-OPEN-2012-016, New York U., New York, Jan, 2012. https://cds.cern.ch/record/1456844.

[136] G. Cowan, *Statistical Data Analysis*. Oxford science publications. Clarendon Press, 1998. https://books.google.co.uk/books?id=ff8ZyW0nlJAC.

[137] G. Cowan, *Statistics for Searches at the LHC*. Springer International Publishing, 2015. https://doi.org/10.1007/978-3-319-05362-2_9.

[138] A. L. Read, *Presentation of search results: The CL(s) technique*, J. Phys. **G28** (2002) 2693–2704. [,11(2002)].

[139] ATLAS, *Search for the electroweak production of supersymmetric particles in $\sqrt{s} = 8$ TeV pp collisions with the ATLAS detector*, arXiv:1402.7029 [hep-ex].

[140] CMS Collaboration, *Searches for electroweak production of charginos, neutralinos, and sleptons decaying to leptons and W, Z, and Higgs bosons in pp collisions at 8 TeV*, The European Physical Journal C **74** no. 9, (2014) 3036. https://doi.org/10.1140/epjc/s10052-014-3036-7.

[141] A. M. Sirunyan, A. Tumasyan, W. Adam, F. Ambrogi, E. Asilar, T. Bergauer, J. Brandstetter, E. Brondolin, M. Dragicevic, and et al., *Search for supersymmetry in events with a τ lepton pair and missing transverse momentum in proton-proton collisions at $\sqrt{s} = 13$ TeV*, Journal of High Energy Physics **2018** no. 11, (2018). http://dx.doi.org/10.1007/JHEP11(2018)151.

[142] G. Aad, B. Abbott, J. Abdallah, O. Abdinov, R. Aben, M. Abolins, O. S. AbouZeid, H. Abramowicz, H. Abreu, and et al., *Topological cell clustering in the ATLAS calorimeters and its performance in LHC Run 1*, The European Physical Journal C **77** no. 7, (2017). http://dx.doi.org/10.1140/epjc/s10052-017-5004-5.

[143] G. Aad, B. Abbott, J. Abdallah, S. Abdel Khalek, A. A. Abdelalim, O. Abdinov, B. Abi, M. Abolins, O. S. AbouZeid, H. Abramowicz, and et al., *ATLAS measurements of the properties of jets for boosted particle searches*, Physical Review D **86** no. 7, (2012). http://dx.doi.org/10.1103/PhysRevD.86.072006.

[144] CMS Collaboration, *Jet algorithms performance in 13 TeV data*, Tech. Rep. CMS-PAS-JME-16-003, CERN, Geneva, 2017. https://cds.cern.ch/record/2256875.

[145] G. Aad, B. Abbott, D. C. Abbott, A. A. Abud, K. Abeling, D. K. Abhayasinghe, S. H. Abidi, O. S. AbouZeid, N. L. Abraham, and et al., *Performance of electron and photon triggers in ATLAS during LHC Run 2*, The European Physical Journal C **80** no. 1, (2020). http://dx.doi.org/10.1140/epjc/s10052-019-7500-2.

[146] G. Aad, B. Abbott, D. Abbott, A. A. Abud, K. Abeling, D. Abhayasinghe, S. Abidi, O. AbouZeid, N. Abraham, H. Abramowicz, and et al., *Electron and photon performance measurements with the ATLAS detector using the 2015–2017 LHC proton-proton collision data*, Journal of Instrumentation **14** no. 12, (2019) P12006–P12006. http://dx.doi.org/10.1088/1748-0221/14/12/P12006.

[147] ATLAS Collaboration, *Tagging and suppression of pileup jets with the ATLAS detector*, tech. rep., CERN, Geneva, May, 2014. https://cds.cern.ch/record/1700870. All figures including auxiliary figures are available at https://atlas.web.cern.ch/Atlas/GROUPS/PHYSICS/CONFNOTES/ATLAS-CONF-2014-018.

[148] S. Alioli, P. Nason, C. Oleari, and E. Re, *Vector boson plus one jet production in POWHEG*, JHEP **01** (2011) 095, arXiv:1009.5594 [hep-ph].

[149] T. Sjöstrand, S. Mrenna, and P. Z. Skands, *A brief introduction to PYTHIA 8.1*, Comput. Phys. Commun. **178** (2008) 852–867, arXiv:0710.3820 [hep-ph].

[150] D. J. Lange, *The EvtGen particle decay simulation package*, Nucl. Instrum. Meth. **462** no. 1–2, (2001) 152 – 155.

[151] J. Pumplin, D. R. Stump, J. Huston, H.-L. Lai, P. Nadolsky, and W.-K. Tung, *New Generation of Parton Distributions with Uncertainties from Global QCD Analysis*, Journal of High Energy Physics **2002** no. 07, (2002) 012–012. https://doi.org/10.1088%2F1126-6708%2F2002%2F07%2F012.

[152] ATLAS Collaboration, *Measurement of the Z/γ^* boson transverse momentum distribution in pp collisions at $\sqrt{s}$=7 TeV with the ATLAS detector*, Journal of High Energy Physics **2014** no. 9, (2014) 145. https://doi.org/10.1007/JHEP09(2014)145.

[153] Z. Marshall, *Re-re-defining the Standard QCD Di-Jet Samples: Beginning to like event weights*, Tech. Rep. ATL-COM-PHYS-2015-417, CERN, Geneva, May, 2015. https://cds.cern.ch/record/2016630.

[154] ATLAS Collaboration, *Electron reconstruction and identification in the ATLAS experiment using the 2015 and 2016 LHC proton–proton collision data at $\sqrt{s}$= 13 TeV*, The European Physical Journal C **79** no. 8, (2019) 639. https://doi.org/10.1140/epjc/s10052-019-7140-6.

[155] ATLAS Collaboration, *ATLAS Fake Tau Tool*, 2019. https://gitlab.cern.ch/atlas-perf-tau/atlasfaketautool.

[156] P. Calafiura, W. Lavrijsen, C. Leggett, M. Marino, and D. Quarrie, *The Athena Control Framework in Production, New Developments and Lessons Learned*,. https://cds.cern.ch/record/865624.

[157] F. a. James, *MINUIT: Function Minimization and Error Analysis Reference Manual*,. https://cds.cern.ch/record/2296388. CERN Program Library Long Writeups.

[158] R. Barlow and C. Beeston, *Fitting using finite Monte Carlo samples*, Computer Physics Communications **77** no. 2, (1993) 219 – 228. http://www.sciencedirect.com/science/article/pii/001046559390005W.

[159] ATLAS Collaboration, M. Aaboud et al., *Search for the direct production of charginos and neutralinos in final states with tau leptons in $\sqrt{s}$ = 13 TeV pp collisions with the ATLAS detector*, Eur. Phys. J. C **78** no. 2, (2018) 154, arXiv:1708.07875 [hep-ex].

[160] ATLAS Collaboration, *Letter of Intent for the Phase-II Upgrade of the ATLAS Experiment*,. https://cds.cern.ch/record/1502664. Draft version for comments.

[161] B. Scholz, *First Observation of Coherent Elastic Neutrino-Nucleus Scattering*. Springer International Publishing, 2018. http://dx.doi.org/10.1007/978-3-319-99747-6.

[162] J. D. Bjorken, *Rapidity gaps and jets as a new physics signature in very high-energy hadron hadron collisions*, Phys. Rev. D **47** (1993) 101–113.

[163] G. Giudice, T. Han, K. Wang, and L.-T. Wang, *Nearly Degenerate Gauginos and Dark Matter at the LHC*, Physical Review D **81** (2010) .

[164] A. G. Delannoy et al., *Probing Dark Matter at the LHC using Vector Boson Fusion Processes*, Phys. Rev. Lett. **111** (2013) 061801, arXiv:1304.7779 [hep-ph].

[165] A. Buckley, J. Butterworth, S. Gieseke, D. Grellscheid, S. Hoche, et al., *General-purpose event generators for LHC physics*, Phys.Rept. **504** (2011). http://arXiv.org/abs/1101.2599.

[166] CMS Collaboration, *Search for supersymmetry in the vector-boson fusion topology in proton-proton collisions at* $\sqrt{s}$*=8 TeV*, Journal of High Energy Physics **2015** no. 11, (2015) 189. https://doi.org/10.1007/JHEP11(2015)189.

[167] ATLAS Collaboration, *Reconstruction of hadronic decay products of tau leptons with the ATLAS experiment*, The European Physical Journal C **76** no. 5, (2016) 295. https://doi.org/10.1140/epjc/s10052-016-4110-0.

This thesis was typeset using the LaTeX typesetting system created by Leslie Lamport.
The body text size is set to 11 pt with *Utopia Regular* with *Fourier* font, part of TeX Live.
The bibliography was typeset using the ATLAS-paper style.